GAS-RICH GALAXIES IN THE ALFALFA SURVEY: FROM HI DWARFS TO GIANTS

A Dissertation

Presented to the Faculty of the Graduate School

of Cornell University

in Partial Fulfillment of the Requirements for the Degree of

Doctor of Philosophy

by

Shan Huang

August 2013

GAS-RICH GALAXIES IN THE ALFALFA SURVEY: FROM HI DWARFS TO GIANTS

Shan Huang, Ph.D.

Cornell University 2013

Making use of galaxy catalog generated by the ALFALFA survey ($\alpha.40$) and photometry from the Sloan Digital Sky Survey (SDSS) and *GALEX*, etc., we investigate the gas, stellar, and star formation (SF) properties of HI-selected galaxies in the local universe. In addition to the HI 21 cm line measurements, stellar masses (M_*) and star formation rates (SFRs) are derived from fitting the UV-optical spectral energy distributions.

We examine 229 low HI mass dwarf galaxies, including a complete sample of 176 galaxies with HI masses $< 10^{7.7}\ M_\odot$ and HI line widths < 80 km s^{-1}. A large fraction of the dwarfs have high specific star formation rates (SSFRs) and estimates of their SFRs and M_* obtained by SED fitting are systematically smaller than ones derived via standard formulae assuming a constant SFR. The increased dispersion of the SSFR distribution at $M_* \lesssim 10^8\ M_\odot$ is driven by a set of dwarf galaxies that have low gas fractions and SSFRs; some of these are dE/dSphs in the Virgo cluster.

We investigate the global scaling relations and fundamental planes linking stars and gas for a sample of 9417 common galaxies: the $\alpha.40$-SDSS-*GALEX* sample. 96% of the $\alpha.40$-SDSS-*GALEX* galaxies belong to the blue cloud, with the average gas fraction $f_{\rm HI} \equiv M_{\rm HI}/M_* \sim 1.5$. A transition in SF properties is found whereby below $M_* \sim 10^{9.5}\ M_\odot$, the slope of the star forming sequence changes, the dispersion in the specific star formation rate (SSFR) distribution

increases and the star formation efficiency (SFE) mildly increases with M_*. The evolutionary track in the SSFR–M_* diagram, as well as that in the color magnitude diagram are linked to the HI content; below this transition mass, the SF is regulated strongly by the HI. Comparison of HI- and optically-selected samples over the same restricted volume shows that the HI-selected population is less evolved and has overall higher SFR and SSFR at a given stellar mass, but lower SFE and extinction, suggesting either that a bottleneck exists in the HI to H_2 conversion, or that the process of SF in the very HI-dominated galaxies obeys an unusual, low efficiency star formation law. A trend is found that, for a given stellar mass, high gas fraction galaxies reside preferentially in dark matter halos with high spin parameters (λs).

We present an Hα dataset of 29 HIghMass galaxies identified from the $\alpha.40$ catalog as HI massive disks with extraordinary $f_{\rm HI}$s. The high gas fractions may due to suppressed SF in the past as a result of the high λ halos. The sample contains several low surface brightness galaxies, which are strong candidates of the galaxies in high λ halos. Alternatively, some others may be attributed to late cold gas accretion given the extended UV disks or the centrally-peaked SF history. There is no evidence of abnormal behavior of massive star formation. The integrated SFRs demonstrate that the HIghMass galaxies exhibit healthy ongoing SF despite of potentially inactive SF in the past. However, the SF activities are spread throughout extended disks so that they have overall lower SFR surface densities and lower surface brightness in the R-band. The majority of HIghMass galaxies have higher EWs and being bluer in the outer disks, implying inside-out disk growth. Downbending double exponential disks are more frequent than upbending disks among the gas-rich galaxies. SF thresholds exist in the downbending disks probably as a result of concentrated gas distribution.

BIOGRAPHICAL SKETCH

Shan Huang was born in Chengdu, China, on April 3, 1985. She grew up in Shenzhen, China. After graduating from high school there, she attended the University of Science and Technology of China, majoring in Physics. Following her graduation from USTC in 2007, Shan began her graduate studies in Astronomy at Cornell University. Her time in Ithaca was mainly spent on researching the properties of galaxies detected by the ALFALFA survey. After graduating from Cornell in Summer of 2013, she will begin a postdoctoral fellowship at ASIAA, Taiwan, supporting the ongoing research projects within the ALMA group.

ACKNOWLEDGEMENTS

Martha and Riccardo – Thank you for giving me the chance to work with you in the ALFALFA group in 2008, and for your guidance since then. Thank you for observing with me and I learned from you how to make best use of time during the run. Thank you for teaching me proposal writing so that I am buried in data. Thank you for your patience in my poor English and making all the changes in my papers for even grammar and spelling issues.

Every member of the ALFALFA collaboration – Thank you for observing, flagging, baselining, flatfielding, and extracting signals for the galaxies that I was able to use in this work.

Jarle Brinchmann – Thank you for passing me your models and always being the first to reply to my emails when I ask for external advice on my papers and proposals.

John Salzer – Thank you for giving me the chance to observe at the 0.9-m WIYN telescope on my own. Thank you for helping me with the Hα image processing.

Betsey, Manolis, and all other EGGs – Thank you for answering all my questions.

Mom, Dad, and all the rest of my family – Thank you for supporting all my decisions.

Yiming – Discussion with you is always enlightening. Your commute, your help, and your love make this work possible.

TABLE OF CONTENTS

LIST OF TABLES

LIST OF FIGURES

CHAPTER 1

INTRODUCTION

The 21cm line arises from a change in the energy state of neutral hydrogen atoms and provides rich information of the gas in galaxies. The line flux and systematic recessional velocity probe simultaneously the gas amount and redshift of the galaxies without costly optical spectroscopic followup. In addition, the HI disks are usually more extended than the optical ones so that the HI line widths can be an inference of dynamic masses. In individual galaxies, it can serve as an index of future star formation (SF) fertility and traces the dynamics of host dark matter halos. Statistically, the relative HI content study in galaxies as cluster or group members is a useful tool to characterize the environmental effect. The next generation of radio telescopes will be designed to use the HI detections in more distant galaxies to estimate cosmological parameters, to understand the evolution of gas density, and to address the questions as the nature of dark energy through the signatures of baryon acoustic oscillation. Thanks to the improvement of sensitivity, spectral and spatial resolution, and bandwidth of modern telescopes, the observation of 21cm lines is becoming increasingly important.

1.1 Galaxy formation and evolution

While it is now generally accepted that galaxies form when cold gas condenses from the hot and ionized material at the centers of dark matter haloes via a hierarchical process, the details of gas acquisition and this assembly remain largely unknown. Recent analysis has been mainly focused on investigating the stellar population and SF. However, the evolution of the gaseous medium, especially

the cold phase ($T < 100$ K) as traced in neutral atomic (HI) or molecular (H_2) hydrogen, should also be monitored. The cold gas plays a fundamental role as the ingredient for SF and it is the only plausible site of SF [Kennicutt and Evans, 2012]. The amount of cold gas in a galaxy at any given time reflects the complex interplay between processes that either replenish it, such as cooling and accretion [Kereš et al., 2005, Sancisi et al., 2008], mergers with other gas-rich galaxies; or deplete it, such as SF, environmental effects, and feedback from massive stars and accreting supermassive blackholes [Croton et al., 2006]. Hence in this framework, galaxy evolution is governed by the cycle of baryons exchanging matter and energy between galaxies and the surrounding intergalactic gas.

At high redshift, the merging mode of SF contributes significantly to the build-up of stellar mass (M_*). However, the existence of a tight correlation between M_* and the star formation rate (SFR), followed by star-forming galaxies up to at least $z \sim 2$, suggests that SF is mainly regulated by secular processes with much longer duty cycles, e.g., smooth accretion of gas. The observations of damped Lyman-α systems show that the cosmic density of HI is characterized by very mild evolution with redshift [Noterdaeme et al., 2009] . It has also been the preferred theoretical model that galaxies live in a slowly-evolving equilibrium between gas inflow, outflow, and SF in the local Universe [Davé et al., 2012]. Collecting observational evidence of all the pieces in the gas circulation will reveal the balance between gas replenishment and depletion: whether the cold gas supply can sustain the current SF, or is a population of galaxies consuming their gas so rapidly that they will soon migrate into the gas-poor regime with their SF quenched?

In order to obtain a complete picture of all the components that are involved

in the processes of galaxy evolution, we conducted a multi-wavelength study of the galaxies detected in the ALFALFA survey. A homogeneous HI-selected sample with ancillary optical and UV data enables a systematic examination of the interplay between the gas, stars, and SF.

1.2 Surveys of HI gas in nearby galaxies

The Arecibo telescope has been playing an important role in the history of HI surveys at which the pioneer programs were carried out. Data of the Arecibo HI Stripe Survey [AHISS; Zwaan et al., 1997] were taken in driftscan mode during the period of 1993 August and 1994 February. Divided into two stripes, its total sky coverage was $\sim 65\ \mathrm{deg}^2$, with a depth of $cz = 7400\ \mathrm{km\,s^{-1}}$. The survey yielded 66 significant extragalactic signals, of which approximately 50% are cataloged galaxies. The Arecibo Dual Beam Survey [ADBS; Rosenberg and Schneider, 2002] covered $\sim 430\ \mathrm{deg}^2$ of sky, detecting 265 galaxies. They are the first generation of blind extragalactic HI surveys with limited sky coverage.

Later, the HI Jodrell All Sky Survey [HIJASS; Lang et al., 2003], making use of the multibeam receiver on the Lovell Telescope, surveyed $\sim 1115\ \mathrm{deg}^2$ of sky. HIJASS reached to 10,000 km s^{-1}, with a velocity resolution of 18.1 km s^{-1} and spatial positional accuracy of $\sim$2.5 arcmin. The published catalog including 222 confirmed sources, out of which 170 are associated with a previously cataloged galaxy. The HI Parkes All Sky Survey [HIPASS; Meyer et al., 2004] is the first real all sky HI survey, which uses the 13-beam receiver on the Parkes Telescope to cover the entire southern region. The claimed velocity range is out to 12,700 km s^{-1}, although the sensitivity drops significantly before reaching the

edge (median redshift only 3,000 km s^{-1}). Their catalog included 4,315 sources.

ALFALFA is a second generation of blind HI line survey conducted at the Arecibo. It is one order of magnitude more sensitive than the HIPASS with four times better angular resolution, three times better spectral resolution, and 1.6 times total spectral bandwidth. As a result, the source density is 29 times that of the HIPASS. Observation has been accomplished in Oct 2012, covering a total of $\sim 7000\ \mathrm{deg}^2$ out to $cz = 18000\ \mathrm{km\,s^{-1}}$. The current published catalog, α.40 [Haynes et al., 2011], includes sources extracted from 40% of the survey area. The 15,041 extragalactic sources are label as code 1 or 2. Code 1 sources are of high signal-to-noise ratio ($\mathrm{S/N} > 6.5$); code 2 sources have $4.5 < \mathrm{S/N} < 6.5$ but coincide with an optical counterpart (OC) of known optical redshift matching the HI measurement. HIPASS detected only 11 objects with $M_{\mathrm{HI}} < 10^{7.5}\ M_{\odot}$ whereas ALFALFA is detecting hundreds of such low mass systems. Taking advantage of the large survey volume, ALFALFA found a rich population of galaxies with $M_{\mathrm{HI}} > 10^{10}\ M_{\odot}$ [Martin et al., 2010]. The ALFALFA enables an exploration of the HI bearers over a cosmologically significant volume with adequate statistics and dynamic range.

1.3 Large multi-wavelength surveys of galaxies

Despite the $\sim 3.5\ \mathrm{arcmic}$ ALFA beam width, the median centroiding accuracy of the HI sources is only $\sim 20\ \mathrm{arcsec}$ allowing the identification of most probable OCs in 97% of cases [Haynes et al., 2011]. The α.40 catalog covers two regions in the Spring sky (i.e., the Virgo direction, $7^{\mathrm{h}}30^{\mathrm{m}} < \mathrm{RA} < 16^{\mathrm{h}}30^{\mathrm{m}}$, $4^{\circ} < \mathrm{Dec} < 16^{\circ}$ and $24^{\circ} < \mathrm{Dec} < 32^{\circ}$) and two in the Fall sky (i.e., the anti-Virgo direction,

$22^{\rm h} < {\rm RA} < 3^{\rm h}$, $14^\circ < {\rm Dec} < 16^\circ$ and $24^\circ < {\rm Dec} < 28^\circ$).

The ALFALFA survey area in spring sky overlaps with the footprint of the Sloan Digital Sky Survey (SDSS) DR7 [Abazajian et al., 2009], providing supplementary optical data of the HI detections. The SDSS Legacy survey is one of the three surveys that make up the SDSS. It images the sky in five bands over a contiguous 7646 deg^2 high-latitude elliptical region in the Northern Galactic Cap, plus an additional 750 deg^2 in the Southern Galactic Cap, together with spectroscopy of complete samples of galaxies and quasars covering about 8200 deg^2. Haynes et al. [2011] attempt to identify the most probable OC of each HI line sources in the α.40 catalog, making use of the information such as coordinate and redshift coincidence, angular size, color and morphology. Of the 15,041 clearly extragalactic HI sources included in the α.40 catalog, 201 have no OC, 2310 lie outside the DR7 footprint, and 60 appear to be in the region of the SDSS imaging survey but cannot be associated with an object in the SDSS photometric database. In most of the latter cases, the OC is evident in the images but is projected close to a bright foreground star or contaminated by its glare. The SDSS pipeline measurements are retrieved according to the identifier provided in Haynes et al. [2011], in order to quantify the stellar properties of the ALFALFA galaxies.

The Galaxy Evolution Explorer (*GALEX*) is a NASA Small Explorer Class mission that observed galaxies in UV light by an orbiting space telescope [Morrissey et al., 2007]. Its imaging survey simultaneously images the sky in FUV (effective wavelength of 1516 Å) and NUV (effective wavelength of 2267 Å), with a circular field of view of $\sim 1.2^\circ$ in diameter. The images were processed through a pipeline, and the resulting image resolutions are 4.3 arcsec (NUV)

and 5.3 arcsec (FUV), respectively. In particular, the exposure time of the median imaging survey (MIS) is typically 1,500s (a single orbit), yielding limiting magnitudes of $\sim$22.7 mag in both the FUV and NUV. It is designed to cover 1000 deg^2 in positions that match the SDSS spectroscopic footprint, although the FUV channel failed before survey completion. The All-Sky Imaging Survey (AIS) data are used in supplementary, covering 26,000 deg^2 of sky. With a typical exposure time of 100s, the depth of AIS is 20.2 mag in both bands. Among 14840 extragalactic α.40 sources with OCs, 1828 (12.3%) have no *GALEX* counterpart returned within 36 arcsec. 516 (3.5%) are excluded because they lie too close to a *GALEX* field edge and 1317 (8.9%) are not matched because all neighbors are detected only in one band but not the other. The remaining 11179 OCs are matched to the nearest neighbor in the *GALEX* GR6 catalog with 7752 (52.2%) matched to UV sources found in the AIS and 3427 (23.1%) to ones in the MIS. The *GALEX* pipeline measurements which characterize the SF in ALFALFA galaxies are assembled.

1.4 Overview

Given the importance of proposed future extragalactic HI surveys at high redshift by the SKA, it is critical to develop a full understanding of the characteristics of gas rich galaxies at the present epoch. However, all surveys are biased by the properties that define them, so that this goal is not addressed by the existing studies of the optically-selected samples. For instance, HI rich galaxies tend to be blue, of late type, and less clustered than their gas-poor counterparts [West et al., 2010]. Since $M_{\rm HI}/L_{\rm opt}$ increases with decreasing $L_{\rm opt}$, HI-selected samples are more inclusive of star-forming galaxies of similar depth. Taking advantage

of the ALFALFA catalog in combination with the optical and UV data, we conducted a multi-wavelength study of the HI-selected population, from the dwarf galaxies to the HI giants.

This dissertation is organized as follows. In Chapter 2, we examine 229 low HI mass dwarf galaxies, including 176 galaxies with $M_{\rm HI} < 10^{7.7}\ M_{\odot}$ and HI line widths < 80 km s^{-1}. General properties and scaling relations of the α.40-SDSS-*GALEX* common sample are investigated in Chapter 3, in comparison with the optically-selected galaxies. Chapter 4 focuses on 34 massive HI-rich galaxies, first discovered by the ALFALFA as a population. The HI measurements are linked to the stellar and SF properties in order to reveal the regulation of galaxy evolution by the gas content. We suggest future work with the massive HI-rich galaxies in Chapter 5.

CHAPTER 2

GAS, STARS AND STAR FORMATION IN ALFALFA DWARF GALAXIES

2.1 Introduction

Principal aims of current studies of galaxy formation and evolution include the exploration of the interplay between the gaseous and stellar components of galaxies and the mechanisms which trigger the conversion of gas into stars. During the last decade, wide area surveys such as the Sloan Digital Sky Survey (SDSS) and the Galaxy Evolution Explorer (*GALEX*) have enabled statistical studies of star formation (SF) in the local universe. For example, galaxies which are currently forming stars, the so-called "blue-cloud galaxies" in the color-magnitude diagram [Baldry et al., 2004], occupy a relatively narrow "star-forming sequence" in a plot of specific star formation rate ($\mathrm{SSFR} = \mathrm{SFR}/M_*$) versus stellar mass M_* [Brinchmann et al., 2004, Salim et al., 2007], with the SSFR declining as the stellar mass increases. Such a trend suggests that the galaxy's stellar mass regulates the overall star formation history (SFH), at least at intermediate masses. This star-forming sequence breaks down above $\sim 10^{10}\ M_\odot$, where the "red sequence", occupied by massive galaxies having lower values of the SSFR, becomes more prominent. The importance of the gaseous component is reflected in the Kennicutt-Schmidt law which relates the gas column density (Σ_{gas}) to the SFR surface density (Σ_{SFR}). A super-linear slope is sometimes reached, e.g. ~ 1.4 as in Kennicutt [1998b], indicating that the star formation

*This chapter is published in Shan et al. (2012a)

efficiency is higher in regions of higher gas surface density. However, the empirical relations among galaxy properties which are derived from such surveys apply to the galaxy populations which dominate them, typically the more massive and luminous galaxies. The same relations may not apply to dwarf or low surface brightness (LSB) galaxies. Of particular relevance to this work, in such objects the environment where star formation occurs may be quite different.

Compared to the optically bright and massive systems which dominate the SDSS, gas-rich dwarf galaxies are often underrepresented in samples selected by stellar mass. Often the optical emission arising in such systems is very blue, patchy and of very low surface brightness or small in extent. However, gas-rich, low mass, low metallicity, low optical surface brightness galaxies are important to the study of star formation because the processes by which gas is converted into stars within such systems may mimic those which occurred in the early universe. As the most chemically unevolved systems within the present-day galaxy population, the faintest dwarfs represent unique laboratories for understanding star formation and galaxy evolution in extreme environments, that is, in regimes of low metallicity, low dust content, low pressure, low shear, and low escape velocity [Begum et al., 2008].

Several recent works suggest that the star formation in dwarf galaxies may proceed quite differently from that in large spirals. Based on a sample of very local dwarf irregular galaxies, the Faint Irregular Galaxies GMRT Survey [FIGGS, Begum et al., 2008, Roychowdhury et al., 2009], found a lower average $\Sigma_{\rm SFR}$ than would be expected from the Kennicutt-Schmidt law [Kennicutt, 1998b]. Moreover, no threshold density is observed below which star formation is completely turned off. Recently, Lee et al. [2007] explored the distribution of the

SSFR against absolute magnitude for a complete sample of $\sim$300 star-forming galaxies within 11 Mpc of the Milky Way, from the 11Mpc Hα UV Galaxy Survey (11HUGS). In addition to confirming the transition in star formation activity at the high mass end, those authors found a second transition, with low luminosity dwarf galaxies ($M_B \gtrsim -15$) having a very large spread in their SSFRs. This second transition suggests that the star-forming behavior may be distinct at the lowest mass range. After showing that other potential drivers are not able to explain the magnitude of observed systematics, Lee et al. [2009a] suggest that the over-prediction of the SFR by the UV flux compared to that estimated from Hα in dwarf systems is consistent with an initial mass function (IMF) deficient in the most massive stars. However, those authors also point out that it is possible that some combination of effects may conspire to produce the observed trend, and thus the requirement of systematic variations in the IMF can be avoided.

The 11HUGS sample is complete in HI mass only above $2 \times 10^8\ M_\odot$, becoming rapidly incomplete at smaller HI masses. To develop further the current understanding of how the gas supply regulates star formation in the lowest mass systems, a larger sample of extreme dwarf galaxies is needed. Making use of the Arecibo L-band Feed Array (ALFA), the on-going Arecibo Legacy Fast ALFA (ALFALFA) extragalactic HI line survey is specially designed to identify low mass, gas rich objects in the local universe [Giovanelli et al., 2005b]. Because of its combination of wide areal coverage, sensitivity, and velocity resolution, ALFALFA has already detected more than 400 galaxies with HI masses $M_{\rm HI} < 10^8\ M_\odot$ [Haynes et al., 2011]. While star formation is more directly linked to the molecular interstellar component, the detection of CO in low-metallicity dwarfs is difficult [Leroy et al., 2005, and references therein], suggesting further that CO no longer traces H_2 well. Furthermore, in many gas-rich dwarf galax-

ies, the HI component dominates both the gas as well as the baryonic mass [e.g. Leroy et al., 2007]. The combination of HI parameters from ALFALFA with complementary multi-wavelength data contributed by SDSS and *GALEX* provides an ideal dataset to investigate the abundance and distribution of gas-rich dwarfs and to explore the relations among their gas content, stellar populations and star formation properties.

This chapter is organized as follows. In §2.2 we define our HI-selected sample and present its basic gas properties. In §2.3 we present the supplementary SDSS and *GALEX* data, especially our re-processed UV photometry. The directly measured colors and selected spectroscopic behavior are also briefly examined. In §2.4 we describe how we utilize SED fitting techniques to obtain physical parameters for the dwarfs, e.g., M_* and the dust extinction-corrected SFR. We discuss in §2.5 the relations between gas, star and star formation in dwarfs, and how they compare to the overall ALFALFA HI-selected population. A summary is presented in §2.6.

All the distance-dependent quantities in this work are computed assuming $\Omega = 0.3$, $\Lambda = 0.7$ and $H_0 = 70$ km s^{-1} Mpc^{-1}, and a Chabrier [2003] IMF is adopted.

2.2 Sample selection

In this section, we use the 40% ALFALFA catalog [α.40: Haynes et al., 2011] to define two HI-selected dwarf galaxy samples, one of which is complete in HI mass and velocity width (*s-com*). The second sample (*s-sup*) is less restrictive in those parameters but supplements the first through the availability of deeper

GALEX NUV/FUV observations. We discuss here the selection of these two samples and their HI properties. In §2.4.1, we will define a third sample *s-sed* as a subset of dwarfs among the *s-com* and *s-sup* samples.

2.2.1 The ALFALFA-SDSS parent sample

Begun in 2005, the ALFALFA survey has been using the 7-beam ALFA receiver to conduct a blind search for HI sources with $cz < 18000$ km s^{-1} over 7000 deg^2 of high galactic latitude sky [Giovanelli et al., 2005b]. The targeted regions cover the sky visible to Arecibo $0 <$ Dec. $< +36^{\circ}$ in both the spring ($07^h30^m <$ R.A. $< 16^h30^m$) and fall ($22^h00^m <$ R.A. $< 03^h00^m$) night sky. With a median cz of $\sim$ 8200 km s^{-1}, ALFALFA for the first time samples the HI population over a cosmologically fair volume, and is expected to detect $\sim$ 30,000 extragalactic HI-line sources out to redshifts of $z \sim 0.06$. As a second generation wide area HI survey, ALFALFA is designed to greatly improve on the HI census derived from previous results. For example, ALFALFA is 8 times more sensitive than the HI Parkes All-Sky Survey [HIPASS Barnes et al., 2001], with 4 times the angular resolution and 3 times the velocity resolution, all of which are essential to the discovery of the lowest HI mass objects. In particular, HIPASS detected only 11 objects with $M_{\rm HI} < 10^{7.5}\ M_{\odot}$ [Zwaan et al., 2005] whereas ALFALFA is detecting hundreds of such low mass systems. For example, at the distance of the Virgo Cluster, ALFALFA is sensitive down to $\sim 3 \times 10^7\ M_{\odot}$ for sources with signal-to-noise ratio S/N ~6.5 [Giovanelli et al., 2007, Haynes et al., 2011]. In addition, HI source positions derived from ALFALFA can be determined with a median accuracy of about 20″ [see Eqn 1 of Haynes et al., 2011], allowing the identification of optical/UV counterparts for the vast majority of HI sources without

the need for follow-up synthesis mapping. While source confusion within the 3.5′ beam can affect sources at large distance, it has little effect on the identification of nearby dwarfs, except when they are located in close proximity to giant neighbors.

The current ALFALFA survey, "$\alpha.40$", covers $\sim 40\%$ of the final survey area, and includes a catalog of 15855 HI sources, 15041 of which are extragalactic [Haynes et al., 2011]. The remainder have no optical counterparts (OCs) and lie at low velocities which are consistent with Galactic phenomena, e.g., as high velocity clouds (HVCs). ALFALFA HI detections are further categorized by source reliability: Code 1 sources are reliable extragalactic detections with high S/N $\gtrsim 6.5$ while Code 2 sources, also known as "priors", have lower S/N ($4.5 \lesssim$ S/N $\lesssim 6.5$) but coincide with an OC of known optical redshift matching the HI measurement. The HVCs are identified as Code 9 objects. Further details are given in Haynes et al. [2011].

HI masses in units of solar mass are obtained from the relation $M_{\rm HI} = 2.356 \times 10^5 D^2\ S_{\rm int}$, where D is the distance in Mpc and $S_{\rm int}$ is the integrated HI line flux density in units of Jy km s^{-1}. In the local universe, distance determinations suffer significantly from the uncertainty introduced by a galaxy's peculiar velocity. In order to minimize the HI mass error introduced by the uncertainty in distances, we adopt a peculiar velocity flow model which incorporates both primary distances available from the literature and secondary distances derived from the SFI++ survey [Springob et al., 2007]. The flow model derived by Masters [2005] is adopted for galaxies with $cz_{\rm CMB} < 6000$ km s^{-1}, while distances for more distant objects are derived from redshifts in the CMB rest frame. Primary distances are assigned to individual galaxies wherever available from the

literature, and following the method discussed in Springob et al. [2007], galaxies identified as members of groups and clusters are placed at the distance to their assigned hierarchical unit. We have been conservative in ambiguous cases, assigning larger distances where a choice is given to avoid the inclusion of higher mass galaxies in the present analysis.

All of the spring sky coverage of ALFALFA and part of the fall sky survey region overlap the footprint of the SDSS Legacy Survey, thereby allowing a direct cross-match of the two. As part of the ALFALFA catalog production process, the HI detections have been cross matched to SDSS DR7 photometric objects for 12470 of the $\alpha.40$ HI detections [Haynes et al., 2011]. Through SED fitting to the five SDSS photometric bands (see §2.4.1), we are able to derive additional basic properties of the full $\alpha.40$-SDSS HI selected parent sample. A more detailed discussion of the $\alpha.40$-SDSS-*GALEX* sample in general, as well as the selection effects characteristic of the $\alpha.40$ survey will be presented in Huang et al. [2012a]. As discussed in Haynes et al. [2011], the identification of OCs to the $\alpha.40$ HI sources and the cross match to the SDSS DR7 is not a perfect process; in individual cases, the wrong counterpart may have been selected, the SDSS photometry may be bad etc. However, the cross match with the SDSS DR7 allows us to make a first statistical study of the relationships between gas, stars and star formation, and provides us with a parent sample of gas-rich galaxies within which we can explore the distinctiveness of the lowest HI mass systems.

2.2.2 A complete HI-selected dwarf sample

The studies which infer global properties derived from the SDSS main galaxy catalog are highly biased against the inclusion of dwarf irregular galaxies because of the magnitude and surface brightness limits on the SDSS spectroscopic targets ($r \lesssim 17.77$ and $\mu_{r,50} \lesssim 23.0$ mag arcsec^{-2}). Since $M_{\rm HI}/L_{\rm opt}$ increases with decreasing $L_{\rm opt}$, HI-selected samples are more inclusive of star-forming galaxies than optical samples of similar depth. Because of their relatively young stellar populations and low dust contents, gas-rich dwarfs are typically blue and often patchy in optical appearance; at the same time, they are often extended and diffuse in HI. Since the cold gas is the fuel needed to sustain star-formation, a blind HI survey of sufficient depth, like ALFALFA, is especially effective in identifying star forming systems at the low mass end, and hence should offer a full census of star forming galaxies in the local universe.

In order to identify a sample of low mass, gas-rich dwarfs, we have applied selection criteria to the $\alpha.40$ catalog as follows: (i) ALFALFA detection code = 1 or 2 (reliable sources and priors, but no HVCs); (ii) $\log M_{\rm HI} < 7.7$; (iii) velocity width of the HI line, $W_{50} < 80$ km s^{-1}; (iv) the optical images were visually inspected to eliminate the ones without optical counterparts, those which appear to be more massive but HI-deficient galaxies. Following the detailed analysis of the HI mass error in Martin et al. [2010] and Haynes et al. [2011], the $\log M_{\rm HI}$ error in the 7.5 bin is ~ 0.2 dex. Hence, requirement (ii) ensures that we are unlikely to miss dwarfs with $\log M_{\rm HI} < 7.5$ due to their HI mass error. Criterion (iii) helps to insure that we include only truly low mass systems. Based on criterion (iv), 2 gas-poor face-on giant galaxies (UGC 7622 = NGC 4469 and UGC 7718 = NGC 4526) have been removed. Both have SDSS r-band absolute Petrosian

magnitudes brighter than -18 and are early type spirals situated in the Virgo cluster; their HI masses and velocity widths are unusually low, probably due to interaction within the cluster environment. Additionally, extragalactic HI sources without OCs (38 of them) are dropped. As discussed by Haynes et al. [2011], the majority of those are part of the extended HI structures in the Leo region: the Leo Ring and Leo Triplet [Stierwalt et al., 2009] or are similar fragments associated with nearby groups of galaxies. With these objects removed, the final complete ALFALFA dwarf galaxy sample, referred to hereafter as *s-com*, contains 176 galaxies.

The designation of 'complete' for this HI-selected sample emphasizes that it is a complete subset of the $\alpha.40$ catalog. Because the ALFALFA sensitivity depends not only on the integrated flux but also on the profile width, there is no simple translation of a limiting flux to the lower limit on the HI mass but the completeness can be well characterized [Haynes et al., 2011]. Of particular relevance here, we note that, at the mean $W_{50} = 36.8$ km s^{-1} of the *s-com* galaxies, $\alpha.40$ is 90% complete to $\log M_{\rm HI} = 7.1$ and 25% complete to $\log M_{\rm HI} = 6.9$, within a distance of 11Mpc. In comparison, the 11HUGS sample is complete in $\log M_{\rm HI}$ only to 8.3 [Lee et al., 2009b] within the same distance. While we include all the low HI mass detections in the *s-com* sample out to a distance of ~ 30 Mpc, the $\alpha.40$ completeness limit at that distance is well above the HI mass upper limit of the *s-com* sample, $\log M_{\rm HI} = 7.7$. Thus, *s-com* sample is not complete in a volume-limited sense, but it does probe the extreme low HI mass tail of the $\alpha.40$ catalog.

2.2.3 Supplementary dwarf galaxies with *GALEX* data

Since ALFALFA is an on-going survey, its catalog of HI detections continues to grow with time. Similarly, the simultaneous undertaking of the *GALEX* satellite mission has provided some opportunity to obtain images in the NUV and FUV bands for early ALFALFA detections, at least until the *GALEX* FUV channel failure in 2009. Because exploration of the population of galaxies which define the low mass end of the HI mass function (HIMF) has always been one of the main goals of ALFALFA, we proposed to obtain *GALEX* MIS (Medium Imaging Survey) level FUV and NUV observations of low HI mass targets, based on early releases of the ALFALFA catalog, in *GALEX* cycles 3, 4 and 5 (GI3-84, GI4-42 and GI5-2). As ALFALFA has progressed, the identification of the lowest HI mass population has likewise been an ongoing process, extending to lower HI masses as its catalog of HI sources has grown. Hence, the complete $\alpha.40$ low mass sample *s-com* as defined above is more restrictive in HI mass than our *GALEX* target dwarf galaxy lists which were based on early ALFALFA catalogs. Fortunately, although the criteria for the *GALEX* target selection derived from the early ALFALFA catalogs were less restrictive in terms of HI mass and velocity width, the ALFALFA-based *GALEX* targets are nonetheless of relatively low mass. Of the 77 galaxies for which we acquired *GALEX* FUV/NUV observations, 24 overlap with the strictly complete sample *s-com*. The remaining 53 galaxies have somewhat higher HI masses (see discussion in §2.2.4); we refer to this supplementary sample as *s-sup*. While the *s-sup* sample is not complete in any sense, the availability of *GALEX* MIS-depth imaging in both FUV and NUV bands for its galaxies allows us to explore with better statistics the low HI mass systems so that we can test for trends (or thresholds) with HI mass at the low mass end of the HIMF.

2.2.4 HI properties of the ALFALFA dwarf sample

The combination of the two samples *s-com* and *s-sup* yields a final ALFALFA-selected set of 229 low HI mass and low velocity width dwarf galaxies upon which we base the analysis presented here. Table 2.1 presents the relevant UV, SDSS and HI properties for them. The magnitudes given in Table 2.1 have been corrected for foreground reddening. Columns are as follows:

- Column(1): ALFALFA catalog identifier (also known as the AGC number).
- Columns(2) and (3): J2000 position of the OC assigned to the HI source.
- Columns(4) and (5): The adopted FUV and NUV magnitudes, with their associated error, respectively, as derived via our reprocessing of the *GALEX* images (see §2.3.2).
- Column(6): The r-band *modelmag* with its associated error, from the SDSS pipeline.
- Column(7): The $u - r$ color with its associated error, from the SDSS pipeline.
- Column(8): The SDSS code sFlag indicating the quality of SDSS photometry as defined in §2.3.3.
- Column(9): The adopted distance with error, in Mpc.
- Column(10): The logarithm of the HI mass and its error, taken from the $\alpha.40$ catalog [Haynes et al., 2011].
- Column(11): The logarithm of the stellar mass and its error, derived from SED fitting (see §2.4.2)
- Column(12): The logarithm of the SFR and its error, in solar masses per year (see §2.4.5)

Table 2.1: Properties of dwarf sample

AGC	RA(J2000)	Dec(J2000)	$m_{\rm FUV}$	$m_{\rm NUV}$	r	$u-r$	sFlag	D	$\log M_{\rm HI}$	$\log M_*$	$\log {\rm SFR}$
	[^{h} ^{m} ^{s}]	[$^\circ$ $'$ $''$]	[mag]	[mag]	[mag]	[mag]		[Mpc]	[$M_\odot$]	[$M_\odot$]	[$M_\odot$ yr^{-1}]
102728*	00 00 21.4	+31 01 19	20.42(0.09)	20.00(0.05)	18.70(0.04)	0.83(0.16)	par	9.1(2.3)	6.78(0.52)	5.73(0.53)	-3.01(0.55)
748778*	00 06 34.3	+15 30 39	19.78(0.09)	19.65(0.05)	18.14(0.05)	0.81(0.19)	par	4.6(2.3)	6.36(1.01)	5.31(1.01)	-3.78(1.12)
102558	00 07 04.6	+27 01 28	20.42(0.10)	20.10(0.06)	17.82(0.02)	0.96(1.31)	pbphot	41.7(2.3)	8.27(0.14)	...	...
748779	00 07 51.8	+15 45 18	...	...	18.86(0.05)	1.08(0.29)	par	12.4(2.3)	7.09(0.38)	...	...
101772	00 11 08.6	+14 14 23	...	...	16.70(0.01)	0.98(0.06)	par	11.7(2.3)	7.54(0.40)	...	...
102655	00 30 13.6	+24 17 59	...	18.90(0.02)	17.32(0.01)	1.02(0.06)	oly	23.1(2.3)	7.81(0.22)	...	...
113753*	01 21 02.1	+26 05 20	19.68(0.07)	19.33(0.04)	17.90(0.01)	0.80(0.05)	oly	42.2(2.3)	8.33(0.14)	7.30(0.13)	-1.80(0.72)
114027	01 34 41.7	+14 38 36	...	...	17.52(0.02)	0.33(0.06)	domi	10.1(2.3)	7.40(0.46)	...	...
112503	01 38 00.3	+14 58 58	...	...	16.29(0.01)	1.24(0.04)	par	10.2(2.3)	7.14(0.46)	...	...
1171	01 39 44.8	+15 53 58	18.21(0.03)	17.74(0.01)	...	...	...	7.3(1.5)	7.42(0.41)	...	...
112505	01 40 09.6	+15 56 24	20.03(0.09)	19.84(0.04)	...	...	...	10.3(2.3)	7.12(0.46)	...	...
112521	01 41 08.0	+27 19 20	20.71(0.13)	20.00(0.07)	...	...	...	4.6(2.3)	6.53(1.02)	...	...
110482	01 42 17.3	+26 22 00	18.23(0.04)	17.95(0.02)	...	...	...	5.6(2.3)	6.99(0.84)	...	...
111945	01 44 42.7	+27 17 18	...	...	...	...	...	6.4(2.3)	7.48(0.73)	...	...
111946	01 46 42.2	+26 48 05	...	...	...	...	...	5.7(2.3)	6.76(0.82)	...	...
111977	01 55 20.2	+27 57 14	18.10(0.03)	17.74(0.02)	...	...	...	5.5(0.3)	6.78(0.13)	...	...
111164	02 00 10.1	+28 49 52	...	...	...	...	...	4.9(0.3)	6.57(0.14)	...	...
122401*	02 28 19.5	+26 07 31	17.76(0.03)	17.39(0.02)	14.92(0.01)	1.69(0.05)	domi	23.0(2.3)	8.19(0.21)	8.43(0.22)	-1.41(0.26)
122206	02 31 00.3	+27 57 30	18.05(0.05)	17.75(0.03)	...	...	...	21.2(2.3)	8.60(0.22)	...	...
122400	02 31 22.1	+25 42 45	...	...	18.71(0.10)	0.59(0.42)	pbphot	12.7(2.3)	7.53(0.37)	...	...
122212*	02 31 39.4	+27 10 46	18.06(0.03)	17.81(0.02)	15.32(0.00)	1.45(0.03)	domi	13.3(2.3)	7.36(0.36)	7.74(0.36)	-2.24(0.46)
123162	02 32 39.7	+29 26 21	...	...	...	...	...	13.3(2.3)	7.30(0.36)	...	...
122397	02 38 05.9	+30 40 16	...	...	...	...	...	11.7(2.3)	7.60(0.40)	...	...

Table2.1 – Continued

AGC	RA(J2000)	Dec(J2000)	$m_{\rm FUV}$	$m_{\rm NUV}$	r	$u-r$	sFlag	D	$\log M_{\rm HI}$	$\log M_*$	$\log {\rm SFR}$
	[^{h} ^{m} ^{s}]	[$^\circ$ $'$ $''$]	[mag]	[mag]	[mag]	[mag]		[Mpc]	[$M_\odot$]	[$M_\odot$]	[$M_\odot$ yr^{-1}]
122219	02 40 55.6	+26 40 05	...	...	16.62(0.02)	1.13(0.07)	par	19.7(2.3)	7.66(0.26)	...	...
123170	02 44 03.2	+29 17 19	...	...	17.34(0.02)	1.67(0.24)	pbphot	12.1(2.3)	7.68(0.39)	...	...
122424	02 45 07.1	+25 56 10	...	...	...	...	...	20.4(2.3)	7.62(0.25)	...	...
122226	02 46 38.9	+27 43 35	...	...	...	...	...	6.8(2.3)	7.39(0.68)	...	...
122900	02 50 27.3	+24 18 34	...	18.56(0.04)	...	...	...	18.5(2.3)	7.94(0.25)	...	...
174585	07 36 10.3	+09 59 11	19.16(0.04)	18.76(0.02)	...	...	...	5.0(2.3)	6.50(0.94)	...	...
174605	07 50 21.6	+07 47 40	...	...	...	...	...	4.8(2.3)	6.55(0.97)	...	...
174514	07 52 30.9	+11 49 40	20.12(0.07)	20.09(0.04)	19.97(0.04)	0.36(0.13)	oly	30.4(2.3)	8.26(0.16)	5.75(0.19)	-2.44(0.17)
4115	07 57 01.9	+14 23 29	15.48(0.01)	15.48(0.01)	15.14(0.01)	1.18(0.03)	pbphot	7.7(0.5)	8.51(0.12)	...	...
181471	08 03 24.6	+15 08 28	18.67(0.03)	18.27(0.02)	17.56(0.02)	1.36(0.11)	pbphot	30.3(2.3)	8.36(0.16)	...	...
182460	08 03 43.9	+10 08 58	18.23(0.02)	18.00(0.01)	17.23(0.01)	0.90(0.03)	pbphot	39.1(2.3)	8.60(0.14)	...	...
188862	08 09 17.8	+08 43 39	...	...	19.47(0.02)	1.47(0.12)	oly	17.2(2.3)	7.54(0.29)	...	...
188955	08 21 37.0	+04 19 01	...	...	18.35(0.03)	0.47(0.07)	pbphot	11.8(2.3)	7.30(0.40)	...	...
188762*	08 23 31.3	+15 09 05	20.01(0.09)	19.65(0.06)	18.60(0.04)	0.63(0.13)	domi	38.7(2.3)	8.38(0.14)	7.29(0.23)	-1.69(0.20)
188875*	08 26 30.6	+11 47 12	19.12(0.04)	18.79(0.02)	16.41(0.01)	1.43(0.05)	par	29.3(2.3)	7.94(0.18)	7.89(0.18)	-2.16(0.55)
182595	08 51 12.1	+27 52 48	...	...	16.47(0.02)	1.27(0.05)	domi	5.9(2.3)	6.53(0.80)	...	...
182462	08 52 33.8	+13 50 28	18.84(0.06)	18.26(0.03)	16.60(0.01)	1.23(0.06)	domi	23.9(2.3)	8.57(0.20)	7.44(0.20)	-1.41(0.24)
191791	09 08 53.8	+14 35 02	20.72(0.10)	20.04(0.06)	17.36(0.03)	0.94(0.09)	par	9.5(0.8)	6.77(0.36)	6.66(0.19)	-3.09(0.60)
198507	09 15 25.8	+25 25 10	...	...	18.48(0.03)	0.52(0.07)	oly	7.4(2.3)	6.95(0.63)	...	...
198354	09 16 30.9	+09 10 24	...	...	18.05(0.03)	1.91(0.25)	oly	20.7(2.3)	7.47(0.26)	...	...
191894*	09 21 15.0	+09 43 52	19.89(0.06)	19.50(0.03)	17.21(0.01)	1.35(0.04)	oly	21.9(2.3)	7.39(0.25)	7.37(0.23)	-2.23(0.37)
198508	09 22 57.0	+24 56 48	...	...	17.47(0.02)	1.15(0.08)	domi	7.7(2.3)	6.71(0.62)	...	...
192039*	09 47 31.4	+10 29 32	19.65(0.06)	19.23(0.04)	17.61(0.02)	1.40(0.08)	oly	47.4(2.3)	8.39(0.15)	7.78(0.14)	-1.48(0.17)
191803	09 48 05.9	+07 07 43	...	...	15.99(0.01)	1.27(0.04)	domi	7.2(2.3)	7.33(0.65)	...	...

Table2.1 – Continued

AGC	RA(J2000) [^{h} ^{m} ^{s}]	Dec(J2000) [$^\circ$ $'$ $''$]	$m_{\rm FUV}$ [mag]	$m_{\rm NUV}$ [mag]	r [mag]	$u-r$ [mag]	sFlag	D [Mpc]	$\log M_{\rm HI}$ [$M_\odot$]	$\log M_*$ [$M_\odot$]	$\log {\rm SFR}$ [$M_\odot$ yr^{-1}]
193921	09 49 14.9	+15 48 27	20.63(0.10)	20.67(0.07)	18.36(0.04)	1.58(0.24)	oly	23.3(2.3)	7.90(0.22)	6.76(0.22)	-3.43(0.67)
731430	09 57 29.4	+27 45 24	...	...	17.44(0.02)	1.11(0.06)	par	19.3(2.3)	7.55(0.26)	...	...
5373	10 00 00.0	+05 19 56	13.66(0.00)	13.44(0.00)	20.60(0.04)	0.30(0.10)	pbphot	1.3(0.6)	7.51(0.91)	...	...
205097	10 00 02.4	+15 46 07	20.46(0.09)	19.78(0.05)	17.52(0.02)	2.17(0.19)	domi	35.9(2.3)	8.21(0.16)	8.38(0.14)	-1.89(0.25)
205104*	10 01 55.2	+15 45 37	19.50(0.05)	19.34(0.03)	17.72(0.02)	1.27(0.11)	par	34.8(2.3)	8.32(0.15)	7.53(0.16)	-1.93(0.19)
205105*	10 02 51.0	+14 33 12	18.35(0.03)	18.17(0.02)	16.87(0.01)	0.96(0.03)	domi	42.8(2.3)	8.27(0.14)	7.73(0.13)	-1.20(0.17)
202240	10 21 20.2	+12 10 37	17.68(0.02)	17.23(0.01)	15.73(0.02)	1.52(0.03)	pbphot	43.3(2.3)	8.83(0.11)	...	...
731448	10 23 45.0	+27 06 39	...	...	16.02(0.01)	1.01(0.02)	oly	7.5(2.3)	7.10(0.62)	...	...
202243*	10 26 41.8	+11 53 51	18.75(0.03)	18.44(0.02)	16.77(0.02)	1.09(0.04)	par	35.3(2.3)	8.78(0.13)	7.71(0.15)	-1.37(0.23)
208394	10 28 43.8	+04 44 04	...	...	21.54(0.12)	0.58(0.38)	pbphot	19.2(2.3)	7.69(0.26)	...	...
731454	10 28 58.6	+25 17 13	...	...	16.90(0.02)	1.31(0.04)	domi	20.7(2.3)	7.31(0.27)	...	...
749315	10 29 06.4	+26 54 38	...	...	18.64(0.02)	0.67(0.06)	oly	9.2(2.3)	6.83(0.52)	...	...
749316	10 30 09.6	+27 23 19	...	...	18.03(0.02)	0.91(0.09)	pbphot	21.7(2.3)	7.69(0.23)	...	...
203709	10 30 44.3	+06 07 31	...	...	15.90(0.02)	1.21(0.04)	domi	8.2(2.3)	7.25(0.57)	...	...
205156	10 30 52.9	+12 26 48	...	...	18.17(0.02)	1.29(0.06)	oly	11.1(0.7)	6.97(0.18)	...	...
202015	10 31 54.1	+12 55 38	20.16(0.08)	19.70(0.05)	20.69(0.07)	2.07(0.80)	pbphot	43.1(2.3)	8.28(0.16)	...	...
731457	10 31 55.8	+28 01 33	17.80(0.02)	17.62(0.01)	16.11(0.01)	1.23(0.03)	pbphot	6.1(2.3)	6.74(0.76)	...	...
204139	10 32 01.3	+04 20 46	...	...	17.51(0.02)	1.11(0.06)	par	18.7(2.3)	7.58(0.27)	...	...
202248	10 34 56.1	+11 29 32	18.87(0.04)	18.63(0.02)	16.89(0.01)	0.96(0.05)	par	11.1(0.7)	7.29(0.15)	6.68(0.15)	-2.56(0.49)
205165	10 37 04.8	+15 20 15	18.51(0.03)	18.01(0.02)	15.56(0.01)	1.53(0.04)	domi	11.1(0.7)	6.94(0.16)	7.44(0.15)	-2.15(0.20)
208397	10 38 58.1	+03 52 27	...	...	20.01(0.05)	0.72(0.21)	oly	10.2(2.3)	7.01(0.47)	...	...
200512	10 39 55.6	+13 54 34	20.04(0.13)	19.10(0.06)	18.85(0.10)	1.25(0.56)	pbphot	11.1(0.7)	6.95(0.16)	...	...
208399	10 40 10.7	+04 54 32	...	...	19.22(0.06)	1.40(0.38)	pbphot	9.9(2.3)	7.39(0.47)	...	...
205078	10 41 26.1	+07 02 16	...	...	18.42(0.05)	0.90(0.19)	par	19.4(2.3)	7.58(0.26)	...	...

Table2.1 – Continued

AGC	RA(J2000)	Dec(J2000)	$m_{\rm FUV}$	$m_{\rm NUV}$	r	$u-r$	sFlag	D	$\log M_{\rm HI}$	$\log M_*$	$\log {\rm SFR}$
	[^{h} ^{m} ^{s}]	[$^\circ$ $'$ $''$]	[mag]	[mag]	[mag]	[mag]		[Mpc]	[$M_\odot$]	[$M_\odot$]	[$M_\odot$ yr^{-1}]
200532*	10 42 00.3	+12 20 07	18.38(0.03)	17.85(0.01)	15.20(0.00)	1.45(0.02)	domi	11.1(0.7)	7.48(0.14)	7.50(0.14)	-2.93(0.51)
203082	10 42 26.5	+13 57 26	...	...	16.57(0.02)	1.58(0.07)	domi	17.5(1.1)	7.59(0.15)	...	...
202024	10 44 57.5	+11 54 58	19.49(0.04)	19.24(0.03)	17.09(0.02)	1.05(0.06)	par	11.1(0.7)	6.82(0.18)	6.74(0.16)	-3.37(0.71)
205270	10 45 09.7	+15 27 00	...	...	16.23(0.00)	1.38(0.03)	oly	17.5(1.1)	7.49(0.17)	...	...
201970	10 46 53.2	+12 44 40	20.84(0.24)	20.13(0.12)	18.63(0.10)	1.24(0.49)	pbphot	11.1(0.7)	7.27(0.13)	...	...
201959*	10 47 27.5	+13 53 22	19.41(0.04)	18.74(0.02)	16.35(0.01)	1.48(0.03)	domi	45.6(2.3)	8.11(0.15)	8.42(0.12)	-0.92(0.18)
200603	10 49 17.1	+12 25 20	17.72(0.03)	17.21(0.01)	16.04(0.01)	1.15(0.03)	pbphot	17.5(1.1)	8.48(0.13)	...	...
205197*	10 49 42.8	+13 49 41	20.76(0.08)	20.64(0.06)	19.31(0.04)	1.29(0.16)	oly	17.5(1.1)	7.45(0.15)	6.24(0.17)	-3.13(0.18)
205198*	10 50 01.8	+13 47 05	18.35(0.02)	18.05(0.01)	16.53(0.00)	0.99(0.02)	oly	17.5(1.1)	7.67(0.15)	7.22(0.14)	-1.82(0.16)
205327*	10 53 35.5	+11 00 21	19.53(0.05)	19.49(0.03)	18.01(0.01)	1.03(0.05)	oly	44.7(2.3)	8.41(0.16)	7.35(0.12)	-1.75(0.17)
6014	10 53 42.7	+09 43 39	16.92(0.01)	16.77(0.01)	15.09(0.01)	1.48(0.05)	pbphot	11.1(0.7)	7.97(0.13)	...	...
202035	10 56 13.9	+12 00 37	17.76(0.02)	17.55(0.01)	16.29(0.01)	0.79(0.04)	domi	11.1(0.7)	7.73(0.13)	6.66(0.14)	-1.97(0.23)
205278*	10 58 52.2	+14 07 46	20.57(0.08)	19.55(0.03)	16.39(0.01)	1.65(0.06)	par	11.1(0.7)	7.01(0.19)	7.17(0.15)	-3.90(0.74)
215256*	11 03 26.3	+16 01 00	19.11(0.04)	18.56(0.03)	16.08(0.03)	1.68(0.07)	domi	21.0(2.3)	7.87(0.23)	7.94(0.24)	-1.71(0.27)
219117*	11 03 46.7	+08 34 19	20.12(0.07)	19.85(0.04)	18.01(0.02)	1.35(0.08)	par	17.5(1.1)	7.69(0.15)	6.80(0.15)	-2.63(0.18)
210023*	11 04 26.3	+11 45 21	17.50(0.02)	17.21(0.01)	15.34(0.01)	1.10(0.02)	par	11.1(0.7)	7.76(0.13)	7.35(0.15)	-1.94(0.29)
213757	11 05 59.6	+07 22 25	...	...	16.77(0.01)	1.34(0.03)	oly	17.5(1.1)	7.64(0.15)	...	...
215262	11 06 35.3	+12 13 48	...	...	17.93(0.03)	1.63(0.22)	pbphot	17.5(1.1)	7.61(0.14)	...	...
731550	11 07 07.7	+28 03 23	...	...	16.76(0.01)	1.12(0.05)	par	24.6(2.3)	7.62(0.26)	...	...
210082*	11 09 23.2	+10 50 03	16.88(0.02)	16.47(0.01)	14.44(0.00)	1.43(0.01)	par	17.5(1.1)	8.29(0.13)	8.36(0.14)	-1.16(0.21)
210111	11 10 25.1	+10 07 34	16.89(0.02)	16.67(0.01)	15.57(0.01)	1.32(0.03)	pbphot	17.5(1.1)	8.34(0.13)	...	...
219368	11 12 21.6	+24 04 39	...	...	21.20(0.12)	1.57(0.94)	pbphot	10.2(2.3)	7.31(0.46)	...	...
6245	11 12 39.8	+09 03 21	17.85(0.02)	16.59(0.01)	12.54(0.00)	2.04(0.01)	domi	17.5(1.1)	8.00(0.14)	9.52(0.16)	-0.92(0.28)
213796*	11 12 52.7	+07 55 19	19.12(0.04)	18.69(0.02)	16.83(0.01)	1.15(0.03)	oly	17.5(1.1)	7.62(0.15)	7.18(0.14)	-1.93(0.17)

Table2.1 – Continued

AGC	RA(J2000) [^{h} ^{m} ^{s}]	Dec(J2000) [$^\circ$ $'$ $''$]	$m_{\rm FUV}$ [mag]	$m_{\rm NUV}$ [mag]	r [mag]	$u-r$ [mag]	sFlag	D [Mpc]	$\log M_{\rm HI}$ [$M_\odot$]	$\log M_*$ [$M_\odot$]	$\log$ SFR [$M_\odot$ yr^{-1}]
215240	11 13 50.8	+09 57 39	...	...	18.04(0.02)	0.95(0.06)	oly	17.5(1.1)	7.52(0.15)	...	...
212824	11 13 59.4	+11 19 49	18.11(0.02)	17.91(0.02)	20.39(0.07)	1.07(0.38)	pbphot	44.5(2.3)	9.04(0.11)	...	...
215282	11 14 25.2	+15 32 02	...	...	16.07(0.00)	1.28(0.02)	pbphot	11.3(2.3)	6.94(0.43)	...	...
202256*	11 14 45.0	+12 38 51	18.98(0.04)	18.70(0.02)	16.87(0.01)	1.22(0.04)	par	10.0(0.6)	7.20(0.13)	6.72(0.14)	-2.61(0.16)
215284	11 15 32.4	+14 34 38	...	...	17.25(0.02)	1.17(0.05)	oly	19.7(2.3)	7.59(0.25)	...	...
215186	11 17 01.2	+04 39 44	...	...	17.75(0.01)	1.41(0.07)	oly	24.0(2.3)	7.56(0.24)	...	...
210220	11 17 01.1	+13 05 55	19.08(0.04)	18.18(0.02)	15.49(0.01)	2.03(0.06)	domi	10.0(0.6)	7.15(0.14)	7.66(0.13)	-1.89(0.16)
215286	11 19 12.7	+14 19 40	...	...	20.32(0.07)	1.68(0.44)	pbphot	10.0(0.6)	7.12(0.13)	...	...
202257	11 19 14.4	+11 57 07	17.75(0.02)	17.54(0.01)	16.32(0.02)	1.32(0.06)	pbphot	10.7(2.3)	7.95(0.44)	...	...
213074	11 19 28.1	+09 35 44	17.80(0.02)	17.58(0.01)	17.01(0.01)	0.45(0.02)	domi	13.7(2.3)	7.98(0.34)	6.28(0.35)	-1.79(0.34)
213511	11 22 23.4	+11 47 38	...	...	17.08(0.01)	1.15(0.03)	oly	17.5(1.1)	7.47(0.18)	...	...
213440	11 23 37.6	+12 53 45	...	19.18(0.03)	16.44(0.01)	1.42(0.05)	oly	10.0(0.6)	6.77(0.17)	...	...
215142*	11 24 44.5	+15 16 32	18.38(0.04)	17.95(0.02)	16.10(0.01)	1.29(0.03)	par	20.0(2.3)	8.37(0.23)	7.61(0.25)	-1.61(0.25)
215296*	11 26 55.1	+14 50 03	19.94(0.08)	19.58(0.04)	18.33(0.03)	0.82(0.07)	par	11.5(2.3)	7.26(0.41)	5.94(0.41)	-2.78(0.59)
219203	11 27 28.9	+05 37 02	...	...	18.03(0.03)	0.95(0.09)	par	25.0(2.3)	7.67(0.21)	...	...
212837	11 30 53.4	+14 08 46	...	17.74(0.02)	16.68(0.01)	1.17(0.07)	pbphot	10.7(2.3)	7.72(0.44)	...	...
215303	11 31 08.8	+13 34 14	...	19.04(0.03)	17.32(0.03)	1.12(0.05)	domi	15.0(2.3)	7.48(0.32)	...	...
215306	11 33 50.1	+14 49 28	...	18.67(0.02)	16.48(0.02)	1.29(0.04)	domi	20.4(2.3)	7.66(0.24)	...	...
215248	11 33 50.9	+14 03 15	...	18.85(0.02)	16.55(0.01)	1.31(0.04)	par	11.3(2.3)	6.80(0.44)	...	...
212838	11 34 53.4	+11 01 10	...	17.70(0.02)	17.35(0.02)	0.32(0.05)	pbphot	10.3(2.3)	7.60(0.45)	...	...
213155	11 37 08.6	+13 15 03	...	...	17.09(0.01)	0.62(0.04)	par	12.0(2.3)	7.64(0.39)	...	...
6655*	11 41 50.5	+15 58 24	16.43(0.01)	16.23(0.01)	14.15(0.00)	1.29(0.01)	oly	8.7(2.3)	7.38(0.54)	7.81(0.54)	-1.81(0.54)
213333	11 43 27.0	+11 23 54	...	...	15.86(0.00)	0.97(0.02)	oly	10.3(2.3)	7.31(0.46)	...	...
731804	11 49 25.8	+25 37 00	...	...	17.68(0.02)	1.33(0.06)	oly	29.2(2.3)	7.65(0.28)	...	...

Table2.1 – Continued

AGC	RA(J2000)	Dec(J2000)	$m_{\rm FUV}$	$m_{\rm NUV}$	r	$u-r$	sFlag	D	$\log M_{\rm HI}$	$\log M_*$	$\log {\rm SFR}$
	[^{h} ^{m} ^{s}]	[$^\circ$ $'$ $''$]	[mag]	[mag]	[mag]	[mag]		[Mpc]	[$M_\odot$]	[$M_\odot$]	[$M_\odot$ yr^{-1}]
210822	11 50 02.7	+15 01 24	...	...	14.95(0.00)	0.45(0.01)	pbphot	8.6(2.3)	7.45(0.54)	...	...
213174	11 51 04.8	+05 14 46	...	18.54(0.02)	17.01(0.01)	0.46(0.03)	par	25.0(2.3)	7.84(0.21)	...	...
215213	11 52 20.2	+15 27 36	...	...	17.61(0.16)	0.96(0.18)	pbphot	9.0(2.3)	7.15(0.52)	...	...
215145	11 54 12.4	+12 26 06	...	18.86(0.03)	19.01(0.08)	0.57(0.30)	par	16.7(4.2)	8.00(0.51)	...	...
224237	12 04 47.1	+10 37 35	18.73(0.04)	18.32(0.02)	16.78(0.01)	0.83(0.03)	par	39.3(2.3)	8.43(0.15)	7.77(0.16)	-0.93(0.20)
226606	12 09 21.2	+25 12 03	...	...	16.29(0.01)	1.29(0.03)	domi	8.7(2.3)	7.01(0.54)	...	...
224231	12 11 59.5	+05 55 02	...	...	16.78(0.01)	1.24(0.05)	par	8.1(2.3)	6.78(0.58)	...	...
220195	12 12 22.7	+06 58 46	19.76(0.05)	19.55(0.02)	17.13(0.01)	1.20(0.08)	par	24.2(4.8)	7.46(0.44)	7.47(0.40)	-2.54(0.55)
223286	12 13 48.1	+12 41 26	...	...	16.33(0.01)	1.44(0.05)	par	17.5(5.1)	7.60(0.59)	...	...
7285	12 15 56.3	+14 25 57	...	...	14.42(0.01)	1.96(0.02)	domi	16.7(1.7)	7.48(0.22)	...	...
220257	12 15 53.7	+14 01 30	...	...	16.68(0.02)	3.78(0.62)	pbphot	16.7(1.7)	7.51(0.21)	...	...
222297	12 16 13.0	+07 55 45	...	18.37(0.02)	14.61(0.00)	1.65(0.02)	domi	24.2(4.8)	7.57(0.45)	...	...
220261	12 16 11.8	+08 22 24	19.56(0.05)	19.22(0.03)	17.53(0.03)	2.40(0.47)	pbphot	16.6(2.0)	7.36(0.27)	...	...
220282	12 16 52.4	+14 30 55	...	...	14.34(0.01)	1.89(0.03)	domi	16.7(1.7)	7.57(0.22)	...	...
220289	12 17 10.7	+06 25 54	...	...	15.91(0.00)	1.31(0.02)	domi	24.2(4.8)	7.55(0.43)	...	...
732041	12 17 42.4	+27 29 03	...	...	16.18(0.01)	1.32(0.04)	par	21.6(2.3)	7.52(0.24)	...	...
223390	12 18 07.7	+05 55 47	19.09(0.04)	18.61(0.02)	16.46(0.01)	0.82(0.03)	oly	29.6(2.3)	7.69(0.23)	7.64(0.17)	-3.70(0.91)
229053	12 18 15.5	+25 34 05	...	...	17.32(0.02)	0.89(0.08)	par	8.1(2.0)	7.08(0.50)	...	...
220321	12 18 15.3	+13 44 56	...	...	15.29(0.00)	1.46(0.02)	oly	16.7(1.7)	7.50(0.22)	...	...
223407	12 18 43.8	+12 23 08	19.09(0.05)	18.41(0.02)	16.11(0.01)	1.45(0.05)	domi	16.7(0.6)	7.53(0.11)	7.59(0.09)	-1.72(0.17)
220336	12 18 51.3	+12 35 50	18.19(0.03)	17.83(0.02)	16.10(0.01)	0.95(0.04)	par	16.7(1.7)	7.60(0.21)	7.32(0.21)	-1.64(0.26)
220354*	12 19 15.6	+06 17 37	18.21(0.02)	17.60(0.01)	15.11(0.01)	1.46(0.02)	domi	16.6(2.0)	7.58(0.26)	7.98(0.25)	-1.62(0.42)
223449*	12 20 43.8	+14 37 51	19.29(0.07)	18.65(0.03)	16.41(0.01)	1.21(0.03)	oly	16.7(0.6)	7.31(0.15)	7.45(0.12)	-1.98(0.95)
220409	12 20 40.2	+13 53 20	...	...	16.27(0.01)	0.31(0.02)	oly	16.7(1.7)	7.65(0.21)	...	...

Table2.1 – Continued

AGC	RA(J2000)	Dec(J2000)	$m_{\rm FUV}$	$m_{\rm NUV}$	r	$u-r$	sFlag	D	$\log M_{\rm HI}$	$\log M_*$	$\log {\rm SFR}$
	[^{h} ^{m} ^{s}]	[$^\circ$ $'$ $''$]	[mag]	[mag]	[mag]	[mag]		[Mpc]	[$M_\odot$]	[$M_\odot$]	[$M_\odot$ yr^{-1}]
229052	12 20 41.1	+24 57 21	...	...	21.29(0.14)	0.80(0.43)	pbphot	9.5(2.3)	7.04(0.50)	...	...
224272*	12 20 38.6	+05 54 32	20.60(0.08)	20.02(0.04)	17.48(0.01)	1.33(0.07)	oly	16.6(2.0)	7.49(0.27)	7.02(0.26)	-2.96(0.63)
220418	12 20 57.6	+06 20 23	...	...	15.33(0.01)	1.41(0.02)	par	16.4(2.5)	7.49(0.32)	...	...
220419*	12 21 00.1	+12 43 33	19.02(0.05)	18.48(0.02)	16.42(0.01)	1.27(0.04)	oly	16.7(1.7)	7.81(0.21)	7.26(0.22)	-2.52(0.83)
220435	12 21 27.2	+15 01 17	20.10(0.12)	19.71(0.06)	20.12(0.09)	0.82(0.34)	pbphot	16.7(1.7)	7.59(0.21)	...	...
220450	12 22 07.6	+15 47 56	18.76(0.03)	17.96(0.01)	16.72(0.04)	0.95(0.09)	pbphot	16.7(1.7)	7.62(0.21)	...	...
220460	12 22 38.3	+06 00 53	...	...	16.26(0.01)	1.57(0.08)	par	16.4(2.5)	7.58(0.32)	...	...
220483	12 23 16.1	+07 41 15	-999(-999)	22.04(0.11)	18.35(0.07)	1.87(0.80)	pbphot	16.4(2.5)	7.23(0.34)	...	...
220493	12 23 28.4	+05 48 59	...	...	15.62(0.01)	1.34(0.02)	par	16.4(2.5)	7.57(0.32)	...	...
226326*	12 23 58.2	+07 27 02	18.60(0.02)	18.50(0.01)	17.70(0.01)	0.59(0.04)	oly	16.6(2.0)	7.63(0.25)	6.39(0.27)	-2.05(0.28)
227889*	12 24 50.9	+07 53 56	19.92(0.06)	19.79(0.03)	18.20(0.02)	1.26(0.14)	par	16.6(2.0)	7.30(0.26)	6.60(0.26)	-2.78(0.28)
220542*	12 25 21.4	+13 04 13	18.61(0.03)	18.30(0.01)	16.27(0.01)	1.20(0.04)	par	16.7(1.7)	7.59(0.21)	7.38(0.22)	-2.11(0.34)
224232*	12 25 31.5	+11 09 30	19.94(0.06)	19.50(0.02)	16.82(0.01)	1.39(0.06)	domi	16.6(2.0)	7.37(0.27)	7.34(0.26)	-3.10(0.59)
749236	12 25 42.4	+26 48 36	...	...	16.14(0.01)	0.59(0.03)	domi	5.9(2.0)	7.26(0.68)	...	...
220555	12 25 47.4	+14 57 08	18.55(0.03)	17.90(0.01)	14.90(0.01)	1.53(0.02)	domi	16.7(1.7)	7.66(0.21)	8.12(0.22)	-2.27(0.52)
749237	12 26 23.4	+27 44 44	...	...	15.94(0.01)	1.28(0.03)	domi	7.0(2.0)	7.32(0.57)	...	...
220609	12 27 30.1	+09 20 28	19.15(0.03)	18.71(0.02)	16.56(0.02)	1.42(0.07)	pbphot	16.4(2.5)	7.22(0.34)	...	...
220616*	12 27 33.4	+10 00 14	19.28(0.04)	18.31(0.02)	14.98(0.01)	1.81(0.04)	par	16.4(2.5)	7.48(0.32)	8.17(0.32)	-2.52(0.74)
223691*	12 28 27.2	+06 56 45	19.98(0.06)	19.47(0.02)	16.93(0.01)	1.42(0.08)	par	16.6(2.0)	7.23(0.27)	7.15(0.25)	-3.36(0.79)
7596	12 28 34.0	+08 38 22	18.27(0.03)	17.22(0.01)	14.57(0.00)	1.73(0.04)	domi	16.4(2.5)	7.52(0.31)	8.20(0.32)	-1.29(0.58)
222021	12 28 55.4	+08 49 00	20.05(0.06)	19.96(0.04)	20.59(0.17)	0.55(0.44)	pbphot	16.6(2.0)	7.68(0.25)	...	...
227861	12 29 59.4	+08 25 54	19.26(0.04)	18.34(0.02)	15.42(0.00)	1.50(0.02)	domi	16.6(2.0)	7.50(0.26)	7.85(0.25)	-2.60(0.76)
223771	12 30 32.3	+10 15 39	...	...	19.62(0.16)	0.92(0.65)	pbphot	16.6(2.0)	7.40(0.26)	...	...
724906	12 30 56.0	+26 30 41	...	...	16.94(0.01)	1.04(0.04)	domi	11.6(2.3)	7.40(0.40)	...	...

Table2.1 – Continued

AGC	RA(J2000)	Dec(J2000)	$m_{\rm FUV}$	$m_{\rm NUV}$	r	$u-r$	sFlag	D	$\log M_{\rm HI}$	$\log M_*$	$\log {\rm SFR}$
	[^{h} ^{m} ^{s}]	[$^\circ$ $'$ $''$]	[mag]	[mag]	[mag]	[mag]		[Mpc]	[$M_\odot$]	[$M_\odot$]	[$M_\odot$ yr^{-1}]
220745*	12 32 22.8	+16 01 07	17.57(0.03)	17.23(0.01)	14.79(0.00)	1.54(0.02)	domi	16.7(1.7)	7.93(0.21)	8.17(0.21)	-1.67(0.25)
220755*	12 32 46.4	+07 47 57	19.04(0.04)	18.63(0.02)	16.01(0.01)	1.32(0.04)	par	16.4(2.5)	7.18(0.35)	7.61(0.32)	-2.67(0.55)
220768	12 33 09.9	+11 20 49	17.89(0.03)	17.28(0.01)	15.00(0.01)	2.88(0.05)	pbphot	16.7(1.7)	7.53(0.26)	...	...
223873	12 34 01.5	+05 57 10	...	...	18.23(0.05)	2.28(0.66)	pbphot	16.6(2.0)	7.44(0.25)	...	...
220819	12 35 30.9	+06 20 02	18.22(0.03)	17.68(0.01)	14.45(0.00)	1.43(0.01)	domi	15.8(6.4)	7.52(0.81)	8.36(0.81)	-3.03(0.91)
223913	12 36 02.8	+07 12 00	22.09(0.55)	19.10(0.04)	15.15(0.01)	2.19(0.05)	domi	16.6(2.0)	7.11(0.35)	8.15(0.26)	-4.17(0.69)
220837	12 36 34.9	+08 03 17	17.64(0.02)	16.88(0.01)	14.30(0.00)	1.82(0.02)	pbphot	16.4(2.5)	7.41(0.31)	...	...
220856	12 38 06.8	+10 09 54	18.03(0.02)	17.89(0.01)	16.60(0.01)	0.65(0.02)	oly	16.7(1.7)	7.49(0.23)	6.80(0.20)	-1.73(0.21)
220860	12 38 15.5	+06 59 40	18.92(0.03)	18.36(0.02)	...	...	...	16.4(2.5)	7.22(0.36)	...	...
749241	12 40 01.7	+26 19 19	19.54(0.04)	19.24(0.02)	18.90(0.04)	0.83(0.15)	pbphot	5.6(2.3)	6.75(0.83)	...	...
220903	12 40 10.4	+06 50 48	...	...	16.00(0.01)	1.26(0.05)	par	16.6(2.0)	7.55(0.25)	...	...
229001	12 40 49.4	+27 33 50	...	...	16.57(0.01)	1.16(0.03)	domi	21.3(2.3)	7.60(0.26)	...	...
7889	12 43 07.7	+12 03 04	17.53(0.02)	16.31(0.01)	13.16(0.00)	1.65(0.01)	domi	16.7(1.7)	7.69(0.21)	8.91(0.23)	-1.66(0.55)
224296	12 43 22.8	+05 45 55	...	...	17.04(0.03)	1.26(0.07)	par	15.6(6.9)	7.60(0.88)	...	...
225876*	12 44 57.9	+12 01 47	20.26(0.07)	20.12(0.05)	19.02(0.04)	0.98(0.14)	par	16.4(6.5)	7.61(0.80)	6.00(0.80)	-2.82(0.82)
221000*	12 46 04.4	+08 28 34	17.04(0.01)	16.69(0.01)	14.80(0.00)	1.29(0.01)	domi	16.6(2.0)	7.46(0.27)	8.09(0.25)	-1.33(0.27)
221004	12 46 15.3	+10 12 20	17.53(0.02)	17.10(0.01)	15.53(0.01)	1.13(0.03)	domi	16.7(1.7)	7.66(0.22)	7.65(0.22)	-1.38(0.28)
221013	12 46 55.4	+26 33 51	...	...	14.21(0.00)	1.43(0.01)	domi	10.4(2.3)	7.23(0.45)	...	...
227897	12 50 04.2	+06 50 51	...	19.26(0.03)	18.14(0.02)	0.66(0.09)	par	16.6(2.0)	7.43(0.27)	...	...
227972	12 50 24.0	+04 54 22	...	...	18.20(0.04)	1.37(0.24)	par	16.6(2.0)	7.41(0.26)	...	...
227973	12 50 39.9	+05 20 52	...	...	19.06(0.05)	1.12(0.21)	oly	16.6(2.0)	7.39(0.25)	...	...
224229	12 53 40.2	+04 04 32	...	...	16.62(0.01)	1.50(0.05)	domi	16.6(2.0)	7.48(0.26)	...	...
224230	12 53 43.3	+04 09 14	...	...	16.80(0.02)	0.62(0.03)	par	16.6(2.0)	7.64(0.25)	...	...
8030	12 54 29.1	+26 18 13	...	...	15.55(0.01)	1.45(0.04)	par	7.8(2.3)	7.38(0.60)	...	...

Table2.1 – Continued

AGC	RA(J2000) [^{h} ^{m} ^{s}]	Dec(J2000) [$^\circ$ $'$ $''$]	$m_{\rm FUV}$ [mag]	$m_{\rm NUV}$ [mag]	r [mag]	$u-r$ [mag]	sFlag	D [Mpc]	$\log M_{\rm HI}$ [$M_\odot$]	$\log M_*$ [$M_\odot$]	$\log$ SFR [$M_\odot$ yr^{-1}]
225878	12 56 03.1	+12 07 59	...	...	19.74(0.06)	1.44(0.36)	oly	16.0(7.7)	7.37(0.98)	...	...
227974	12 56 03.5	+04 52 01	...	...	19.48(0.05)	2.89(1.20)	pbphot	16.6(2.0)	7.68(0.25)	...	...
227975	12 57 18.1	+04 59 29	...	...	18.77(0.05)	0.83(0.13)	oly	16.6(2.0)	7.53(0.25)	...	...
8091	12 58 40.4	+14 13 02	...	...	15.59(0.01)	1.43(0.03)	pbphot	2.1(0.1)	7.05(0.12)	...	...
732418	12 59 08.2	+26 22 39	...	...	16.83(0.01)	1.23(0.04)	par	15.0(3.1)	7.15(0.44)	...	...
225851	12 59 42.6	+11 04 38	18.24(0.04)	17.90(0.02)	16.19(0.01)	1.10(0.02)	pbphot	42.4(2.3)	8.62(0.13)	...	...
225852	12 59 41.9	+10 43 40	18.39(0.04)	18.07(0.02)	16.35(0.01)	1.02(0.03)	domi	16.6(2.0)	7.67(0.25)	7.26(0.25)	-1.82(0.28)
233575*	13 02 52.5	+13 09 23	20.42(0.18)	20.17(0.10)	18.74(0.04)	1.55(0.20)	domi	46.4(2.3)	8.54(0.12)	7.14(0.13)	-1.98(0.21)
238737	13 13 04.4	+06 17 07	...	...	17.32(0.02)	0.90(0.09)	par	16.9(5.4)	7.46(0.65)	...	...
233627	13 19 53.0	+13 48 23	18.84(0.04)	18.63(0.02)	18.69(0.03)	0.72(0.11)	pbphot	16.8(5.2)	7.98(0.62)	...	...
732602	13 21 04.8	+24 08 36	...	...	16.06(0.01)	1.19(0.03)	domi	11.6(2.3)	7.41(0.41)	...	...
238691*	13 25 17.6	+05 32 36	20.42(0.10)	19.73(0.06)	16.79(0.02)	1.42(0.07)	par	16.7(4.9)	7.30(0.60)	7.31(0.60)	-3.51(0.95)
233559	13 28 47.3	+10 57 41	19.69(0.08)	19.89(0.05)	18.81(0.05)	1.13(0.24)	pbphot	16.0(5.0)	7.42(0.63)	...	...
238890	13 32 30.3	+25 07 24	...	...	15.96(0.01)	1.71(0.04)	domi	6.6(2.0)	6.56(0.62)	...	...
8638	13 39 19.3	+24 46 28	...	...	14.43(0.00)	1.57(0.02)	pbphot	4.3(0.4)	7.27(0.17)	...	...
238847	13 45 09.7	+27 20 11	...	...	19.03(0.05)	0.60(0.15)	pbphot	14.1(2.3)	7.47(0.34)	...	...
233681	13 47 16.0	+13 10 38	...	...	17.60(0.02)	1.04(0.10)	oly	21.2(2.3)	7.69(0.24)	...	...
713655	13 48 22.8	+08 12 41	...	...	17.06(0.01)	0.63(0.03)	oly	21.7(2.3)	7.55(0.23)	...	...
231980	13 54 33.5	+04 14 40	19.29(0.05)	18.81(0.03)	21.05(0.11)	0.87(0.41)	pbphot	2.6(0.2)	6.11(0.17)	...	...
238643	13 55 58.3	+08 59 36	19.21(0.04)	18.88(0.02)	18.97(0.02)	0.35(0.07)	pbphot	22.3(2.3)	7.61(0.23)	...	...
233718*	13 58 43.4	+14 15 41	18.28(0.02)	18.06(0.01)	16.54(0.01)	1.12(0.02)	domi	23.1(2.3)	8.01(0.21)	7.59(0.22)	-1.69(0.24)
732832	13 58 45.0	+24 09 05	...	...	16.40(0.00)	1.46(0.02)	oly	18.4(2.3)	7.58(0.27)	...	...
243852	14 07 04.5	+10 42 46	18.40(0.03)	18.07(0.01)	16.59(0.01)	0.63(0.03)	pbphot	21.5(2.3)	7.90(0.23)	...	...
244129	14 18 53.5	+09 17 29	...	...	17.30(0.02)	1.12(0.05)	domi	21.7(2.3)	7.56(0.25)	...	...

Table2.1 – Continued

AGC	RA(J2000)	Dec(J2000)	$m_{\rm FUV}$	$m_{\rm NUV}$	r	$u-r$	sFlag	D	$\log M_{\rm HI}$	$\log M_*$	$\log {\rm SFR}$
	[^{h} ^{m} ^{s}]	[$^\circ$ $'$ $''$]	[mag]	[mag]	[mag]	[mag]		[Mpc]	[$M_\odot$]	[$M_\odot$]	[$M_\odot$ yr^{-1}]
241893*	14 39 44.5	+05 21 12	18.66(0.03)	18.24(0.02)	16.14(0.01)	1.25(0.04)	domi	28.4(2.3)	7.68(0.23)	8.01(0.18)	-1.35(0.20)
253922*	15 32 13.0	+12 01 21	20.10(0.06)	19.93(0.04)	18.52(0.03)	1.08(0.15)	oly	45.8(2.3)	8.41(0.14)	7.19(0.14)	-1.81(0.22)
253923	15 33 58.9	+12 03 51	19.56(0.05)	19.48(0.03)	17.68(0.03)	1.61(0.17)	domi	41.3(2.3)	8.08(0.15)	7.63(0.15)	-1.95(0.18)
262734	16 34 24.7	+24 57 41	...	...	17.59(0.01)	1.21(0.05)	oly	19.1(2.3)	7.35(0.29)	...	...
321203	22 13 03.0	+28 04 20	18.31(0.04)	18.19(0.02)	...	...	...	16.4(2.3)	7.83(0.29)	...	...
321434	22 47 44.0	+30 45 12	...	...	15.80(0.00)	1.43(0.02)	oly	14.1(2.3)	7.62(0.34)	...	...
320926	22 55 58.5	+26 10 07	18.41(0.03)	18.02(0.02)	16.90(0.01)	1.08(0.05)	domi	39.2(2.3)	8.92(0.12)	7.68(0.15)	-0.98(0.21)
333351	23 00 32.5	+30 42 21	...	...	...	...	...	13.3(2.3)	7.55(0.36)	...	...
333363	23 07 41.5	+30 07 16	...	...	...	...	...	12.5(2.3)	7.51(0.38)	...	...
332912	23 12 01.0	+27 17 41	19.67(0.06)	19.28(0.03)	...	...	...	12.7(2.3)	7.31(0.37)	...	...
12613	23 28 36.2	+14 44 34	15.71(0.01)	14.71(0.01)	14.42(0.01)	1.79(0.06)	pbphot	0.9(0.0)	6.62(0.07)	...	...
333210	23 48 41.8	+25 54 40	20.25(0.11)	19.38(0.05)	...	...	...	23.3(2.3)	7.96(0.21)	...	...
12791	23 48 49.3	+26 13 14	16.73(0.02)	16.42(0.01)	...	...	...	12.1(2.3)	8.33(0.38)	...	...
333214	23 51 37.9	+27 28 10	19.84(0.07)	19.68(0.04)	...	...	...	40.3(2.3)	8.30(0.13)	...	...

Figure 2.1 shows histograms of the recessional velocity cz, adopted distance, observed HI line width and logarithm of the HI mass for the combined ALFALFA dwarf sample, with shaded areas identifying the complete sample, *s-com* and the open areas indicating the additional *s-sup* galaxies. As expected since the lowest HI masses are detected only nearby, most galaxies lie within the Local Supercluster at $cz < 3000$ km s^{-1}. The peak in the distance distribution at 16.7 Mpc arises from the assignment of Virgo membership to a significant number of the dwarf galaxies. A cross match with the VCC catalog [Binggeli et al., 1985] shows that there are 37 Virgo members belonging to the dwarf sample defined here (35 in *s-com* and 2 in *s-sup*). The dashed vertical line in the HI line width histogram corresponds to the adopted line width cutoff, $W_{50} < 80$ km s^{-1}. The mean uncertainty on the line width measurement is 6.7 km s^{-1}. Note that only one galaxy in the *s-com* sample is included in the last bin below this cutoff, suggesting that the low HI mass and narrow line width criteria are consistent: we are not missing a population of high line width but still low mass dwarfs because our line width cutoff is set to be too narrow, and the low HI mass criterion is more important than the narrow line width one in the definition of the *s-com* sample. In agreement with this point, a quick check of the *s-sup* galaxies reveals the fact that they all have $\log M_{\rm HI} > 7.7$, although by the definition of the *s-com* subset, it is possible that galaxies in the *s-sup* sample could have $\log M_{\rm HI} < 7.7$ but $W_{50} > 80$ km s^{-1}. In another words, the supplemental sample *s-sup* does not include low mass dwarf galaxies which are excluded from the *s-com* one through the restriction to the velocity width, $W_{50} < 80$ km s^{-1}. As anticipated, galaxies in the *s-sup* sample span a wider range of W_{50} and distance than the stricter low HI mass sample. In the histogram of $\log M_{\rm HI}$, the low mass tail extends to $\log M_{\rm HI} \sim$6; the sharp edge at $\log M_{\rm HI} = 7.7$ (our upper limit for *s-com*)

reflects the fact that the *s-sup* galaxies represent only a small subset of the $\alpha.40$ galaxies in the higher HI mass range. Figure 2 of Haynes et al. [2011] shows the similar distributions for the full $\alpha.40$ catalog.

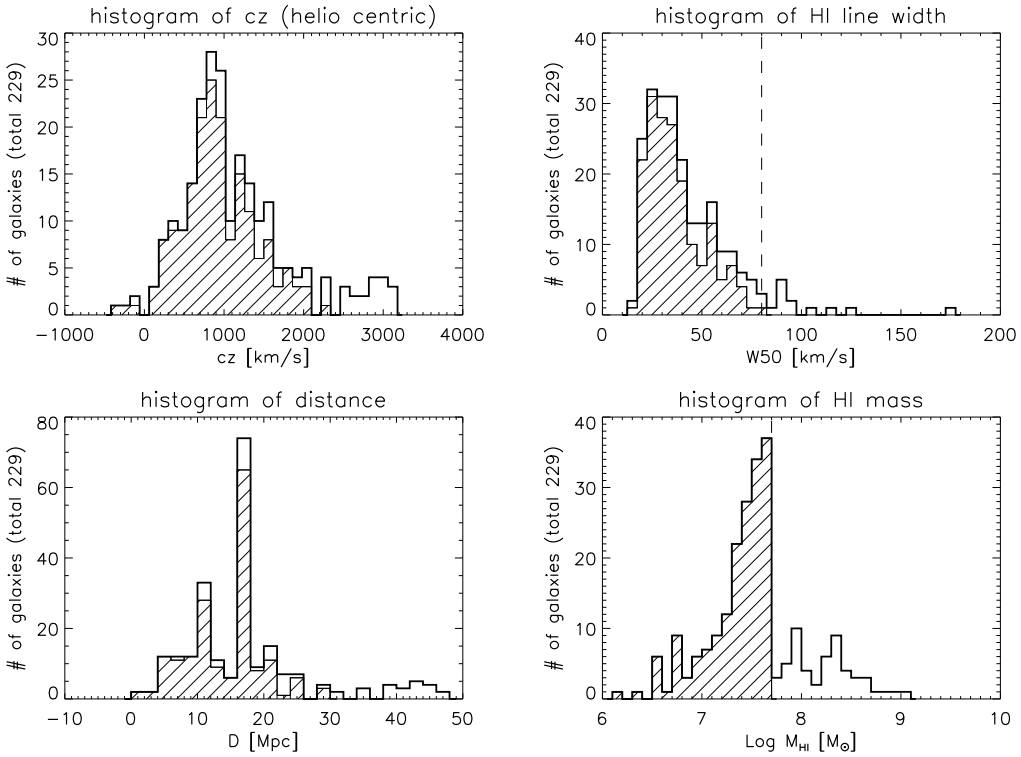

Figure 2.1: HI properties of the full ALFALFA dwarf sample. In all panels, the shaded area identifies the galaxies in the complete HI mass/velocity width-limited sample *s-com* (total = 176) while the unfilled area represents the additional galaxies with *GALEX* photometry in the *s-sup* sample (total = 53). *Top left:* the distribution of HI line recessional velocity $cz_{\rm HI}$. *Top right:* the distribution of HI line velocity width W_{50}. The dashed vertical line corresponds to the W_{50} cut-off ($W_{50} < 80$ km s^{-1}) imposed on the *s-com* sample. *Bottom left:* the distribution of adopted distance to the ALFALFA dwarfs. The peak in the distribution at 16.7 Mpc reflects the assignment of 37 galaxies to membership in the Virgo cluster. *Bottom right:* the distribution of HI mass. The dashed vertical line corresponds to the $M_{\rm HI}$ cutoff ($M_{\rm HI} < 10^{7.7}\ M_{\odot}$) imposed on the *s-com* sample.

Previous studies of dwarf galaxies have focused mainly on optically selected samples and contain relatively few objects with $\log M_{\rm HI} < 7.7$. For example, the FIGGS sample of Begum et al. [2008] contains only 41 galaxies with $\log M_{\rm HI} < 7.7$, compared to 176 in the ALFALFA *s-com* sample. The majority of

the FIGGS targets lie within 8 Mpc and have been selected from existing optical surveys. Similarly, the volume-limited 11HUGS sample is complete in $M_{\rm HI}$ to $2 \times 10^8\ M_\odot$ [Lee et al., 2009b]. In fact, only seven of the *s-com* plus *s-sup* galaxies are included in the 11HUGS catalog; at the same time, 54 of the ALFALFA dwarfs lie at distances of less than 11 Mpc. Figure 2.2 shows a Spaenhauer plot of HI mass versus distance for the ALFALFA dwarfs, with filled circles denoting the *s-com* members. The lower edge of the distribution represents the ALFALFA sensitivity limit [Haynes et al., 2011]. Compared to the similar plot in Figure 1 from Lee et al. [2009b], the distribution of ALFALFA dwarfs is shifted toward the lower HI mass range, just where the deviation of the UV-based SFR from that inferred from Hα is more likely to show up [Lee et al., 2009a]. Benefiting from its improved sensitivity and angular and spectral resolution, the ALFALFA survey catalog allows us to draw a statistically significant sample of the lowest HI mass galaxies in the local universe.

2.3 Data

In this section, we describe the *GALEX* and SDSS datasets used, including reprocessed UV photometry from *GALEX*. In addition, the UV-to-optical color and emission-line diagnostics critical to the appraisal of star formation in the dwarf galaxies are discussed.

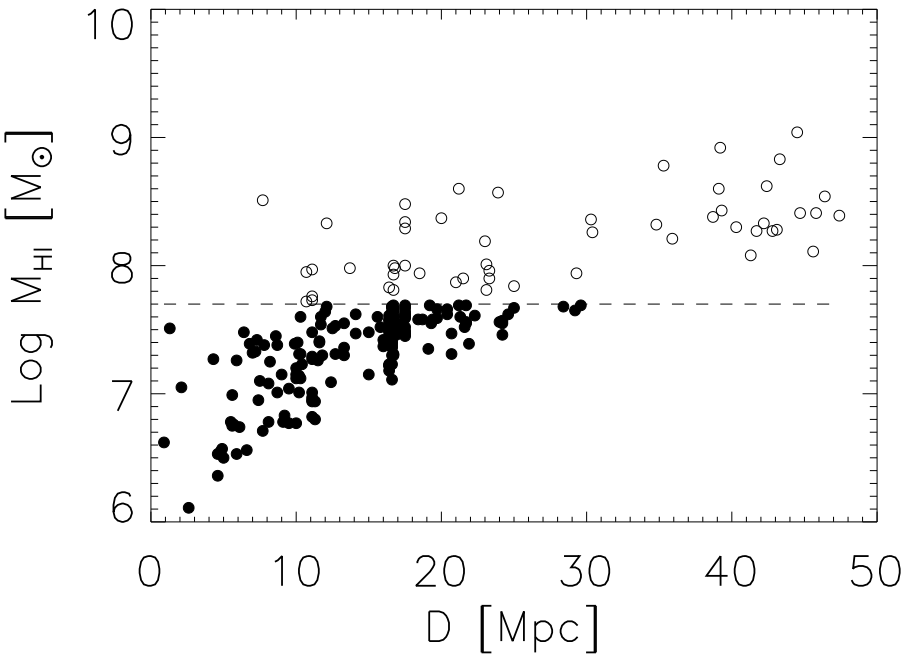

Figure 2.2: Spaenhauer diagram showing HI mass versus distance for the ALFALFA dwarf galaxy sample. Filled circles denotes the lowest HI mass *s-com* members; whereas open ones identify the supplementary *s-sup* galaxies. The horizontal dashed line corresponds to the $M_{\rm HI}$ cutoff at $M_{\rm HI} = 10^{7.7}\ M_\odot$ imposed on the *s-com* sample.

2.3.1 Targeted *GALEX* observations

In dusty starbursting galaxies, a dominant fraction of the UV emission may be obscured by dust and reprocessed at FIR wavelengths [Treyer et al., 2007]. In red sequence galaxies, older evolved stars make significant contributions to the UV luminosity [Wyder et al., 2007]. However, the ALFALFA-selected dwarf galaxies are likely to suffer less from extinction and their young stellar populations contribute the bulk of the UV light. The FUV luminosity $L_{\rm FUV}$ is generally thought to give the most robust measure of the SFR in individual galaxies with low total SFRs and low dust attenuation. Dwarfs are known to be low in metal-

licity and dust content, so that IR indicators of the SFR, which are calibrated via massive spirals, may be less reliable. In contrast to Hα emission, FUV photons primarily originate in the more abundant and relatively longer-lived population of B-stars so that the FUV flux is not as vulnerable to stochastic effects. Furthermore, FUV photons are emitted directly from the stellar photospheres, and thus do not suffer from possible uncertainties in the photoionization of the gas in low density media [Lee et al., 2011].

In order to explore the UV properties of the faint and low surface brightness galaxies in the ALFALFA dwarfs, we examined all available moderate exposure (MIS-depth) *GALEX* images coincident with them, including both ones from our own GI programs as well as others available in the *GALEX* archive. *GALEX* simultaneously imaged the sky in the FUV (effective wavelength of 1516 $\mathrm{\AA}$) and NUV (effective wavelength of 2267 $\mathrm{\AA}$), with a circular field of view of $\sim 1.2^{\circ}$ in diameter [Morrissey et al., 2007]. The images were processed through the *GALEX* pipeline, and the intensity maps with a 1.5″ pixel scale were retrieved. With typical exposure times of ∼1500 sec, the images reach limiting magnitudes of ∼22.7 mag in both the FUV and NUV, corresponding to surface brightness limits of ∼27.5 mag arcsec^{-1} or a SFR of $\sim 10^{-3}\ M_{\odot}\ \mathrm{yr}^{-1}\ \mathrm{kpc}^{-2}$ [Lee et al., 2011]. As discussed in §2.2, all 53 *s-sup* galaxies were included in our *GALEX* GI programs, though five of them were only observed in the NUV due to the failure of the FUV detector. Since the final *s-com* sample was extracted from the $\alpha.40$ catalog after the FUV channel was completely turned off, we also searched the *GALEX* archive for any additional MIS-depth images with adequate coverage of ALFALFA dwarf galaxies. Among the final ALFALFA-*GALEX*/MIS sample of 77 *s-com* galaxies, seven were observed in the NUV only.

Using a standard ellipse fitting extraction of the magnitudes (GALPHOT; see below), 67 of the 70 extreme dwarfs in the *s-com* sample are clearly detected in the FUV band. Two of the remaining three are extremely faint and LSB in the FUV, but magnitudes are still measurable in concentric apertures (ELPHOT; see below). Furthermore, all of the sources in the higher HI mass supplementary *s-sup* sample which have FUV images are detected in FUV. Thus, only one out of the 118 dwarfs in the combined *s-com* plus *s-sup* sample with FUV MIS level images is a non-detection. A similarly high detection rate was found by Lee et al. [2011]. Only 22 of the 390 galaxies in their 11HUGS sample observed by *GALEX* were not detected in FUV. About half of these are galaxies classified as faint dwarf ellipticals/spheroidals (dE/dSph) and lack any evidence of recent star formation; nearly all the others were found in images of exposure times less than 200 sec. Those authors concluded that, despite the variable, episodic or bursty star formation histories of dwarfs, the fluctuations in the SFR do not go to zero on timescales comparable to the lifetimes of UV emitting stars ($\sim$100 Myr). Furthermore, Lee et al. [2011] propose the need to examine the possible complete cessation of SF in low luminosity systems via an HI selected sample probing masses down to 10^7 $M_\odot$, exactly what the ALFALFA *s-com* sample is. The presence of HI selects against the very gas-poor dE/dSph population, so our even higher FUV detection rate is not unexpected. This result clearly suggests that virtually all HI-bearing dwarf galaxies exhibit some level of recent star formation.

2.3.2 *GALEX* photometry

Because we rely mainly on the FUV luminosity to infer SFRs, it is essential to obtain accurate FUV photometry. Given the typical faint, LSB and patchy nature of the UV emission of dwarf galaxies, extra attention must be paid to the extraction of magnitudes. The standard *GALEX* pipeline, which is based on the SExtractor code [Bertin and Arnouts, 1996], suffers from shredding if multiple star forming sites are resolved. It also suffers from blending if foreground stars or UV-bright background galaxies are viewed in projection with the target galaxy. Additionally, the background determination matters more than that in high surface brightness regions, since the background subtraction uncertainty, rather than the photon noise, dominates in LSB regions [Gil de Paz et al., 2007]. For these reasons, we developed our own tools to perform the photometric extraction on the *GALEX* images of the ALFALFA dwarf galaxies.

For each of the target galaxies, we extracted a portion of the intensity map retrieved from the MAST website. Further reduction of the image was performed within the IRAF [1]/STSDAS environment using a set of scripts developed for previous *I*-band imaging surveys undertaken by our group, referred to as the GALPHOT package [Haynes et al., 1999], and appropriately modified to accommodate the *GALEX* images. Because the morphology of galaxies in the FUV is not necessarily the same as in the NUV, and because foreground stars are often much brighter in the NUV images, we elected to work on the two channels separately rather than adopt a single identical set of apertures.

A constant value associated with the sky background was subtracted using

[1]IRAF is distributed by the National Optical Astronomy Observatory, which is operated by the Association of Universities for Research in Astronomy (AURA) under cooperative agreement with the National Science Foundation.

a procedure that allows the user to mark boxes that are free of bright stars and galaxies on each frame. The boxes are placed so that they surround the target galaxy but are far enough from it to avoid the influence of faint extended emission. In contrast to the circumstances applied to optical images, the UV sky is so dark that the pixel values in sky boxes follow a Poisson distribution rather than a Gaussian one. The subtracted sky value in the UV case is the mean intensity obtained within the sky boxes after iteratively clipping out the pixels whose values are more than 3σ above the mean value, a process which removes the faint stars and galaxies within the sky boxes. Usually this process converges quickly after 1 or 2 clipping cycles.

To clean the regions over which the galaxy photometry is to be derived, we first used an automatic procedure to mask UV sources at least 2 galaxy radii away from its center, and then masked by hand sources within 2 radii deemed to be unrelated to the galaxy itself. Starting from an initial guess marked by hand, elliptical surface brightness contours were then fitted to the cleaned images, using the STSDAS package ISOPHOTE, outward to the radius at which the fitting fails to converge, and inward to the seeing limit. This process yields the azimuthally-averaged surface brightness profile as well as the variation with semi-major axis of the ellipse centroid, its position angle and ellipticity; these ellipses are then used later as the apertures for the photometric extraction and allows for the interpolation of masked regions. The disk portion of the surface brightness profile is then fit by a linear function, using an interactive procedure that allows specification of the inner and outer disk radii, as discussed by Giovanelli et al. [1994] and Haynes et al. [1999]. Figures 2.3 to 2.6 illustrate examples of the isophotal fitting result for four representative cases. Selected SDSS and *GALEX* images of them are shown in Figure 2.7.

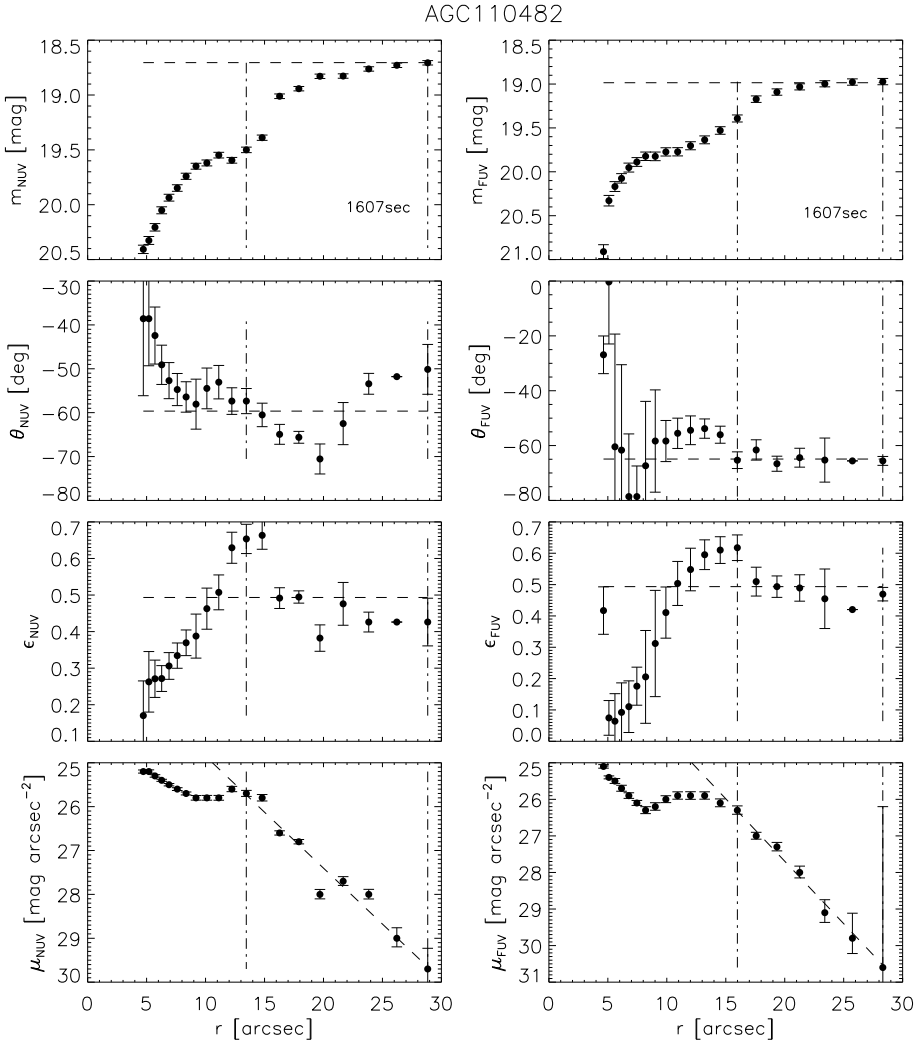

Figure 2.3: Example of the UV isophotal fitting result for AGC 110482 = KK 13, a galaxy which shows star formation in two UV bright knots. The enclosed magnitude (m), position angle (θ), ellipticity ($\epsilon = 1-b/a$), and surface brightness (μ) of the elliptical isophote as a function of the semi-major axis of the isophote (r), are plotted in rows from top to bottom. Results for the NUV image are shown in the left panels, for the FUV image on the right. Numbers at the corners of each plot in the top row give the exposure times in each channel. The marked disk region is denoted by the vertical dash-dotted lines. Horizontal dashed lines represent the adopted magnitude m_{8r_d} (flux within $8r_\mathrm{d}$) in the m plot, and final values determined from the mean of data points in the disk region in the θ and ϵ plots. Dashed lines in the μ plots show the linear fit to the light profile in the adopted disk region, assuming and exponential drop off in surface brightness.

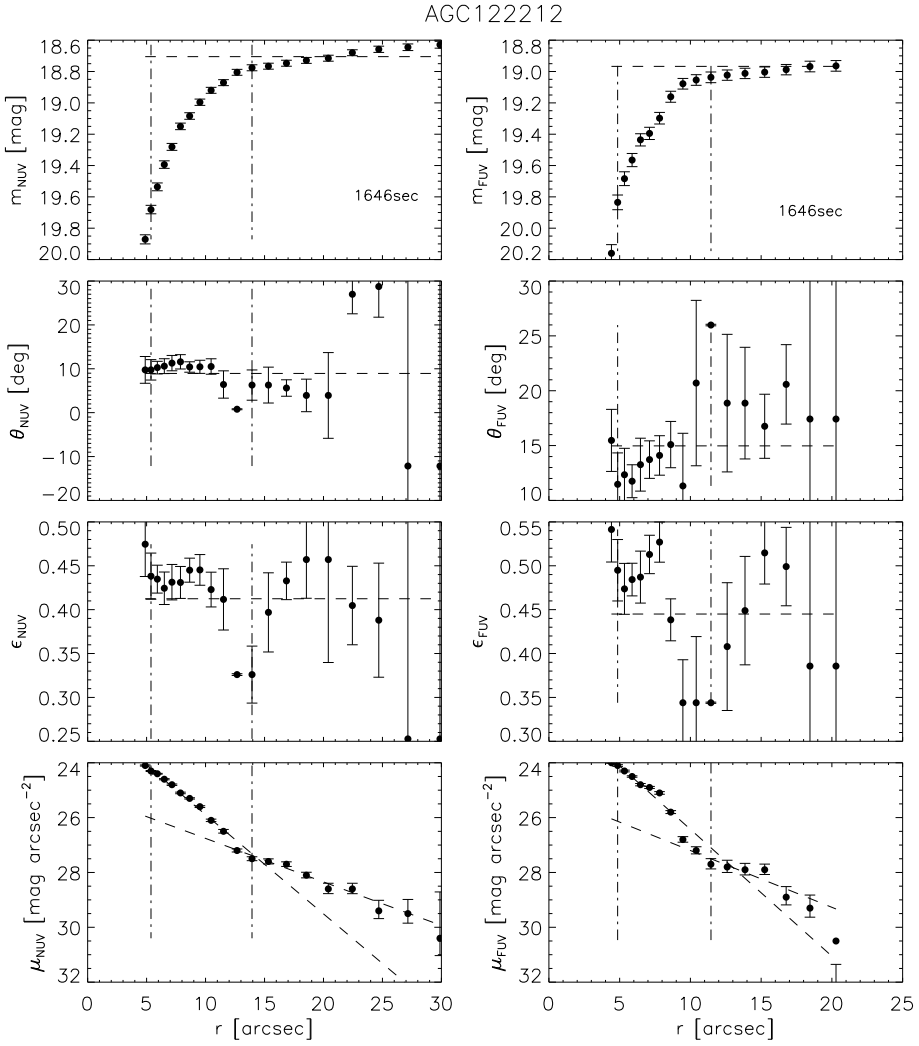

Figure 2.4: Example of the isophotal fitting result for AGC 122212 fit best by a combination of two disks. The symbol definition is the same as that in Figure 2.3. This galaxy has a shallower outer disk in both the NUV and FUV images. Separate linear functions are fit to the inner and outer regions; the inner fit determines the disk scale length and the outer fit is used for extrapolating the profile.

Figure 2.3 shows the result for AGC 110482 = KK 13, a patchy dwarf galaxy whose FUV flux is dominated by two bright knots. The GALPHOT isophotes are centered on the brighter knot in the inner region but the ellipse fitting treats the merged light from the two knots as a single disk at large radius. This process results in a second peak in the surface brightness profile, when the ellipses reach

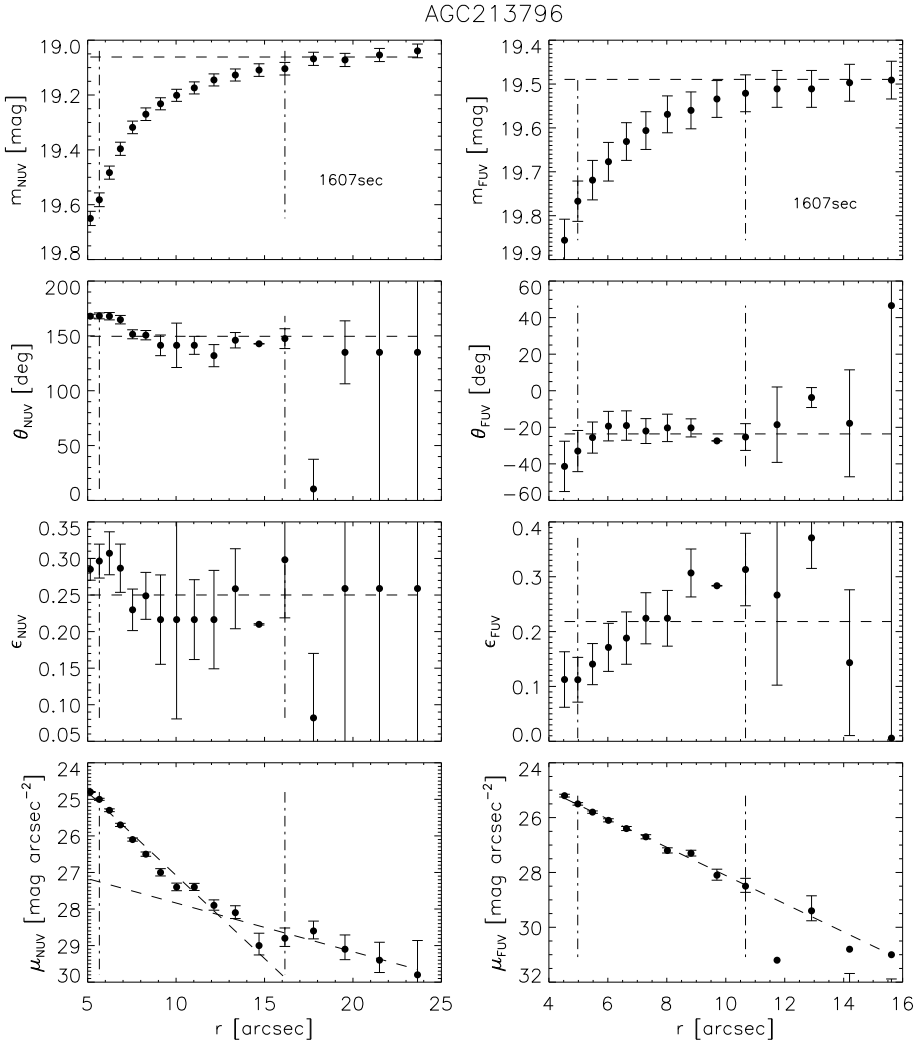

Figure 2.5: Example of the isophotal fitting result for AGC 213796. The symbol definition is the same as that in Figure 2.3. This galaxy exhibits a two-disk structure only in the NUV, either because the emission in the FUV image is too weak to trace the outer disk, or the extended outer disk is not actively forming stars. The traceable FUV disk matches the inner NUV disk. Similar results are observed in a total of 15 galaxies which are assigned to this category.

the center of the fainter knot, but at large radii, the surface brightness profile falls exponentially as expected, yielding a valid total magnitude.

This process of fitting the disk assumes that the surface brightness profile of dwarf irregulars follows an exponential falloff [Hunter et al., 2010] so that disk

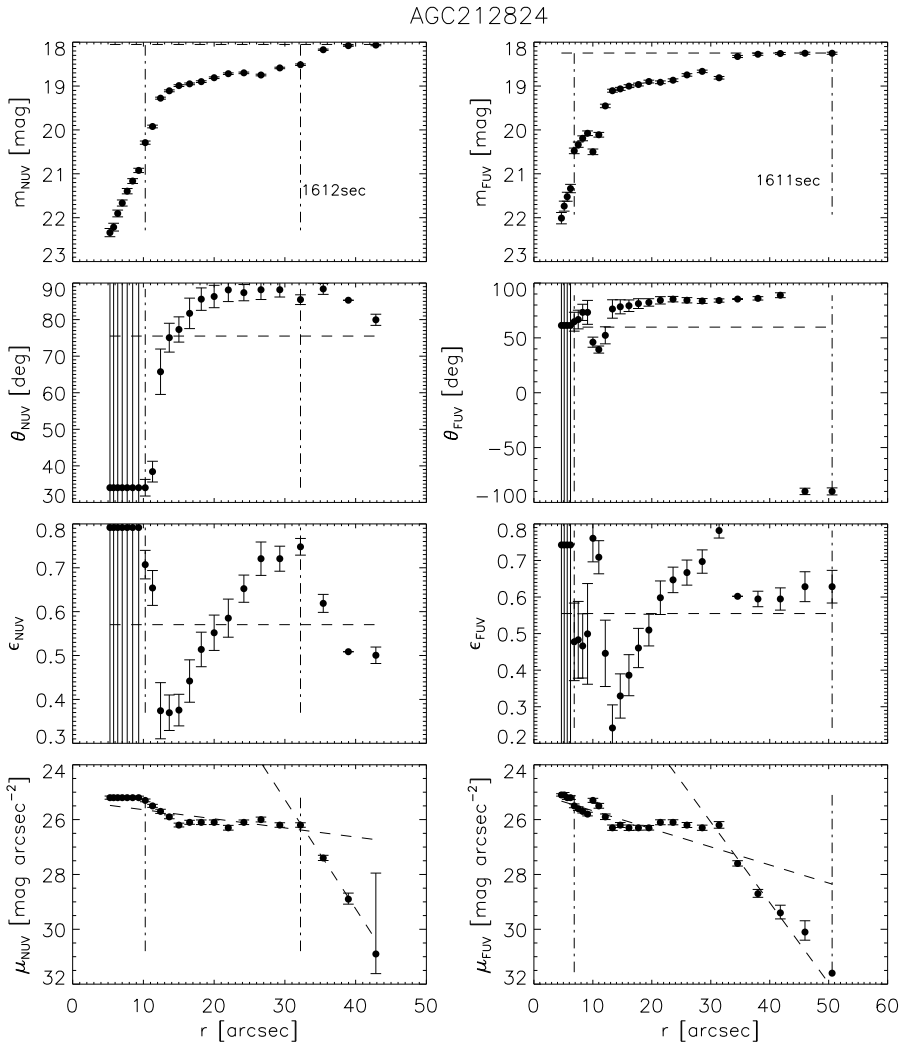

Figure 2.6: Example of the isophotal fitting result for AGC 212824 = KK 100, which has an outer disk that is steeper than the inner one. The symbol definition is the same as that in Figure 2.3. This object has the highest HI mass of any galaxy in the supplementary *s-sup* sample, log $M_{\rm HI}$ = 9.04. The flattening of the UV profile may be due to higher extinction in the center regions or, alternatively to a higher efficiency of star formation in the inner disk.

scale lengths can be determined. However, dwarfs sometimes show multiple disk components, with clearly different slopes in inner and outer regions. In such cases, we fit two linear functions to each portion individually, and use the inner fit to determine the general disk properties, e.g. scale length, position angle, etc, whereas the outer fit is used to extrapolate the surface brightness

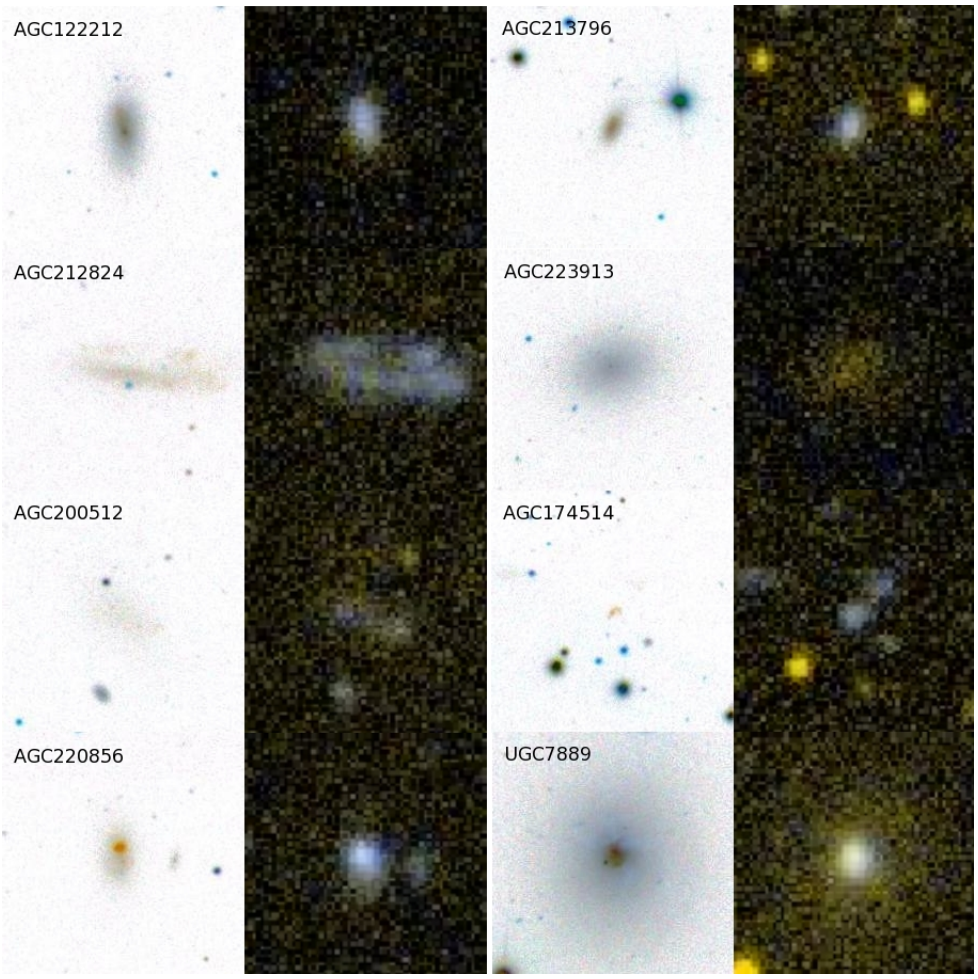

Figure 2.7: Gallery of ALFALFA dwarf galaxies discussed in text. Inverted SDSS images, 1.5′ on a side, are shown to the left of the *GALEX* images (not inverted) of the same galaxies. *First row:* AGC 122212 (left) and AGC 213796 (right) both belong to the *s-com* sample and have shallower outer disks in NUV. The latter has no FUV outer disk. *Second row:* AGC 212824 - KK 100(left) is patchy and has a steeper UV outer disk. It is also the most HI massive galaxy in the ALFALFA dwarf sample, belonging to the *s-sup* set. AGC 223913 = VCC 1649 (right) is a dE/dSph in Virgo with the lowest SSFRs among the *s-sed* set (see its definition in §2.4.1), i.e. its SF is suppressed. *Third row:* AGC 200512 = LeG 6 (left) is LSB and thus is shredded by the *GALEX* pipeline measurement in FUV. AGC 174514 (right) has the highest $f_{\rm HI}$ value and bluest $u-r$ color among the *s-sed* galaxies. Faint patches nearby may be associated with the same object. *Bottom row:* AGC 220856 = VCC 1744 (left) and UGC 7889 = NGC 4641 (right) are both BCDs in Virgo. The former suffers from serious emission line contamination and has the highest b-parameter value among the *s-sed* objects.

profile beyond the outermost measured isophote. Among the 130 ALFALFA dwarfs observed in *GALEX* (12 with no FUV exposure), 28 have such double disks. The majority of those (20/28) have shallower outer disks in the NUV (e.g. AGC 122212 in Figure 2.4 and its images in Figure 2.7), but 15/20 of them show no outer disk in the FUV (e.g. AGC 213796 in Figure 2.5 and images in Figure 2.7). Of the 8 blue compact dwarfs (BCDs) studied by Hunter et al. [2010], 5 also have NUV double exponentials, all of which drop more shallowly in the outer disk. Those authors argue that the shallower outer profile represents the underlying stellar population, while the steeper inner profile is dominated by the centrally concentrated and intense recent star formation. Consistent with this interpretation, the shallow outer disks are frequently not in evidence in the FUV. Further evidence for this scenario arises from the fact that the disk scale length is smaller in the FUV band compared to that seen in the NUV, again suggesting that recent star formation is more centrally concentrated than is the overall stellar disk, i.e., the active star-forming region is shrinking.

On the other hand, of the 29 dwarf irregulars studied by Hunter et al. [2010], eight have clear double exponential profiles in the NUV; in only one of those is the outer exponential shallower than the inner one. Similarly, most of the ALFALFA dwarfs with steeper outer disks (7/8) belong to the higher $M_{\rm HI}$ *s-sup* sample; it is possible that some may be more massive galaxies with more extinction in the inner regions. An example of this case is shown in Figure 2.6 for AGC 212824 = KK 100 (see its images in Figure 2.7) which has the highest $M_{\rm HI}$ in our sample. Another possible explanation for the apparent flattening of the UV profile was proposed in Boissier and Prantzos [2000], namely that the SFR in the inner disk has been higher than the infall of the gas, leading to a progressive consumption of gas toward the center. In the outer parts however, star forma-

tion is less efficient, and the infall of gas proceeds on longer timescales. As a result, the gas reservoir of the outer disk is not exhausted, and the shape of the exponential profile is preserved. The steeper outer disk may thus be more evident in the gas rich dwarf irregulars, while the lower $M_{\rm HI}$ *s-com* dwarfs which are gas-poor relative to the overall ALFALFA population (see §2.5.3) frequently show flatter outer UV profiles.

Once ellipses are fit, magnitudes are calculated using the IRAF routine POLYPHOT to measure the total flux within the ellipses and the disk fits are used to extrapolate beyond the measured isophotes. Following Haynes et al. [1999], several sets of magnitudes are recorded, including ones at fixed isophotal levels, partial magnitudes integrated to a certain number of disk scale lengths, and asymptotic magnitudes extrapolated to infinity. The extrapolation helps to recover the LSB outer emission below the sky level. While magnitudes extrapolated to infinity are adopted by the 11HUGS studies [Gil de Paz et al., 2007], we follow the discussion in Haynes et al. [1999] and adopt in this work a total magnitude computed at a radius of eight disk scale lengths $8r_{\rm d}$. Note that for the majority of the galaxies, a radial extent of $8r_{\rm d}$ lies beyond the outermost radii marked as defining the disk region, except in a few cases that the UV emission is compact and the image is particularly deep (e.g., AGC 225852 in the NUV and AGC 220609 in the FUV). To determine the error in the total magnitude, following Salim et al. [2007], we add the zero-point calibration errors of 0.052 (FUV) and 0.026 (NUV) mag to the Poisson errors, and the uncertainty in the determination of the sky level, which is formally the rms noise of the pixel values in the sky boxes after masking the sources contained within them. We do not account for other types of errors, e.g., the flat-fielding errors, which are improved in the products of the latest version of the *GALEX* pipeline (GR6).

Because of their extreme LSB in the UV, two galaxies, AGC 201970 = LeG 18 and AGC 223913 = VCC 1649 (see its images in Figure 2.7), fail to produce convergence of fitted isophotal ellipses. The former one is also LSB in the SDSS images, but AGC 223913, a dE/dSph in Virgo, is only faint in the UV (see §2.3.4 for more discussion). For these two objects, the *GALEX* pipeline extracts a handful of unmatched faint sources in the NUV and FUV at the location of the target galaxy. We assign concentric elliptical apertures with increasing semi-major axis by hand to extract a curve of growth and adopt their magnitudes from those measured in the outermost aperture.

Only one galaxy, AGC 220483 = VCC 628 is too faint in the FUV to yield a reliable magnitude; it is also undetected by the *GALEX* pipeline to a limiting magnitude ∼22.7 mag. It is a dwarf irregular (Im) associated with the Virgo B Cluster but moving at very high velocity; it exhibits LSB also at optical wavelengths. It remains the lone object in our sample of ALFALFA dwarfs with MIS-depth *GALEX* FUV imaging to exhibit no traceable FUV emission.

A comparison between our GALPHOT/ELPHOT-derived magnitudes and the *GALEX* pipeline magnitudes (GR6) is shown in the upper row of Figure 2.8 for the NUV (left) and FUV (right) channels respectively. The magnitude difference is defined as $(\mathrm{mag_{GALPHOT}} - \mathrm{mag_{GR6}})$. Filled and open circles denote the galaxies in the *s-com* and *s-sup* samples respectively. In addition to AGC 220483 = VCC 628, which was not detected in the FUV as discussed above, several galaxies are excluded from these plots because they were not detected by the *GALEX* pipeline in either one band or the other: AGC 205097 in the NUV (2 NUV-bright stars are nearby), AGC 112505 in the NUV (blend with 1 nearby NUV-bright star and also very close to UGC 1176 = DDO 13), AGC 223913

in the FUV (= VCC 1649, dE in Virgo, LSB in the NUV, invisible in the FUV by eye; SDSS and *GALEX* images shown in Figure 2.7). In addition to these non-detections, several clear outliers are seen in Figure 2.8. The outliers in the FUV plot have a brighter magnitude obtained by the 'GALPHOT' ellipse fitting than that measured by the *GALEX* pipeline. Close inspection shows that they are mostly extended irregulars with large disk scale lengths and patchy UV emission; they suffer from significant shredding by the *GALEX* pipeline, e.g. UGC 4415 and AGC 122206 in the NUV; AGC 200512 in the FUV (SDSS and *GALEX* images are shown in Figure 2.7); AGC 201970 in both the NUV and FUV. Several galaxies lie at such nearby distances that they have resolved HII regions visible in the FUV (e.g. UGC 12613 with a distance of only 0.9 Mpc; UGC 5373 = Sextans B at 1.3 Mpc). After excluding the non-detections and outliers which arise from blending or shredding by the pipeline process, the magnitudes we derive are in reasonable agreement with the pipeline magnitudes. The improved GR6 pipeline magnitudes agree better with our results, especially in the NUV.

The bottom row of Figure 2.8 shows the same magnitude difference versus the disk scale length $r_{\rm d}$ on a logarithmic scale. As evident in Figure 2.8, our photometric extraction technique, which is specifically designed to capture all of the low surface brightness flux, yields brighter magnitudes for a significant number of galaxies. The median magnitude difference is -0.035 and -0.073 mag in the NUV and FUV, respectively. A weak trend is seen such that, as the galaxies become more extended (larger $r_{\rm d}$), the *GALEX* pipeline misses the outer LSB UV emission and hence underestimates the true UV magnitude. For the remainder of this work, we use our own measurements of *GALEX* UV magnitudes, denoted as $m_{\rm NUV}$ and $m_{\rm FUV}$.

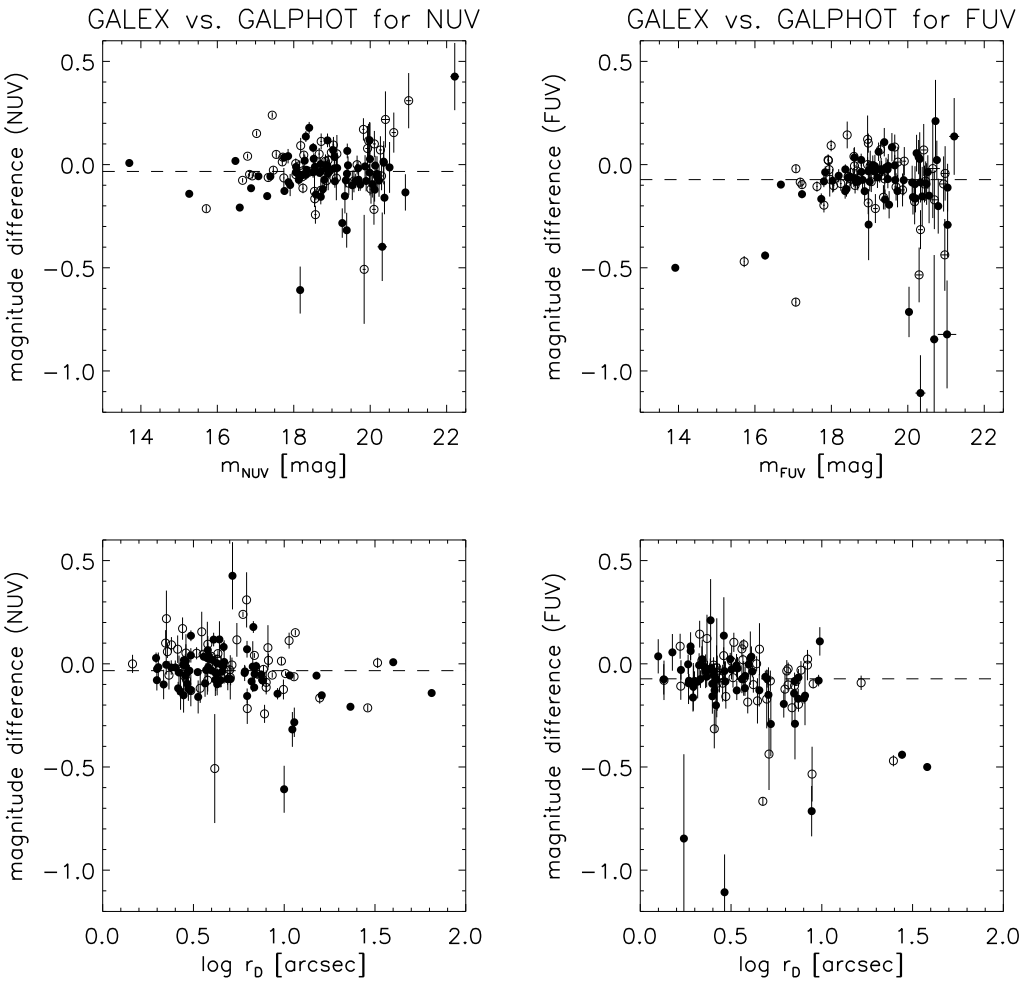

Figure 2.8: Comparison of the total UV magnitudes of the ALFALFA dwarf sample obtained by using the GALPHOT package with those derived from the *GALEX* pipeline. The magnitude difference is defined as $(\mathrm{mag_{GALPHOT}} - \mathrm{mag_{GR6}})$. Results for the NUV channel are shown in the left panel, for the FUV on the right. Filled circles denote the galaxies within the complete *s-com* sample and open ones, the additional *s-sup* objects. The galaxies which are completely missed by the pipeline are excluded from these plots. *Upper* : The magnitude difference as a function of our measurements. In general, the GALPHOT photometry measures a brighter magnitude for a significant number of galaxies, especially in the FUV. *Lower* : The magnitude difference as a function of disk scale length r_{d} on a logarithmic scale. A weak trend is seen that the pipeline becomes ineffective at detecting all emission in the more extended galaxies. Disk scale lengths are smaller on average in the FUV, i.e., the SFR is more centrally concentrated.

2.3.3 SDSS data

In addition to the UV photometry from *GALEX*, we use optical data from the SDSS Data Release 7 [Abazajian et al., 2009]. The SDSS database provides photometry in five bands ($u,\ g,\ r,\ i,\ z$) and spectroscopic follow-up for most galaxies with $r < 17.77$. For the present work, we use the SDSS archival measurements to derive the properties of the underlying stellar population, but because of issues of shredding and blending similar to those found with the *GALEX* magnitudes, significant caution is applied. Given the higher resolution of the SDSS imaging and the higher density of bright stars, the problems associated with magnitude estimation are worse in the optical than in the UV. To check for such issues, we inspected visually each galaxy and the magnitudes derived from the SDSS pipeline, and adopted the photometric properties associated with the best photometric crossmatch along with its reported quality code, sFlag (see below). As suggested by the SDSS team, *modelmag* magnitudes are adopted to derive stable colors while still capturing most of the total light.

Of the 229 galaxies in the *s-com* and *s-sup* samples, 24 lie outside of the SDSS Legacy Survey footprint; most of these are found in the fall sky region of ALFALFA ($22^h <$ R.A.$< 3^h$, $0 <$ Dec. $< +36°$). It is well known that the SDSS photometric pipeline is optimized for small, high surface brightness objects [West et al., 2010], not the clumpy and LSB dwarf galaxies typical of our sample. In fact, of the 205 ALFALFA dwarfs in the SDSS sample, only 44 ALFALFA dwarfs are extracted as single photometric objects by the SDSS pipeline (sFlag="oly" as given in Column 8 of Table 2.1). Since multiple peaks are usually evident in the light profiles of patchy dwarfs (the "parent" object), these are often deblended by the standard pipeline into pieces (the "child" objects). Accurate

magnitudes can be recovered in those cases where the "parent" object contains all (or nearly all) of the emission associated with the galaxy and is not blended with any other nearby objects. 53 of the ALFALFA dwarfs belong to this category (sFlag="par"); in these cases, the magnitudes of the associated *parentID* are adopted. For the remaining objects for which the "parent" objects still suffer from blending, we examined the magnitudes of each "child" object within the region of the target galaxy. According to West et al. [2010], roughly 75% of galaxies have more than 90% of their flux contained in the brightest child. We used the magnitudes of the brightest child where it is brighter than the second brightest child by at least 3 magnitudes, implying that it contains the vast majority of the galaxy's flux. 55 of the 205 ALFALFA-SDSS dwarfs fit this category (sFlag="domi") so that the SDSS magnitudes contribute a satisfactory lower limit of the optical flux. The remaining 53 galaxies have photometry too uncertain to be used further, usually because the parent object is blended with other sources or has no dominant child (sFlag="pbphot"). It is relevant to note that most are dropped for one of two specific reasons: either (1) because they are very patchy or (2) because they are contaminated by the presence of nearby or superposed stars. The latter reason has nothing to do with the galaxy itself, but the first is particularly common for this sample of dwarf galaxies. We checked the distribution of HI properties for the excluded objects, and find that they span the full range in distance, line width, and HI mass evident in Figure 2.1, suggesting that the inclusion of a criterion of acceptable SDSS photometry introduces no extra bias in terms of HI parameters. Although we have not reprocessed the SDSS photometry as did West et al. [2010], the careful visual inspection technique applied here effectively avoids the shredding or blending of the SDSS magnitudes which are the main causes of the failure of the SDSS

pipeline to deliver reliable photometry for diffuse, patchy and/or LSB galaxies.

However, because of the typical faintness and LSB optical appearance of the ALFALFA dwarfs, the percentage of the photometric objects that are targeted for SDSS spectroscopy is quite low: only 114/205 have a counterpart in the SDSS spectroscopic survey. This circumstance further validates the importance of HI-selection for deriving a complete sample of dwarfs in the local universe. Furthermore, only 101 of the 114 spectroscopic targets are included in the MPA-JHU DR7 release of SDSS spectral measurements [http://www.mpa-garching.mpg.de/SDSS/DR7/, Brinchmann et al., 2004], which contains reprocessed line flux, etc. We confirm that all these 101 dwarfs are star-forming or low S/N star forming galaxies, following the classification in Brinchmann et al. [2004]. In comparison with the SDSS-selected population, the HI-selected dwarf sample includes a much smaller representation of galaxies containing AGNs or are classified as 'non-star-forming'; this finding also implies that the SDSS magnitudes are more likely to be contaminated by line emission. Similarly, a quick inspection shows that all the ALFALFA dwarf galaxies with SDSS $D_n(4000)$ measurements have a value below 1.6, the demarcation in the bimodal distribution derived in Kauffmann et al. [2003b]. This result suggests that these dwarfs have been actively forming stars throughout their history.

2.3.4 UV-to-optical colors of the ALFALFA dwarfs

The global color-magnitude diagram (CMD) is a powerful tool for the assessment of the basic properties of a sample of galaxies. The bimodal nature of the field galaxy CMD is well demonstrated with the large datasets available

from recent large scale galaxy surveys, in particular SDSS [Baldry et al., 2004]. It is clear that galaxies separate into the 'red sequence' of early type galaxies which show little or no evidence of ongoing star formation (corresponding to the low SSFR portion in the SSFR versus M_* diagram), and the 'blue cloud' of star-forming spirals (corresponding to the star forming sequence in that diagram). Compared to the traditional optically-based CMDs, a CMD constructed from a UV-to-optical color provides a more powerful diagnostic [Wyder et al., 2007, Schiminovich et al., 2007, Salim et al., 2007]. By contrasting the recent star formation, as indicated by the UV light, to the total past star formation, as indicated by the optical light, the UV to optical color provides a more concrete diagnostic of a galaxy's SFH [Salim et al., 2005].

To produce the CMD shown in Figure 2.9, the magnitudes given in Table 2.1 have been corrected for foreground reddening. For the SDSS bands, we adopted the pipeline extinction correction. For the *GALEX* bands, we used $E(B-V)$ values based on the FIR DIRBE maps of Schlegel et al. [1998], the Cardelli et al. [1989] extinction law with $R_V = A_V/E(B-V) = 3.1$, and $A(\lambda)/E(B-V) = 8.24$ for the FUV and 8.2 for the NUV bands respectively, following Wyder et al. [2007]. Of the 229 galaxies listed in Table 2.1, 51 belonging to the complete *s-com* sample and 32 to the higher $M_{\rm HI}$ supplementary *s-sup* set have both acceptable SDSS photometry (sFlag not "pbphot") and NUV magnitudes, making it possible to estimate a color ($m_{\rm NUV} - r$). Their distribution in the combined UV-optical CMD is shown in the left panel of Figure 2.9, with filled circles denoting objects in the *s-com* sample and open ones representing the additional *s-sup* galaxies.

The first obvious difference of this work from most previous studies is the much fainter absolute magnitude range probed by the ALFALFA dwarfs. For

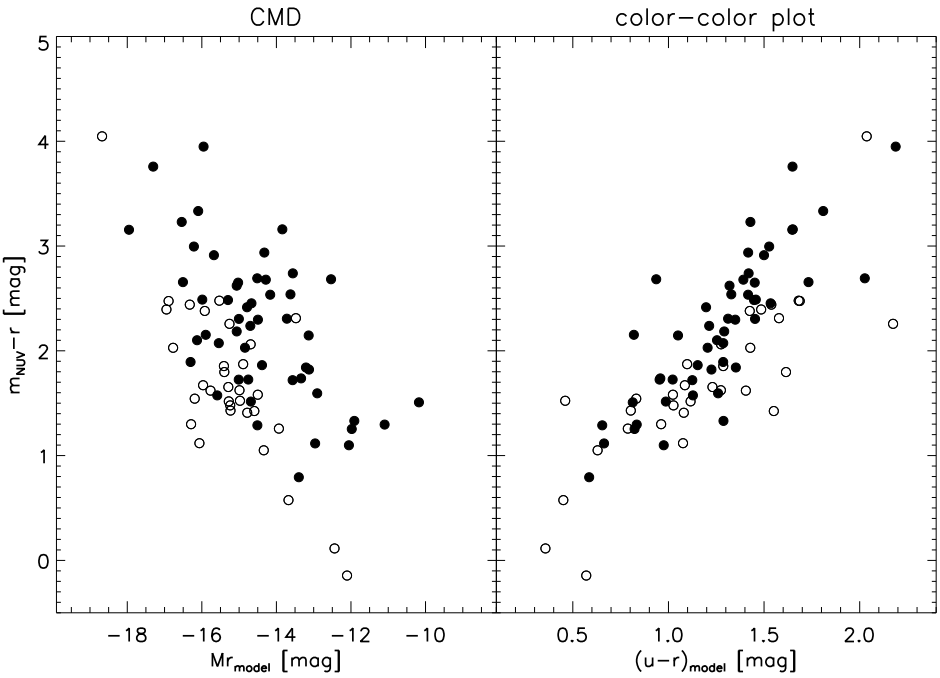

Figure 2.9: The UV-to-optical colors of the ALFALFA dwarfs. Filled circles identify dwarfs in the lowest HI mass complete *s-com* sample, while open ones represent the additional *s-sup* galaxies. *Left:* Color-magnitude diagram. Unsurprisingly, nearly all the ALFALFA dwarf galaxies are less luminous than $M_r \simeq -18$, and lie below the blue cloud – red sequence divider quoted by Salim et al. [2007], $m_{\rm NUV} - r \lesssim 4$. *Right:* Color-color plot. Within the blue color range occupied by the sample overall, the $m_{\rm NUV} - r$ color is well correlated with the $u - r$ color, with the former probing a larger dynamical range, $\delta(m_{\rm NUV} - r)/\delta(u - r) \sim 2$.

example, as clear from Figure 1 of Salim et al. [2007], the majority of galaxies in that study have $-24 \lesssim M_r \lesssim -18$, whereas nearly all of the ALFALFA dwarfs are less luminous than $M_r \simeq -18$, with the mean $M_r \sim -15$. Second, HI selection results in no obvious color bimodality in dwarfs, because nearly all HI-bearing galaxies are blue, actively star-forming systems; HI selection is highly biased against the red sequence [West et al., 2009, Haynes et al., 2011]. Based on the distribution of their full *GALEX*-SDSS matched catalog, Salim et al. [2007] identified blue cloud galaxies as those with $m_{\rm NUV} - r \lesssim 4$. Given the color-magnitude relation, fainter galaxies are bluer on average and the dividing criterion shifts to $m_{\rm NUV} - r \sim 3.5$ at $M_r \sim -17$, according to Figure 1 in Kim et al.

[2010]. As evident in Figure 2.9, virtually all the ALFALFA dwarf galaxies are below the division of $m_{\rm NUV} - r = 4$. Only three objects, UGC 6245, AGC 223913 = VCC 1649 and AGC 222297 = VCC 180 (the latter two early type galaxies associated with the Virgo Cluster) have $m_{\rm NUV} - r > 3.5$, lying in the green valley or blue edge of the red sequence. At fixed M_r, galaxies with lower $M_{\rm HI}$ (the filled circles) have, on average, redder colors, indicating that they also exhibit a lower gas fraction ($f_{\rm HI}$, defined as $M_{\rm HI}/M_*$ throughout this work); this trend confirms the general association of lower $f_{\rm HI}$ and redder color (see also §2.5.3). As a result, in the range of $-18 \lesssim M_r \lesssim -10$, a population of extremely low gas fraction dE/dSph would have $M_{\rm HI}$ lower than the detection limit of ALFALFA; they would sit on the red sequence in this low luminosity range, but are not included in this sample. This point is further discussed in the case of the Virgo cluster by Hallenbeck et al. [2012]. In addition, there is a trend for lower luminosity objects to have bluer colors, as is also found in studies of large samples of massive galaxies [Wyder et al., 2007]. As is the case with the full ALFALFA sample [Haynes et al., 2011, Huang et al., 2012a], the CMD shown in Figure 2.9 confirms that, in comparison with large optical-UV samples, an HI-selected dwarf sample is highly biased against red sequence galaxies.

The right panel of Figure 2.9 presents a color-color plot, with the horizontal axis showing the optical color $(u - r)$. Not surprisingly, there is a strong correlation such that as a galaxy becomes redder in $m_{\rm NUV} - r$, it also becomes redder in $u - r$. As found by Wyder et al. [2007] for blue galaxies, the two colors are very well correlated with a slope of $\delta(u - r)/\delta(m_{\rm NUV} - r) \sim 0.5$; this slope is roughly consistent for the ALFALFA dwarf sample. Those authors also found that, for galaxies with colors redder than $m_{\rm NUV} - r \approx 3.5$, the $u - r$ color begins to increase less quickly with $m_{\rm NUV} - r$ than for bluer $u - r$ colors. The ALFALFA

sample shows no obvious change in slope, as expected since most lie on the blue side of the division.

We also examine the $m_{\rm FUV} - m_{\rm NUV}$ color, a sensitive probe of the rate of current star formation. There are 117 galaxies (69 belonging to the complete *s-com* sample and 48 to the supplementary *s-sup* one) which have detectable magnitudes in both the FUV and the NUV. As described in Gil de Paz et al. [2007], late-type spiral and irregular 'blue-cloud' galaxies can be roughly separated from early-type 'red-sequence' galaxies using a division at $m_{\rm FUV} - m_{\rm NUV} = 0.9$. According to that demarcation, 92% of our galaxies fall on the blue side. 72% of the combined (*s-com* plus *s-sup*) sample have $m_{\rm FUV} - m_{\rm NUV} < 0.5$; among the lower HI mass *s-com* galaxies, this percentage drops to 64%. Furthermore, the median UV color is 0.36 mag for the *s-com* plus *s-sup* galaxies (0.42 mag for the *s-com* and 0.31 mag for the *s-sup* galaxies). Evaluation of the K-S statistic shows that the probability that the UV color distributions of the two samples (*s-com* vs. *s-sup*) are drawn from the same underlying distribution is only 2.6%. The galaxies with the lowest HI mass (*s-com*) are *redder* than comparable galaxies with higher HI masses, that is, the HI mass cutoff imposed on the *s-com* results in a sample with redder UV colors on average at *fixed optical luminosity* (see also §2.5.3).

In comparison, the sample studied by Lee et al. [2011], mainly drawn from the 11HUGS, has 79% of the galaxies with $m_{\rm FUV} - m_{\rm NUV} < 0.5$, and a median UV color of 0.29 mag, bluer than the ALFALFA dwarf galaxies, especially the *s-com* ones. Figure 2.10 examines more closely the distribution of absolute magnitude M_B for the ALFALFA dwarf and 11HUGS samples. The solid histograms trace the distribution of the 152 ALFALFA dwarfs with acceptable SDSS magnitudes

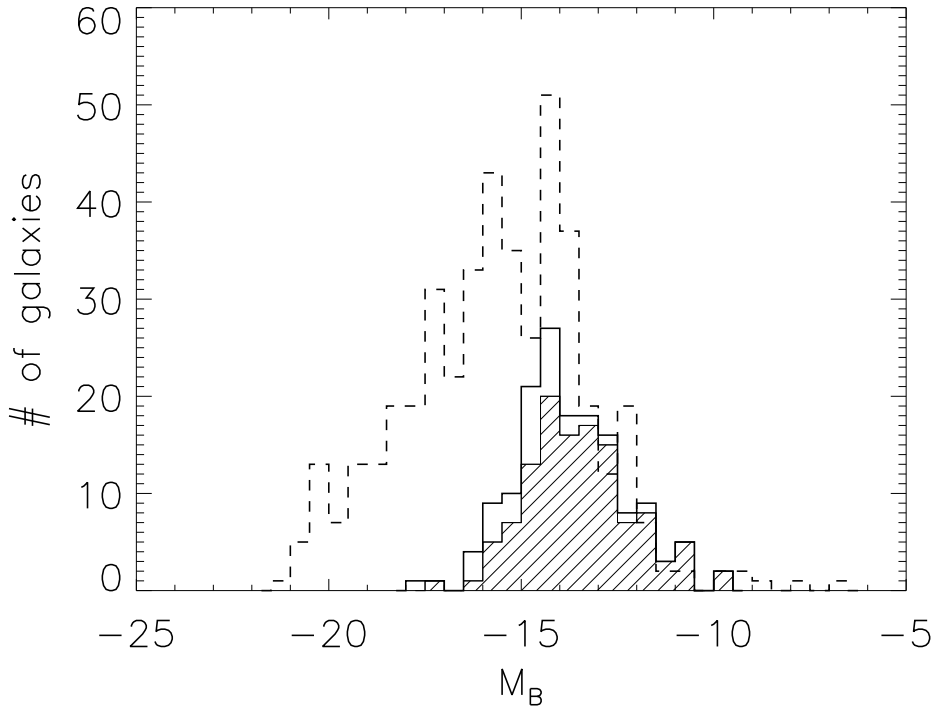

Figure 2.10: B-band absolute magnitude distribution of the 152 galaxies with acceptable SDSS magnitudes. Solid histograms indicate the ALFALFA dwarf galaxies, with the shaded area tracing the *s-com* sample and the open area, the *s-sup* galaxies. In comparison, the dashed histogram shows the distribution for the 11HUGS sample. Although the *s-com* sample extends to lower HI mass and its galaxies have, on average, lower gas fractions, both ALFALFA and 11HUGS probe to comparably faint optical absolute magnitudes.

(see §2.3.3), with the shaded area identifying the complete *s-com* sample and the open area, the *s-sup* galaxies. To convert the SDSS bands to B-band, the transformation equation is used, $B = g + 0.3130(g-r) + 0.2271$. For comparison, the dashed histogram represents the parent 11HUGS sample with their B-band absolute magnitudes drawn from Table 3 of Kennicutt et al. [2008]. Although the ALFALFA *s-com* sample extends to considerably lower HI mass, the faintest optical magnitudes probed by both ALFALFA and 11HUGS are similar. Relative to the 11HUGS galaxies, the lower gas fractions typical of the *s-com* dwarfs are

consistent with their redder colors.

One of the ALFALFA dwarfs, AGC 223913 = VCC 1649 (see its images in Figure 2.7) even has $m_{\rm FUV} - m_{\rm NUV} = 3$, implying that it is in a quiescent stage of star-formation. It is a dE/dSph in Virgo, whose red UV color could result from a recent quenching of star formation activity, possibly due to gas loss by ram pressure stripping [e.g. Boselli et al., 2008]. This object and the other early type dwarfs detected by ALFALFA in the Virgo cluster are discussed in more detail elsewhere [Hallenbeck et al., 2012].

2.4 The derivation of the physical properties of ALFALFA dwarf galaxies

In this section, we use the datasets discussed above to derive the physical properties of the ALFALFA dwarf galaxies (*s-sed*): their stellar masses, internal extinction, metallicity and SFR.

2.4.1 SED fitting

While studies of resolved stellar populations provide the best means to determine the star formation histories of galaxies, it is not yet feasible to conduct such studies on the majority of the ALFALFA dwarfs. Hence we analyze their integrated light and global properties by SED fitting, following the method of Salim et al. [2007], with a slight change in the prior distribution of the effective optical depth in V band, τ_V (see §2.4.3). Of the full ALFALFA dwarf sample,

reprocessed FUV and NUV magnitudes and acceptable quality SDSS pipeline photometry as described above are available for a total of 74 galaxies, 45 belonging to the more restrictive *s-com* sample and 29 to the additional *s-sup* set. The full likelihood distributions of parameters are derived for this combined sample, referred to hereafter as *s-sed*, by fitting the seven observed SDSS ($u\ g\ r\ i\ z$) and *GALEX* (FUV NUV) bands to an extensive library of model SEDs [Gallazzi et al., 2005], generated using the B&C 03 stellar population synthesis code [Bruzual and Charlot, 2003]. Dust is accounted for with the Charlot and Fall [2000] two-component model to include attenuation from both the diffuse interstellar medium (ISM) and short-lived (10 Myr) giant molecular clouds. It is proposed to produce consistent treatment for both the Hα and UV continuum attenuation. However, we do note that recent studies show that the extinction curve may be a function of stellar mass, SSFR, axis ratio and stellar surface mass density, etc [e.g. Johnson et al., 2007, Wild et al., 2011]. A Chabrier [2003] IMF is assumed, and random bursts are allowed to be superimposed on a continuous SFH.

A concern for the study of HI-selected galaxies is whether the parameter space used for building the library is set wide enough to cover the intrinsic values of the metal- and dust-poor ALFALFA dwarfs. For example, following Salim et al. [2007], the effective V-band optical depth lies in the range $0 \leqslant \tau_V < 6$, and the μ factor, i.e., the fraction of the optical depth that affects stellar populations older than 10 Myr, varies from 0.1 to 1. A commonly-used prescription by Calzetti [1997] adopts $E(B-V)_{\rm star} = 0.44E(B-V)_{\rm line}$ (see also discussion in §2.4.3). Furthermore, the metallicity of the stellar population is uniformly distributed between 0.1 and 2 $Z_{\odot}$. In particular, we can anticipate that in some cases, the emission lines may be so strong that the observed col-

ors may deviate from the adopted line-free continuum model [Salim et al., 2007, West et al., 2009], e.g. the Hα emission may dominate the r-band luminosity to offset the observed $r-i$ color blueward of the models. However, outliers affected by line emission can be identified in a color-color plot, e.g. $r-i$ versus $g-r$. As a result, the χ^2-value of the best-fitting model, $\chi^2_{\rm best}$, would have a mean larger than that predicted by the degree of freedom of the fitting. We checked the distribution of $\chi^2_{\rm best}$ and found it is generally good, implying that the library does, in fact, reproduce most of the observed SEDs. However, there is a tail of large $\chi^2_{\rm best}$ objects, and we confirm by visual inspection that their deviation is likely caused by strong line emission (e.g. AGC 220856 = VCC 1744 and AGC 223390 = VCC 274, two Virgo BCDs; the SDSS and *GALEX* images of the former are included in Figure 2.7). Additionally, although we already excluded the "shredded" sources, there remain a few objects with suspicious SDSS magnitudes, e.g. AGC 205165 (problematic de-blending of a superposed star) and AGC 191791 = LSBC D634-03 (unusual color in the SDSS image), which also lead to large $\chi^2_{\rm best}$. For these reasons, we emphasize that the SED fitting results should be interpreted only in a statistical sense, with these large $\chi^2_{\rm best}$ objects being less reliable. The galaxies with $\chi^2_{\rm best} < 10$ are noted by a '*' over the AGC numbers in Table 2.1.

Compared to SED fitting to the optical SDSS bands only, fitting with the addition of the *GALEX* UV bands yields better constraints on the parameters, especially on the dust optical depth and the SFR over a timescale of 100 Myr, comparable to the lifetime of UV bright stars [Salim et al., 2005]. We use the likelihood-weighted average as our nominal estimate of the logarithm of the parameter value, rather than the mode, to avoid sensitivity to binning, and $1/4$ of the 2.5-97.5 percentile range as a proxy for what would have been the un-

certainty estimate in the Gaussian distribution [Kauffmann et al., 2003a, Salim et al., 2007]. An extra term which accounts for distance uncertainties is added for distance-dependent quantities, e.g. the stellar mass and SFR. This term always dominates the SED fitting error (characterized by the probability distribution function, PDF) for the nearby dwarfs in the stellar mass estimates, but not for the errors in the SFRs. Note that systematic uncertainty is not included in the error estimate. When the UV bands are excluded, the median uncertainty in the $\log M_*$ estimate is 0.217; in $\log \tau_V$, it is 0.455; in $\log \mathrm{SFR}$, it is 0.323. When the UV data are incorporated, those values decrease to 0.212, 0.367, 0.277, corresponding to median improvement of 1%, 21% and 7% respectively. While the constraint on the stellar mass is least improved, the incorporation of the UV data is critical to the other parameters, both of which are more sensitive to changes in the UV luminosity.

2.4.2 Stellar mass

Based on the SED fitting error term characterized by the PDF, the M_* is the best constrained parameter in the SED fitting. The logarithm of M_*, in units of solar mass, is listed in Column (11) of Table 2.1. $\langle \log M_* \rangle$= 7.40 for the *s-sed* dwarfs (7.28 for the lower HI mass *s-com* galaxies and 7.58 for the additional *s-sup* objects), significantly lower than those of typical SDSS or *GALEX* samples [Brinchmann et al., 2004, Salim et al., 2007]. This result further confirms that the imposition of an HI line width cutoff effectively eliminates most of the HI deficient but high luminosity objects. The only two galaxies with $\log M_* > 8.5$ are UGC 6245, a low luminosity SB0 galaxy viewed almost face-on so that its true velocity width may be much larger, and UGC 7889 (= NGC 4641), a BCD

in Virgo. The former has the highest stellar mass $\log M_* = 9.52$ and a low gas fraction, but is left in the *s-sup* sample because of the availability of its *GALEX* image from our GI program (see §2.2).

Another widely used method to estimate the stellar mass from optical magnitudes employs the relation of mass to light ratio versus color as calibrated by Bell et al. [2003]. However, the SFH adopted by Bell et al. [2003] does not fully account for the impact of the bursty behavior seen in nearby dwarfs [Lee et al., 2009b]. Gas-rich dwarfs have b-parameters ($b \equiv \mathrm{SFR}/\langle \mathrm{SFR} \rangle$, the current SFRs normalized to the average past SFRs) which are high on average (see §2.5.1). As a result, application of the standard Bell et al. [2003] calibration would produce stellar masses that are more massive for the same optical color. Additionally, at low redshift, Hα emission may contribute to the r band flux and [OIII] and Hβ to that at the g band. On the other hand, the $g - r$ color is largely unchanged [West et al., 2009] and the i band contains almost no emission lines. Therefore, following [West et al., 2009], we also calculate the stellar mass using the i band luminosity and the $g - r$ color. We apply K-corrections using the IDL code "kcorrect" ($v4\_1\_4$), described in Blanton and Roweis [2007] and estimate internal extinction corrections based on equation (12) in Giovanelli et al. [1997]. The latter has little effect on the stellar mass estimate, since when the luminosity is increased, the color also becomes bluer by an associated amount such that the two effects cancel each other [Bell et al., 2003].

The two stellar mass estimates, i.e., that derived from Bell et al. [2003] calibration versus that derived from SED fitting, agree for the most massive galaxies with $M_* \gtrsim 10^{10}\ M_\odot$ and low b-parameters, but systematic deviations between the two become non-negligible at the low mass end. While the Bell et al. [2003]

method gives a median $\log M_*$=7.73 for the *s-sed* ALFALFA dwarfs (converted to Chabrier IMF), SED fitting yields a considerably lower median of 7.45 corresponding to a factor of two difference. Furthermore, because the most gas rich galaxies (i.e. higher $M_{\rm HI}$ for their M_*) with higher b-parameters in this stellar mass range are excluded from the dwarf sample in this work (see §2.5), the deviation is even larger among the full low stellar mass ALFALFA population [Huang et al., 2012a]. We find a discrepancy of similar magnitude to that found by Wyder et al. [2007], ∼0.4 dex on average at 10^8 $M_\odot$, and we confirm that the galaxies which are estimated to be more massive by the Bell et al. [2003] method have generally higher b-parameters. To incorporate reasonably the effects of stochastic star formation, bursty behavior in dwarf galaxies should be a key feature of modeling the SEDs.

2.4.3 Internal extinction

Although the FUV luminosity provides a more robust estimate of the recent SFR in dwarf galaxies than optical measures, it is subject to significant uncertainties because of the required dust attenuation corrections which themselves are subject to large scatter produced by the large range of possible dust content, dust distribution, and geometry relative to the stars and ISM in galaxies. Even at $0.02Z_\odot$, I Zw 18 contains a non-negligible amount of reddening, determined from optical observations to be equivalent to $A_V = 0.5$ [Cannon et al., 2002]. In the dwarf galaxy SBS 0335-052 ($0.025Z_\odot$), A_V values as high as 20 to 30 have been suggested from MIR observations [Thuan et al., 1999]. On the other hand, arguing that dwarf galaxies are expected to be extremely dust poor, Roychowdhury et al. [2009] chose to neglect internal extinction entirely in their

study of the FIGGS dwarf galaxy sample. Based on that assumption, they found a lower average $\Sigma_{\rm SFR}$ for the FIGGS dwarfs than would be expected from the Kennicutt-Schmidt law [Kennicutt, 1998b]. Similarly, Hunter et al. [2010] took $E(B-V) \sim 0.05$ and Lee et al. [2009a] found $A_{\rm H\alpha} < 0.1$ for the faintest galaxies. Here, rather than ignoring extinction, we have attempted to quantify its contribution by SED fitting using the optical/UV photometry.

Salim et al. [2007] already have pointed out the difference between the effective optical depth in V band derived from emission-line fitting, $\tau_{V,{\rm H\alpha}}$, and that derived from SED fitting, $\tau_{V,{\rm UV}}$, as a function of stellar mass. $\tau_{V,{\rm H\alpha}}$ arises to first order from the Balmer decrement, whereas the latter is mainly constrained by the UV spectral slope. At lower masses, $\tau_{V,{\rm UV}}$ is higher than $\tau_{V,{\rm H\alpha}}$, but the situation is reversed at the high mass end. According to those authors, $\tau_{V,{\rm UV}} - \tau_{V,{\rm H\alpha}} \sim 0.25$ dex (equivalent to 0.27 mag in A_V) at $\log M_* = 8.5$. This finding can be linked to that found by Wild et al. [2011] that $\tau_{V,{\rm cont}}/\tau_{V,{\rm line}}$ strongly increases with increasing SSFR, i.e., the galaxies with high SSFRs have a higher fraction of diffuse dust and their dust is more centrally concentrated. Adopting the same prior distribution of τ_V and μ as in Salim et al. [2007], we find, for the *s-sed* sample, mean values of $A_{\rm FUV}$ = 1.47 mag and $A_{\rm NUV}$ = 1.08 mag; the the Balmer decrement yields systematically smaller values of $A_{\rm FUV}$, assuming the Calzetti law (see below). In one object, UGC 7889 (= NGC 4641; see its images in Figure 2.7), the $A_{\rm FUV}$ value reaches 6.9 mag. This object is one of the few BCDs in Virgo detected by ALFALFA and, among the dwarf *s-sed* sample, it is one of the reddest in $m_{\rm FUV} - m_{\rm NUV}$ color, has one of the highest stellar masses, has a low gas fraction and is relatively metal-rich. Given its UV color, the high $A_{\rm FUV}$ value of UGC 7889 derived by the SED fitting is consistent with that predicted by the IRX-β relation (see below) as calibrated for starburst galax-

ies [Meurer et al., 1999], but other methods such as the Balmer decrement and the IRX-SFH-color relation (see below), give quite lower extinction estimates. Given the possible degeneracy of its red color arising from either high extinction or strong SF quenching in the Virgo environment, it is probable that the large extinction implied by the SED fitting for this galaxy is unreliable.

Another approach which we suggest is relevant here anticipates that extinction should be lower in less luminous and face-on systems with low metallicities [e.g. Giovanelli et al., 1995, Xiao et al., 2012]. Salim et al. [2007] showed that the derived $\tau_{V,\mathrm{UV}}$ is sensitive to the assumed prior distribution of τ_V in the model library. Therefore, to constrain better $\tau_{V,\mathrm{UV}}$, we first try to estimate τ_V, following Giovanelli et al. [1995], and trim out the models with unrealistically high extinctions. With this improvement in the SED fitting, the mean values for the ALFALFA dwarf *s-sed* sample become A_{FUV} = 1.33 mag and A_{NUV} = 0.96 mag, with formal uncertainties of 0.42 and 0.32 mag, respectively. In particular, the A_{FUV} value is reduced to 2.36 mag for UGC 7889. Since the A_{FUV} estimates are reduced by 0.14 mag on average, the $\log \mathrm{SFR}$ is reduced correspondingly by 0.06 dex (see values in §2.4.5). As noted previously (§2.4.2), such improvement has little effect on estimates of stellar mass.

To convert the extinction to an estimate of the dust mass, we adopted Equation (44) from Popescu et al. [2011], $M_{\mathrm{dust}} = 0.9912[M_\odot\ \mathrm{pc}^{-2}]h_S^2\tau_B^f$, where h_s is the stellar disk scale length in parsec and τ_B^f is the face-on optical depth in the B-band. SDSS g-band values are used to approximate values in the B-band. Following Giovanelli et al. [1994] and Shao et al. [2007], the observed disk scale lengths and optical depths are converted to face-on values. The resulting dust to HI gas mass ratio is 0.003 on average for the *s-sed* galaxies (0.002 for the *s-sup*

sample and 0.004 for the lower HI mass *s-com* population); this ratio is below the mean value of 0.007 quoted in Draine et al. [2007]. In comparison, a dust-to-gas ratio of 0.002 was determined in the nearby starbursting dwarf galaxy NGC 4214 [Lisenfeld et al., 2012]. We also note that Boissier et al. [2004] found that the dust-to-gas ratio is proportional to $(Z/Z_{\odot})^{0.88}$.

In order to assess fairly the accuracy of our results, we have examined correlations between the FUV extinction $A_{\rm FUV}$ and various relevant quantities, in particular those for which relations have been established for samples of more massive galaxies. We find no significant trend with axial ratio, mainly because our sample includes no high axial ratio systems; nearly all show $\log a/b < 0.5$. As discussed in §2.2.4, it is unlikely that we are missing edge-on dwarfs because of the line-width cutoff. Rather, the observed distribution implies that dwarf galaxies are intrinsically thicker or that the distribution of SF sites within them are quite irregular, making the tracing of their disks more complicated. Similarly, Xiao et al. [2012] suggested that dust reddening is not so sensitive to axial ratio at low metallicity as at high metallicity. We have also looked for trends in $A_{\rm FUV}$ with M_* and $f_{\rm HI}$. The trend seen by Salim et al. [2005] that attenuation increases with stellar mass, is not evident among the ALFALFA dwarf galaxies; the latter of course include no really massive galaxies. However, in comparison with Figure 2 of Salim et al. [2005], we find that the highest value of $A_{\rm FUV}$ reached by gas-rich galaxies (as identified by high $f_{\rm HI}$) is lower than that estimated for relatively gas-poor galaxies. Such a result is reasonable assuming that the galaxies which are gas-rich for their stellar masses are less evolved, have lower dust content and metallicity, and thus exhibit less attenuation.

Other common approaches to estimating extinction exploit the infrared

wavelengths. In this case however, the Spitzer archive contains too few of the ALFALFA dwarfs to permit a direct measurement of the infrared excess (IRX) incorporating MIPS wavelengths. Instead we examine how $A_{\rm FUV}$ varies with UV color (β), equivalent to the IRX-β relation following Salim et al. [2007]. In comparison with the relation given for normal star-forming galaxies by those authors, the ALFALFA dwarfs only marginally follow the trend, with the more massive *s-sup* members showing less scatter about the relation. A number of the lowest HI mass *s-com* galaxies fall below the relation for normal galaxy samples; their $A_{\rm FUV}$ would thus be over-predicted by the standard IRX-β relation given their UV color, possibly because of their different SFH and/or dust geometry [Kong et al., 2004, Cortese et al., 2006]. We also find that $A_{\rm FUV}$ is better correlated with the $m_{\rm FUV} - m_{\rm NUV}$ color than with the $m_{\rm NUV} - r$ color.

In addition, we use the spectroscopic Balmer lines to compare the observed flux ratios in the Hα to Hβ lines with the theoretical value (2.86 for Case B recombination) to estimate $A_{\rm H\alpha}$. We assume that $A_{\rm FUV} = 1.8 A_{\rm H\alpha}$, following the Calzetti law [Calzetti et al., 2000], with the caveats about large variations in UV extinction curves and aperture effects. We approximate the ratios using the line flux measurements from the MPA-JHU DR7 catalog (see §2.3.3). This method is applied to 42 galaxies which are common to both the *s-sed* sample and the MPA-JHU catalog. Surprisingly, this crude application of the Balmer decrement method gives systematically smaller extinction estimates, with a mean $A_{\rm FUV}$ = 0.64 mag when we adopt the Calzetti law. Given that the $A_{\rm FUV}$ values are presumably dominated by attenuation by the diffuse ISM whereas the emission lines probe the local attenuation within the clouds in which they originate, one might expect the opposite result as is found in massive galaxies [Calzetti et al., 2000], and incorporated into the factor of 1.8 between the FUV and Hα extinc-

tions. However, we note that Wild et al. [2011] also found a strong decrease in emission line-to-continuum attenuation ratio with increasing SSFR, in agreement with the overall high SSFRs of the ALFALFA dwarf sample relative to the massive galaxies (see §2.5.1) and likely indicative of the variation of the dust geometry with the SSFR. Furthermore, there is large uncertainty in the UV extinction curve so that the constant in the $A_{\rm FUV} = 1.8A_{\rm H\alpha}$ relation suffers from large uncertainty and is most likely underestimated. For the low stellar surface mass density galaxies ($\mu_* < 3 \times 10^8\ M_\odot\ {\rm kpc}^{-2}$) with $A_V = 1$, Wild et al. [2011] found 0.3 mag more attenuation in the NUV compared to the Calzetti law which is derived for starburst galaxies. Similarly, Buat et al. [2011] found a steeper dust extinction curve in ordinary star-forming galaxies than found in starburst galaxies by Calzetti et al. [2000]. In addition, the bump strength of the 2175 Å dust feature is known to vary. Incorrectly assuming a dust curve with no 2175 Å feature (e.g. the Calzetti law for starburst galaxies) would lead to an underestimate in the amount of dust, in turn leading to the incorrect conclusion that the stellar populations are extremely metal poor [Wild et al., 2011]. In particular, the steep FUV rise and small 2175 Å feature in dwarf galaxies, resembling the observed extinction curve of some regions in the LMC, may be due to different dust grain properties in low mass galaxies [e.g. Galliano et al., 2003].

As a final approach, we have explored the extended IRX-SFH-color relation based on the $m_{\rm NUV} - r$ color and the $D_n(4000)$ measurement derived in Johnson et al. [2006], which is commonly used by local *GALEX* studies [Wyder et al., 2007, Schiminovich et al., 2007]; application of this relation to the ALFALFA dwarfs predicts a much larger extinction $A_{\rm FUV}$ in many of the lowest mass *s-com* galaxies.

At the end of this analysis of the various methods of estimating the internal extinction, we conclude that (a) SED-fitting using the UV continuum is the most reliable currently available tool to obtain $A_{\rm FUV}$ values for the ALFALFA dwarfs, but that (b) there is large uncertainty in the extinction estimates. It is inappropriate to ignore completely a correction for extinction at UV wavelengths (the mean of $A_{\rm FUV}$ is 1.33 mag), although attenuation in the dwarfs is smaller than that found in more massive SDSS galaxies, e.g. 2.03 mag in Salim et al. [2005]. We note that taking attenuation into account can bring the dwarf galaxies in the FIGGS study of Roychowdhury et al. [2009] closer to the Kennicutt-Schmidt star formation law obtained for more massive galaxies. However, it will not lead to a change in the slope of the relation. As was found by Roychowdhury et al. [2009], the relationship between the HI density and the SFR in gas-rich dwarfs is steeper than the Kennicutt-Schmidt star formation law.

2.4.4 Metallicity

Standard recipes used to convert FUV luminosities to SFRs [e.g. Kennicutt, 1998a] are derived on the assumption of solar metallicity stellar populations, $Z_{\odot}$. However, in the general population of star-forming galaxies, the gas-phase metallicity Z of the ISM is known to increase with stellar mass, e.g. Tremonti et al. [2004]. This dependence is consistent with simple closed-box models [e.g. Garnett, 2002], whereby high gas fraction galaxies are relatively unevolved and thus have experienced low metal enrichment. Especially in low mass systems, ISM blow-out can follow episodic star formation events. The adoption of an incorrect Z to estimate the SFR through the observed FUV luminosity can significantly bias the result, as a relative deficiency of metals would result in higher

temperatures in the photospheres of forming stars and thus in a greater number of UV photons produced per unit stellar mass.

It is thus legitimate to question the validity of SFRs derived for low M_* systems such as the ALFALFA dwarfs, if an account for their presumed low Z is not considered. Short of specific measurements through optical spectroscopy, the stellar population metallicity may be estimated via SED fitting. Unlike other well constrained parameters such as M_* however, Z is poorly constrained by SED fitting; in fact deriving Z from SED fitting often yields a likelihood distribution with multiple peaks. While we would normally expect that the mean estimates of metallicity $\langle Z \rangle$ derived for larger samples are more reliable, we note that the Salim et al. [2005] sample yields $Z \simeq Z_{\odot}$, while for the ALFALFA dwarf *s-sed* sample we obtain $0.48Z_{\odot}$ ($0.44Z_{\odot}$ for the low HI mass *s-com* galaxies and $0.54Z_{\odot}$ for the additional *s-sup* ones). Therefore, for our estimates of SFR, we adopt Kennicutt's relation, with a correction of 1.1 as given by Hunter et al. [2010], appropriate for a Salpeter IMF and $Z \sim 0.4Z_{\odot}$.

The stellar population metallicity is correlated with gas-phase metallicity, though with large scatter [Gallazzi et al., 2005]. Given the shallow potential well of dwarf galaxies, the gas-phase metal enrichment can be easily lost by outflow. Oxygen abundance measures from the MPA-JHU DR7 release of SDSS spectral [Tremonti et al., 2004] are available for 58 ALFALFA dwarf galaxies, with a mean of $12 + \log(O/H) = 8.26$ (8.27 for 44 low HI mass *s-com* members and 8.22 for 14 *s-sup* galaxies). The oxygen abundances can be converted to gas-phase metallicities in units of solar metallicity ($Z_{\odot} = 0.02$), adopting a value of $12 + \log(O/H)_{\odot} = 8.66$ [Asplund et al., 2004]. The mean of the gas-phase metallicity for the ALFALFA dwarf galaxies corresponds to $0.4Z_{\odot}$. How-

ever, according to the mass-metallicity relation derived in Tremonti et al. [2004], based mainly on more massive galaxies $8.5 < \log M_* < 11.5$, the stellar mass of $\log M_* = 7.4$ corresponds to $12 + \log(O/H) = 7.78$. Almost all of the ALFALFA dwarfs lie above this relation.

2.4.5 Star formation rates

As a next step, we derive the global SFR for the ALFALFA dwarf galaxies both from the FUV luminosity alone, $\mathrm{SFR_{FUV}}$, and by SED fitting, $\mathrm{SFR_{SED}}$. The latter is averaged over the last 100 Myr, comparable to the lifetimes of UV bright stars. Compared to SFRs derived from the Hα luminosity, both $\mathrm{SFR_{FUV}}$ and $\mathrm{SFR_{SED}}$ are sensitive to very low levels of star formation and hence are particularly relevant for application to the ALFALFA dwarf sample.

$\mathrm{SFR_{SED}}$ values are given, in logarithmic units of $M_\odot\ \mathrm{yr}^{-1}$, in Column (12) of Table 2.1 for the ALFALFA *s-sed* galaxies. The mean is -2.18 (-2.48 for the lower HI mass *s-com* sample and -1.71 for the *s-sup* galaxies), within a minimum of ~ -4. In comparison with values found for typical SDSS samples [Salim et al., 2005], the ALFALFA dwarfs overall show very low values of SFR. In such a regime where only a handful of O-stars are formed over timescales comparable to their lifetimes (i.e., a few million years), Hα emission will appear weak or even absent. The SFRs inferred from Hα deviate from those of FUV at $\log \mathrm{SFR} \simeq -2$, but such stochastic effects may begin to play a role below $\log \mathrm{SFR} \simeq -3$, according to Lee et al. [2009a]. Low mass stars may form continuously but at a very low rate so that no change in the IMF is required. However, Lee et al. [2009a] have shown that other factors, including internal

dust attenuation, stellar model uncertainties, metallicity, ionizing photon loss and starbursts, if considered alone, are insufficient to explain the amplitude of the underestimate of the SFR derived from Hα relative to that implied by the UV luminosity. They also suggested that an IMF deficient in high mass stars is consistent with their results. While the current dataset is insufficient to provide conclusive insight, the ALFALFA dwarfs with their very low SFRs, will provide an ideal opportunity to test the hypothesis of a non-universal IMF.

To obtain $\mathrm{SFR_{FUV}}$, a commonly used standard conversion factor from the dust-corrected FUV luminosity into the SFR is given by Kennicutt [1998a], assuming solar metallicity, a Salpeter IMF, and a constant SFH over at least the past ~ 100 Myr in the stellar mass interval of $0.1M_{\odot} - 100M_{\odot}$:

$$\mathrm{SFR}[M_{\odot}\ \mathrm{yr}^{-1}] = 1.4 \times 10^{-28} L_{\nu}[\mathrm{erg\ s^{-1}\ Hz^{-1}}], \tag{2.1}$$

where the FUV flux is derived from the AB magnitude [Lee et al., 2009a]: $f[\mathrm{mJy}] = 10^{(23.9-m_{\mathrm{FUV}})/2.5}$. Taking into account the sub-solar metallicity (see §2.4.4), and adopting a Chabrier IMF which predicts a smaller SFR for the same luminosity than a Salpeter IMF by a factor of 1.58 [Salim et al., 2007], equation (2.1) becomes

$$\mathrm{SFR}[M_{\odot}\ \mathrm{yr}^{-1}] = 0.81 \times 10^{-28} L_{\nu}[\mathrm{erg\ s^{-1}\ Hz^{-1}}]. \tag{2.2}$$

The upper panels in Figure 2.11 shows a comparison of the two measures, $\mathrm{SFR_{FUV}}$ (obtained via equation 2.2) and $\mathrm{SFR_{SED}}$, before (panel a) and after (panel b) extinction corrections are applied, for all the ALFALFA *s-sed* galaxies. Filled circles denote the low HI mass *s-com* members, whereas open ones identify the additional *s-sup* galaxies. As evident in panel (a), in the absence of an extinction correction, the FUV luminosity underestimates the SFR, because, although

small, the extinction at UV wavelengths is not negligible. Moreover, the deviation from the one-to-one relation (dashed line) is greater at the higher SFR end, suggesting that attenuation is larger for higher SFRs. Applying the extinction corrections $A_{\rm FUV}$ derived from the SED fitting (as discussed in §2.4.3) gives the result seen in panel (b): the scatter about and deviation from the one-to-one relation is significantly reduced. The relatively tight correlation evident here confirms that the stellar population synthesis model we used is consistent with what was used in Kennicutt [1998a].

However, as is still evident in panel (b), the FUV luminosity alone tends to overestimate the SFR compared to estimates derived from SED fitting, especially for the lowest SFRs, i.e. SFR below $\sim 10^{-2}\ M_{\odot}$ yr^{-1}. Although we do not compare the SFR$_{\rm FUV}$ with SFR$_{\rm H\alpha}$ here, we note that this threshold is close to the critical value identified by Lee et al. [2009a]. Similarly, Salim et al. [2007] found that, since their sample is characterized by a wide variation in SFH, the conversion factor from FUV luminosity to SFR is smaller than that which would apply for a constant SFH. Compared to their sample, the ALFALFA dwarfs are currently forming more stars relative to the accumulated stellar masses (see §2.5.1). It is possible that the b-parameters become systematically larger in dwarf systems, i.e. a higher fraction of their stars have been formed more recently. For the same amount of observed FUV luminosity, the SFRs averaged over 100 Myr would be smaller than those derived if the SFRs had remained constant. If so, the standard Kennicutt [1998a] conversion factor from $L_{\rm FUV}$ to SFR$_{\rm FUV}$ would be too large in the case of dwarf galaxies. On the other hand, a bursty SF behavior would have less impact on the SFR$_{\rm H\alpha}$, because the SFR is more likely to remain constant during the much shorter life times of O-stars. These results suggest not only that the SFR$_{\rm H\alpha}$ values may be suspicious [Lee et al., 2009a], but so also

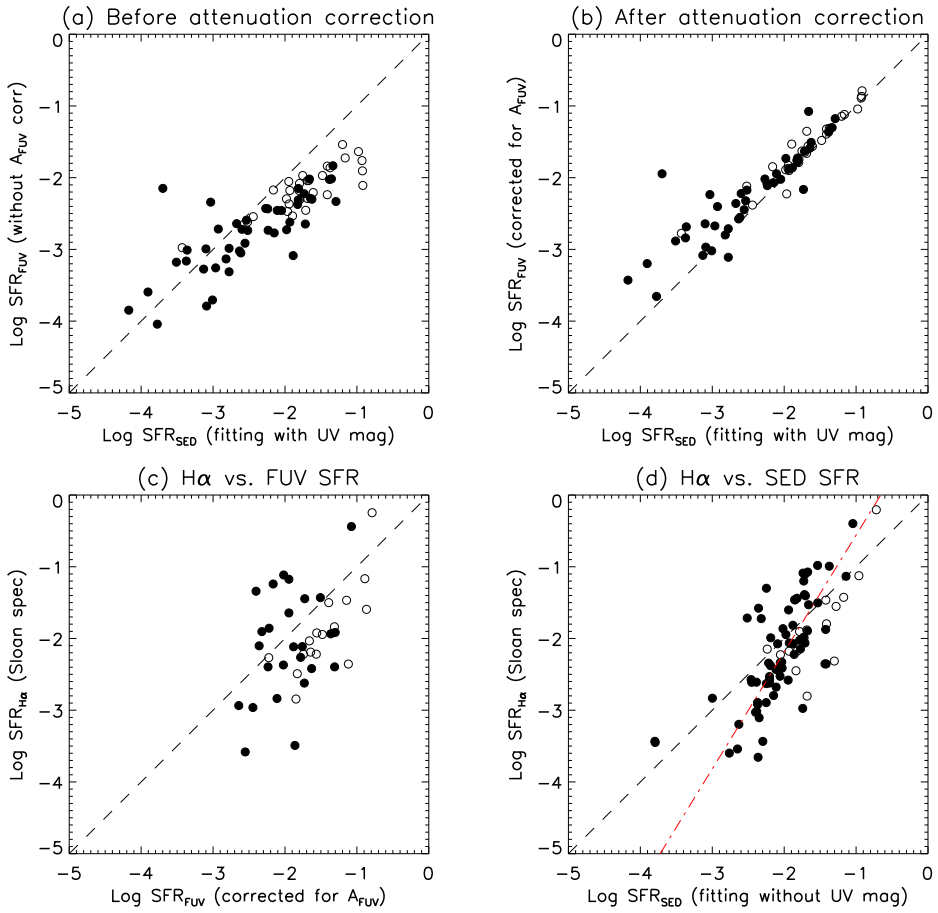

Figure 2.11: Comparison of SFR measures for the ALFALFA dwarf sample with open circles identifying the lower HI mass *s-com* galaxies and filled ones, the additional *s-sup* galaxies in each panel. *Panel (a):* $\mathrm{SFR_{FUV}}$ obtained by the standard conversion from FUV luminosity, (Eqn 2.2) without attenuation correction, versus $\mathrm{SFR_{SED}}$ derived from SED-fitting. *Panel (b):* Same as panel (a) except that A_{FUV}, derived by SED fitting, have been applied to $\mathrm{SFR_{FUV}}$. The FUV magnitudes tend to over-predict SFRs below $\sim 10^{-2}\ M_{\odot}\ \mathrm{yr}^{-1}$, which may be due to the bursty nature of star formation in dwarfs. *Panel (c):* $\mathrm{SFR_{FUV}}$ compared with $\mathrm{SFR_{H\alpha}}$, derived from the SDSS spectroscopic data (MPA-JHU DR7 measurements). Though our aperture correction tends to overestimate $\mathrm{SFR_{H\alpha}}$, the deficiency of $\mathrm{SFR_{H\alpha}}$ is still visible. We are limited by the small number of the *s-sed* galaxies with usable SDSS data. *Panel (d):* SFRs derived from SED fitting only to the SDSS bands compared with $\mathrm{SFR_{H\alpha}}$. A weak trend exists that Hα under-predicts the SFR below $\sim 10^{-2}\ M_{\odot}\ \mathrm{yr}^{-1}$. The dash-dotted line is the linear fit to the data points, with a slope steeper than the one-to-one dashed line.

may be the estimates of $\mathrm{SFR_{FUV}}$ derived using standard conversions obtained for samples of more typical and more massive galaxies.

At this point, we do not have available Hα images, but we can make a crude attempt to quantify the SFRs with the Hα line flux derived from the SDSS spectra, $\mathrm{SFR}_{\mathrm{H}\alpha}$, for those galaxies with such measures. We again use the standard conversion factor calibrated in Kennicutt [1998a], taking into account the metallicity and IMF difference. The MPA-JHU reprocessed Hα line flux is corrected for attenuation, given by the Balmer decrement as in §2.4.3. We correct for the aperture effect by using the ratio of the fluxes corresponding to the entire galaxy r-band magnitude and the magnitude through the fiber in the same band, following Hopkins et al. [2003]. The aperture correction implicitly assumes that the emission measured through the fiber is characteristic of the galaxy as a whole. However, in almost all of the ALFALFA dwarfs the $u-r$ colors are bluer within the fiber than across the galaxy, a fact which can be explained if the bluest star-forming peaks in surface brightness are usually the targets of the spectroscopic observations. As a result, our crude scaling by the r-band light should overestimate $\mathrm{SFR}_{\mathrm{H}\alpha}$. However, the bottom panels in Figure 2.11 still show a systematic deficiency in $\mathrm{SFR}_{\mathrm{H}\alpha}$, relative to both $\mathrm{SFR}_{\mathrm{FUV}}$ (panel c) and $\mathrm{SFR}_{\mathrm{SED}}$ (panel d), albeit with large scatter. As evident in panel (c), the number of galaxies in the *s-sed* sample and with SDSS spectra is quite limited. In panel (d), we attempt to improve the statistics by dropping the requirement of UV data and thus calculating an $\mathrm{SFR}_{\mathrm{SED}}$ by fitting only to the SDSS bands. Albeit crude, the best linear fit line to the data points (the red dashed-dotted line) has a slope larger than 1, suggesting that while the $\mathrm{SFR}_{\mathrm{FUV}}$ could be an overestimate due to stochastic effects, we cannot rule out the possible systematic deficiency of $\mathrm{SFR}_{\mathrm{H}\alpha}$, compared to $\mathrm{SFR}_{\mathrm{SED}}$, and thus a non-universal IMF. We are in the process of obtaining Hα images for this sample and plan to present a more comprehensive comparison of SFR measures in a future work.

2.5 Stars, star formation and gas in the ALFALFA dwarfs

Numerous previous works have explored the relationships between stars, star formation and gas in galaxies, and in this section, we explore how the ALFALFA dwarf galaxies, specifically the *s-sed* sample galaxies, compare to others. In comparison with results obtained for large samples derived from the SDSS [e.g., Brinchmann et al., 2004], the imposition of criteria associated with HI-selection and narrow HI line width renders the ALFALFA dwarf sample a still diverse population of low luminosity blue cloud dwellers. In the context of examining the *s-sed* sample, it is therefore useful to compare it to a sample of higher mass objects selected by similar HI criteria. To do that, we make use of a subset of 12154 galaxies contained in the $\alpha.40$ catalog presented in Haynes et al. [2011] and which are also contained in the SDSS DR7. Haynes et al. [2011] present a cross reference between the $\alpha.40$ and SDSS DR7 databases which is used as the basis for the parent HI-selected population. To derive stellar masses and SFRs for the larger sample, we make use here of the methodologies described in §2.4, but restricted only to the optical SDSS DR7 photometry. A more complete discussion of the $\alpha.40$-SDSS-*GALEX* sample will be presented elsewhere [Huang et al., 2012a].

2.5.1 The ALFALFA dwarfs on the star-forming sequence

Besides the well-known correlation that the SFR increases with stellar mass [e.g., Brinchmann et al., 2004, Bothwell et al., 2009], the 'star-forming sequence' in a specific SFR ($\mathrm{SSFR} = \mathrm{SFR}/M_*$) versus stellar mass diagram is identified by the fact that the SSFRs of lower mass galaxies appear to be confined to a rela-

tively narrow range of SSFR that declines as the stellar mass increases [Salim et al., 2007, Schiminovich et al., 2007]. At masses above $\sim 10^{10}\ M_{\odot}$, some galaxies exhibit much lower values of the SSFR; i.e., the sequence turns over. The tightness of the 'star-forming' sequence strongly suggests that a galaxy's mass regulates its overall SFH. However, a second transition, near $M_B \sim -15$, has been reported [Lee et al., 2009b, Bothwell et al., 2009], below which the dispersion in SSFRs broadens again: low luminosity, low mass galaxies also show a wide range of SSFR. Based on a sample of $\sim$1000 galaxies with both Hα and HI measures available in the literature, Bothwell et al. [2009] have argued that possible causes of this behavior can be categorized under two main headings; first, the various physical mechanisms that underlie the star formation properties of dwarf galaxies not only exhibit a large spread, but also are decoupled from their gas contents. A second possibility proposed by those authors is that at low luminosities, the SFR is not faithfully traced by the Hα luminosity, leading to a mischaracterization of the SFR. Since the SSFRs used here are based on SED fitting, the second explanation proposed in Bothwell et al. [2009], i.e., that Hα does not adequately trace the SFR in dwarfs, is not relevant to this work. Lee et al. [2009b] have also found that, whereas the dispersion in SSFR(Hα) increases toward the lowest luminosities by $\sim 60\%$, the increase is only $\sim 25\%$ when SSFR(FUV) is adopted. Those authors interpreted this difference as evidence that UV measures are less affected by purely stochastic variations in the formation of high mass stars.

Specifically presented for comparison with similar diagrams presented by other authors [e.g., Bothwell et al., 2009, Lee et al., 2011, Salim et al., 2007], Figure 2.12 presents various ways of examining the star formation properties of the *s-sed* galaxies in the context of the parent $\alpha.40$-SDSS sample. The horizontal

layout shows the run of stellar mass, $u-r$ color, and the $m_{\rm NUV}-r$ color, from left to right respectively. In the vertical direction, from top to bottom, panels show the SFR, SSFR and the birthrate parameter b. In all panels, the 74 colored symbols represent the galaxies in the *s-sed* ALFALFA dwarf sample; for those objects, physical properties are determined by SED-fitting (see §2.4.1) to both the UV and optical magnitudes. In the left two columns, black contours and grey small points depict the distribution for the parent $\alpha.40$-SDSS sample in high and low number density regions respectively, derived from SED fitting to the SDSS bands only. Because *GALEX* photometry is not examined here for the $\alpha.40$-SDSS sample, the right panels show only the ALFALFA dwarfs. Filled symbols show the less HI massive *s-com* galaxies (45) while open symbols denote the additional *s-sup* ones (29). Red squares identify galaxies which are members of the Virgo cluster (17) while blue circles show all the others. Bigger symbols represent galaxies with SED fitting $\chi^2_{\rm best} < 10$ (46) while smaller ones have $\chi^2_{\rm best} > 10$ (28). Typical error bar estimates for the *s-sed* sample are plotted in the bottom left corners of Figures 2.12, 2.13 and 2.14, with the same symbol definition in these plots. Note that the $m_{\rm NUV}-r$ range is scaled to be two times that of the $u-r$ color (refer to Figure 2.9).

In general, the parent $\alpha.40$ sample exhibits the known trends that the SFR increases with stellar mass and that a bimodal distribution in SFRs is evident at the highest stellar masses. However, as is clear in Figure 2.12, at low stellar masses, the SFR distributions fall below the extrapolation of the ridge defined by the massive systems. In particular, the ALFALFA *s-sed* dwarfs (the circles and squares) correspond to the systems of lowest stellar mass and define a low, broad tail of the SFR distribution. In the SFR versus $u-r$ color plot, while most of the ALFALFA dwarfs lie on the blue branch, the colors remain almost

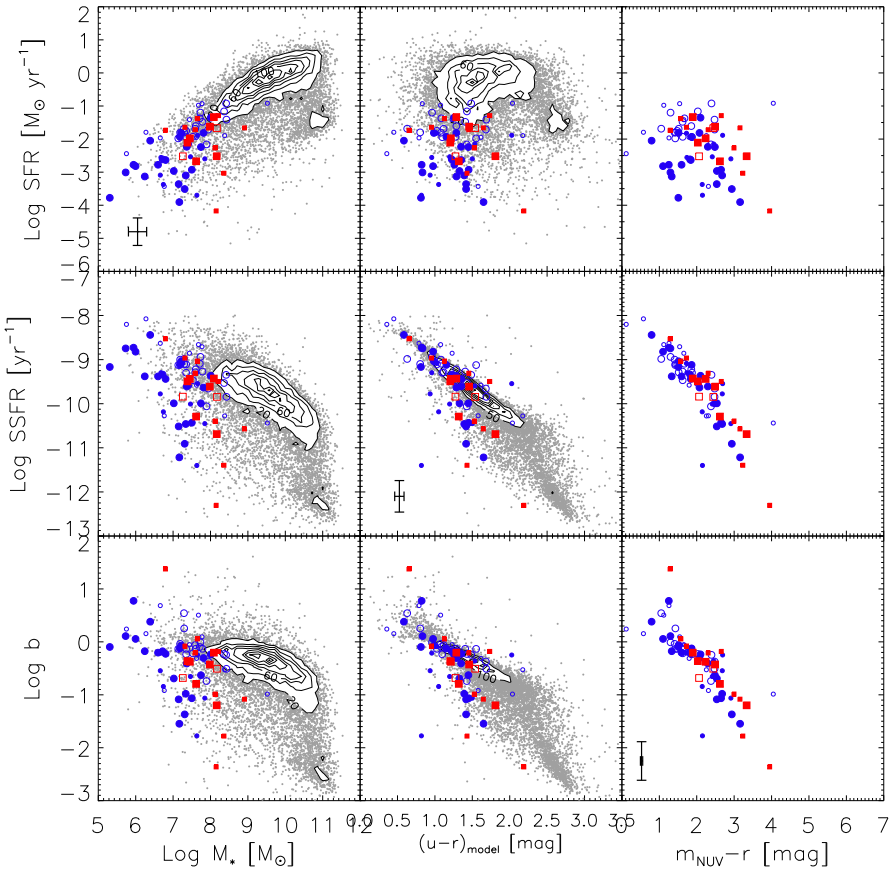

Figure 2.12: ALFALFA dwarfs on the star forming sequence. Black contours and grey small points depict the distribution for the parent $\alpha.40$-SDSS sample, in high and low number density regions respectively. All the other colored symbols represent the *s-sed* galaxies (74 of them) with reliable UV/optical magnitudes so that the SED fitting can be applied. Filled symbols belong to the *s-com* (45) while open ones to the *s-sup* sample (29); red squares denote Virgo Cluster members (17) while blue circles are outside of Virgo (57); bigger symbols represent galaxies with SED fitting $\chi^2_{\rm best} < 10$ (46) while smaller ones have $\chi^2_{\rm best} > 10$ (28). The typical error bars for the *s-sed* galaxies are plotted in the bottom left corners. The horizontal layout shows the run of stellar mass, $u-r$, and the $m_{\rm NUV}-r$ color. In the vertical direction we examine the SFR, SSFR and the birthrate parameter b. Note that the $m_{\rm NUV}-r$ range is scaled to be two times that of the $u-r$ color (refer to Figure 2.9).

unchanged despite their varying, but relatively small, SFRs.

As shown also by Haynes et al. [2011], the ALFALFA catalog is clearly biased

against red sequence galaxies. Still, the bimodal nature of the distributions of SSFR is evident in the left panel of the second row of Figure 2.12. At the high mass end, a relatively small population of red sequence $\alpha.40$ galaxies occupies the low SSFR regime. The contours of the blue star-forming sequence reflect the general trend that the SSFR generally decreases with increasing stellar mass. At the same time, compared to that in the intermediate mass range ($10^8 - 10^{10}\ M_\odot$), the dispersion of the SSFR distribution in a given stellar mass bin increases below $M_* \sim 10^8\ M_\odot$. The standard deviation of the $\log SSFR$ distribution for galaxies in a given $\log M_*$ bin is 0.55 dex in $9.25 < \log M_* < 9.75$, 0.71 dex in $7.75 < \log M_* < 8.25$ and increases to 0.83 dex in $6.75 < \log M_* < 7.25$. Most of the ALFALFA dwarfs lie in this low stellar mass regime, and not surprisingly, they show a large dispersion in SSFR. Moreover, because of the HI mass cutoff used to define the ALFALFA dwarf sample, it actually includes galaxies with low HI mass for their stellar mass, e.g., they are relatively gas-poor in comparison with the parent $\alpha.40$-SDSS sample (see §2.5.3). This selection tends to exaggerate the dispersion of the SSFRs to low values, and a concentration of small grey points from the parent sample with higher SSFRs is visible above the *s-sed* galaxies within the same M_* range. For the same reason, the additional *s-sup* galaxies with their higher gas fractions have higher SSFRs on average than the lower HI mass *s-com* ones. The few extreme outliers from the star-forming sequence with low SSFRs are mostly galaxies drawn from the lowest HI mass *s-com* sample (filled circles and squares). Several of them are dEs/dSphs in Virgo (e.g. AGC 220819 = VCC 1617 and AGC 223913 = VCC 1649; see images of the latter shown in Figure 2.7), among the very few early type Virgo dwarfs detected by ALFALFA [Hallenbeck et al., 2012].

For galaxies with low SSFRs, a blind HI survey is more efficient at the de-

tection of galaxies at both the low and high stellar mass ends [Huang et al., 2012a]. Moreover, a blind Hα survey would be biased against galaxies with low SSFRs. The sample analyzed by Bothwell et al. [2009] is heterogenous, making use of existing compilations of HI and Hα data derived for other purposes. For example, the local low SSFR galaxies with low M_* were particularly targeted for the 11HUGS program which contributes significantly to the Hα data used by Bothwell et al. [2009]. Similarly, the HI data analyzed in Bothwell et al. [2009] include a large population of massive cluster galaxies which have low SSFRs and were included in the targeted but deep surveys of nearby rich clusters [Springob et al., 2005]. ALFALFA probes to a slightly lower stellar mass range than the sample examined by Bothwell et al. [2009] and reveals outliers from star-forming sequence at both mass ends similar to those noticed by those authors. Thus, the break-down of the star-forming sequence at the low mass end is real and indicates that the stellar mass is no longer the dominant regulator of SF in dwarfs. It is possible that dwarfs are more vulnerable to environmental effects so that their gas supply can be easily disturbed, and thus star formation quenched. In the intermediate M_* range, many outliers with extremely low SSFRs exist within the $\alpha.40$ parent sample, but their number density relative to the contoured region is so low that the dispersion of SSFRs remains low. However, while ALFALFA reveals that outliers with anomalously low SSFR for their stellar mass exist at all masses, intermediate mass outliers are missing in similar plots (e.g. Figure 8) from Bothwell et al. [2009]. Given the heterogenous sample which the Bothwell et al. [2009] analysis is based on, the absence of low SSFR galaxies in the intermediate mass range could be due to some combined bias in the sample selection criteria by the dual requirement of Hα and HI (from the Cornell digital HI archive, selected typically by luminosity, optical size and/or

cluster membership) measures.

The contours in the SSFR versus $u-r$ diagram (middle column) show that the SSFRs of $\alpha.40$ galaxies are tightly correlated with the $u-r$ color: for HI-selected galaxies nearly all of which are blue, the SSFRs, and thus the recent star-formation histories, are well constrained by the $u-r$ color itself. Given the fact that the NUV band better traces star formation than the u-band, we would have expected that the $m_{\rm NUV}-r$ color would be better correlated with SSFR than is the $u-r$ color. However, such an improvement is not obvious in the right panel: the larger attenuation correction introduces a greater dispersion in the observed NUV, so that a better correlation between SSFRs and $m_{\rm NUV}-r$ colors is in fact not clearly evident among the *s-sed* dwarf galaxies.

Finally, we consider another quantity related to the SSFR, namely, the birthrate or b-parameter, $b = {\rm SFR}/\langle{\rm SFR}\rangle = ({\rm SFR}/M_*)TR$, where T is the age of the galaxy and R is the fraction of the mass formed over the galaxy's lifetime that does not eventually get returned to the ISM or IGM [Brinchmann et al., 2004]. A typical value of R is ~ 0.5 [Brinchmann et al., 2004], and on the assumption that all galaxies started forming stars shortly after the big bang, $T \sim 13$ Gyr. For these choices of T and R, a galaxy with $b = 1$, i.e. a constant SFR, would have an SSFR of $10^{-9.8}$ yr $^{-1}$. Thus, galaxies with SSFRs larger than this value appear to have current SFRs above their lifetime average. With the caveat that SFR measures based on Hα emission in the low SFR regime may be systematically underestimated, Lee et al. [2009b] found that only ∼6% of low mass 11HUGS galaxies are currently experiencing massive global bursts (Hα EW above 100 Å or $b \gtrsim 2.5$). Here, we find that 13 galaxies (18%) of the ALFALFA *s-sed* sample have $b > 1$ and 5 galaxies (7%) even have $b > 2.5$. Because

of the relationship between the SSFR and the b-parameter, the distributions of $\log b$ vs. stellar mass, $u-r$ and $m_{\rm NUV}-r$ colors, shown in the bottom row of Figure 2.12, resemble the corresponding distributions in the second row, suggesting that dwarfs have both higher SSFRs and b-parameters, on average, compared to higher mass galaxies. For this reason, it is even more essential to take bursty behavior into account when modeling the SEDs of HI-selected dwarfs. At the same time, the equivalent widths of emission lines, e.g. Hα, which also characterize the SSFRs or b-parameters [Lee et al., 2009b], could be large enough to modify the continuum emitted by the underlying stellar population, leading to large χ^2 in the SED fitting (§2.4.1). Despite the caveats, the wide spread in b values evident among the *s-sed* sample suggests that the SFHs of the ALFALFA dwarfs are highly variable and no longer a strong function of M_*. This result suggests further that other factors including environmental effects may play an important role in the regulation of star formation in HI-selected dwarfs.

2.5.2 Star formation efficiency and the gas depletion timescale

In addition to normalizing the SFRs by stellar mass to infer the level of the current SFR relative to its past average, we can also normalize the SFR by the HI mass to infer the ratio relative to potential future star formation, as inferred from the present amount of HI gas. Following Schiminovich et al. [2010], we define the star formation efficiency as $\mathrm{SFE} = \mathrm{SFR}/M_{\rm HI}$, and its reciprocal, as the gas consumption timescale $T_{\rm cons} = M_{\rm HI}/\mathrm{SFR}$, also known as the Roberts time [Roberts, 1963]. Observationally, low SFEs have been measured for low-mass galaxies and LSB galaxies [Boissier et al., 2008], and conversely, high efficiencies have been measured in starburst galaxies and interacting systems.

Based on a sample of ∼1000 local galaxies $10^7 M_\odot \lesssim M_* \lesssim 10^{11} M_\odot$, with HI and H$\alpha$ fluxes compiled from the literature, Bothwell et al. [2009] found that, with increasing luminosity, the HI gas fraction $M_{\rm HI}/M_*$ drops off faster than the Hα-derived SFR, resulting in shorter $T_{\rm cons}$ for more luminous galaxies. Those authors report $T_{\rm cons}$ in excess of several Hubble times (t_H) for samples of dwarf irregular galaxies. In contrast, using the FUV luminosity instead of Hα to measure the SFR, Lee et al. [2011] found that dwarf galaxies may not be as drastically inefficient in converting gas into stars as suggested by Hα estimates, with SFEs exceeding t_H^{-1}. Although the Bothwell et al. [2009] sample also exploits HI measures for a large sample to derive gas fractions, it is based on optical, rather than HI, selection, deriving most of its HI properties from the extensive compilation of HI spectra contained in the Cornell digital HI archive [Springob et al., 2005]. In fact, it is important to note that more than $2/3$ of ALFALFA HI detections are new and were not included in any of the extensive pointed observations which contributed to the digital archive dataset [Haynes et al., 2011]. In terms of the availability of HI measures, the $\alpha.40$ parent sample is more homogeneous and its size is more than 10 times larger than the Bothwell et al. [2009] sample. Moreover, we rely on SED fitting to derive physical quantities, rather than deriving stellar masses based on the M/L versus color relation (see §2.4.2), or the Hα luminosity for the SFR (see §2.4.5). In addition, the ALFALFA dwarf population used here extends to lower HI masses compared to those in Lee et al. [2011]. Therefore, the ALFALFA-based galaxy sample is more comprehensive than either of those two previous studies both in terms of probing the general trends exhibited by HI-selected galaxies as well as exploring the behavior of the lowest mass dwarfs.

Figure 2.13 shows the distribution of SFE versus M_*, $u-r$ and $m_{\rm NUV}-r$

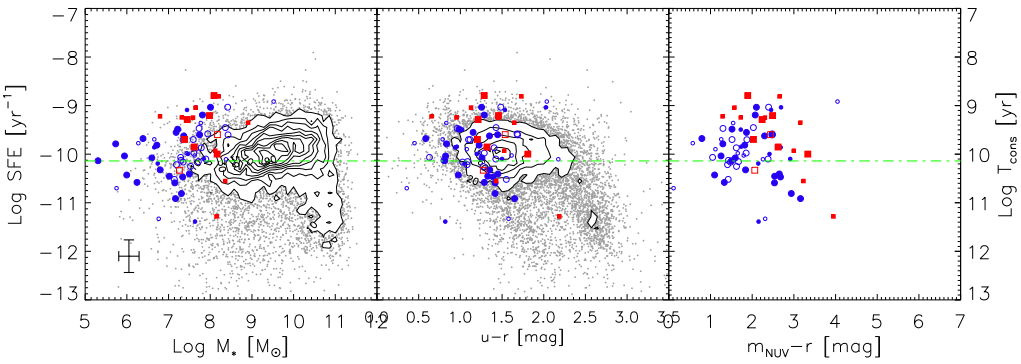

Figure 2.13: Star formation efficiency ($\mathrm{SFE} = \mathrm{SFR}/M_{\mathrm{HI}}$) and gas depletion timescale ($T_{\mathrm{cons}} = \mathrm{SFE}^{-1}$). Symbol definition follows Figure 2.12. The green dash-dotted line corresponds to $\mathrm{SFE} = t_H^{-1}$, where t_H is the Hubble time. *Left:* SFE against stellar mass. The SFEs of ALFALFA detections are on average lower than optically selected galaxies. The averaged SFEs in each stellar mass bin increase slowly with stellar mass, with the $\mathrm{SFE} \sim t_H^{-1}$ at the low mass end. Selected to have lower f_{HI} compared to the $\alpha.40$-SDSS galaxies in this stellar mass range, the *s-sed* galaxies have higher SFEs compared to the general trend if extrapolated into this stellar mass range. A large portion of them even have $T_{\mathrm{cons}} \lesssim t_H$. In particular, the majority of Virgo members in the *s-sed* sample have $T_{\mathrm{cons}} \lesssim t_H$. *Middle and right:* The SFE is seen to vary very little with color in either the optical or optical/UV bands.

colors for the ALFALFA samples. Contours and grey small points in the left two panels depict the distribution of the full $\alpha.40$-SDSS dataset, and the symbol definition follows the same convention as in Figure 2.12. The superposed dash-dotted line corresponds to $\mathrm{SFE} = t_H^{-1}$. Three main conclusions can be drawn from the general distribution. First, as discussed more fully elsewhere [Huang et al., 2012a], ALFALFA galaxies have, on average, higher SFRs but lower SFEs than optically-selected ones, due to their higher than average HI masses. At the same time, the SFEs are barely dependent on either the $u-r$ or $m_{\mathrm{NUV}}-r$ color as shown in the center and right panels of Figure 2.13. Second, although the variation in the average SFR is mild across the stellar mass range of $10^8 - 10^{11}\ M_\odot$ ($\delta \log\langle \mathrm{SFE} \rangle \sim 0.5$ dex), the averaged SFE in each stellar mass bin increases with stellar mass. At the low mass end, the $\mathrm{SFE} \sim t_H^{-1}$, albeit with considerable scat-

ter. Thirdly, a population of galaxies with very low SFE, arising mainly because of their low SFR (see Figure 2.12), stands distinct from the general distribution at the high mass end ($M_* \gtrsim 2 \times 10^{10}\ M_\odot$).

Notably, despite the fact that they are selected to have the lowest HI masses in the $\alpha.40$ catalog, the *s-sed* dwarfs (circles and squares) typically have higher SFEs regardless of their low SFRs, compared to an extrapolation of the general trend into this stellar mass range. In contrast to the extremely low SFEs derived from Hα emission for the dwarfs studied by Bothwell et al. [2009], the ALFALFA dwarfs studied here are forming stars efficiently, and a large portion of them even have $T_{\rm cons} \lesssim t_H$. In particular, 14 out of 17 Virgo dwarfs (red squares) detected by ALFALFA have $T_{\rm cons} < t_H$, suggesting that the cluster environment may actually play a role in enhancing their SFEs by either accelerating their evolution and thus driving them to the gas-poor side, or simply stripping part of their gas away. In contrast, AGC 223913 and AGC 220819, both dE/dSphs in Virgo, have low SFEs and $T_{\rm cons} > t_H$.

2.5.3 HI mass and gas fraction

As specified in §2.3.4, we define the gas fraction here simply as the ratio of the HI mass to the stellar mass ($f_{\rm HI} = M_{\rm HI}/M_*$), without a correction for the presence of helium or for other phases of hydrogen. Little is actually known about the molecular content of dwarf galaxies other than that it is low. Numerous other studies, e.g. Walter et al. [2007], have shown that dwarf galaxies, including ones detected in HI, are notoriously difficult to detect in CO and contain only small masses of dust. Moreover, the relationship between CO and H_2 may break

down in galaxies of low metallicity. Since the fraction of the ISM contributed by very cold molecular material is likely to be insignificant [e.g. Leroy et al., 2007], and the uncertainty in it, large, we assume that the ALFALFA dwarfs are likely dominated by HI at least on global scales and equate the HI mass with their total gas mass.

Figure 2.14 presents the distribution of HI mass (upper panels) and gas fraction $f_{\rm HI}$ (lower panels) as a function of stellar mass, $u-r$ and $m_{\rm NUV}-r$ colors, respectively. As before, in the left two panels, the ALFALFA dwarf galaxies in the *s-sed* sample are shown as circles and squares superposed on the parent $\alpha.40$-SDSS sample (black contours and grey points). The horizontal dashed line in the upper panels marks the HI mass cutoff $M_{\rm HI} < 10^{7.7} M_\odot$ imposed on the *s-com* sample. In the lower plots, horizontal dashed line traces $M_{\rm HI} = M_*$ while in the lower left panel, the diagonal dash-dotted line traces the locus where $M_{\rm HI} = 10^{7.7} M_\odot$. The distributions for the full ALFALFA population are smooth, with the mean $M_{\rm HI}$ increasing with M_*, and the mean $f_{\rm HI}$ decreasing monotonically as M_* grows. Unsurprisingly, $f_{\rm HI}$ is tightly correlated with both the $u-r$ and $m_{\rm NUV}-r$ color: bluer galaxies have higher gas fractions. Note again that ALFALFA probes significantly lower masses, both stellar and HI, than other surveys. Imposing a limit in $M_{\rm HI}$ confines the ALFALFA *s-com* sample to fall below the horizontal dashed line in the upper panels and to the left of the dash-dotted line in the bottom left panel.

As evident in the bottom row of panels, some of the lowest mass galaxies have extremely high gas fractions ($f_{\rm HI} > 100$). Visual inspection of the most egregious cases shows that these values are corrupted by poor SDSS photometry or, possibly, by the assignment of the wrong OC. Although we have checked

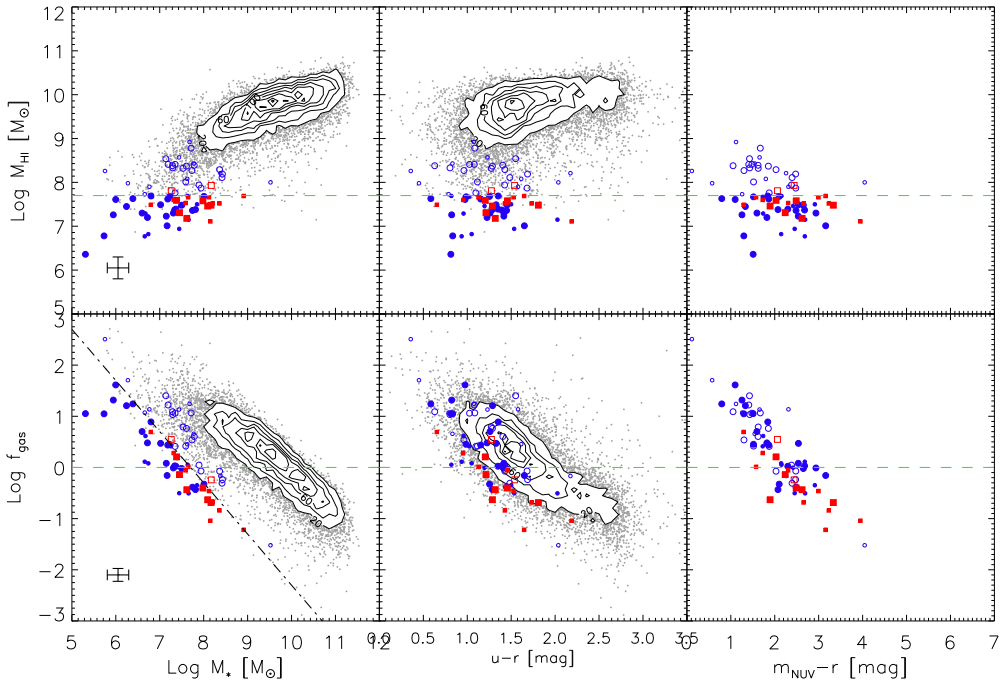

Figure 2.14: HI mass and gas fraction, $f_{\rm HI} = M_{\rm HI}/M_*$. Symbol definition follows Figure 2.12. *Upper row:* $M_{\rm HI}$ as a function of stellar mass and colors. The dashed line corresponds to the cutoff in $M_{\rm HI}$ of the *s-com* sample.The $M_{\rm HI}$ increases with M_*, with the *s-sed* lying on the low mass tail. At a given $M_{\rm HI}$, Virgo members (red squares) have on average lower $f_{\rm HI}$. *Bottom row:* $f_{\rm HI}$ as a function of the three. The dashed line corresponds to $M_{\rm HI} = M_*$, while the black dash-dotted line shows again $M_{\rm HI} = 10^{7.7} M_\odot$. Because ALFALFA is biased against gas-poor galaxies, the correlation that $f_{\rm HI}$ decreases with increasing M_* is clean. Specifically, the HI mass selection of the ALFALFA dwarf sample results in low $f_{\rm HI}$, relative to the $\alpha.40$-SDSS in this *stellar mass* range. However, 46 of the 74 *s-sed* ALFALFA dwarfs still have $f_{\rm HI} > 1$. For galaxies blueward of $u - r = 2$, $f_{\rm HI}$ is lower in the redder ones.

the photometry for the dwarf sample individually, only a portion of the OCs in the $\alpha.40$-SDSS sample has been inspected individually to set a SDSS photometric quality flag [Haynes et al., 2011]. As a result, it is not surprising that some of the $\alpha.40$ galaxies with $f_{\rm HI} > 100$ suffer from shredding, with a fainter child assigned as the SDSS cross-match and thus producing an underestimate of M_*. In other cases, confusion within the ALFA beam may result in a match to the wrong object albeit the "most probable" OC. The complexities and caveats in-

volved in assigning OCs to the ALFALFA dataset are discussed in Haynes et al. [2011]. However, some dwarfs really do appear to be highly HI dominated. For example, AGC 174514 in the supplementary *s-sup* sample also has a $f_{\rm HI} > 100$; its images are shown in Figure 2.7. It is the bluest galaxy among the *s-sed* sample, suggesting that it is truly a galaxy with lots of gas and not many stars. However, it may not be a single object and the $f_{\rm HI}$ could be a slight overestimate due to the uncertainty of the distribution of the HI; there are several additional small blue LSB clumps within the ALFALFA beam which may contribute comparable optical luminosities, thereby raising the stellar mass by some factor, but certainly not 10^2; this galaxy remains an unusual object with a very high gas fraction.

Using a similar $f_{\rm HI}$ vs. M_B diagram, Bothwell et al. [2009] found a population of outliers, namely early type galaxies with extremely low $f_{\rm HI} < 0.05$, extending below the main distribution (Figure 3 of that paper) at the bright end ($M_B < -18$). They further identified this phenomenon with the large spread in the SSFRs of massive galaxies, suggesting that a dearth of fuel for star formation causes the extremely low SSFRs. In comparison with Figure 3 of Bothwell et al. [2009], Figure 2.14 reveals no concentration of galaxies with low $f_{\rm HI}$ below the main distribution at the high mass end, despite the existence of many low SSFR massive galaxies. The absence of very low $f_{\rm HI}$ massive galaxies in ALFALFA is not surprising given its well-characterized flux completeness and near-constant integration time. In contrast, some of the HI measures contributed by the Springob et al. [2005] dataset and used by Bothwell et al. [2009] made use of very deep targeted observations designed specifically to probe to very low gas fractions in massive early type and cluster galaxies. The desire to probe the true range of gas fractions representative of the most massive galaxies likewise

motivated the targeted deep observations of the GASS program [Catinella et al., 2010].

At the same time, they found that the population of low mass galaxies with a large spread in SSFRs is not matched by an equivalent shift to a larger range of $f_{\rm HI}$. On the other hand, the broadening of the $f_{\rm HI}$ distribution at the low mass end is more evident in the ALFALFA dataset, compared to that seen by Bothwell et al. [2009]. Among the 176 ALFALFA dwarfs in the low HI mass *s-com* set, only 2 are included in the Springob et al. [2005] catalog. Hence, it is not surprising that Bothwell et al. [2009] see no broadening of the $f_{\rm HI}$ distribution at the low mass end. HI selection yields a high overall gas fraction across the full range of sampled masses, and at the same time, still a larger dispersion in the SSFR distribution at both the high and low stellar mass ends (see §2.5.1).

In Figure 2.14, the ALFALFA dwarfs in the *s-sed* sample (circles and squares) lie on the low mass tail of both the $M_{\rm HI}$ and $f_{\rm HI}$ distributions: at low stellar masses, the ALFALFA dwarfs probe a relatively low gas fraction population. This departure from the norm for the majority of the ALFALFA detections results from the imposition of the low HI mass cutoff. Among the low mass *s-com* galaxies (filled symbols), at a given $M_{\rm HI}$, the Virgo members (red squares) have, on average, higher M_* and thus lower gas fractions, than the non-Virgo ones (blue circles). Given the general trend between $f_{\rm HI}$ and M_*, the most gas-rich galaxies have very low M_*. Even if their $f_{\rm HI} > 1$, the least massive may lie below the HI sensitivity of ALFALFA at the Virgo distance (log $M_{\rm HI} \sim 7.3$). Alternatively, the low gas fractions may reflect a possible connection between the cluster environment and relative gas poorness; in fact, Hallenbeck et al. [2012] show that some morphologically early Virgo dwarfs contain "normal" gas frac-

tions and argue that they must have recently accreted their HI. Here, as is seen in Figure 2.14, more than half (46) of the *s-sed* galaxies have $f_{\rm HI} > 1$, meaning that their baryonic mass is dominated by their atomic gas, rather than by their stars.

2.5.4 The star formation law and the global interplay of gas and stars

It is well known that the local surface density of the star formation rate is strongly correlated with the local surface density of gas, $\Sigma_{\rm SFR} \propto \Sigma_{\rm gas}^{\alpha}$, at least when averaged over $\sim$ kpc scales. A precise measurement of its exponent is the 'Kennicutt-Schmidt law' [Kennicutt, 1998b],

$$\log(\Sigma_{\rm SFR}[M_\odot\ {\rm yr}^{-1}\ {\rm kpc}^{-2}]) = \alpha \log(\Sigma_{\rm gas}[M_\odot\ {\rm pc}^{-2}]) + C, \tag{2.3}$$

where $C = \log\left[\frac{(2.5\pm0.7)\times10^{-4}}{1.5}\right]$, $\alpha = 1.4 \pm 0.15$ and $\Sigma_{\rm gas} = \Sigma_{\rm HI} + \Sigma_{\rm H_2}$. The denominator of C, 1.5, results from the Chabrier IMF adopted in this work. Such a super-linear Schmidt law ($\alpha > 1$) suggests a star formation efficiency which rises with gas surface density. Measurements of azimuthally averaged gas and SFR profiles show that the SFR correlates better with the molecular hydrogen component than with the total gas density at least within the optical disk [Bigiel et al., 2008]. Yet, on global scales averaged over the whole galaxy, SFRs appear to correlate better with the total gas (HI + H_2), rather than the molecular gas, surface density [Kennicutt, 1998b]. Global quantities such as those available to us sample a range of gas surface densities, timescales and conditions within the ISM, and since we have only global HI measures, we can only estimate $\Sigma_{\rm gas}$ by proxy, using the global HI mass and the optical size of the stellar disk.

Albeit crude in comparison to more detailed studies of spatial resolved atomic and molecular distributions, we examine via Figure 2.15 the correlations of global quantities related to the Schmidt law to demonstrate the constraints placed by the global HI measures on global SFRs. As before, both the $\alpha.40$ and the dwarf *s-sed* samples are shown, with symbol definitions following Figure 2.12. Panel (a) of Figure 2.15, shows the distribution of the SFR as a function of $M_{\rm HI}$; this can be thought of as the global atomic and volumetric star formation law. The green dotted line with a slope of 1.2 is the linear fit to all the $\alpha.40$-SDSS galaxies. The dashed line, of slightly steeper slope 1.5, is the linear fit to the galaxies in the dwarf *s-sed* sample only. While it is natural to expect higher SFRs in galaxies with more gas available to form stars, the ALFALFA *s-sed* dwarf galaxies define the low HI mass tail of the distribution of star forming galaxies. Note also the presence of a second tail exhibited by the parent $\alpha.40$-SDSS population at very low SFRs; these galaxies may include a population of objects whose HI distributions extend beyond their star-forming disks. In §2.5.2, we have already presented the result that the SFE increases slowly with M_*. In fact, other recent works demonstrate that the $\Sigma_{\rm SFR} - \Sigma_{\rm gas}$ relation steepens at low gas surface densities due to the transition from atomic to molecular hydrogen [e.g., Bigiel et al., 2008]. The dependence of SFR on $M_{\rm HI}$ for the ALFALFA dwarfs shown in panel (a) shows a suggestive mild steepening at low $M_{\rm HI}$. Similarly, Roychowdhury et al. [2009] found that the SFR is generally lower in gas rich dwarfs than predicted by the 'Kennicutt-Schmidt law'. Again, we note that the linkage of the scaling between SFR and $M_{\rm HI}$ with the power law derived for $\Sigma_{\rm SFR}$ and $\Sigma_{\rm gas}$ is subject to various uncertainties, including the contribution from molecular gas, and the relative extent of the star forming and HI disks. Therefore, this comparison of global quantities yields only a suggestive empiri-

cal result.

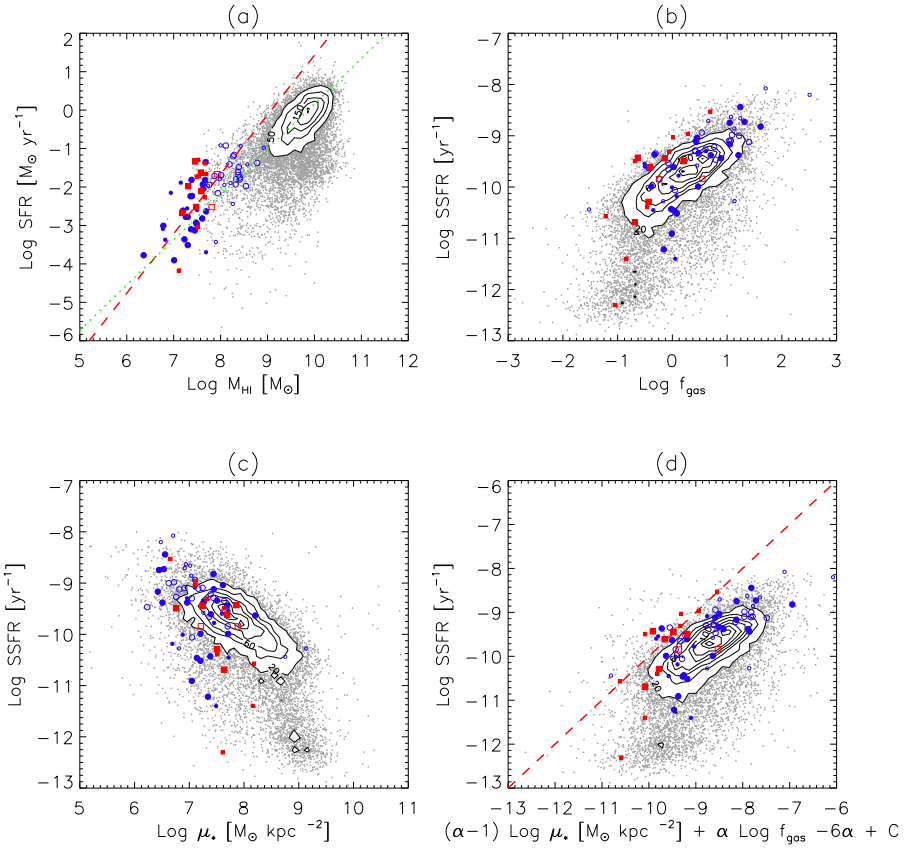

Figure 2.15: Gas content and star formation. Symbol definition follows Figure 2.12. *Panel (a)*: The SFR increases with the HI mass. The dotted line has a slope of 1.2, corresponding to the linear fit to all the $\alpha.40$-SDSS galaxies. The dashed line, of slightly steeper slope 1.5 is the linear fit to the *s-sed* only. *Panel (b)*: Both axes in panel (a) are normalized by the stellar mass. Besides the general trend that the SSFR increases with the gas fraction, the SSFRs of a subset of galaxies drop dramatically once the gas fraction is below ~ 0.3. *Panel (c)*: SSFRs decrease with increasing stellar surface mass density, μ_*. *s-sed* have relatively low μ_*. *Panel (d)*: By assuming that the aperture with a radius of $r_{50,z}$ also contains half of the stellar mass, SFR and HI mass, the star formation law Kennicutt [1998b] is substituted into the expression of SSFR, resulting in the quantity on the x-axis. The adopted values of the scaling factor C and exponent α reflect the Kennicutt [1998b] result. Although a clear correlation appears, the main distribution is shifted to the right of the dashed one-to-one line.

In panel (b), we normalize both axes by M_*, giving the relationship between SSFR and $f_{\rm HI}$. Normalization by M_* moves the galaxies in the ALFALFA dwarf *s-sed* sample from the tail seen in panel (a) back to within the main distribution. For the majority of ALFALFA galaxies, except those with extremely low SSFR, a clear trend exists: the more gas-rich (higher gas fraction), the higher is the SFR relative to the accumulated stellar mass (higher SSFR).

Given the fact that the majority of HI disks are un-resolved by ALFALFA, we cannot quantify $\Sigma_{\rm gas}$ directly. However, we can characterize the surface densities by introducing an area-related quantity: the stellar surface mass density, μ_*. Following Schiminovich et al. [2010], we define the stellar surface mass density:

$$\mu_*[M_\odot\ {\rm kpc}^{-2}] = \frac{0.5 M_*[M_\odot]}{\pi (r_{50,z}[{\rm kpc}])^2},$$

where $r_{50,z}$ is the Petrosian half-light radius according to the SDSS pipeline measurements. Panel (c) of Figure 2.15 shows that SSFR decreases with increasing μ_* in general, and that the dwarf *s-sed* galaxies, on average, have lower μ_* than the full ALFALFA population. For comparison with other studies, we adopt an aperture of radius $r_{50,z}$ and assume that, by definition, it encloses also one half of the stellar mass. Although it is likely not a correct assumption, we assume first that this aperture also contains exactly half of the global SFR, as well as half of the HI mass, and thus

$$\log(\Sigma_{\rm SFR}[M_\odot\ {\rm yr}^{-1}\ {\rm kpc}^{-2}]) = \log \frac{0.5 {\rm SFR}[M_\odot {\rm yr}^{-1}]}{\pi (r_{50,z}[{\rm kpc}])^2}$$

$$\log(\Sigma_{\rm HI}[M_\odot\ {\rm pc}^{-2}]) = \log(\Sigma_{\rm HI}[M_\odot\ {\rm kpc}^{-2}]) - 6 = \log \frac{0.5 M_{\rm HI}[M_\odot]}{\pi (r_{50,z}[{\rm kpc}])^2} - 6$$

The star formation law averaged within this aperture can be re-written from equation (2.3) as:

$$\log(\Sigma_{\rm SFR}[M_\odot\ {\rm yr}^{-1}\ {\rm kpc}^{-2}]) = \alpha(\log \mu_*[M_\odot\ {\rm kpc}^{-2}] - 6) + \alpha \log f_{\rm HI} + C \qquad (2.4)$$

Certainly the adoption of the right hand side of equation (2.4) to infer $\Sigma_{\rm SFR}$, is crude at best. It is true or, at least, likely that (i) star formation may be more concentrated than the older population (see §2.3.2), so that $\Sigma_{\rm SFR}$ is underestimated; (ii) the HI disk is more extended than the stellar one so that $\Sigma_{\rm HI}$ and thus $\Sigma_{\rm SFR}$ are both overestimated; (iii) ignoring the contribution of H_2 to the $\Sigma_{\rm HI}$ also leads to an underestimate of $\Sigma_{\rm SFR}$.

With the above caveats, equation (2.4) gives a crude relation between the SSFR, μ_* and $f_{\rm HI}$:

$$\begin{aligned}\log {\rm SSFR}[{\rm yr}^{-1}] &= \log \frac{0.5{\rm SFR}[M_\odot {\rm yr}^{-1}]}{\pi(r_{50,z}[{\rm kpc}])^2} - \log \frac{0.5M_*[M_\odot]}{\pi(r_{50,z}[{\rm kpc}])^2} \\ &= (\alpha-1)\log \mu_*[M_\odot\ {\rm kpc}^{-2}] + \alpha \log f_{\rm HI} - 6\alpha + C. \end{aligned} \quad (2.5)$$

Adopting the values of C and α from equation 2.3, we plot the right hand side of this equation on the x axis of Figure 2.15 panel (d) and the left hand side ($\log {\rm SSFR}$) on the y axis. Although these two quantities are correlated as expected with a slope of ~ 1, the main distribution is shifted from the one-to-one correlation, represented by the red dashed line, in the sense that the right hand side overestimates the SSFR, i.e. $\Sigma_{\rm SFR}$. Among the three possible caveats to the adoption of the right hand side of equation (2.4) to infer $\Sigma_{\rm SFR}$ which might lead to systematic errors in the $\Sigma_{\rm SFR}$ estimates, only the second one, that the HI gas extends beyond the stellar disk, would yield a shift in the correct direction. Additional factors that might cause such a shift include: (iv) The ALFALFA galaxies have sub-solar metallicity on average, requiring an even smaller C (see §2.4.4); (v) because they are gas-rich in general, they also have lower SFEs relative to the typical SDSS galaxies (see §2.5.2), and thus smaller C values. Both these interpretations are consistent with what is evident in Figure 2.15 panel (d), i.e., the standard C [Kennicutt, 1998b] may be an overestimate for an HI selected

population. Furthermore, a plot with the same x and y axes as in Figure 2.15(d) but color coded by the mean SFEs of galaxies within each grid cell clearly shows that the offset from the one-to-one line increases with decreasing SFE.

Rather than adopting C and α values from the Kennicutt-Schmidt law, Zhang et al. [2009] calibrated an empirical estimator of $f_{\rm HI}$ from SSFR and μ_*, reformulated as,

$$\log {\rm SSFR} = 2.96 \log \mu_* + 3.85 \log f_{\rm HI} - 32.81,$$

corresponding to larger α and smaller C values than given in equation 2.3. Their best estimator of $f_{\rm HI}$ had SSFR substituted by $g-r$ color, since optical colors can be good proxies for SSFRs (see §2.5.1). In agreement with Zhang et al. [2009], we also prefer a smaller SFE scaling factor than the Kennicutt [1998b] value (see Eqn 2.3). However, Zhang et al. [2009] calibrate their $f_{\rm HI}$ estimator from an SDSS selected sample with existing HI data and therefore relatively gas poor compared to the ALFALFA HI-selected population. For this reason, their estimator systematically underpredicts the $f_{\rm HI}$ of the $\alpha.40$-SDSS galaxies by $\sim$0.3 dex.

Panel (d) of Figure 2.15 shows that, compared to the full $\alpha.40$ distribution, the ALFALFA dwarf galaxies appear slightly closer to the one-to-one line given by equation (2.5). Again, this result may arise from their selection as the lowest $M_{\rm HI}$ systems. As we have seen, the dwarfs studied here are relatively gas-poor (see §2.5.3) and have higher SFEs (see §2.5.2) compared to those estimated for the full $\alpha.40$ population in the same *stellar mass* range. Therefore the fact that the dwarfs lie closer to the one-to-one relation traced by equation (2.5) is consistent with the finding above that lower than typical SFEs drive the overall ALFALFA distribution to lower SSFRs for their μ_* and $f_{\rm HI}$. Comparisons of the star forming

properties of samples selected either by stellar mass or by HI mass must account for the biases imposed on those properties by the various selection criteria.

2.6 Summary

With unprecedented sensitivity, areal coverage, angular and velocity resolution, the ALFALFA extragalactic HI survey provides us with a homogeneous parent sample of gas-bearing galaxies which approaches a full census of star-forming galaxies. More than 2/3 of ALFALFA sources are new HI detections and thus would not have been included in previous star formation studies of large HI samples based on optical target selection, e.g. Bothwell et al. [2009]. In this chapter, we have examined the population of galaxies detected by ALFALFA with the lowest HI masses, combining photometric and spectroscopic data from the SDSS and new UV images from *GALEX* to probe the relationship between their HI, stellar and star-forming components. Compared to other dwarf studies such as FIGGS [Begum et al., 2008] or 11HUGS [Lee et al., 2007], the ALFALFA dwarf sample includes a much larger number of very low HI mass objects ($\log M_{\rm HI} < 7.7$). Moreover, only 56% of the ALFALFA dwarfs within the SDSS footprint have a counterpart in the SDSS spectroscopic survey confirming that the ALFALFA survey is providing an important contribution to the census of dwarf galaxies in the nearby universe.

Being sensitive to very low levels of star formation activity (below $10^{-2}\ M_\odot\ {\rm yr}^{-1}$), the FUV luminosity is a more robust tracer of the SFR in metal- and dust-poor dwarfs than the Hα or IR predictors. We have reprocessed all of the available MIS-level *GALEX* FUV images for 118 ALFALFA dwarfs. Only

one out of those 118 dwarfs is not detected in the FUV: virtually all HI-selected gas-rich dwarfs show some evidence of recent star formation. Examinations of the CMD, UV colors, BPT diagram and $D_n(4000)$ all confirm the general notion that HI-selected dwarf galaxy samples are dominated by faint blue cloud galaxies and are more likely to be star-forming than galaxies typically included in optical-UV selected samples [e.g. Brinchmann et al., 2004, Salim et al., 2007, Wyder et al., 2007, Catinella et al., 2010].

SED fitting to UV/optical bands is improved via trimming out the models with unrealistically high extinction. We demonstrate that estimates of the $\mathrm{SFR_{FUV}}$ still suffer from internal extinction in the ALFALFA dwarfs. Even in such low metallicity, low luminosity systems, neglecting the extinction at FUV wavelengths A_{FUV}, as has been the practice of some authors, e.g. Roychowdhury et al. [2009], will lead to the systematic underestimate of FUV luminosity. At the same time, application of the standard IRX-β relation given their UV colors would over-predict A_{FUV} in many of the lowest HI mass galaxies, possibly because of their different SFH and/or dust geometry.

Although limited to the SDSS fiber apertures, the SFRs derived from SDSS Hα line flux are compared to those derived from SED-fitting and we cannot rule out systematic deficiency in the SFR values derived from Hα as might be consistent with Lee et al. [2009a]. Because the ALFALFA dwarfs have low SFRs on average, they provide an ideal sample for Hα imaging to probe this question; this work is in progress.

Many ALFALFA dwarfs have high SSFRs and b-parameters greater than 1, suggesting that they are currently forming stars in a bursty manner. As a result, it is essential to take the possibility of bursty star formation into full account

when modeling their SEDs. If a constant SFH is assumed, the calibrations used most often will over-predict the derived properties, e.g. the stellar mass as derived from the mass to light ratio versus color relation [Bell et al., 2003], or the SFR obtained from the FUV luminosity [Kennicutt, 1998a, Lee et al., 2009a].

In the SSFR vs. M_* diagram, the red sequence galaxies possess low SSFRs. The dispersion in the SSFR distribution increases at both the high and low mass ends. Factors other than M_* such as environmental effects likely play important roles in the regulation and quenching of star formation in low mass galaxies. In the $f_{\rm HI}$ vs. M_* plot, although Bothwell et al. [2009] reported broadening in the $f_{\rm HI}$ distribution only at the high mass end, we find a mild increase in the dispersion of $f_{\rm HI}$ only at the low mass end. Within the ALFALFA dwarf *s-sed* sample, Virgo cluster members have lower gas fractions at a given $M_{\rm HI}$ with a wide spread also in the distributions of SSFR or the b-parameter. A study of the gas and stars in a larger sample of VCC Virgo dwarfs selected by optical criteria will be presented elsewhere [Hallenbeck et al., 2012].

A clear decrease of the $f_{\rm HI}$ with increasing M_* is seen for the whole distribution, i.e. on average, the low mass galaxies are extremely gas rich for their M_* and relatively unevolved. However, because the ALFALFA dwarfs are selected to be the sources with lowest HI masses, the imposition of an HI mass cutoff leads to the selection of a dwarf sample with lower gas fractions for their stellar mass than is characteristic of the $\alpha.40$ sample overall. Therefore, a large portion of the ALFALFA dwarfs studied here still have $T_{\rm cons} \lesssim t_H$, in particular the more gas poor Virgo members.

The HI mass correlates well with the SFR on global scales. Under the simple assumption that the aperture subtended by the half light radius also contains

exactly half of the stellar mass, HI mass and star formation, we substitute the general "Kennicutt-Schmidt" star-formation law [Kennicutt, 1998b] into the expression of the SSFR, leading to a predicted relation between SSFR, stellar surface mass density and gas fraction as given by equation (2.5); this relation also depends on the exponent α and scaling factor C in the star formation law. The observed trend is consistent with the assumption that HI disks are in general more extended than the corresponding stellar ones. Additional possible contributions are that ALFALFA galaxies have generally sub-solar metallicity and, probably more importantly, lower SFEs, both of which may lead to lower C values.

A statistical sample such as that provided by ALFALFA allows the study only of global relations between the constituent populations within the galaxies. Clearly, a full understanding of the interaction between gas and stars and the physical mechanisms responsible for laws of star formation requires resolved maps of the distribution of HI, and where feasible, the molecular component as well as deeper and better probes of the stellar population. ALFALFA is already providing the fundamental target list for an on-going EVLA/Spitzer/HST project exploring the lowest HI mass galaxies detected by ALFALFA: SHIELD [Survey of HI in Extremely Low Mass Dwarfs, Cannon et al., 2011]. The completion of the ALFALFA survey over then next few years will yield an even richer sample of dwarf galaxies than that studied here.

CHAPTER 3

THE ARECIBO LEGACY FAST ALFA SURVEY: THE GALAXY POPULATION DETECTED BY ALFALFA

3.1 Introduction

In the last decade, the galaxy catalogs contributed by legacy programs like the Sloan Digital Sky Survey (SDSS) and the Galaxy Evolution Explorer (*GALEX*) satellite extragalactic surveys have enabled us to quantify properties associated with the stellar populations of galaxies in the local universe. Through their statistically-based insight into the stellar component and the interrelationship of the physical parameters, these surveys have provided quantitative clues of importance to our understanding of the formation and evolution of galaxies [e.g. Brinchmann et al., 2004, Salim et al., 2007]. The bimodal distribution evident in the color-magnitude diagram [Baldry et al., 2004, Schiminovich et al., 2007] suggests a likely evolution scenario whereby galaxies in the blue cloud form stars vigorously and grow through mergers and later, after depleting their gas reservoirs, then migrate to the red sequence. This picture is also supported by tracers of the star formation history (SFH): e.g., the specific star formation rate (SSFR), the star formation rate (SFR) per unit stellar mass, is seen to vary with the total stellar mass [Brinchmann et al., 2004]. The star-forming sequence (high SSFR) is associated with actively star forming blue cloud galaxies. Indeed, the stellar mass appears to be the crucial quantity governing the star formation

*This chapter is published in Shan et al. (2012b)

(SF) along this sequence. In the absence of mergers or other events that trigger a starburst, blue galaxies on the sequence evolve towards higher stellar mass and lower SSFR, and eventually become red and dead.

In statistical terms, all surveys are biased by the properties that define them. For example, optical surveys are biased in terms of optical flux and possibly surface brightness. The SDSS legacy galaxy redshift sample has an apparent r-band Petrosian magnitude limit of 17.77, as well as a surface brightness limit of 23.0 mag arcsec^{-2} at the half light radius in r [Strauss et al., 2002]. In contrast, blind HI surveys are unbiased by optical characteristics but have their own limitations in terms of HI line emission sensitivity, usually as a function of HI line width [Martin et al., 2010, Haynes et al., 2011]. Because $M_{\rm HI}/L_{\rm opt}$ increases with decreasing $L_{\rm opt}$, HI-selected samples are more inclusive of star-forming galaxies than optical samples of similar depth. Indeed, since almost all star-forming galaxies contain neutral gas, an HI-selected sample can approach a full census of star-forming galaxies. For example, West et al. [2010] demonstrated the HI-selection identifies galaxies with lower surface brightness, smaller absolute magnitudes, bluer colors and smaller stellar masses than those used in typical SDSS studies. However, the limitation with an HI-selected sample is that it will miss the early type galaxies, which contain very little neutral gas [Garcia-Appadoo et al., 2009]. Furthermore, analysis of the spatial correlation function $\xi(r)$ shows that the HI-selected galaxies represent the least clustered population on small scales [Martin et al., 2012], a fact important for interpreting the results of future HI intensity mapping experiments.

Exploiting the mapping capability of the Arecibo L-band feed array (ALFA) and the sensitivity of the Arecibo 305 m antenna, the Arecibo Legacy Fast ALFA

(ALFALFA) survey [Giovanelli et al., 2005b,a] is an ongoing blind HI survey, aimed at mapping ∼7000 square degrees of high galactic latitude sky between 0° and $+36^\circ$ in declination. When complete, the survey will detect more than 30,000 galaxies out to redshift of 0.06 with a median recessional velocity, cz, of $\sim 8200\ \mathrm{km\ s^{-1}}$ [Haynes et al., 2011]. Compared to the HI Parkes All Sky Survey [HIPASS: Barnes et al., 2001, Meyer et al., 2004, Wong et al., 2006], ALFALFA is 8 times more sensitive, its spectral coverage extends over 1.6 times the bandwidth of HIPASS, and the angular resolution of ALFA is 4 times better than that of the Parkes multifeed receiver. The combination of sensitivity and spectral bandwidth enables ALFALFA to detect thousands of massive HI disks with $M_{\mathrm{HI}} > 10^{10}\ M_\odot$. In addition, the Arecibo spectral backend yields a finer velocity resolution than characterized HIPASS, making it possible to detect sources with HI line widths as narrow as $\sim 15\ \mathrm{km\ s^{-1}}$. As discussed in Haynes et al. [2011] and earlier papers in the ALFALFA series, the median centroiding accuracy of the HI sources is $\sim 20''$ allowing the identification of most probable optical counterparts in 97% of cases. ALFALFA provides the first full census of HI-bearing objects over a cosmologically significant volume of the local universe [Martin et al., 2010] so that its population includes the very rare objects missing from the smaller volumes sampled by previous blind HI surveys. It enables the study of the characteristics of HI-selected galaxies in comparison with the galaxy populations included in the SDSS and *GALEX* surveys.

The 2011 ALFALFA catalog, '$\alpha.40$', covers $\sim 40\%$ of the final targeted sky area [Haynes et al., 2011], giving HI masses, systemic velocities and HI line widths for ∼16000 high quality detections (§3.2.1). In addition to the HI line parameters, the $\alpha.40$ catalog also includes an assignment of the most probable optical counterpart (OC) to each HI line detection. Haynes et al. [2011] discuss

the process of assigning OCs to the HI sources, and where the footprints of the surveys overlap, the HI sources are cross-referenced to the SDSS Data Release 7 [DR7: Abazajian et al., 2009], permitting the derivation of properties associated with the stellar components of the HI-bearing galaxies detected by ALFALFA. As shown by Haynes et al. [2011], the $\alpha.40$ population is highly biased against red-sequence objects.

In this chapter, we investigate further the nature of the stellar counterparts of the $\alpha.40$ HI line detections, adding to the optical SDSS data photometric measures from the *GALEX* catalog (§3.2.2). By combining the measurements of the gaseous and stellar components, we characterize the $\alpha.40$ galaxy population and study in §3.3 global trends within it. SED-fitting to the seven bands from the UV to optical is applied to derive the principal stellar properties, including the stellar masses (§3.3.1) and SF (§3.3.2). To understand better the characteristics of the gas-bearing galaxies and the potential bias associated with HI-selection, we define a volume-limited sub-sample extracted from the $\alpha.40$ catalog with a similar one extracted from the SDSS-DR7 (§3.4.1) and compare the two in §3.4.2 in terms of survey depth, extinction, color, SF behavior, etc. The empirical distribution of the halo spin parameter is derived in §3.5, which suggests that the HI-selected galaxies favor high spin parameter halos. Our conclusions are summarized in §3.6.

3.2 Sample and Data

3.2.1 ALFALFA parent sample

The HI parent sample used here is drawn from the $\alpha.40$ catalog presented in Haynes et al. [2011]. The $\alpha.40$ catalog covers two regions in the Spring sky (i.e., the Virgo direction, $7^{\rm h}30^{\rm m} < {\rm RA} < 16^{\rm h}30^{\rm m}$, $4^\circ < {\rm Dec} < 16^\circ$ and $24^\circ < {\rm Dec} < 32^\circ$) and two in the the Fall sky (i.e., the anti-Virgo direction, $22^{\rm h} < {\rm RA} < 3^{\rm h}$, $14^\circ < {\rm Dec} < 16^\circ$ and $24^\circ < {\rm Dec} < 28^\circ$). As discussed in Haynes et al. [2011], ALFALFA HI line detections are categorized according to their signal-to-noise ratio (S/N) and corresponding reliability. Code 1 sources have S/N $\gtrsim$ 6.5 and are highly reliable. Another set of entries, designated as "code 2" sources, or "priors", have lower S/N but coincide with a likely OC at the same redshift. Most of these sources are likely to be real [Haynes et al., 2011]. The catalog includes 15041 extragalactic HI sources, 11941 with code 1 and 3100 with code 2. In this chapter, we consider both the code 1 and 2 $\alpha.40$ detections and adopt the HI measures, distances and HI masses presented in the $\alpha.40$ presented by Haynes et al. [2011]. It is important to note that $\sim$70% of the ALFALFA sources are new HI detections proving that previous targeted surveys based on optical selection (magnitude, size and morphology), most notably the extensive collection contained in the Cornell digital HI archive [Springob et al., 2005], missed large segments of the local gas-bearing population.

In particular, one of the most surprising results of ALFALFA to date is the richness of the high HI mass galaxy population [Martin et al., 2010]. With its combination of sensitivity and depth, ALFALFA reveals that there still exists at $z \sim 0$ a population of massive galaxies which retain massive HI ($M_{\rm HI} > 10^{10}\ M_\odot$)

disks. Some, in fact, contain a dominant fraction of their baryons in HI gas. As the most HI massive local galaxies, they are the $z \sim 0$ analogs of the massive disks detected at $z \sim 0.2$ [Catinella et al., 2008] and those that will dominate the deep surveys being planned for even higher z with the EVLA, APERTIF, ASKAP and MeerKAT and eventually the Square Kilometre Array (SKA). By design, ALFALFA provides a census of HI bearing galaxies within a cosmologically significant volume over a wider dynamic range of HI masses than previous studies. It thus serves as the reference $z \sim 0$ HI-selected population.

3.2.2 Optical and UV counterparts of ALFALFA HI sources

In addition to the HI measurements, Haynes et al. [2011] attempt to identity the most probable optical counterpart (OC) of each HI line source in the $\alpha.40$ catalog. Ancillary information such as redshift coincidence, angular size, color and morphology is used in making the OC assignment. As discussed by Haynes et al. [2011], the process is not perfect, particularly for low signal-to-noise sources for which the centroiding accuracy can exceed 30″ and in regions of source confusion. Nonetheless, the vast majority of OC assignments are probably valid and thus permit the comparison of the stellar and gaseous components of the ALFALFA population.

SDSS photometry

Towards this aim, Haynes et al. [2011] also provide a cross reference of the assigned OCs with the SDSS-DR7 [Abazajian et al., 2009] where the two surveys have overlapping sky footprints. The northern Fall region is not covered by the

SDSS legacy imaging survey DR7. Of the 15041 HI source included in the $\alpha.40$ catalog, 201 have no OC assigned by Haynes et al. [2011], 2310 lie outside the DR7 footprint, and 60 appear to be in the region of the SDSS imaging survey but cannot be associated with an object in the SDSS photometric database. In most of the latter cases, the OC is evident in the SDSS images but is projected close to a bright foreground star or contaminated by its glare.

As discussed by numerous authors e.g., West et al. [2010], gas rich nearby galaxies are often blue and patchy with the result that their overall optical emission is shredded among several photometric objects by the SDSS pipeline measurements. The ALFALFA-SDSS cross-reference given in Table 3 of Haynes et al. [2011] includes a photometric code that identifies objects with suspicious SDSS photometry, and we exclude such objects (293/12470) from the SED-fitting. For the others, we require that model magnitudes are available in all five SDSS bands (*u, g, r, i, z*) and retrieve the SDSS photometric parameters from the standard SDSS-DR7 database.

The current $\alpha.40$ catalog used here relies on the optical identifications and photometry derived from the SDSS/DR7 database as cross-referenced in Table 3 of Haynes et al. [2011]. Blanton et al. [2011] have presented a new method for background subtracting the SDSS imaging which they apply to the SDSS-III DR8 images. As ALFALFA progresses, we will migrate to use of the improved SDSS pipeline. Especially for purposes of comparison with results obtained by other authors who have likewise relied on DR7, we retain the use of DR7 in the present work.

GALEX **photometry**

Using a similar approach, we have conducted a separate cross-match of the ALFALFA OCs to the *GALEX* UV photometric catalog. The imaging mode of the *GALEX* instrument surveys the sky simultaneously in two broad bands, one in the FUV (effective wavelength of 1516Å) and a second in the NUV (effective wavelength of 2267Å). The *GALEX* field of view is $\sim 1.2^{\circ}$ in diameter [Morrissey et al., 2007], although image quality deteriorates in the outer annulus beyond a radius of 0.55°. We use the *GALEX* GR6 data release, with its improvements to flat fielding, adjustment to the photometric zero-point, etc. Given the poorer image resolution ($\sim 4.5''$ FWHM), compared to that of the SDSS, as well as the lower UV source density, visual inspection shows that the *GALEX* DR6 pipeline measurements corresponding to the ALFALFA galaxies suffer less from shredding issues. We have also validated that the *GALEX* pipeline photometry is in close agreement with our own photometric reprocessing of the *GALEX* images for a sample of dwarf galaxies detected by ALFALFA [Huang et al., 2012b].

The *GALEX* mission includes several survey modes that differ in their exposure time per tile: The All-sky Imaging Survey(AIS) is the shallowest ($\sim$100 sec), while the Medium Imaging Survey (MIS, $\sim$1500 sec) is designed to maximize the coverage of the sky that is included in the SDSS. The latter also includes the Nearby Galaxy Survey (NGS), a selected set of targeted fields of similar depth as the standard MIS. A third Deep Imaging Survey (DIS) is much deeper but covers only a small solid angle. In adopting the *GALEX* counterparts, we give preference to sources extracted from the MIS, NGS or DIS, but make use of the AIS for those objects not included in the deeper surveys.

To cross-match the ALFALFA OCs to the *GALEX* catalog, we first search

the position of the ALFALFA OCs for all *GALEX* neighbors within 36″. Objects close to the *GALEX* field edge, i.e. with a distance from the field center $> 0.55°$, are dropped to avoid duplications with objects in overlapping tiles and known *GALEX* imaging artifact effects. To permit homogeneous SED-fitting to all 7 bands (FUV, NUV, *ugriz*), we require that UV images of comparable depth must exist for both of the UV bands; this criterion results in the adoption of AIS measurements where the MIS catalog is incomplete, e.g. because of the failure of the FUV detector. In other cases, matches are missed because the FUV and NUV sources may fail to coincide because of, e.g. astrometry error or shredding in one or both bands. Among the 14840 extragalactic ALFALFA sources with OCs 1828 (12.3%) have no *GALEX* counterpart returned within 36″, either because they lie outside of the *GALEX* footprint or have no detected UV emission in both bands. 516 (3.5%) are excluded because they lie too close to a *GALEX* field edge and 1317 (8.9%) are not matched because all neighbors are detected only in one band but not the other. The remaining 11179 OCs are matched to the nearest neighbor in the *GALEX* catalog with 7752 (52.2%) matched to UV sources found in the AIS and 3427 (23.1%) to ones in the MIS. The median separation between the coordinates of the OC and the cross-matched *GALEX* object is only 1.6″.

Although the addition of the *GALEX* UV photometry sets better constraints on the SF properties and dust extinction [Salim et al., 2005], the requirement that UV sources must be detected in both bands introduces an additional bias against non star-forming galaxies. SED-fitting to the SDSS bands only [Huang et al., 2012b] demonstrates that 13.5% of the 12156 galaxies in the $\alpha.40$-SDSS DR7 cross-match have $\log \mathrm{SSFR} < 10^{-11}\ \mathrm{yr}^{-1}$, and therefore belong to the quiescent population. This fraction drops to 3.9% of the 9417 $\alpha.40$ galaxies that have

counterparts in both the SDSS and *GALEX* photometric catalogs. As we discuss in §3.4, the HI-selection produces the stronger bias against the red sequence.

UV-to-optical colors of ALFALFA galaxies

Figure 3.1 presents the optical-UV color–color diagram derived for the 9417 galaxies which have complete entries in all three of the ALFALFA-$\alpha.40$, the SDSS-DR7 and *GALEX*-DR6 catalogs and for which the 7-band SED-fitting produces a valid result (see §3.3), denoted as the $\alpha.40$-SDSS-*GALEX* sample hereafter. Contours and points depict the distribution for the $\alpha.40$-SDSS-*GALEX* sample in high and low number density regions respectively, with typical error bars shown in the upper left corner (pipeline magnitude errors). Colors hereafter are all corrected for Galactic extinction but not internal extinction (see §3.4.2). In the optical, the SDSS pipeline extinction-corrected values are used, while at UV wavelengths, we adopt the $E(B-V)$ values based on the maps of Schlegel et al. [1998], the Cardelli et al. [1989] extinction law with $R_V = A_V/E(B-V) = 3.1$, and $A(\lambda)/E(B-V) = 8.24$ for the FUV and 8.2 for the NUV, following Wyder et al. [2007]. Because of the bandwidth limit of ALFALFA, only low redshift galaxies with small K-correction are included, and we ignore this term in computing colors, i.e., no K-correction is applied.

Because it contrasts the recent SF, as indicated by the UV light, with the total past SF, as indicated by the optical light, the UV-to-optical color is a stronger diagnostic of SFH than colors derived from the optical bands only. This result is also evident in Figure 3.1. Based on the distribution of their *GALEX*-SDSS matched catalog, Salim et al. [2007] define their blue cloud galaxies as those with $(\mathrm{NUV}-r) < 4$. Using the same cutoff, 96% of the $\alpha.40$-SDSS-*GALEX* galaxies

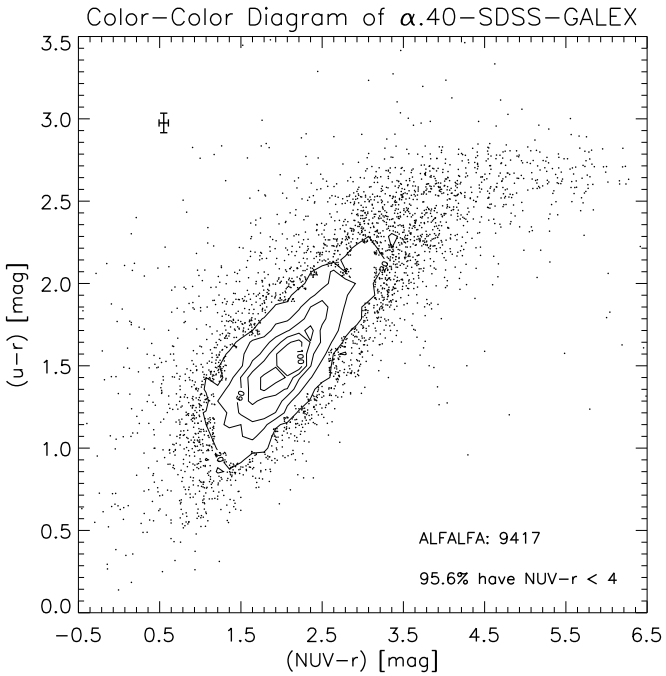

Figure 3.1: UV-optical color-color diagram. Contours and points represent the $\alpha.40$-SDSS-*GALEX* common sample. The number density of galaxies in each gird cell is labeled on selected contours, e.g., the lowest contour level beyond which scatter points are plotted is 20 galaxies per grid cell. The grid size is shown by the interval of minor ticks on both axes. Among these 9417 galaxies, 96% have $(\mathrm{NUV} - r) < 4$ and thus lie in the blue cloud by the criteria of Salim et al. [2007]. The $(\mathrm{NUV} - r)$ and $(u - r)$ colors are well correlated among the blue galaxies, with a slope of $\delta(u - r)/\delta(\mathrm{NUV} - r) \sim 0.6$, but the distribution flattens among the reddest population. The $(\mathrm{NUV} - r)$ color serves as a stronger diagnostic of SFH than colors derived only from the optical bands.

lie on the blue side, suggesting that HI-selection induces a strong preference for blue star-forming galaxies, or conversely, a strong bias against red sequence galaxies. Bluewards of this division, the two colors are well correlated with a slope of $\delta(u - r)/\delta(\mathrm{NUV} - r) \sim 0.6$, which is comparable to what was found by Wyder et al. [2007], $\delta(u - r)/\delta(\mathrm{NUV} - r) \sim 0.5$. Although only a small population (411) of galaxies appear redward of $(\mathrm{NUV} - r) = 4$, the $(u - r)$ colors of the red objects increase less quickly with $(\mathrm{NUV} - r)$ and the distribution of the reddest tail is nearly flat. As discussed in §3.4.2 the degeneracy of $(u - r)$

among the red populations is even more pronounced in an optically-selected sample with more red galaxies. Therefore, the SED-fitting to the SDSS bands only is sufficient to constrain the SF for the HI-selected blue galaxy population in general [e.g. Huang et al., 2012b] but gives systematic overestimates of SFRs for optically-selected red galaxies such as those in the Virgo cluster known to have quenched SF [e.g. Hallenbeck et al., 2012], i.e., it is crucial to include the UV bands in the SED-fitting to infer the SF of the red population. As a result, we adopt the UV-optical color ($\mathrm{NUV} - r$) rather than the optical-only ($u - r$) in the analysis of SF and gas properties below.

3.3 Global Properties of the ALFALFA Galaxy Population

To derive the global properties of the stellar components of the ALFALFA galaxies, we adopt the methodology of Salim et al. [2007]. In particular, stellar masses and SFRs are derived from SED-fitting the seven *GALEX*/SDSS bands. Further details of the method and fitting quality as applied to the $\alpha.40$ sample are found in Huang et al. [2012b] which focuses on the lowest HI mass dwarf population. In addition, the Gaussian prior distribution of the effective optical depth in V band, τ_V, is applied, with the mean predicted by Giovanelli et al. [1997] and a standard deviation of 0.55 dex. Such an improvement reduces the overestimate of internal extinction and SFR with decreasing stellar mass, as identified by Salim et al. [2007] (see §3.4.2 for more details), but still accounts for the effect of dust in disk systems. In this section, we discuss the results for the full $\alpha.40$-SDSS-*GALEX* overlap sample (9417 galaxies).

3.3.1 Gas and stars

Current understanding interprets the standard SDSS color magnitude diagram (CMD) in terms of an evolutionary scenario under which galaxies migrate from the blue cloud to the red sequence as they assemble their mass. This picture is further reinforced by the presence of the star-forming sequence in the SSFR vs. stellar mass diagram; more massive galaxies show lower SSFRs. Consistent with this picture, one would expect galaxies to grow increasingly gas poor and thus having lower HI fractions $f_{\rm HI}$ (defined throughout this work as $f_{\rm HI} = M_{\rm HI}/M_*$) as they assemble their mass. Therefore, blue galaxies with high gas fractions indicate disks Which are stable against collapse, making their SF much less efficient [West et al., 2009].

HI versus stellar mass

In the last decades, many studies have investigated how the HI content varies with stellar properties in galaxies, such as morphology, luminosity, size and SF activity [Gavazzi et al., 1996, Boselli et al., 2001, Kannappan, 2004, Disney et al., 2008, Garcia-Appadoo et al., 2009, West et al., 2009, 2010, Toribio et al., 2011]. Despite the complex interplay of dynamics, SF, chemical enrichment and feedback etc., the stellar and HI components, as well as the dark matter halo, exhibit correlations with each other. However, many of these studies have relied on relatively small and/or inhomogeneous samples limited to the very nearby universe. Although the main scaling relations were known, constraints on the accuracy of these relationships, as well as the quantification of their scatter are still not well determined. Based on an Hα narrow-band imaging survey of $\sim$400 galaxies selected from ALFALFA, Gavazzi et al. [2012, 2013] also investigate the

relationships between HI and newly-formed stars, emphasizing the study of environment effects. Here we focus on the nature of the population detected by the ALFALFA survey.

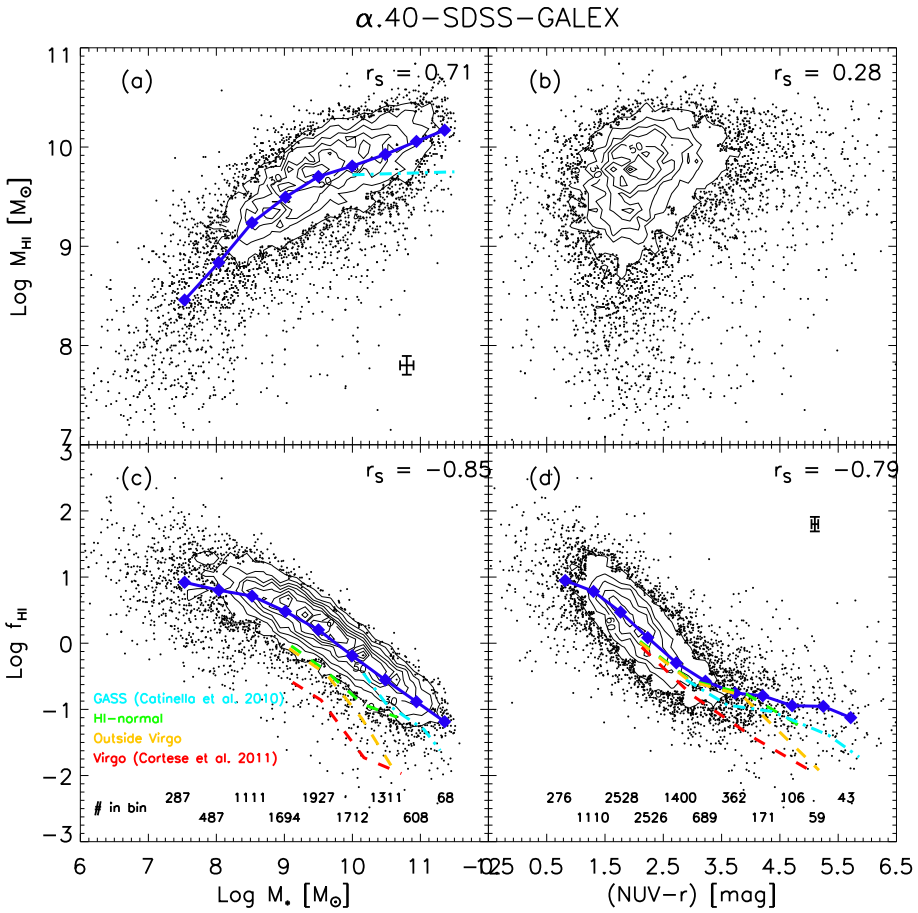

Figure 3.2: Scaling relations between HI mass, stellar mass and color. Contours and points follow the definitions in Figure 3.1. Blue diamonds and solid lines indicate the $\langle \log y \rangle$ values in each $\log x$ bin. The number of galaxies in each $\log x$ bin is listed at the bottom of panels (c, d). Cyan dash-dotted lines in panels (c, d) denote the average values of the GASS galaxies with $M_* > 10^{10}\ M_\odot$ [Catinella et al., 2010]. Dashed lines in the same panels are from Cortese et al. [2011] derived for galaxies belong to different environments: 'HI-normal' (green on top), 'outside Virgo' (yellow in middle) and 'inside Virgo' (red at bottom). Typical error bars of individual galaxies are given in the corner of panels (a, d). Spearman's rank correlation coefficients, r_S, are listed in all panels.

Figure 3.2 illustrates the relationships of the HI mass and $f_{\rm HI}$ (the vertical axes) with the stellar mass and color (horizontal axes). The contours and points

outline the distributions of the galaxies in the $\alpha.40$-SDSS-*GALEX* sample; the blue diamonds and solid lines trace the average values $\langle \log y \rangle$ and $\langle \log x \rangle$ in bins of $\log x$, with a bin size of 0.5 dex in panels (a), (c) and (d). The number of galaxies in each stellar mass or $(\mathrm{NUV} - r)$ color bin is given at the bottom of panels (c, d). Typical error bars of individual galaxies are shown in the corners of panels (a) and (d). The Spearman's rank correlation coefficients of the relation, r_S, are shown in the upper right corner of all panels. Compared to similar studies that have previously probed the global scaling relations involving $M_{\rm HI}$ [e.g. Bothwell et al., 2009, Catinella et al., 2010], the $\alpha.40$ sample offers a more complete statistical sampling of the full range of HI and stellar masses. As discussed in Haynes et al. [2011], ALFALFA's combination of sensitivity, sky coverage and bandwidth yields a sample that probes a wide dynamical range in HI mass (7-11 dex with a mean of 9.56 dex), from the most massive giant spirals with $M_{\rm HI} > 10^{10}\ M_\odot$ to the lowest HI mass dwarfs with log $M_{\rm HI} < 10^{7.5}\ M_\odot$. In fact, the stellar mass range that is probed is slightly wider: 6–11.5 dex, with a mean of 9.43 dex. As an HI-selected sample, $\alpha.40$-SDSS-*GALEX* demonstrates the ability to recover galaxies with small M_*.

Figure 3.2(a) shows the distribution of $M_{\rm HI}$ with M_*. The cyan dash-dotted line traces the linear fit to the GASS sample of high stellar mass galaxies [$M_* > 10^{10}\ M_\odot$; Catinella et al., 2010]:

$$\log\langle M_{\rm HI}(M_*)\rangle = 0.02 \log M_* + 9.52.$$

Note that those authors chose to calculate $\log\langle M_{\rm HI}\rangle$ rather than $\langle \log M_{\rm HI}\rangle$ because the $\langle \log M_{\rm HI}\rangle$ value is depressed by the contribution of gas-poor galaxies in their M_*-selected sample; a similar effect results in their adoption of $\log\langle f_{\rm HI}\rangle$ rather than $\langle \log f_{\rm HI}\rangle$. In contrast, an HI-selected sample such as ours does not sample the low HI fraction massive objects so that, as a function of $\langle \log M_*\rangle$, $\langle \log M_{\rm HI}\rangle$

and $\langle \log f_{\rm HI} \rangle$ adequately trace the main distribution. Moreover, as pointed out in Cortese et al. [2011], the distribution of $f_{\rm HI}$ is closer to log-normal than Gaussian, and thus they also prefer $\langle \log f_{\rm HI} \rangle$ to $\log \langle f_{\rm HI} \rangle$.

We confirm the previous findings that $M_{\rm HI}$ increases with M_*. However, the correlation does not appear to be a simple linear one, i.e. $\delta M_{\rm HI}/\delta M_*$ is smaller at the high mass end. The linear fit to the blue diamonds in Figure 3.2(a) is

$$\langle \log M_{\rm HI} \rangle = \begin{cases} 0.712 \langle \log M_* \rangle + 3.117, & \log M_* \leq 9; \\ 0.276 \langle \log M_* \rangle + 7.042, & \log M_* > 9. \end{cases} \tag{3.1}$$

This trend is consistent with the idea that once AGNs are turned on in massive galaxies, gas is lost due to AGN feedback. The fact that $f_{\rm HI}$ is lower in massive SF/AGN composites than in purely SF galaxies of the same mass may be the cause of a similar break in slope of the star-forming sequence (see §3.3.2, at a slightly higher transition mass, $\log M_* \sim 9.5$). Furthermore, compared to the high stellar mass GASS galaxies, the ALFALFA population is overall more gas-rich for the same stellar mass ($\log M_* > 10$) and traces a steeper slope in the $M_{\rm HI}$ vs. M_* scaling relation, i.e. there is a systematically larger discrepancy in the typical HI content of the ALFALFA and GASS populations in the largest M_* bins. Besides the change in slope, there appears to be an increased scatter in the $M_{\rm HI}$ distribution below $\log M_* \sim 9$, a regime only poorly sampled by other studies. In fact, Huang et al. [2012b] point out that at the lowest HI masses, ALFALFA detects a population of dwarf galaxies with low $f_{\rm HI}$ for their M_*; some of these objects are dwarf ellipticals/spheroidals (dE/dSph) galaxies in the Virgo cluster and may have accreted their current gas supply only recently [Hallenbeck et al., 2012]. The HI gas can be easily removed in low mass systems due to their shallow potential wells, so that the galaxy migrates onto the red sequence as its SF quenches.

Figure 3.2(c) shows how the HI fraction $f_{\rm HI}$ depends on M_*. The cyan dash-dotted line again traces the GASS result for the high stellar masses [Catinella et al., 2010], while the green (upper), red (lower) and yellow (middle) dashed lines trace the separate samples of HI-normal galaxies, ones in Virgo and outside-Virgo respectively from Cortese et al. [2011] who looked for trends among galaxies in different environments. Again, the known trend that higher M_* galaxies have lower $f_{\rm HI}$ is clearly evident, with a correlation coefficient $r_S = -0.85$. M_* depends more strongly on $f_{\rm HI}$ than on $M_{\rm HI}$ ($r_S = 0.71$) partly because the same measure of the M_* enters also in the computation of $f_{\rm HI}$. Compared to other findings, the ALFALFA population uniformly includes galaxies which are more gas rich for a given M_*. Their extraordinarily high $f_{\rm HI}$ indicates little integrated past SF, while their blue colors may be attributed to a SFH that steadily rises to the present day or a truly young stellar component [Garcia-Appadoo et al., 2009].

Both the GASS and Cortese et al. [2011] samples include galaxies that have lower $f_{\rm HI}$ and lie below the ALFALFA HI detection threshold. For example, the Virgo cluster is well known to contain a significant population of HI deficient galaxies [Davies and Lewis, 1973, Giovanelli and Haynes, 1985, Solanes et al., 2002] whose HI line flux densities are too low for them to be detected by the short ALFALFA observations; their detections were made using longer duration, target Arecibo observations. The offset of the ALFALFA population from the other samples is therefore as expected. However, it is interesting to note that the scaling of $f_{\rm HI}$ with log M_* derived here and by Cortese et al. [2011] for the HI-normal galaxies, while they do not coincide in amplitude, do show comparable slopes at intermediate masses, and perhaps the same is true for all samples at log $M_* < 9.7$. A "fast", shallow survey like ALFALFA derives the same trend

as one which relies largely on much deeper, pointed observations. The flattening off of $f_{\rm HI}$ at $\log M_* \lesssim 9$ is traced only by the ALFALFA dwarfs [Huang et al., 2012b].

It is important to note that the nearby, low mass galaxies are the ones most susceptible to shredding by the SDSS pipeline so that, statistically, their stellar masses are more likely to be underestimated, resulting in an extreme tail of galaxies with unrealistically high $f_{\rm HI}$. By exclusion of objects with suspect SDSS photometry as noted by Haynes et al. [2011], the most egregious cases have been excluded from this analysis. Similar problems with the use of the SDSS pipeline measurements have much less effect on the main distribution. At the same time, source confusion within the ALFA beam (FWHM $\sim 3'.5$) is more likely among more distant systems so that the $M_{\rm HI}$ (and $f_{\rm HI}$) of some high $M_{\rm HI}$ sources may be overestimated. However, other than cases of major mergers, the highest $M_{\rm HI}$ galaxies are always significantly more massive than their small companions, so that the change in $f_{\rm HI}$, if the contribution from companions is removed, would only be small. Overall, the trend of falling $f_{\rm HI}$ with increasing M_* seen in the ALFALFA galaxies is well defined. For the ALFALFA population overall, the median $f_{\rm HI} \sim 1.5$. HI-selected galaxies are uniformly gas rich for their stellar mass following a scaling relation over the range of *stellar mass* $8.0 < \log M_* < 11.0$.

In Figure 3.2(c), the number density of points drops sharply on the upper edge of the main distribution: there is a real cutoff in the galaxy population with even higher $f_{\rm HI}$ than ALFALFA detects. The increased dispersion in the contours on the lower edge of the $f_{\rm HI}$ distribution with substantial numbers of outliers with lower $f_{\rm HI}$ than the main population confirms that, because of its

HI-selection, ALFALFA misses much of the gas-poor galaxy population. Longer integration times would obviously detect galaxies of lower $M_{\rm HI}$ and thus lower $f_{\rm HI}$ at constant M_*. The GASS observing strategy [Catinella et al., 2010] is specifically designed to probe to constant $f_{\rm HI}$ by conducting significantly longer but targeted HI observations. The GASS program thus characterizes the overall population of galaxies selected by stellar mass at the high mass end. The ALFALFA survey, on the other hand, samples well the full dynamical range of the HI-rich (for their stellar mass) population

Figures 3.2(b, d) explore the variation of $M_{\rm HI}$ and $f_{\rm HI}$ with $({\rm NUV}-r)$. Definitions of diamonds and lines in panel (d) are the same as in panel (c). As noted in Figure 3.1, nearly all ALFALFA galaxies are blue, and the population is highly biased against the red sequence. While there is a wide spread in $M_{\rm HI}$, there is little trend of $M_{\rm HI}$ with color ($r_S = 0.28$). In fact, there are 128 $\alpha.40$-SDSS-*GALEX* red galaxies (${\rm NUV}-r > 4$) with $\log M_{\rm HI} > 10$, including the early type galaxies with quenched SF but unusually high HI masses (e.g. AGC 260442), the edge on galaxies with significant internal extinction (e.g. UGC 6312 has a dust lane evident in the SDSS image), and even the "red spirals" found in the Galaxy Zoo [Masters et al., 2010], e.g. UGC 9624 and UGC 9283. There are 116 red galaxies (${\rm NUV}-r > 4$) with $\log M_{\rm HI} < 9.5$; most are early type "dead" galaxies. Cortese et al. [2011] found that the blue cloud galaxies have the same $f_{\rm HI}$ regardless of environment, whereas for the red galaxies, Virgo members are significantly gas poorer than HI-normal systems (see dashed lines in Figures 3.2d). In particular, their fit for HI-normal galaxies (green) agrees well with the main trend for the $\alpha.40$ galaxies.

In contrast, $f_{\rm HI}$ is a strong function of color among the ALFALFA population

($r_S = -0.79$ in panel d), at least among the blue cloud galaxies, i.e. the bluer galaxies tend to have higher HI fractions. However, this trend gradually flattens for the very red galaxies ($\mathrm{NUV} - r \gtrsim 3.5$), i.e. the very red galaxies among the ALFALFA population have higher f_{HI} than would be predicted by extrapolation of the trend traced by the blue galaxies. Compared to the f_{HI} vs. ($\mathrm{NUV} - r$) trends derived by Catinella et al. [2010] or Cortese et al. [2011], traced by the dash-dotted and dashed curves respectively in panel (d), the offset of blue diamonds on the blue side is small, but the deviation becomes systematically larger in the redder bins. Such a change in behavior can be partly explained by the fact that ALFALFA detects only a very small subset of these red galaxies. The presence of HI in this small population of otherwise "red and dead" galaxies is most easily explained if their HI gas has been acquired only recently, as has been invoked previously to explain the HI in ellipticals [e.g., Wardle and Knapp, 1986, Morganti et al., 2006], and the annular HI distributions seen in many S0s [e.g., van Driel et al., 1988, Donovan et al., 2009]. Deep HI synthesis imaging of the SAURON and ATLAS^{3D} samples of early-type galaxies shows that HI is commonly detected in galaxies which do not reside in cluster cores [e.g., Oosterloo et al., 2010, Serra et al., 2012]. A significant fraction of non-cluster early-types contain some cool HI gas, with the large spread in HI content likely due to differences in their accretion histories.

Predictors of HI gas fraction

The tight correlation between f_{HI} and ($\mathrm{NUV} - r$) can be used as a predictor of M_{HI} given measures of color, i.e., the 'photometric gas fraction' technique [Kannappan, 2004]. Furthermore, a 'fundamental plane' of f_{HI}–($\mathrm{NUV} - r$)–μ_*

has been identified by the GASS survey [Catinella et al., 2010], where the stellar mass surface density is defined as $\mu_* \ [M_\odot \ kpc^{-2}] = 0.5 M_* \ [M_\odot] / \pi (r_{50,z} \ [\mathrm{kpc}])^2$ and $r_{50,z}$ is the radius containing 50% of the Petrosian flux in the z-band. Their best fit 'plane' is

$$\log f_{\rm HI} = -0.240(\mathrm{NUV} - r) - 0.332 \log \mu_* + 2.856,$$

and the scatter of such a $f_{\rm HI}$ predictor is reduced relative to the $f_{\rm HI}$–$(\mathrm{NUV} - r)$ correlation with the additional parameter μ_*. Because colors essentially trace the SSFRs (see also §3.3.2), similar predictors are calibrated by Zhang et al. [2009] for an optically-selected sample as:

$$\log f_{\rm HI} = \begin{cases} -1.25(g-r) - 0.54 \log \mu_* + 4.66; \\ 0.26 \log \mathrm{SSFR} - 0.77 \log \mu_* + 8.53. \end{cases}$$

It should be noted that no correction for internal extinction is applied in those analyses, although it is well known that the inner disks of spirals are optically thick [e.g., Giovanelli et al., 1995]. We discuss the need for an internal extinction correction below in §3.4.2. The $f_{\rm HI}$ predicted by these formulae are plotted on the horizontal axes in Figures 3.3(a-c), respectively. Compared to the ALFALFA measurements of the $f_{\rm HI}$ (vertical axes), they all predict systematically smaller $f_{\rm HI}$. This reaffirms that the HI-selected sample is biased towards the gas rich population. The deviation from the one-to-one dashed line increases with $f_{\rm HI}$ in the case of the GASS calibration (Figure 3.3a). The Zhang et al. [2009] estimators (Figure 3.3b and c) systematically underpredict $f_{\rm HI}$ of the $\alpha.40$-*GALEX*-SDSS galaxies by $\sim$0.3 dex.

Exactly which scaling relation to use to predict the properties of a population depends of course on what the scientific objective is. For example, the scaling relations for an optically-selected sample may be valid for a stellar mass

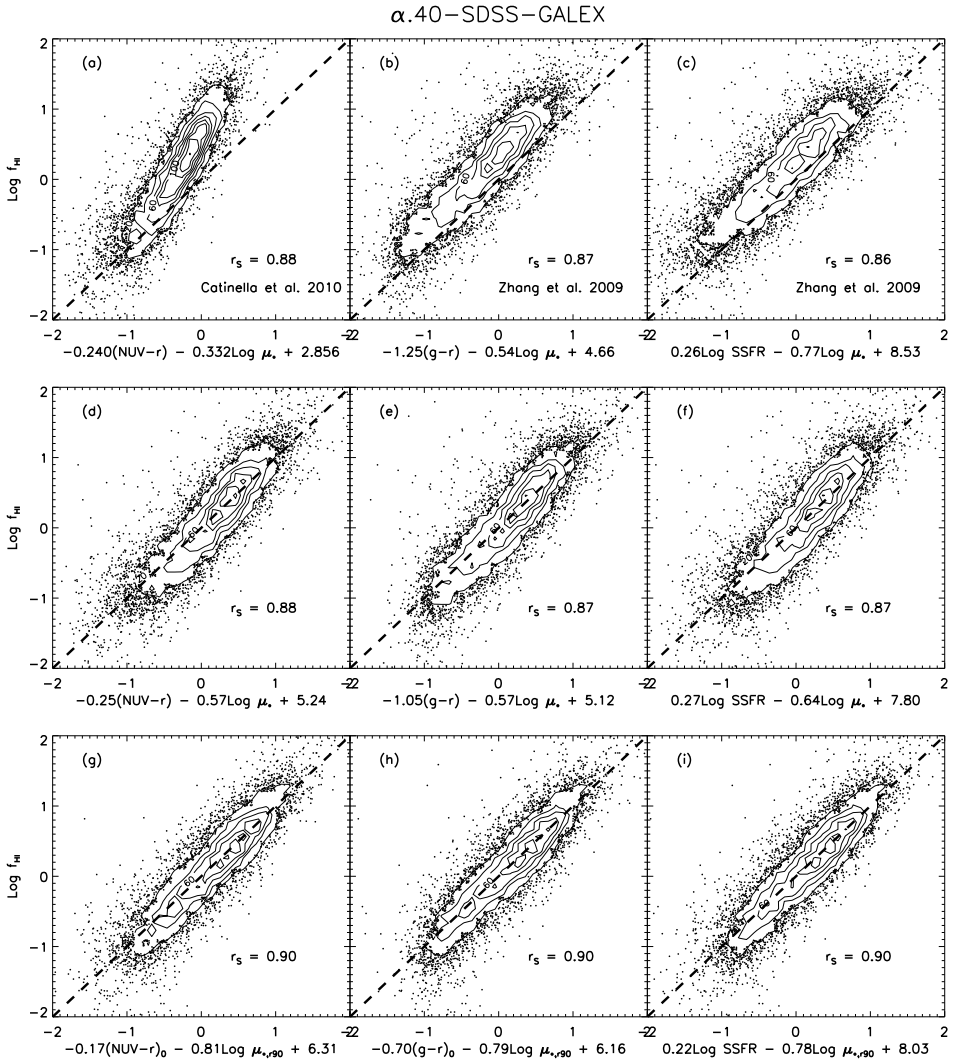

Figure 3.3: HI fraction estimators. Dashed lines are the one-to-one lines. Contours and points follow the definitions in Figure 3.1. Spearman's rank correlation coefficients are shown in the lower right corners of all panels. *Upper panels* - The ALFALFA-observed $f_{\rm HI}$ versus the predicted values based on the fundamental planes calibrated from the GASS sample [Catinella et al., 2010] in panel (a), as well as from the SDSS-selected sample [Zhang et al., 2009] in panels (b) and (c). *Middle panels* - Observed $f_{\rm HI}$ versus the values predicted by the best fit to similar planes in this work, given the $\alpha.40$-SDSS-*GALEX* sample. The systematic offsets are removed and the correlations are tighter. *Bottom panels* - Compared to the predictors in the middle row, the colors have been corrected for internal extinction and the stellar mass surface density is based on $r_{90,r}$, so that the scatter is reduced.

selected population. However, the relations derived for ALFALFA give better predictions for the HI detection rate for future SKA surveys which will likewise be HI-selected. Previous simulations of SKA detection rate are mostly based on the HIPASS results locally [e.g., Abdalla and Rawlings, 2005, Obreschkow et al., 2009]. But HIPASS suffered from limitations in its volume sensitivity, and in fact, ALFALFA detects more HI sources at the high $M_{\rm HI}$ end [Martin et al., 2010]. Based on the $\alpha.40$-*GALEX*-SDSS galaxies, linear regression gives:

$$\log f_{\rm HI} = -0.25({\rm NUV}-r) - 0.57\log\mu_* + 5.24; \tag{3.2}$$

$$= -1.05(g-r) - 0.57\log\mu_* + 5.12; \tag{3.3}$$

$$= 0.27\log{\rm SSFR} - 0.64\log\mu_* + 7.80. \tag{3.4}$$

Note that for comparison with other authors, the colors used here are corrected for Galactic extinction but not for internal extinction. In Figures 3.3(d-f), the ALFALFA $f_{\rm HI}$ measures are plotted against the values predicted by equations (3.2)-(3.4), with the correlation coefficients $r_S = 0.88$, 0.87 and 0.87 respectively. The systematic offset is removed according to our best fit and the correlations are as tight as the Catinella et al. [2010] ($r_S = 0.88$) and the two different Zhang et al. [2009] ($r_S = 0.87$ and 0.86) results. Among the three planes, the $f_{\rm HI}$–$({\rm NUV}-r)$–μ_* correlation has the least scatter and it is also tighter than the $f_{\rm HI}$–$({\rm NUV}-r)$ correlation ($r_S = -0.79$).

Note that the fundamental plane found here is noticeably different from the GASS relationship [Catinella et al., 2010]. The main trend in Figure 3.3(d) reveals a break in slope at $\log f_{\rm HI} \sim -0.5$, whereas the GASS relation is confined to only below this critical $f_{\rm HI}$. Although the GASS sample is complete in the massive M_* domain, it does not probe the lower stellar mass, gas rich systems. Blindly applying the fundamental plane defined by the massive gas-poor galax-

ies through extrapolation into the gas-rich regime results in serious underprediction of $f_{\rm HI}$. Because of the change in slope, the deviation from [Catinella et al., 2010] is systematically larger in the high $f_{\rm HI}$ galaxies.

Because the HI population is so overwhelmingly dominated by blue cloud dwellers and since HI is presumably a constituent of a galaxy's disk, not its bulge or halo, it seems appropriate to explore scaling relations which are tied more heavily to the galaxy's disk. Hence, we define a disk stellar mass surface density $\mu_{*,r90}\ [M_\odot\ {\rm kpc}^{-2}] \equiv 0.9 M_*\ [M_\odot]/\pi(r_{90,r}\ [{\rm kpc}])^2$, where $r_{90,r}$ is the radius containing 90% of the Petrosian flux in the r-band. Compared to μ_*, $\mu_{*,r90}$ is based on the r-band flux with higher S/N and less bulge contribution. In addition, adopting colors corrected for internal extinction (see §3.4.2), we derive improved predictors as follows:

$$\log f_{\rm HI} = -0.17({\rm NUV}-r)_0 - 0.81\log\mu_{*,r90} + 6.31; \tag{3.5}$$

$$= -0.70(g-r)_0 - 0.79\log\mu_{*,r90} + 6.16; \tag{3.6}$$

$$= 0.22\log{\rm SSFR} - 0.78\log\mu_{*,r90} + 8.03. \tag{3.7}$$

The values given by equation (3.5)-(3.7) are plotted on the horizontal axes in Figures 3.3(g-i). They show less scatter from the one-to-one dashed line with better $r_S = 0.90$. We suggest that scaling laws which incorporate properties which reflect the disk nature of the HI distribution, and specifically the above relations, provide the most appropriate approach to predicting the characteristics of HI-selected populations.

Assessing the molecular gas H_2 contribution

ALFALFA is an extragalactic HI line survey and, as such, probes only the neutral ISM. Yet, the process of SF in most galaxies is more directly coupled to the molecular gas, and the question of which gas component – HI, H_2 or total gas – correlates best with SF is still debated. To account for the full gas content, we thus need to assess the expected contribution of molecular gas to the total gas mass in the ALFALFA population galaxies.

An outgrowth of the GASS survey of high stellar mass galaxies, COLD GASS is a legacy survey which has measured the CO(1-0) line of $\sim$350 randomly selected GASS sample galaxies ($0.025 < z < 0.05$) with the IRAM 30m telescope. COLD GASS has uncovered the existence of sharp thresholds in galaxy structural parameters such as μ_*, concentration index and $(\mathrm{NUV} - r)$ color, above which the detection rate of the CO line drops suddenly. These thresholds correspond approximately to the transition between the blue cloud and red sequence [Saintonge et al., 2011b]. Even though Catinella et al. [2010] found some red sequence galaxies with a surprisingly large HI component, none of the 68 galaxies in the first installment of COLD GASS with $(\mathrm{NUV} - r) > 5$ are securely detected in CO. At the same time, only 1.4% of the $\alpha.40$-*GALEX*-SDSS galaxies have $(\mathrm{NUV} - r) > 5$, so that the HI-selected galaxies should have a high detection rate in CO.

Under the assumption that molecular gas forms out of lower density clouds of atomic gas, one might naively expect a tight correlation between M_{HI} and $M_{\mathrm{H_2}}$. However, within the subsample of galaxies detected both in HI and CO by COLD GASS, the fraction $(M_{\mathrm{H_2}}/M_{\mathrm{HI}})$ varies greatly, from 0.037 up to 4.09; the two quantities are only weakly correlated [Saintonge et al., 2011a]. The relative

proportions of molecular and dense atomic gas in giant molecular clouds depend on the cloud column density and metallicity [Krumholz et al., 2008], and the clouds could even be primarily atomic if the metallicity is sufficiently low [Ostriker et al., 2010].

Of all the parameters that Saintonge et al. [2011b] investigated, the mean molecular gas fraction ($f_{\rm H_2} \equiv M_{\rm H_2}/M_*$) among the COLD GASS galaxies correlates most strongly with their ($\rm NUV - \it r$) color, with

$$\log f_{\rm H_2} = -0.219(\rm NUV - \it r) - 0.596,$$

although it is weaker than the $f_{\rm HI}$–($\rm NUV - \it r$) correlation, probably because $\rm H_2$ resides in the inner region where extinction is higher, whereas HI dominates in the outer disks [Saintonge et al., 2011a]. At the same time, they find that $f_{\rm H_2}$ is only a weak decreasing function of M_*. As a result, although ALFALFA probes a lower stellar mass range than COLD GASS does, the $f_{\rm H_2}$–($\rm NUV - \it r$) correlation above can still be roughly applied to the $\alpha.40$-*GALEX*-SDSS galaxies. Specifically, since the $\alpha.40$-*GALEX*-SDSS galaxies have a mean ($\rm NUV - \it r$) of 2.24, the results of COLD GASS predict a mean $f_{\rm H_2}$ of 0.082 for the HI-selected population, higher than the 0.066 of the COLD GASS detections.

We note that although $f_{\rm H_2}$ is only a weak decreasing function of M_*, $f_{\rm HI}$ clearly decreases with increasing M_*, i.e., the $M_{\rm H_2}/M_{\rm HI}$ fraction appears to decline in less massive galaxies [see also Blanton and Moustakas, 2009]. For luminous galaxies, a substantial fraction of the gas is sometimes in molecular form, but the detection of CO in low mass galaxies has been shown to be very difficult [e.g., Leroy et al., 2009]. Therefore, we conclude that $f_{\rm H_2} \lesssim 0.1$ for the ALFALFA population and thus ignore its contribution to the total gas fraction, focusing instead on the well-determined atomic gas fraction $f_{\rm HI}$.

3.3.2 Star formation properties

In addition to the stellar mass, SED-fitting also yields an estimate of the current SFR averaged over the last 100 Myr. Salim et al. [2005] have shown the importance of including the *GALEX* UV bands, especially the FUV, to reduce the uncertainties in SFRs derived from SED-fitting. In addition to the SFR itself, several other quantities of physical interest also become available. For example, the SSFR, defined as SFR/M_*, compares the current SFR with that in the past (as measured by M_*), and thus is well correlated with the birthrate-, or $b-$ parameter, defined as $\mathrm{SFR}/\langle\mathrm{SFR}\rangle$. Both the SSFR and the $b-$parameter describe the SFH. At the same time, normalization of the SFR by M_{HI} instead of M_* yields the star formation efficiency (SFE), defined as $\mathrm{SFR}/M_{\mathrm{HI}}$. The SFE compares the current SFR with its potential in the future, the latter regulated by M_{HI}, the available fuel. The reciprocal of the SFE is the Roberts time, $t_R = M_{\mathrm{HI}}/\mathrm{SFR}$ [Roberts, 1963, Sandage, 1986], the timescale for depletion of the HI gas reservoir, assuming a constant SFR at the current level.

Figure 3.4 shows a montage illustrating how the SF related properties, SFR, SSFR, SFE (y axes) vary with M_*, M_{HI} and the $(\mathrm{NUV}-r)$ color (x axes). As before, contours and points trace the $\alpha.40$-SDSS-*GALEX* population. Spearman's rank correlation coefficients are shown in the lower left corners of all panels. Typical error bars of individual galaxy estimates are plotted in the lower right corners of panels (a, e, i). In the bottom row, tracing the SFE, the cyan dashed line shows the average value obtained by Schiminovich et al. [2010] for the high stellar mass GASS sample, while the green dash-dotted line marks the value corresponding to the Hubble timescale.

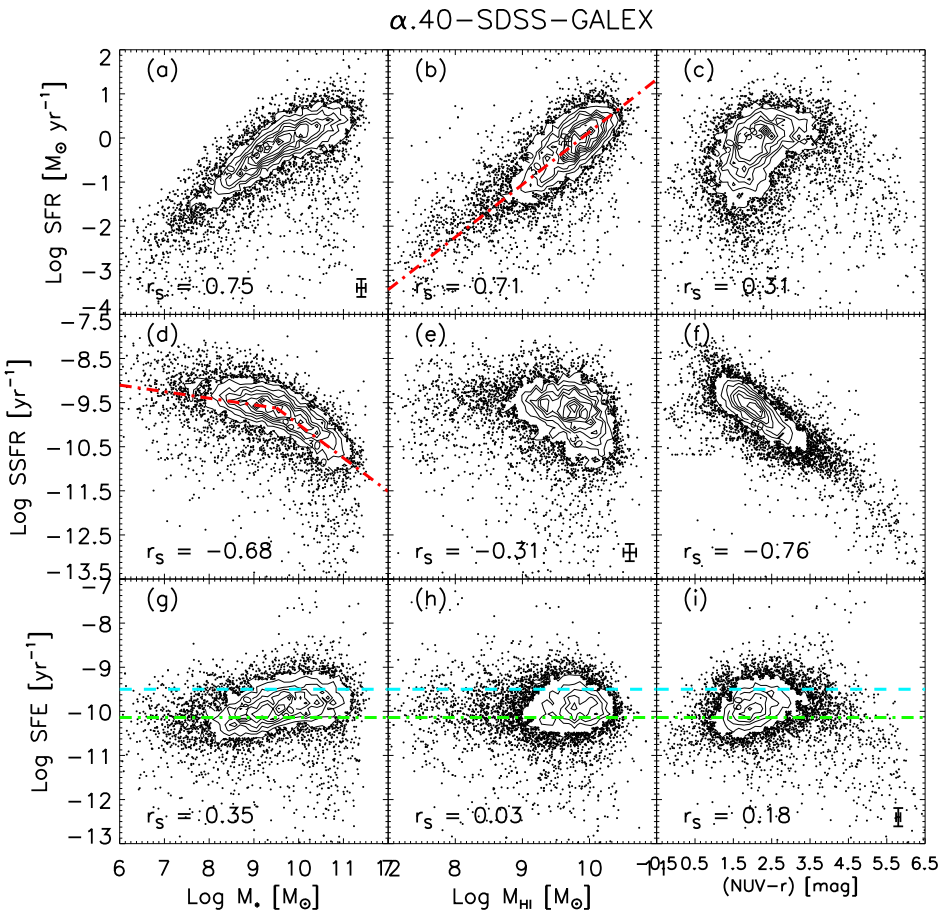

Figure 3.4: SF properties of the $\alpha.40$-SDSS-*GALEX* population. Contours and points follow the definitions in Figure 3.1. Spearman's rank correlation coefficients are shown in the lower left corners of all panels. Colors here are not corrected for internal extinction. Typical error bars of individual galaxy estimates are plotted in the lower right corners of panels (a, e, i). The red dash-dotted line in panel (b), with a slope of 1.19, represents a global, atomic, volumetric SFL defined by the $\alpha.40$-SDSS-*GALEX* galaxies. The red dash-dotted line in panel (d) represents the linear fit to the star-forming sequence given in equation (3.8). In the bottom row, tracing the SFE, the cyan dashed line shows the average value obtained by Schiminovich et al. [2010] for the GASS sample, while the green dash-dotted line corresponds to the Hubble timescale.

The SFR and SSFR in HI-selected Galaxies

Among the ALFALFA population and in agreement with previous studies, e.g. Salim et al. [2007], SFRs generally increase but SSFRs decrease with increasing

stellar mass (Figure 3.4a, d). Similar trends are also evident with $M_{\rm HI}$ (Figure 3.4b, e), albeit with larger scatter, especially in the SSFR vs. $M_{\rm HI}$ distribution ($r_S = -0.31$). The trend of decreasing SSFR with increasing stellar mass suggests the "downsizing" scenario of structure formation [Cowie et al., 1996], such that the high M_* galaxies form most of their stars in the first ~ 3 Gyr after their formation [Bell et al., 2003] and today exhibit relatively suppressed SF. In contrast, the low mass systems in such a picture remain active in SF throughout their histories. Under a hierarchical dark matter halo assembly scenario in which the low mass structures form first and then merge to form massive galaxies, the "downsizing" concept suggests a late epoch of gas replenishment and regrowth in low mass systems.

Although an HI-selected sample like ALFALFA is biased against massive galaxies with low SFRs and low SSFRs (see also §3.4.2), there is a hint in Figures 3.4(a, d) that the number density of such galaxies increases in the $M_* \gtrsim 10^{10}\ M_\odot$ regime in comparison to the intermediate mass range ($10^8\ M_\odot \lesssim M_* \lesssim 10^{10}\ M_\odot$). The presence of some points in the lower right corner of the SFR vs. M_* plot suggests that at least some objects with large stellar masses and detectable HI but very low SFRs are included in the ALFALFA population. More importantly however, there is not a comparably rich population of massive HI disks with low SFRs, i.e., the number density of galaxies in the lower right corner of Figure 3.4b is lower than that in the lower right corner of 3.4a. Where there is a lot of HI, there is always some SF.

As evident in Figure 3.4(c), the expected correlation between SFR and $(\mathrm{NUV} - r)$, that galaxies bluewards of $(\mathrm{NUV} - r) \simeq 4$ have higher SFRs than ones redwards of that value [e.g. Salim et al., 2005], is not so well defined by the

ALFALFA population ($r_S = 0.31$), mainly because ALFALFA detects only a few very red galaxies. In particular, we lack sufficient dynamic range in ($\mathrm{NUV}-r$) to probe the trend along the red sequence seen in optically-selected samples that galaxies bluer in ($\mathrm{NUV}-r$) have higher SFRs, especially if colors after extinction correction are plotted.

On the other hand, the SSFR is a strong function of the ($\mathrm{NUV}-r$) color (Figure 3.4f), with the Spearman's rank correlation coefficient $r_S = -0.76$. This is also the tightest among all the correlations shown in Figure 3.4. It is natural to expect that ($\mathrm{NUV}-r$) is closely tied to the SSFR. Since the NUV luminosity largely reflects the SF and the r-band luminosity the stellar mass, the ($\mathrm{NUV}-r$) color, as the ratio of the two, serves as a proxy for the SSFR. Given the fact that NUV better characterizes the SFR than the u-band, one may also expect the SSFR to correlate better with ($\mathrm{NUV}-r$) color than with ($u-r$). However, because NUV suffers more from internal extinction and the associated corrections can be highly uncertain, extra scatter is introduced when the NUV is used with accounting for the impact of extinction. In fact, as demonstrated in (§3.4.2) and Figure 3.8(b), a shift towards blue colors and an even tighter correlation between SSFR and ($\mathrm{NUV}-r$) become apparent when extinction-corrected colors are used.

The star formation law in HI-selected galaxies

The underlying question linking gas to stars in galaxies, the "star formation law" (SFL), is what limits SF: the formation of molecular gas out of HI or the efficiency at which the available molecular gas is converted into stars [Schruba et al., 2011]. Various forms of the SFL are studied, perhaps most common among them the empirical law describing how the SF surface density (Σ_{SFR}) is regu-

lated by the gaseous surface density [e.g., $\Sigma_{\rm HI+H_2}$ in Kennicutt, 1998b].

It should be noted that since most galaxies are unresolved by the ALFA 3.5′ beam, ALFALFA measures only the global HI content. Our estimate of the SFL will thus be globally averaged. Numerous recent studies focusing on more detailed observations of smaller yet representative samples have demonstrated the regulation of SF by molecular gas. For example, the HI Nearby Galaxy Survey [THINGS; Walter et al., 2008] and the HERA CO Line Extragalactic Survey [HERACLES; Leroy et al., 2009] provide measurements of the surface densities of total gas, atomic and molecular gas, and SFR in ∼kpc-sized regions within a number of nearby galaxies. Measurements of the azimuthally averaged gas and SFR profiles show that the SFR correlates better with the molecular hydrogen component than with the total gas density within the optical disk [e.g. Bigiel et al., 2008], suggesting that the SFR is controlled by the amount of gas in gravitationally bound clouds and that H_2 is directly important for cooling. Krumholz et al. [2012] collated observations of the relationship between gas and SFR from resolved observations of Milky Way molecular clouds, from kpc-scale observations of Local Group galaxies, and from unresolved observations of both disk and starburst galaxies in the local universe and at high redshift. Those authors showed that the data are consistent with a simple, local, volumetric SFL and that the SFR is simply ∼1% of the molecular gas mass per local free-fall time. Furthermore, Schruba et al. [2011] found a tight and roughly linear relationship between IR (inferring $\Sigma_{\rm SFR}$) and CO (inferred $\Sigma_{\rm H_2}$) intensity, with $\Sigma_{\rm H_2}/\Sigma_{\rm SFR} \sim 1.8$ Gyr. This relation does not show any notable break between regions that are dominated by molecular gas and those dominated by atomic gas, although there are galaxy-to-galaxy variations in the sense that less massive galaxies exhibit larger ratios of SFR-to-CO, an ef-

fect which may due to depressed CO relative to H_2 in low metallicity galaxies. Similarly, Bigiel et al. [2011] demonstrated a roughly constant H_2 consumption time ($\Sigma_{H_2}/\Sigma_{SFR} \sim 2.35$ Gyr).

However, other works show that the relationship between SF and gas varies systematically depending on the local environment. Bigiel et al. [2010b,a], found an evident correlation between SF and HI in the outer disks of spirals and in dwarf galaxies where HI is likely to dominate the ISM. Given the poor correlation between HI and SFR found inside star-forming disks, this finding strongly hints that different physics governs the formation of star-forming clouds, and that the HI column is perhaps the key environmental factor in setting the SFR [Bigiel et al., 2010b]. Furthermore, the SFL is likely to have a distinct form in the atomic-gas-dominated regime [e.g. $\Sigma_{SFR} \propto \Sigma_{HI+H_2}\sqrt{\rho_{sd}}$, theoretically by Ostriker et al., 2010, where ρ_{sd} is the midplane density of stars plus dark matter]. Therefore, we may expect a steeper dependence of Σ_{SFR} on Σ_{HI+H_2} if there is a dropoff in the stellar and dark matter density with radius. There is no single universal slope predicted for the SFL in the diffuse-gas-dominated regime. In low gas surface density or low metallicity regions where gas is significantly atomic, thermal and chemical processes become dominant in determining where stars can form, and the gravitational potential of the stars and dark matter may have a significant effect. Similarly, the model developed by Krumholz et al. [2009] suggests Σ_{SFR} becomes a steep function of Σ_{HI+H_2} when complexes of gas become primarily atomic, for low ISM surface density. Observations also confirm steeper slopes for the low density outer HI-dominated regions of spiral galaxies, as well as dwarf galaxies, compared to the inner molecular-dominated regions of spirals [Bigiel et al., 2010b].

The increasing SFR with HI mass evident in Figure 3.4(b) suggests the regulation of SF by the HI gas, with a correlation coefficient of $r_S = 0.71$. The red dash-dotted line in Figure 3.4(b) shows the linear fit to the $\alpha.40$-SDSS-*GALEX* galaxies, with a slope of 1.19, suggesting a global, atomic, volumetric SFL. The close to unit slope indicates a SFE close to constant as a function of $M_{\rm HI}$. The correlation between SFR and $M_{\rm HI}$ appears to be in conflict with the earlier finding that most galaxies show little or no correlation between $\Sigma_{\rm SFR}$ and $\Sigma_{\rm HI}$ [Bigiel et al., 2008]. The high $f_{\rm HI}$ galaxies represented by the ALFALFA population appear to obey an unusual SFL which may not only depend on the H_2, but also on the HI, stellar and dark matter properties. Additional observational and theoretical work is needed to evaluate how the SF efficiency of bound clouds depends on the relative amounts of cold HI versus molecular gas.

The SFE in HI-selected galaxies

Figures 3.4(g-i) illustrate the distribution of the SFE with M_*, $M_{\rm HI}$ and the $({\rm NUV}-r)$ color. The timescale for atomic gas depletion for the majority of the ALFALFA galaxies is shorter than the Hubble time t_H, and comparable to it for many of those with low stellar masses, $M_* < 10^9\ M_\odot$.

For the high stellar mass GASS population, Schiminovich et al. [2010] found that, unlike the SSFR which decreases with increasing stellar mass, the SFE remains relatively constant with a value close to ${\rm SFE} = 10^{-9.5}$ yr $^{-1}$, or equivalently $t_R \sim 3$ Gyr. This value is longer than the molecular gas depletion timescale (see §3.3.2). Furthermore, those authors also found little variation in the SFE with stellar mass surface density μ_*, the $({\rm NUV}-r)$ color or the concentration index, a result which they interpreted as an indication that external pro-

cesses or feedback mechanisms which control the gas supply are important for regulating SF in massive galaxies. Considering that $\log \mathrm{SSFR} = \log \mathrm{SFE} + \log f_{\mathrm{HI}}$, an interesting implication of the weak correlation between the SFE and the stellar mass is that the fit to the $\log \mathrm{SSFR}$ versus $\log M_*$ distribution would have a similar slope to that of the $\log f_{\mathrm{HI}}$ vs. $\log M_*$, specifically -0.288 for $\log M_* \leq 9$ and -0.724 for $\log M_* > 9$ (see equations 3.1 in §3.3.1). However, the red dash-dotted line in Figure 3.4(d) shows the linear fit to the 'star-forming sequence' defined by the $\alpha.40$-SDSS-*GALEX* galaxies:

$$\log \mathrm{SSFR} = \begin{cases} -0.149 \log M_* - 8.207, & \log M_* \leq 9.5 \\ -0.759 \log M_* - 2.402, & \log M_* > 9.5. \end{cases} \tag{3.8}$$

The differences in the slopes suggest that $\langle \mathrm{SFE} \rangle$ is a weak increasing function of $\langle M_* \rangle$ in the low M_* range but remains relatively constant above $\log M_* \sim 9.5$; this trend is also evident in the bottom row of panels($r_S = 0.35$). The mild trend of increasing SFE with stellar mass seen in Figure 3.4(g) was not evident in the GASS study [Schiminovich et al., 2010] because the GASS sample includes only galaxies with $M_* > 10^{10}\ M_\odot$.

Rather than a simple continuous scaling relation, the change of slope given in equation (3.8) and evident in Figure 3.4(d), suggests that a transition mass exists at $M_* \sim 10^{9.5}\ M_\odot$ in the way in which star formation scales with total M_*. A similar transition mass at $M_* \sim 10^{9.4}\ M_\odot$ in SSFR is adopted by Salim et al. [2007] for their blue galaxies with $(\mathrm{NUV} - r) < 4$. Those authors suggested that the lower SSFR is a consequence, at the high M_* end, of a population of systems which are both star-forming and have AGN, thereby yielding lower SSFRs than pure SF galaxies of the same mass. Similarly, Kannappan et al. [2009] identified a "threshold" stellar mass of several times $10^9\ M_\odot$, below which the number of blue sequence E/S0 galaxies sharply rises. Those authors matched the threshold

to the mass scale below which the mean HI content of low-z galaxies increases substantially both on the red sequence and within the blue cloud. Abrupt shifts in the SFE and gas richness near the "threshold mass" have been linked to the interplay of gas infall, supernova-driven winds, and changes in mass surface density. However, it is important to note that such a threshold falls below the "transition" mass characteristic of the "green valley", identified in the, e.g., $f_{\rm HI}$ versus M_* and μ_* relations, at a stellar mass $M_* \sim (2-3) \times 10^{10}\ M_\odot$ proposed in many other works [e.g. Kauffmann et al., 2003a, Baldry et al., 2004, Bothwell et al., 2009, Catinella et al., 2010] and suggested to be indicative of the SF quenching in massive galaxies as they migrate from the blue cloud to the red sequence.

Perhaps surprisingly, the ALFALFA galaxies have on average *lower* SFE, or equivalently, longer t_R, compared to the optically-selected population, with a mean of $\rm SFE = 10^{-9.95}$ yr $^{-1}$, or equivalently $t_R = 8.9$ Gyr, compared to the $t_R \sim 3$ Gyr derived for the GASS galaxies. We note that the average t_R value was volume corrected in Schiminovich et al. [2010], but not in Figure 3.4(g-i). However, we confirm that the volume correction (see §3.4.1) results in only subtle changes in the mean t_R as a function of M_* for the $\alpha.40$-SDSS-*GALEX* galaxies, and it is still longer than $t_R \sim 3$ Gyr. As we demonstrate in §3.4.2, the HI-selected galaxies have, on average, higher SFRs at a fixed stellar mass, so that the lower SFEs must result from their higher HI masses rather than from less active states of SF. This result reaffirms the general conclusion that HI-selected samples are strongly biased towards the most gas-rich galaxies. In agreement with the low SFEs characteristic of the ALFALFA population, Bigiel et al. [2008] have seen a decrease in SFE in the HI-dominated THINGS galaxies. Furthermore, Bigiel et al. [2010b] found that the SFE decreases with galactocen-

tric radius among the THINGS sample across the outer disks beyond the optical radius, where HI dominates the ISM, with t_R well above Hubble time. In the THINGS dwarf galaxies, the contribution of H_2 to the total gas budget is generally small even in the inner disks, also corresponding to a low SFE [Bigiel et al., 2010b]. All these results are consistent with the conclusion that SFEs are low, on average, in HI-rich systems.

However, we note that the low HI SFE may not be in conflict with the usual H_2 SFL. The HI-selected high $f_{\rm HI}$ galaxies may still follow the normal behavior of how stars form from H_2, but rather that a bottleneck exists in the process by which star-forming molecular clouds assemble. The conversion of HI to H_2 depends on environment inside a galaxy and the relative abundance of HI and H_2 is key to setting the SFR [Bigiel et al., 2010a]. Although the low HI SFE suggests the inefficiency of HI-to-H_2 conversion, the HI-to-H_2 ratio cannot be arbitrarily high. Ostriker et al. [2010] assumed an equilibrium state, in which cooling balances heating and pressure balances gravity. This balance can be obtained by a suitable division of the gas mass into star-forming (gravitational bound) and diffuse components such that their ratio is proportional to the vertical gravitational field. If too large a fraction of the total surface density is in diffuse gas, the pressure will be too high while the SFR will be too low. In this situation, the cooling would exceed heating, and mass would drop out of the diffuse gas component to produce additional star-forming gas.

Close examination of the SFE vs. M_* diagram in Figure 3.4(g) also reveals a considerable number of outliers with relatively high SFE at the high M_* end, falling well above the main distribution. In general, high SFEs have been measured in starburst galaxies and interacting systems which are consuming their

gas reservoirs on very short timescales. However, a close inspection of 13 $\alpha.40$-SDSS-*GALEX* galaxies with $\log \mathrm{SFE} > -8$ shows that 9 of them are members of the Virgo Cluster. Ram pressure stripping results in strong HI deficiency and very short t_R in these extreme outliers. In contrast, the outliers below the main distribution can either be red, massive, low SSFR galaxies against which ALFALFA is strongly biased, or abnormally gas rich (for their stellar mass) but quiescent ones. The latter include candidates of recent re-accretion or systems in which the HI gas is somehow inhibited from forming stars. We return to this point in §3.5.

Figures 3.4(h, i) illustrate that the SFE barely changes with either $M_{\rm HI}$ or color ($r_S = 0.03$ and 0.18 respectively) and the scatter in both correlations is large.

Linking the gas fraction $f_{\rm HI}$ to SF

As first discussed by Roberts [1963], it is not surprising that SF appears to be regulated by gas content. We have already argued that the $\log \mathrm{SSFR}$ vs. $\log M_*$ diagram (Figure 3.4d) is similar to the $\log f_{\rm HI}$ vs. $\log M_*$ one (Figure 3.2c), both showing similar slopes along the main trend; the distributions of $\log \mathrm{SSFR}$ and $\log f_{\rm HI}$ in given stellar mass bins also become broader at both the high- and low-mass ends. Hence, the star-forming sequence in the former diagram can also be understood as a sequence of gas-depletion in the latter one.

Previously, Kannappan [2004] also linked the $f_{\rm HI}$ to bimodalities in galaxy properties. She suggested that the bimodality in SFHs may be intimately related to changes in $f_{\rm HI}$, and the transition in SF modes at $M_* \sim (2-3) \times 10^{10}\ M_\odot$, found by those authors, is not a cause but an effect of changing $f_{\rm HI}$, as predicted

in cold-mode accretion scenarios. Figure 3.5 illustrates these relationships by showing the averaged $\log f_{\rm HI}$ of galaxies which lie in different loci in the CMD (left panel) and the $\log {\rm SSFR}$ vs. $\log M_*$ diagram (right panel). Contours indicate the number density within the $\alpha.40$-SDSS-*GALEX* sample in each grid point in the map, while the shade scale traces the mean HI fraction, $\langle \log f_{\rm HI} \rangle$. As mentioned in §3.2.2, 96% of ALFALFA galaxies lie on the blue side of the optical-NUV CMD, whereas a smaller fraction (84%) lie on the blue side of an optical-only CMD (see §3.4.2 below). Some of this difference can be attributed to the greater impact of shredding on the SDSS pipeline magnitudes relative to that of the *GALEX* photometry. Because of the color gradient of galaxies (outer disks are bluer), the shredded central redder object is identified as the OC. As a result, the adopted photometric object may be redder in $(u-r)$ than the galaxy as a whole actually is. Moreover, the u-band is not as sensitive and thus yields photometry with large uncertainties for some of the galaxies. Additionally, the $({\rm NUV}-r)$ color is a stronger diagnostic of the SFH. For similar reasons, the $\langle \log f_{\rm HI} \rangle$ of grid points in regions of low number density should be interpreted with caution. However the general trends (1) that the red-sequence is associated with low $f_{\rm HI}$ and (2) that blue cloud galaxies are gas rich are clearly evident. At a given M_r, redder $({\rm NUV}-r)$ colors, on average, indicate lower $f_{\rm HI}$. Furthermore, such a variation of $f_{\rm HI}$ along the $({\rm NUV}-r)$ axis is more evident in the fainter M_r range: $\delta\langle \log f_{\rm HI} \rangle / \delta \langle {\rm NUV}-r \rangle \simeq 0.75$ at $M_r \simeq -16$, whereas $\delta\langle \log f_{\rm HI} \rangle / \delta \langle {\rm NUV}-r \rangle \simeq 0.25$ at $M_r \simeq -22$. Therefore, the correlation of $({\rm NUV}-r)$ and $f_{\rm HI}$ at a given M_r is hard to see in a sample with only massive galaxies, e.g. GASS [Wang et al., 2011].

Similarly, the right panel of Figure 3.5 illustrates how the HI fraction varies in the M_*-SSFR plane. As galaxies assemble their stellar mass and evolve along

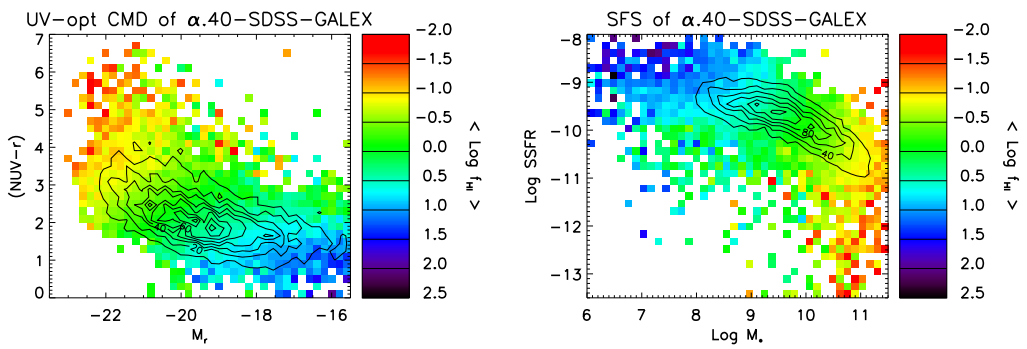

Figure 3.5: Diagrams of the $\alpha.40$-SDSS-*GALEX* sample with shade scale showing the averaged HI fraction in each grid, while number density is indicated by the contours. *Left panel* - UV-to-optical CMD. The blue cloud galaxies dominate in number and are associated with higher $f_{\rm HI}$ on average. At given M_r, a redder $(\rm NUV - r)$ color on average indicates lower $f_{\rm HI}$; this trend is more evident at the faint end. *Right panel* - The star forming sequence as traced by the contours. As galaxies assemble M_* and evolve along the sequence, their HI fractions follow a decreasing trend. At a fixed M_*, galaxies with lower SSFRs on average have lower $f_{\rm HI}$, which is also more evident among low mass galaxies with $M_* \lesssim 10^{9.5}\ M_\odot$ The broadenings of the distributions of color, SSFR and $f_{\rm HI}$ at the low mass end are correlated to each other.
(A color version of this figure is available in the online journal.)

the star forming sequence, represented by the contours of high number density, their HI fractions decrease. In addition, for fixed M_*, galaxies with lower SSFRs have, on average, lower $f_{\rm HI}$. Again this is more clearly evident at the low stellar mass end, and is consistent with the broadening in both the $f_{\rm HI}$ and SSFR distributions at low M_* [Huang et al., 2012b]. In contrast, the variation of $\langle \log f_{\rm HI} \rangle$ along the $\log \rm SSFR$ axis at a given M_* is less evident for galaxies with $M_* \gtrsim 10^{9.5}\ M_\odot$. These two trends suggest that, for low M_* systems, high $f_{\rm HI}$ galaxies are more likely to be starburst galaxies (defined as high SSFR galaxies), whereas galaxies in the high M_* regime selected by high $f_{\rm HI}$ are less likely to be starbursts. In summary, Figure 3.5 clearly demonstrates that the color, SF

and gas evolution of galaxies are closely related to one another, as expected. Moreover, the regulation of SF by $M_{\rm HI}$ is stronger in the less massive galaxies.

3.4 The Impact of Optical Versus HI-selection

Future surveys of HI in galaxies at intermediate to high redshifts that will be enabled by the next generation of centimeter-wavelength radio telescopes (e.g. the SKA) will aim to infer the gas evolution from high redshift populations to the local well-studied ones. It is important therefore to understand the fundamental properties of local HI-selected galaxies, as represented by the ALFALFA catalog, and their biases relative to the overall galaxy population. In §3.3, we examined the global properties of gas, stars and SF within the ALFALFA galaxies themselves. They form an HI-rich, blue and less evolved population with low SFE; these characteristics are more pronounced in lower mass systems. $M_{\rm HI}$ and $f_{\rm HI}$ are linked to the SF related quantities, demonstrating the role that HI plays in the regulation of galaxy evolution along the star forming sequence. To understand how the HI-selected population is biased relative to ones selected by stellar mass or optical flux, in this section we construct samples from both the $\alpha.40$ and SDSS catalogues and then compare their similarities and differences.

3.4.1 Construction of control samples

In order to ensure the galaxies contained in each of the optically- and HI-selected samples are both representative of their respective population and fair enough to permit comparison with the other, we construct subsamples of both

$\alpha.40$ and the SDSS in the same sky volume within their common footprint. The volume-limits imposed are similar to those discussed by Martin et al. [2010]. Comparable selection criteria are applied with a further requirement that acceptable *GALEX* pipeline photometry must also be available, so that stellar masses and star formation properties can be derived robustly via SED-fitting.

ALFALFA selected sample, $S_{\rm HI}$

As discussed by Martin et al. [2010], radio frequency interference from the San Juan airport FAA radar transmitter at 1350 MHz makes ALFALFA blind to HI signals in a spherical shell ~ 10 Mpc wide centered at a distance of ~ 215 Mpc. Therefore, as did those authors, we exclude 568 galaxies of the sample presented in §3.3 which lie beyond 15000 km s^{-1} ($D_{\rm sur}$ hereafter). To maximize the overlap of contiguous sky coverage between the current ALFALFA and SDSS DR7, we consider only the two regions in the northern Galactic hemisphere ($8^{\rm h}00^{\rm m} <$ RA $< 16^{\rm h}30^{\rm m}$, $4^\circ <$ Dec $< 16^\circ$ and $7^{\rm h}40^{\rm m} <$ RA $< 16^{\rm h}40^{\rm m}$, $24^\circ <$ Dec $< 28^\circ$, see Figure 3.6c). Applying these restrictions yields a sample within a sky volume of $V_{\rm sur} = 1.987 \times 10^6$ Mpc^3, a sky area of 1989 deg^2 and including 7638 $\alpha.40$-SDSS-*GALEX* galaxies.

Next, a weight, $V_{\rm sur}/V_{\rm max}$, is assigned to each galaxy, where $V_{\rm max}$ is given by the maximum distance, $D_{\rm max}$, at which an HI source can be detected by ALFALFA, if $D_{\rm max} < D_{\rm sur}$, with $V_{\rm sur}/V_{\rm max} = 1$ for the galaxies which can be detected all the way outwards to the $D_{\rm sur}$. Because the ALFALFA sensitivity depends not only on the integrated HI line flux density, $S_{\rm int}$ [Jy km s^{-1}], but also on the HI line profile width, W_{50} [km s^{-1}], specifically, the fit to $S_{\rm lim}$, the limiting integrated HI line flux density that can be detected at S/N above 4.5 (code 1 and 2,

25% complete), as given in Haynes et al. [2011], is:

$$\log S_{\rm lim} = \begin{cases} 0.5 \times \log W_{50} - 1.11 - 0.202, \text{ if } \log W_{50} < 2.5; \\ 1.0 \times \log W_{50} - 2.36 - 0.202, \text{ if } \log W_{50} \geqslant 2.5. \end{cases}$$

Then, $D_{\rm max}$ can be calculated given $S_{\rm lim}$ and $M_{\rm HI}$, based on the standard equation $M_{\rm HI} = 2.356 \times 10^5 D^2_{\rm Mpc} S_{\rm int}$. In order to characterize the stellar component of the galaxies, we also perform a cross-match to the SDSS and *GALEX* databases. The application of such a weight scheme, or volume correction, is equivalent to resampling the galaxies by their HI properties ($M_{\rm HI}$ and W_{50}) alone, thereby reemphasizing the impact of HI-selection.

To further trim the sample, we drop galaxies whose weight $V_{\rm sur}/V_{\rm max} > 60$, i.e., we consider only galaxies that could be detected in more than 1.67% of the survey volume. This cutoff corresponds approximately to a lower $M_{\rm HI}$ limit of $\sim 10^{8.2}\ M_\odot$ (see Figure 3.6). There is not a hard $M_{\rm HI}$ cutoff because W_{50} also plays a role. The galaxies with $V_{\rm sur}/V_{\rm max} > 60$ are all relatively nearby ($D_{\rm max} < 54.7\ {\rm km\ s^{-1}}$, or assuming Hubble flow, $cz_{\rm max} < 3829\ {\rm km\ s^{-1}}$, $z_{\rm max} < 0.0128$), and are low HI mass galaxies less representative of the survey overall. Further motivations for applying such a weight cutoff include: (a) for these very local sources, distance dependent quantities, e.g. $M_{\rm HI}$, have large uncertainties due to their peculiar velocities; (b) such galaxies are also underrepresented in the SDSS redshift sample (see below); (c) for resolved, patchy dwarf systems especially, the SDSS pipeline magnitudes can suffer from shredding. The lowest HI mass systems have been considered separately in Huang et al. [2012b].

The final HI-selected sample referred to as $S_{\rm HI}$ includes 7157 galaxies.

SDSS selected sample, $S_{\rm opt}$

To construct an optically-selected control sample out of the same sky volume, $V_{\rm sur}$, we queried the SDSS DR7 in the same RA and Dec ranges for photometric objects which have valid model magnitudes and were also spectroscopic targets. We also require them to (a) have a spectral classification of "galaxy"; (b) have an SDSS redshift, $z_{\rm SDSS}$, determined with high confidence; (c) lie within the same redshift range as $S_{\rm HI}$, $cz_{\rm SDSS} < 15000$ km s^{-1}; (d) have Galactic extinction-corrected r-band model magnitudes brighter than 17.77. 24379 galaxies meet these criteria. Note the redshifts adopted for this sample use the SDSS measurement, whereas that for the $S_{\rm HI}$ comes from the HI line measures. Given the $cz_{\rm SDSS}$ and coordinates, distances are estimated in the same manner as for the $\alpha.40$ sample using a local flow model for $cz < 6000$ km s^{-1}, and Hubble distance otherwise [Haynes et al., 2011]. Following the same procedure as for $S_{\rm HI}$, we searched for *GALEX* cross-matches, and applied similar SED-fitting to the UV/optical bands.

To match the weight cutoff of the HI-selected $S_{\rm HI}$ sample, we also calculate weights for the SDSS-selected sample but here according to their optical fluxes. In this case, $D_{\rm max}$ is the maximum distance at which the object, given its r-band flux, could be included in the SDSS main galaxy redshift sample. As for the HI-selected sample, we drop galaxies with weights greater than 60. Given the magnitude limit of the SDSS redshift survey ($m_r < 17.77$ mag), such a weight cut directly corresponds to an r-band absolute magnitude limit of ~ -16 mag. Furthermore, since the mass-to-light ratio varies only mildly with color, the luminosity cut approximately translates to a stellar mass lower limit of $\sim 10^{7.6}\,M_{\odot}$. Finally, a small number of galaxies are removed because they are included in the

$\alpha.40$ catalog but have been previously noted by individual inspection to have suspect photometry [Haynes et al., 2011]. The final optically-selected sample referred to as $S_{\rm opt}$ includes 16817 galaxies, of which 34% are cross-matched to the $\alpha.40$ catalog (see §3.2.2). The remainder are missed by ALFALFA either because they are (1) gas poor, (2) lie at a sufficient distance that their HI line flux densities falls below the HI sensitivity limit, or (3) for some other reason, e.g. their HI spectrum is contaminated by RFI or was not sampled at all (small gaps in ALFALFA coverage), or they correspond to one "child" of a shredded photometric parent object, but another photometric child is favored as the best match to the ALFALFA detection.

We note that the distributions of weight, $V_{\rm sur}/V_{\rm max}$, for both the samples highly peak at 1, and that the weight cut of 60 applied to each dataset is confirmed to be high enough to retain the main populations. Especially for the $S_{\rm opt}$, 69% of the galaxies have a unit weight, i.e. can be detected outwards to the edge of $V_{\rm sur}$ as we defined here. The number of galaxies in bins associated with a weight above 1 drops more rapidly among the $S_{\rm opt}$ sample, confirming that the SDSS is deeper than ALFALFA.

3.4.2 Comparison of control samples

Basic properties

Figure 3.6 illustrates the comparison of quantities relevant to sample selection between the $S_{\rm HI}$ and the $S_{\rm opt}$ populations. In panels (a-c), red points denote galaxies in $S_{\rm opt}$, whereas blue points denote galaxies in $S_{\rm HI}$. In the histograms, red lines illustrate the distribution of $S_{\rm opt}$ and blue lines trace $S_{\rm HI}$; above each

histogram, separate panels show the fraction of $S_{\rm opt}$ galaxies that are cross-matched to $\alpha.40$ in each bin. The numbers in each subset are indicated in panels (a) and (b).

The top row contains two Spaenhauer diagrams showing, respectively, the r-band absolute magnitude (panel a) and HI mass (panel b) versus distance. The solid vertical line represents the cz cutoff, 15000 km s^{-1}. We use the SDSS redshifts to derive distances for the $S_{\rm opt}$ and ALFALFA HI velocity for the $S_{\rm HI}$. As discussed also by Martin et al. [2010], a survey must sample sufficient volume to detect very massive galaxies in either stellar (panel a) or HI (panel b) mass. ALFALFA for the first time provides a full census of HI-bearing objects over a cosmologically significant volume of the local universe.

As evident in Figure 3.6(a), SDSS is volume limited to $M_r \sim -19$ mag. The sharp lower edge of the $S_{\rm opt}$ distribution above $D \sim 60$ Mpc results from the magnitude limit of the SDSS main galaxy redshift sample; as noted before, the adopted weight cutoff corresponds to $M_r \sim -16$ mag (horizontal dashed line). Since no limit on any optical quantity is applied to the $S_{\rm HI}$ subset, many blue points from $\alpha.40$ show up faintwards of the lower edge of $S_{\rm opt}$, as faint as $M_r \sim -14$. We note that the blue points lying faintwards of the lower edge of $S_{\rm opt}$ and above $D \sim 60$ Mpc are still detected by the SDSS, but most often only as photometric objects; hence their optical redshifts are generally unknown. To enable SED-fitting however, all the $S_{\rm HI}$ galaxies are required to be detected in the SDSS; the very rare "dark" HI clouds without identified OCs included in $\alpha.40$ are outside the scope of this work and are not included in this discussion.

Figure 3.6(b) shows how $M_{\rm HI}$ increases with distance. The HI measures of $S_{\rm opt}$ all come from the $\alpha.40$ catalog (5653 out of 16817 $S_{\rm opt}$ galaxies, i.e., a cross-

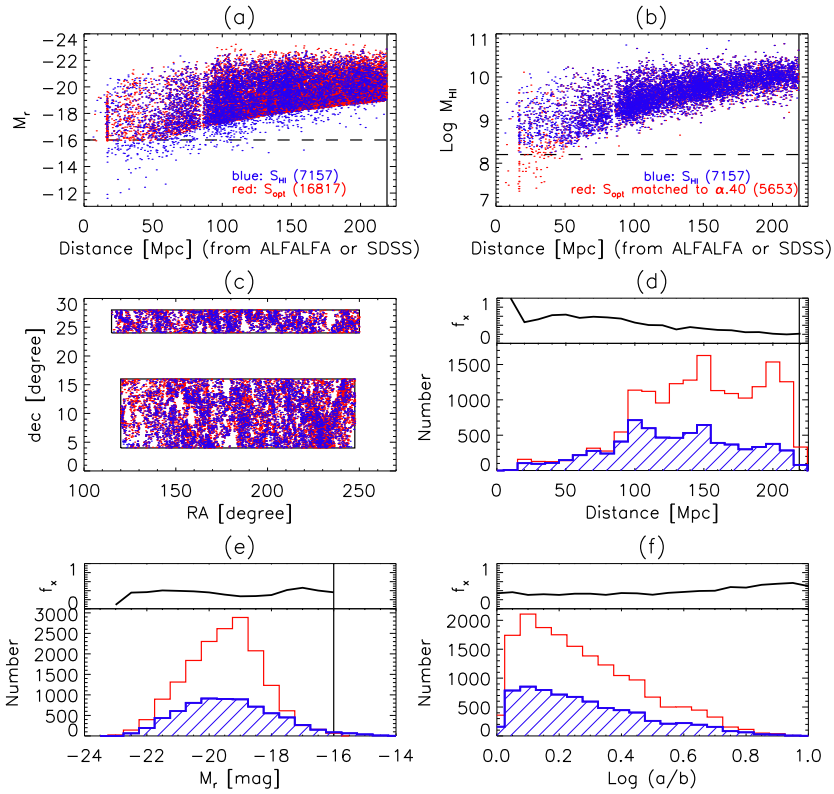

Figure 3.6: Comparison of the basic properties relevant to the sample selection of the HI-selected sample $S_{\rm HI}$ (7157 galaxies selected from the $\alpha.40$, blue points and blue histograms) and the optically-selected one $S_{\rm opt}$ (16817 galaxies selected from the SDSS, red points and red histograms). The panels above the histograms show the fraction of the $S_{\rm opt}$ galaxies that are cross-matched to $\alpha.40$ in each bin, similar to an HI detection rate of the $S_{\rm opt}$ galaxies by ALFALFA. Both samples are extracted from the same sky area (panel c), lie within $cz = 15000$ km s^{-1} (panel d) and are cross-matched to the *GALEX* catalog. Spaenhauer diagrams are in panels (a) and (b), i.e. r-band absolute magnitude, M_r, and $M_{\rm HI}$ against distance. A weight (or volume correction) cut of 60 applied on $S_{\rm opt}$ results in M_r brighter than ~ -16, whereas applied on $S_{\rm HI}$ results in $M_{\rm HI} \gtrsim 10^{8.2}\ M_\odot$. Though the two samples probe similar M_r ranges (panel e), the SDSS is deeper than ALFALFA, as evident in the distance distribution (panels d). No bias against edge-on galaxies in the $S_{\rm HI}$ population is seen in panel (f).
(A color version of this figure is available in the online journal.)

match rate of 34%). The weight cutoff applied to the $S_{\rm HI}$ sample results in an approximate limit of $M_{\rm HI} \simeq 10^{8.2}\ M_\odot$ (horizontal dashed line). The red points

below $10^{8.2}$ $M_\odot$ are still detected by $\alpha.40$, but are excluded from the $S_{\rm HI}$ simply because of their high weights. Because of the way distances are derived [Haynes et al., 2011] from the observed redshifts, an insignificant difference (0.1 Mpc) of the median distance arises for the same galaxies in the $S_{\rm opt}$–$S_{\rm HI}$ overlap sample. This difference is mainly due to the fact that the $S_{\rm HI}$ galaxies may be assigned membership in group whereas such information has not been applied to the $S_{\rm opt}$ sample. A few red outliers below the main distribution indicate objects without robust SDSS redshifts.

Panel (c) shows the sky distribution of the two samples. Besides the large scale structure, the required availability of *GALEX* photometry also contributes to the pattern. For example, the Virgo region is densely covered by at least MIS level visits, whereas the patches of sky blank in either sample and with regular edges arise from the lack of *GALEX* coverage in FUV and/or NUV. The distribution of distance is shown in panel (d). The two samples roughly coincide within ∼100 Mpc. Above the histogram, the fraction of the $S_{\rm opt}$ galaxies that are cross-matched to $\alpha.40$ is shown. The first peak in number density coincides with the Virgo cluster (∼16.5 Mpc), where $S_{\rm opt}$ clearly out numbers $S_{\rm HI}$. Since the two distributions agree with each other again at larger distances ∼50 Mpc, the disagreement at the Virgo distance indicates a real underdensity of gas-rich detections in $S_{\rm HI}$, reflecting the well-known HI deficiency [Davies and Lewis, 1973, Giovanelli and Haynes, 1985, Solanes et al., 2002]. Beyond ∼100 Mpc, $S_{\rm opt}$ significantly overtakes $S_{\rm HI}$, though the shapes of peaks or gaps still agree. This suggests that ALFALFA is capable of detecting HI massive objects at large distances, although the survey is not as deep as SDSS. Although in a given distance bin, the least massive objects contained in $S_{\rm HI}$ are even fainter than those in $S_{\rm opt}$ (i.e., the blue points below the lower edge of red distribution in panel a),

ALFALFA is not as complete as SDSS at large distances.

The distributions of M_r for both samples are shown in panel (e). The vertical solid line denotes the equivalent weight cut applied to $S_{\rm opt}$. While $S_{\rm opt}$ peaks at a slightly fainter M_r than $S_{\rm HI}$, the two samples probe a similar M_r range so that their comparison is valid.

The distributions of axial ratio, given by the SDSS pipeline measures of the exponential fit a/b in r-band, are shown in panel (f). Because the ALFALFA sensitivity depends on the HI line profile width (see §3.4.1), $S_{\rm HI}$ might be expected to be biased against edge-on galaxies with high a/b values. For example, West et al. [2010] demonstrated that their Parkes Equatorial Survey [ES, a search through HIPASS cubes; Garcia-Appadoo et al., 2009] – SDSS common sample is slightly biased towards face-on galaxies, relative to an SDSS DR4 sample, with the mean $\log a/b$ equal to 0.17 and 0.21 for their ES–SDSS and DR4 samples respectively. However, panel (f) shows no such obvious bias. Both $S_{\rm HI}$ and $S_{\rm opt}$ have the same $\langle \log a/b \rangle = 0.28$. Furthermore, the cross-match rate even slightly rises for high a/b galaxies, with only a mild drop in the very last bin. Visual inspection shows that shredding can cause large errors in the a/b measures by the SDSS pipeline. The $S_{\rm opt}$ sample contains more galaxies with bulges making their a/b values appear to be smaller; in contrast, $S_{\rm HI}$ is biased against such galaxies.

Internal extinction in HI-selected galaxies

Previously, and in many analyses of SDSS derived samples, internal extinction is ignored. However, while the outer parts of galaxy disks are transparent, it is

well established that the inner regions are optically thick at short wavelengths. Therefore, the neglect of internal extinction in disk-dominated galaxies is likely to introduce systematic inclination-dependent effects. In this section, we discuss (a) how internal extinction varies with stellar mass, (b) how internal extinction may introduce scatter into relationships involving colors and (c) how the extinction characteristics of the $S_{\rm HI}$ HI-selected galaxies compare to those derived from an optically selected sample $S_{\rm opt}$. In the three figures associated with this section, Figure 3.7 - 3.9, typical error bars on individual points are plotted in selected panels in as well as the Spearman's rank correlation coefficients.

Estimates of internal extinction are derived from UV/optical SED-fitting as before. The two-component dust model [Charlot and Fall, 2000] is incorporated into the construction of the library of model SEDs [Gallazzi et al., 2005]; the process accounts for both the diffuse interstellar medium (ISM) and short-lived (10 Myr) giant molecular clouds. Such estimates have overall larger uncertainties among the red-sequence galaxies relative to the blue cloud ones [e.g. Saintonge et al., 2011b], and contribute to the SFR uncertainties. Furthermore, Salim et al. [2007] identified differences between the effective optical depth in V band, τ_V, derived from emission-line fitting and that derived from SED-fitting, as a function of stellar mass. Specifically, at lower masses, the SED-fitting-derived value is systematically higher than the line-fitting-derived one, but the situation is reversed at the high mass end. Therefore, we applied a Gaussian prior distribution of τ_V for each model, given the absolute magnitude and axial ratio of the individual galaxies (see §3.3). The mean of the prior distribution is given by equation (12) in Giovanelli et al. [1997], which depends on the axial ratio and absolute magnitude, i.e. more luminous edge-on galaxies have larger extinctions.

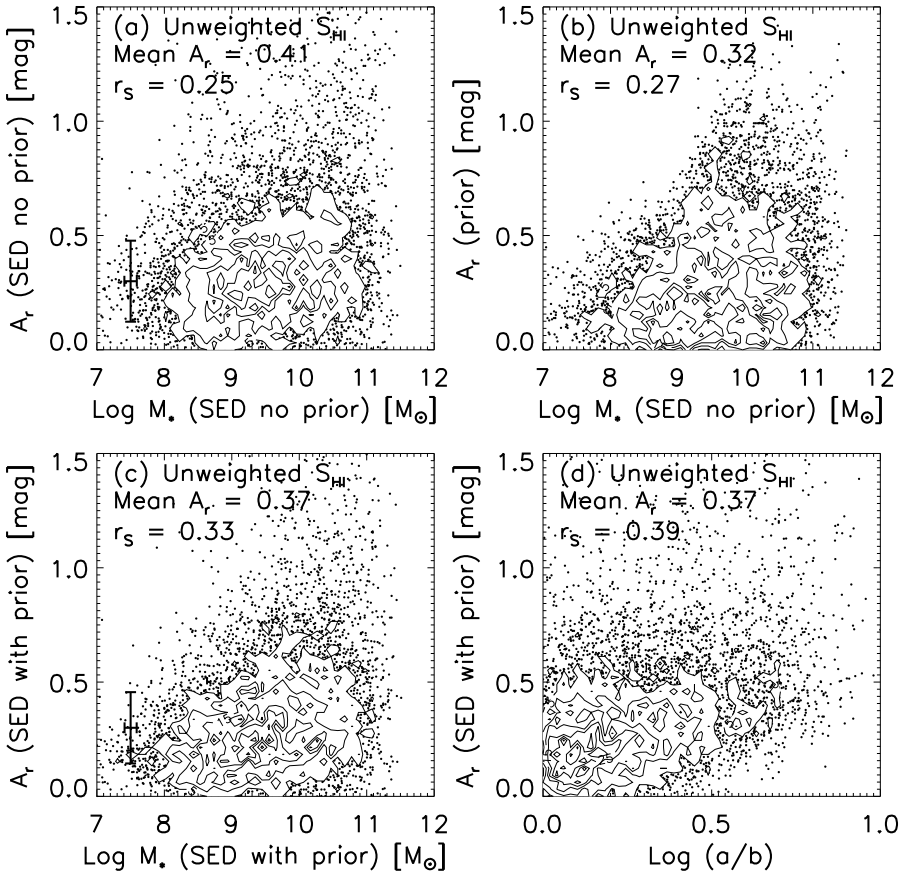

Figure 3.7: *Panels (a-c)* - The r-band internal extinction versus stellar mass. The values in panel (a) are derived by SED-fitting without the application of a prior τ_V distribution. The mean of the prior distribution is plotted in panel (b), based on equation (12) in Giovanelli et al. [1997]. The SED-fitting has been improved by adopting the prior τ_V distribution as evident in panel (c). Internal extinction is a weakly increasing function of M_* with the greatest correlation, with a coefficient = 0.33, shown in panel (c). *Panel (d)* - Internal extinction is systematically higher in more inclined galaxies, as expected.

Figures 3.7 (a-c) show plots of r-band internal extinction versus stellar mass for the $S_{\rm HI}$ galaxies. Despite the large uncertainty, internal extinction is a weakly increasing function of M_* in all these panels. Panel (a) shows SED-fitting-derived values before the prior distribution applied. A population of low mass

red galaxies have unrealistically high A_r (SED no prior), because of the age-extinction degeneracy. The mean of the prior distribution of internal extinction, A_r (prior), is in panel (b). Although the A_r (prior) values of low mass galaxies are confined to low values, a population of massive galaxies have unrealistically low A_r (prior) likely due to the underestimate of a/b. Visual inspection shows that shredding tends to describe sources as rounder in edge-on galaxies; dominant bulges, dust lanes and seeing effects will also lead to systematic underestimates of the axial ratio. Panel (c) plots the SED-fitting-derived values after the prior distribution is applied, A_r (SED with prior). Both a lack of high mass galaxies with low A_r as well as of low mass ones with high A_r are evident in panel (c). Combining the distributions in panel (a) and (b), the A_r (SED with prior)–M_* correlation is the tightest of the three, with a correlation coefficient $r_S = 0.33$. Whereas applying the prior reduces the systematic offsets of the A_r estimates by SED-fitting, as well as the SFR values, it has little effect on the stellar mass values [Huang et al., 2012b]. Figure 3.7 (d) demonstrates that, as expected, the derived values of A_r (SED with prior) are higher in more edge-on galaxies. Neglect of corrections for internal extinction will lead to the systematic underestimate of luminosity, so that hereafter we apply the SED-fitting with prior corrections.

For the subset of the $S_{\rm HI}$ galaxies (6164/7157) which are included in the MPA-JHU DR7 release of SDSS spectral measurements [http://www.mpa-garching.mpg.de/SDSS/DR7/, Brinchmann et al., 2004], we have verified that at $M_* \lesssim 10^{10} M_\odot$ the A_r inferred from the Balmer decrement and from the SED fitting using an A_r prior are in good agreement and the offset observed in Salim et al. [2007] is reduced. Above this mass the Balmer decrement leads to larger A_r values, but this is not unexpected as the SDSS spectra observe only a small

region, typically towards the center of the galaxy where metallicities and dust attenuations are higher.

Another way to explore the importance of extinction correction in a population involves examining the scatter in the $\log \mathrm{SSFR}$ – color diagram, as shown in Figure 3.8. Results for individual points (unweighted) for the S_{opt} sample are shown in the left panels and for the S_{HI} galaxies on the right, using the colors $(\mathrm{NUV}-r)_0$ in the top row and $(u-r)_0$ in the bottom, respectively. The subscript '0' in the labels indicates that the colors are corrected for internal extinction. As demonstrated in §3.3.2, SSFR is an intrinsically strong function of $(\mathrm{NUV}-r)$, because NUV traces the SFR and the r-band luminosity is related to the stellar mass. For the HI-selected population, comparison can be made directly of the volume-limited S_{HI} sample shown in Figure 3.8(b) with the corresponding result, uncorrected for internal extinction, shown in Figure 3.4(f) for the full α.40-SDSS-*GALEX*. As evident by inspection, in addition to a shift bluewards of the points in Figure 3.8(b), the dispersion about the mean relation is greatly reduced when the extinction correction is applied, and the Pearson correlation coefficient likewise improves from $r_P = -0.78$ to $r_P = -0.86$. This analysis indicates that the scatter in Figure 3.4(f) is substantially amplified by the lack of a correction for dust extinction. Other factors causing scatter include different SFHs, metallicities, as well as different population synthesis models and even IMFs [Gunawardhana et al., 2011]. However, dust extinction dominates among these factors. Furthermore, the star-forming S_{HI} galaxies have on average bluer $(\mathrm{NUV}-r)_0$ colors than the S_{opt} ones (median 1.42 versus 1.74 mag). Meanwhile, the tail of red and low SSFR galaxies in panel (a) disappears in panel (b), again reflecting the bias present in the HI-selected population. An additional result of the HI-selection is that the typical error bar in panel (b) is slightly smaller than

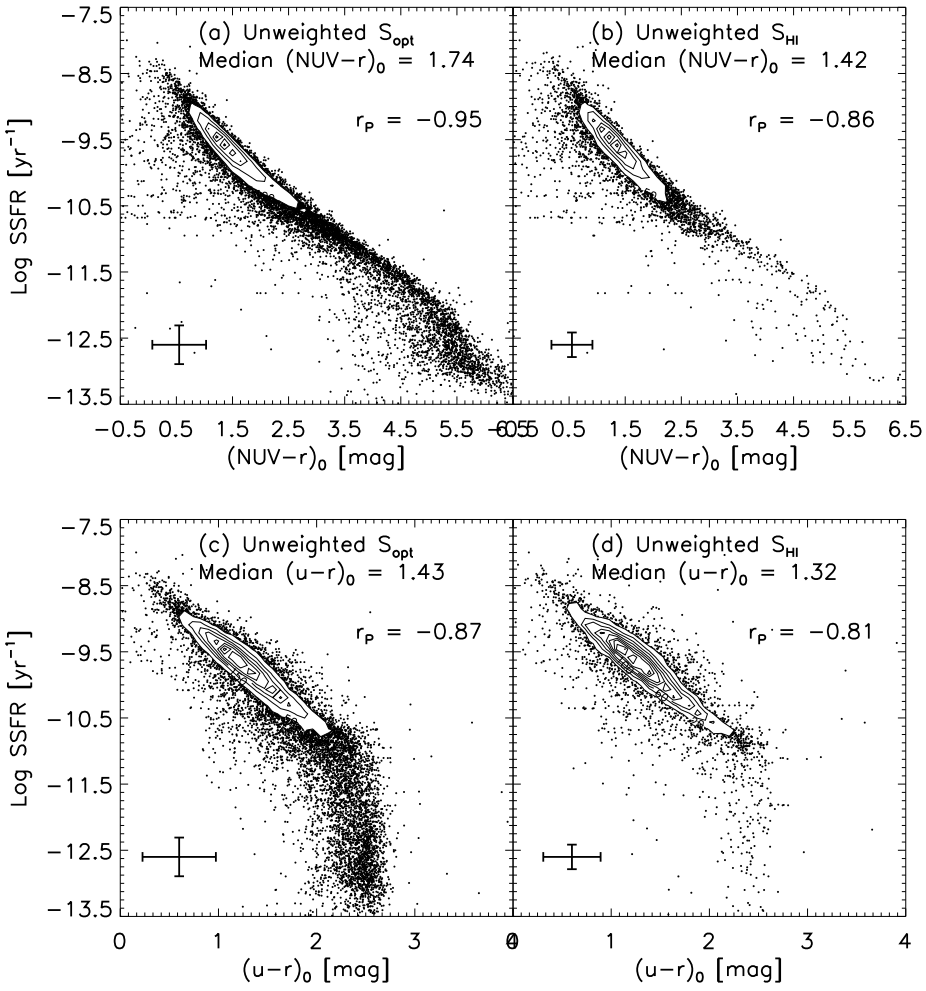

Figure 3.8: SSFR versus intrinsic colors, denoted by the subscript zero, after correction for internal extinction. The left column shows results for $S_{\rm opt}$ while the right shows $S_{\rm HI}$. Pearson correlation coefficients and typical error bars are also shown and the median intrinsic colors are indicated. In addition to the blueward shift of the distribution in panel (b) the scatter here is also greatly reduced compared to the similar plot shown in Figure 3.4(f) where no internal extinction correction has been applied. The $(\rm NUV - \it r)$ color breaks down the degeneracy of $(u - r)$ in the red range when inferring the SFH. The red and low SSFR tail in $S_{\rm opt}$ disappears in $S_{\rm HI}$. $S_{\rm HI}$ is on average intrinsically bluer than $S_{\rm opt}$ in both colors.

in (a).

The lower panels in Figure 3.8 examine the optical SDSS colors $(u-r)_0$. As discussed previously in §3.2.2, on average $\delta(u-r)/\delta(\mathrm{NUV}-r) \sim 0.6$. Figure 3.8(c) shows that galaxies with $\mathrm{SSFR} \lesssim 10^{-11}$ yr^{-1} have similar $(u-r)$ colors, forming a vertical tail in these plots; this red tail is much less pronounced in panel (d). The adoption of $(\mathrm{NUV}-r)$ as the color index breaks down the degeneracy of $(u-r)$ in the red range ($u-r \gtrsim 2.3$) when inferences on the SFH are inferred. Furthermore, the SSFR correlates more linearly with $(\mathrm{NUV}-r)_0$ than with $(u-r)_0$, e.g. $r_P = -0.95$ versus -0.87 in S_{opt}.

Given a simple assumption of the dust and stellar geometry, a well calibrated $\mathrm{IRX}-\beta$ relation (IRX, infrared-excess defined as $L_{\mathrm{TIR}}/L_{\mathrm{FUV}}$; β, the UV spectral slope) is sufficient to predict the A_{FUV} (tightly correlated with IRX) from the UV color (characterizing the UV spectral slope, β), in starburst galaxies [Calzetti et al., 1994]. However, the $\mathrm{IRX}-\beta$ relation in normal star-forming galaxies has a shallower slope with larger scatter [Salim et al., 2007]. This result may be due to differences in the SFH [Kong et al., 2004], or dust geometry [Cortese et al., 2006]. Therefore, the loci of galaxies on an A_{FUV} versus $(\mathrm{FUV}-\mathrm{NUV})$ plot give an indication of the dust extinction behavior.

Following this approach, the two samples S_{HI} and S_{opt} are compared in Figure 3.9, with results for S_{opt} on the left and S_{HI} on the right, both before and after applying the weight correction (see §3.4.1) in the upper and bottom rows respectively. The red dashed line corresponds to the fit to star-forming galaxies derived in Salim et al. [2007], based on a typical local SDSS-*GALEX* cross-matched catalog. Despite the large scatter, it is on average in close agreement with the distribution of the S_{opt} galaxies. Galaxies closer to the fit have overall

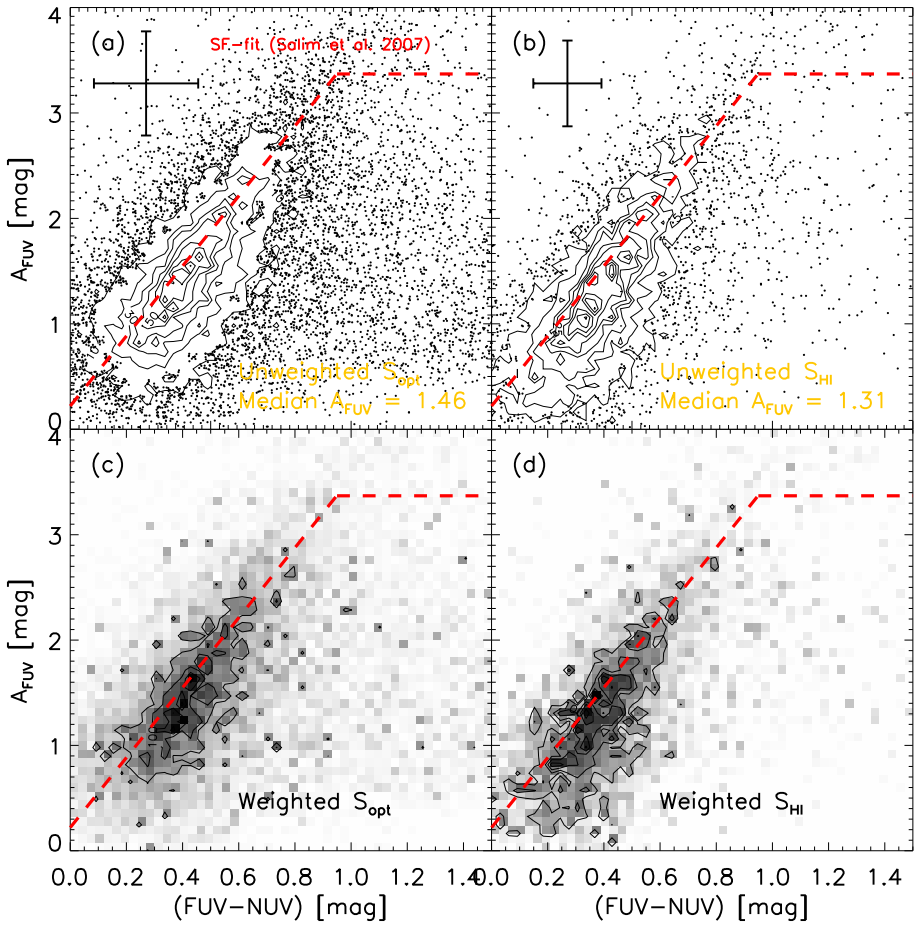

Figure 3.9: Computed $A_{\rm FUV}$ – UV color diagrams for $S_{\rm opt}$ in the left column and $S_{\rm HI}$ in the right column. The upper row shows the results for the galaxies themselves, without weighting while the bottom row shows results after applying the $V_{\rm sur}/V_{\rm max}$ weighting scheme. Typical error bars are shown in the corners of panels (a) and (b), together with the median $A_{\rm FUV}$ values listed for both the samples. The red dashed line corresponds to the fit to the star-forming galaxies derived by Salim et al. [2007], based on a typical local SDSS-*GALEX* cross-matched catalog. It is in agreement with $S_{\rm opt}$. In contrast, the $S_{\rm HI}$ distribution is offset from the fit, with lower $A_{\rm FUV}$ at a fixed $({\rm FUV}-{\rm NUV})$ color, which may due to lower metallicity, different SFH, and/or dust geometry of the HI-selected galaxies.

higher weights so that the correlation appears to be slightly tighter in panel (c) than in (a). However, the distribution of the $S_{\rm HI}$ galaxies is offset from the fit in panels (b) and (d), toward the lower $A_{\rm FUV}$ side, i.e. for a given $({\rm FUV}-{\rm NUV})$

color, the HI-selected galaxies on average have lower extinctions. This result is also confirmed by the generally lower $A_{\rm FUV}$ of the $S_{\rm HI}$ sample overall, with a median value of 1.31 mag, relative to that of $S_{\rm opt}$, 1.46 mag. Such a deviation of the main trend from the SF-fit of Salim et al. [2007] suggests that the HI-selected galaxies have different SFHs or dust geometries.

Unfortunately, the metallicity of the stellar population is poorly constrained by the SED-fitting. Nevertheless, given the correlation between dust and metallicity [e.g. Draine et al., 2007], the lower extinction infers that the $S_{\rm HI}$ galaxies have lower metallicity. Besides the well-known mass-metallicity (gas-phase) relation [e.g. Tremonti et al., 2004], Mannucci et al. [2010] demonstrate that at lower $M_*(< 10^{10.9}{\rm M}_\odot)$, metallicity decreases sharply with increasing SFR, while at high stellar mass, metallicity does not depend on the SFR. Given the bias towards high SFR of the $S_{\rm HI}$ sample at a given M_* (see §3.4.2), the bias towards low metallicity and low extinction is expected. The gas-phase metallicity measures (oxygen abundance) from the MPA-JHU DR7 release [Tremonti et al., 2004] are available for 4211/7157 of the $S_{\rm HI}$ galaxies and 10311/16817 of the $S_{\rm opt}$ galaxies. In addition to the caveat of the small SDSS fiber aperture, the requirement of being an SDSS spectroscopic target may reduce the difference between the two subsets. The mean $12+\log(O/H)$ is only slightly higher among the $S_{\rm opt}$ galaxies (8.74) than in the $S_{\rm HI}$ galaxies (8.71). The overall lower extinction among the $S_{\rm HI}$ galaxies is consistent with the idea that HI-selected galaxies are relatively gas rich and less evolved, with more likely gas infall, lower SFE and metallicity, less dust and thus lower extinction.

Distribution in the intrinsic CMD

The bimodal distribution in the optical CMD [Baldry et al., 2004] has been interpreted as an evolutionary sequence, with the blue-cloud galaxies growing through mergers and the consumption of gas and later migrating to the red sequence. This evolutionary scenario also predicts that galaxies evolve from a state of low stellar mass, high SSFR and high HI fraction to the opposite. As discussed in §3.3.1, the HI fraction is lower in redder galaxies leading to the result that an HI-selected sample like $S_{\rm HI}$ is biased against red galaxies whereas those are commonly included in, and may even dominate, an optically-selected one like $S_{\rm opt}$. Here, we use the CMD to quantify this bias.

Figure 3.10 shows the CMDs of the $S_{\rm opt}$ (left panels) and the $S_{\rm HI}$ (right panels); before and after applying weight corrections in the upper and bottom rows respectively. In these plots, absolute magnitudes $(M_r)_0$ and $(u-r)_0$ colors are corrected for internal extinction as given by the SED-fitting with the prior applied. A similar CMD for the whole $\alpha.40$-SDSS population but without corrections can be found in Figure 7 of Haynes et al. [2011]. The dash-dotted curve is based on the best fit to the division of the red and blue populations derived by Baldry et al. [2004] but with shifts toward bluer colors and brighter M_r applied in the amount of the mean extinction of the $S_{\rm opt}$ sample.

As is obvious in panels (a) and (b), the red sequence is far more pronounced in $S_{\rm opt}$ than in $S_{\rm HI}$. Among the $S_{\rm opt}$ galaxies, only 68% lie on the blue side of the division, whereas the percentage of blue galaxies in the HI-selected $S_{\rm HI}$ population is as high as 84%. The small population of 'red' galaxies with HI represents candidate objects which (i) have recently migrated onto the red sequence retaining some residual gas, or (ii) will transit back to the blue cloud via late gas

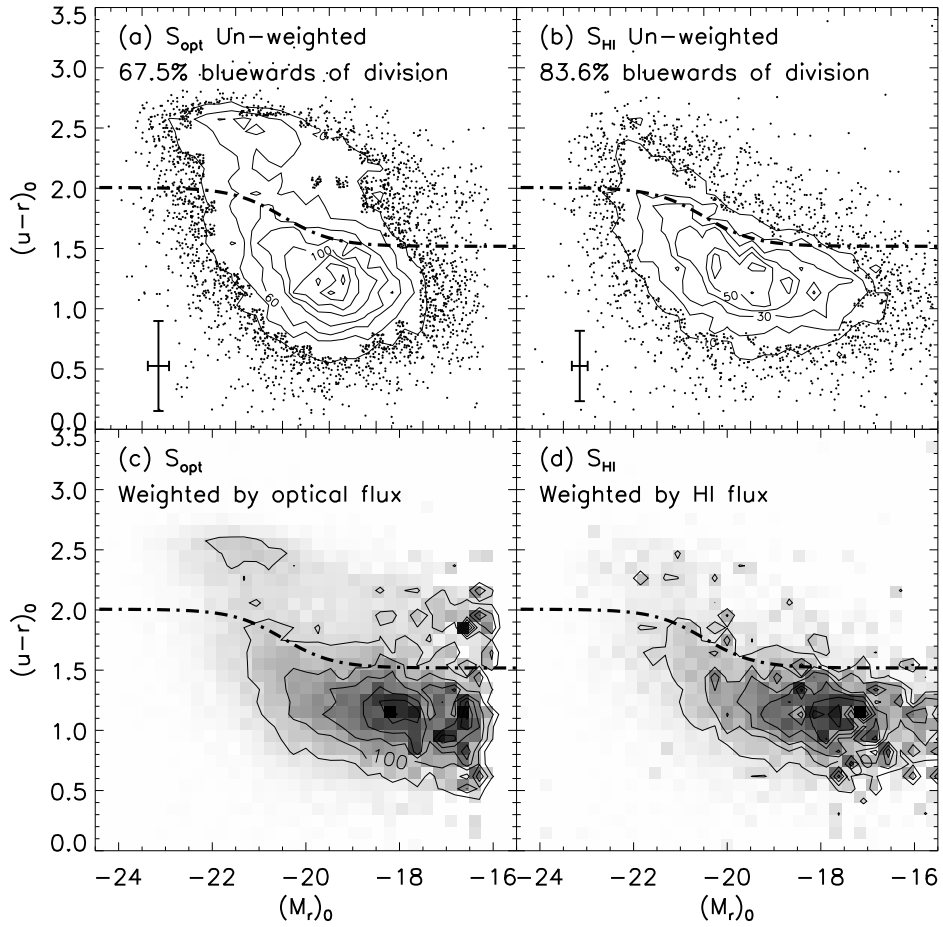

Figure 3.10: Intrinsic optical color-magnitude diagram of $S_{\rm opt}$ (left panels) and $S_{\rm HI}$ (right panels); before (upper) and after (lower) applying the $V_{\rm sur}/V_{\rm max}$ weight correction. The dash-dotted curve is derived in Baldry et al. [2004] as the best fit to the division of red sequence and blue cloud, shifted for the extinction corrections. Typical error bars including the uncertainties in the extinction corrections are plotted in the lower left corner of panels (a) and (b). The bimodel distribution is more evident in the $S_{\rm opt}$ representations; colors become generally bluer in fainter galaxies for both populations. The weighted panels better represent the luminosity function, which predicts more faint galaxies relative to the bright ones in the blue cloud. However, a second peak of number density at the faint end is seen on the red sequence, which suggests a diversity of SFH within the dwarf galaxies. A higher percentage of galaxies lie bluewards of the division in $S_{\rm HI}$ (84%) relative to $S_{\rm opt}$ (67.5%). HI surveys such as ALFALFA are highly biased against red sequence galaxies.

re-accretion [Cortese and Hughes, 2009]. Note that most of the red HI-bearing galaxies optically luminous. The HI mass of the faint red galaxies is usually so low that their HI line flux densities are below the sensitivity limit of ALFALFA.

In the $V_{\rm sur}/V_{\rm max}$ weight corrected diagrams (panels c and d), the peaks of number density shift to fainter $(M_r)_0$ in both samples. Galaxies densely occupy the faintest $(M_r)_0$ bins, especially in the $S_{\rm opt}$ sample. This result is consistent with the optical luminosity function of the blue population [Baldry et al., 2004]. A peak of the number density on the red sequence around $(M_r)_0 \sim -21$ also coincides with the maxima of the luminosity function derived by Baldry et al. [2004]. However, a second peak appears on the red sequence at the faint end. Note that the data points in Baldry et al. [2004] also suggest a rise in number density in the faintest bins of the red sequence luminosity function (see their Figure 7), though those authors ignore these objects when they fit the Schechter function. In agreement with this, Hogg et al. [2003] reported a non-monotonic density trend along the red sequence, seen as a dip in the typical density for intermediate-mass red-sequence galaxies despite higher densities at higher and lower masses. Similar to the finding of a sudden broadening in the SSFR distribution faintwards of $M_B \sim -15$ [Lee et al., 2007], a sudden broadening in the color distribution faintwards of $(M_r)_0 \sim -16$ is seen in the $S_{\rm opt}$ sample. This increased spread suggests that, unlike the galaxies of intermediate mass in which the SF is mainly regulated by stellar mass and for which the blue population dominates in number, the gas in dwarfs can be easily removed so that SF suddenly quenches driving their migration onto the red sequence.

Figure 3.10(c) shows a CMD for an optically-selected population similar to Figure 2 of Baldry et al. [2004]. However, $S_{\rm opt}$ is limited to $cz < 15000$ km s^{-1}

whereas the low-redshift sample Baldry et al. [2004] studied has $1200\ \mathrm{km\ s^{-1}} < cz < 24000\ \mathrm{km\ s^{-1}}$. The imposition of the volume cut here clearly decreases the presence of luminous red galaxies; the local volume is dominated by blue star-forming galaxies. This effect is also enhanced by the additional UV selection applied to the S_{opt} sample.

The near-absence of the red sequence among the S_{HI} population is clear in panel (d); as we have noted before, a blind HI survey like ALFALFA is highly biased against red sequence galaxies. Additionally, in both populations galaxies appear to be bluer as their M_r gets fainter, though with large scatter. Such a trend is weaker but still visible after internal extinction corrections are applied. Therefore, the slope is not only due to extinction, but is intrinsic.

Besides comparing the CMDs of S_{opt} and S_{HI}, we can also study the impact of HI selection through an examination of the fraction of S_{opt} galaxies that are cross matched to $\alpha.40$. As was discussed in §3.4.1, 34% of the S_{opt} galaxies are cross-matched to the $\alpha.40$ catalog. However, we note that such a fraction is a lower limit of the HI-detection rate of optical-UV selected galaxies in $\alpha.40$, because some S_{opt} objects may be a shredded photometric object of a gas bearer while another piece is cross-matched to the $\alpha.40$ entry. The fraction of these objects should however not be large [see Haynes et al., 2011].

Figure 3.11 explores the fraction of the S_{opt} population included in the $\alpha.40$ within the CMD (left) and the SSFR–M_* diagram (right). In the left panel, the NUV-to-optical CMD with internal extinction corrections is color coded by the fraction of galaxies in the optically-selected S_{opt} sample which are also included in the $\alpha.40$; the contours trace the total number density of the S_{opt} galaxies. Clearly, an HI survey like ALFALFA is more efficient at detecting blue galaxies

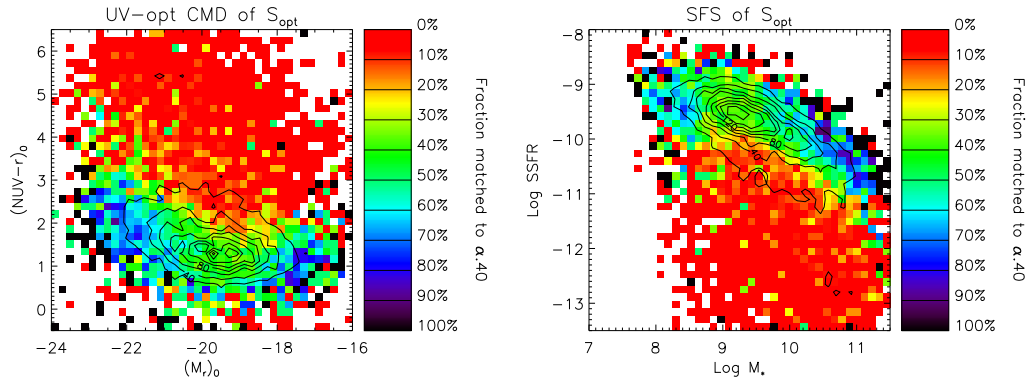

Figure 3.11: Diagrams with shade scale showing the fraction of galaxies in $S_{\rm opt}$ that are cross-matched to the $\alpha.40$ in each grid, which is close to the HI detection rate of the $S_{\rm opt}$ by $\alpha.40$. The $S_{\rm opt}$ number density is indicated by the contours. The cross-match fraction is the lower limit of the detection rate of $S_{\rm opt}$ galaxies by $\alpha.40$; its overall average is 34%. *Left panel* - Intrinsic UV-to-optical CMD of $S_{\rm opt}$. ALFALFA is more efficient in detecting blue galaxies, especially (i) the very bright and blue galaxies with huge gas reservoirs and (ii) the galaxies with the highest HI fraction lie on the faint end of the blue cloud. However, starting from the redder edge of the blue cloud, the cross-match rate drops below 10% and to even ∼0% throughout most of the red sequence. *Right panel* - SSFR versus stellar mass for the $S_{\rm opt}$ galaxies. The cross-match rate is the highest among the galaxies with high SSFRs at both high and low stellar mass ends and is close to the overall average throughout the high number density region along the star forming sequence. However, it drops to below ∼20% from the lower edge of the sequence to even ∼0% in the low SSFR regime.
(A color version of this figure is available in the online journal.)

than red ones. Especially at very bright end of the blue cloud (lower left corner), the detection rate is close to 100%. Furthermore, the ALFALFA population also detects the majority of optically faint blue galaxies with the detection rate again approaching ∼100% (lower right corner). The latter have the highest HI fractions (see also Figure 3.5). HI survey is most efficient in detecting galaxies with large diameter and high $M_{\rm HI}/L$ values [Garcia-Appadoo et al., 2009]. The general shape of the color scale variation above a cross-match rate of ∼40% resem-

bles that of the number density variation on the bluer side of the blue cloud. In contrast, starting from the red edge of the blue cloud and throughout the whole red sequence region, the rate of detection by ALFALFA drops below 10% and even to ∼0%. These results again demonstrate that HI-selection is highly biased against galaxies on the red sequence and furthermore, that such bias begins to become pronounced on the redder portions of what still is considered the blue cloud. The precise location of this limit to some extent reflects the 'fast' nature of ALFALFA (only 40 seconds integration per beam); a deeper survey of comparable solid angle would probe to lower gas fractions and hence deliver a higher cross-match rate.

Star-formation sequence

The scaling relation that the SFR increases with M_* among the $\alpha.40$ galaxies is demonstrated in §3.3.2 (Figure 3.4a). Figure 3.4(d) similarly shows the well confined star forming sequence in the SSFR–M_* diagram. Based on the ES–SDSS sample, West et al. [2009] suggested that the significant offset towards bluer colors, induced by HI-selection can be explained by enhanced recent bursts of star formation. Furthermore, rising SFHs, i.e. high $b-$parameter, are required to explain the colors of HI-selected galaxies bluer than $g - r < 0.3$, which may result from gas infall and enhanced SF subsequently. Here, we compare the distributions of the $S_{\rm HI}$ and $S_{\rm opt}$ galaxies, on and off the star-forming sequences to explore further the impact of HI-selection.

Figure 3.12 examines the SFR versus M_* scaling relation for the optical (left) and HI (right) selected samples. The upper row shows the individual galaxies while the lower traces the $V_{\rm sur}/V_{\rm max}$ weighted distributions. The cyan dashed

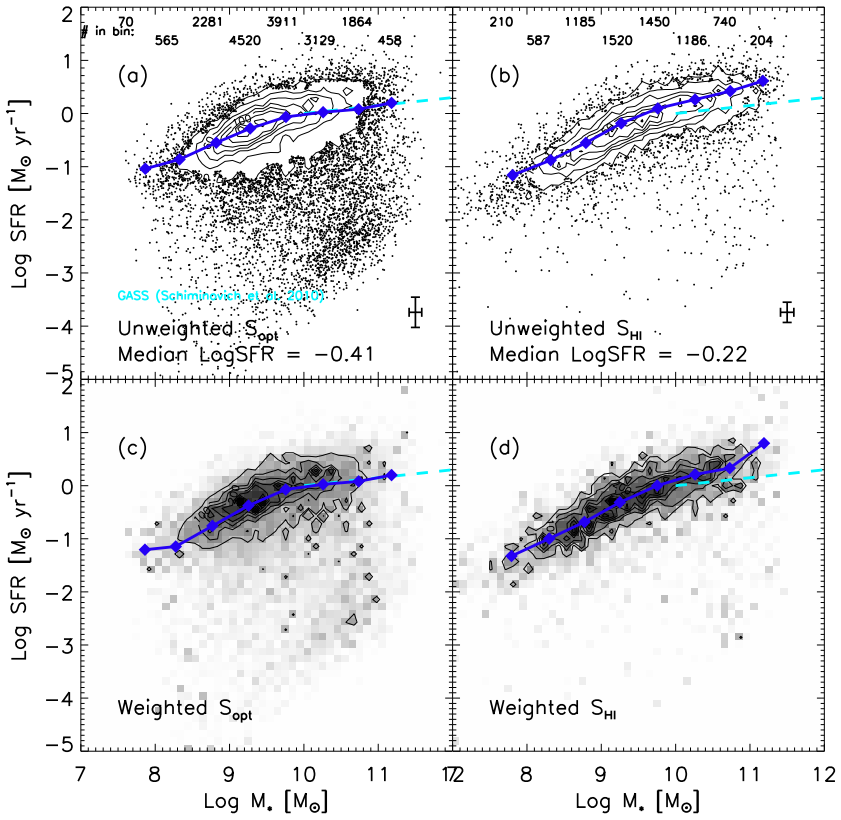

Figure 3.12: SFR versus M_* for the $S_{\rm opt}$ (left) and the $S_{\rm HI}$ (right) samples; upper panels show the individual galaxies while the low ones show the results of applying the $V_{\rm sur}/V_{\rm max}$ weighting. The cyan dashed lines above $M_* = 10^{10} M_\odot$ show the fit to this relation obtained by Schiminovich et al. [2010], based on the GASS sample. The blue diamonds and lines represent the corresponding $\log\langle {\rm SFR}\rangle$ of our datasets. The number of galaxies in each stellar mass bin is listed at the top in panels (a) and (b), together with the typical error bars plotted in the lower right corners. The median SFRs for both the samples are indicated. The GASS fit is consistent with the distribution seen for the $S_{\rm opt}$ sample but is systematically below the average of the HI-selected galaxies. The slope of the relation appears to steepen below $M_* \sim 10^{9.5} M_\odot$. The $S_{\rm HI}$ sample has a higher overall SFR value than the $S_{\rm opt}$ galaxies, and probes to slightly lower M_* ranges with generally lower SFRs. The data points reveal a concentration of massive low SFR galaxies below the main trend in $S_{\rm opt}$, which are largely absent from the $S_{\rm HI}$ population. An HI survey samples the star-forming population. The flattening of the trend in the lowest mass bin in the $S_{\rm opt}$ plots is artificial, due to the weight cut applied.

line at $M_* \geq 10^{10}\ M_\odot$ shows the fit to this relation obtained by Schiminovich et al. [2010], based on the high M_* GASS sample in all four panels:

$$\log\langle \mathrm{SFR}(M_*)\rangle = 0.15 \log M_* - 1.5,\ \ \log M_* > 10.0.$$

Like $S_{\rm opt}$, GASS is essentially an SDSS selected sample but only includes the high stellar mass end. The blue diamonds and lines represent $\log\langle \mathrm{SFR}\rangle$ derived for $S_{\rm opt}$ or $S_{\rm HI}$ in each stellar mass bin. Note these are different from the average trends in Figure 3.2 or Figure 3.4. The values are weighted averages in the weighted panels. The numbers of galaxies in each stellar mass bins are listed at the top of panels (a) and (b). Typical error bars are shown in panels (a, b).

The main distribution, consisting of the star forming galaxies, is associated with the parameter space inside the contours. In the un-weighted diagrams, the GASS fit is consistent with $S_{\rm opt}$ in the high mass range (panel a), but falls below the average of $S_{\rm HI}$ (panel b). This offset indicates that even when only the star forming sequence is considered, an HI-selected population has a higher SFR overall, because $S_{\rm HI}$ is not complete even within the blue population (see also Figure 3.11). Similarly, the blue diamonds in the weighted $S_{\rm opt}$ plot roughly coincide with the GASS fit (panel c). At the same time, the $\log\langle \mathrm{SFR}\rangle$ of $S_{\rm HI}$ galaxies becomes systematically larger than the GASS fit with increasing M_* (panel d).

Below the locus of star forming galaxies, the $S_{\rm opt}$ sample contains a large population of passive galaxies visible as the cloud of points extending to very low SFRs (panel a). However, this population is barely seen in the same diagram for the $S_{\rm HI}$ galaxies (panel b), i.e. an HI-selected sample is highly biased against non-star-forming galaxies.

Because $S_{\rm opt}$ is truncated at the low mass end due to the applied $V_{\rm sur}/V_{\rm max}$

weight limit (see §3.4.1), $S_{\rm HI}$ probes to lower M_* and thus lower SFRs on average. Despite this dwarf tail, the average SFR is still slightly higher in $S_{\rm HI}$. The median SFR is $0.4\ M_\odot\ {\rm yr}^{-1}$ in $S_{\rm opt}$ versus $0.6\ M_\odot\ {\rm yr}^{-1}$ in $S_{\rm HI}$. In the weighted plots, the correlation extending to the low M_* range is better illustrated (panel d). There is a hint of a change of slope in the SFR–M_* scaling relation below the SF transition mass $M_* \simeq 10^{9.5} M_\odot$ noted earlier (§3.3.2 and equation 3.8), with the slope at high M_* being shallower, especially evident in the $S_{\rm opt}$ plots. We note that the trend appears to flatten again in the lowest M_* bin in panel (c) because of the weight cut. To be more specific, at a given M_r, the bluer galaxies with higher SSFRs have on average lower stellar masses, according to the mass-to-light ratio versus color relation. Therefore, the uniform M_r cutoff applied on the $S_{\rm opt}$ sample makes the distribution of M_* extend to lower limits in higher SSFR bins; this effect is visible in the $S_{\rm opt}$ diagrams (Figure 3.12a, c; see also the right panel of Figure 3.11). This effect artificially results in the higher $\log\langle{\rm SFR}\rangle$ value in the lowest stellar mass bin. Furthermore, the lowest M_* bin only contains 70 galaxies, so that the average is even less reliable for statistical reasons. Such a sudden flattening is not seen within the $S_{\rm HI}$ population (panel d), which probes to lower M_* and with better sampling.

Figure 3.13 shows similar plots of the SSFR - M_* correlation. The cyan dashed line again denotes the $\log\langle{\rm SSFR}\rangle$ values tabulated in Schiminovich et al. [2010], derived from the high M_* GASS sample. The contoured region roughly represents the star forming sequence defined in Salim et al. [2007]. The red dashed line is the fit of the sequence to the blue galaxies (${\rm NUV} - r < 4$) only as derived by those authors for a typical local SDSS-*GALEX* cross-matched catalog, with

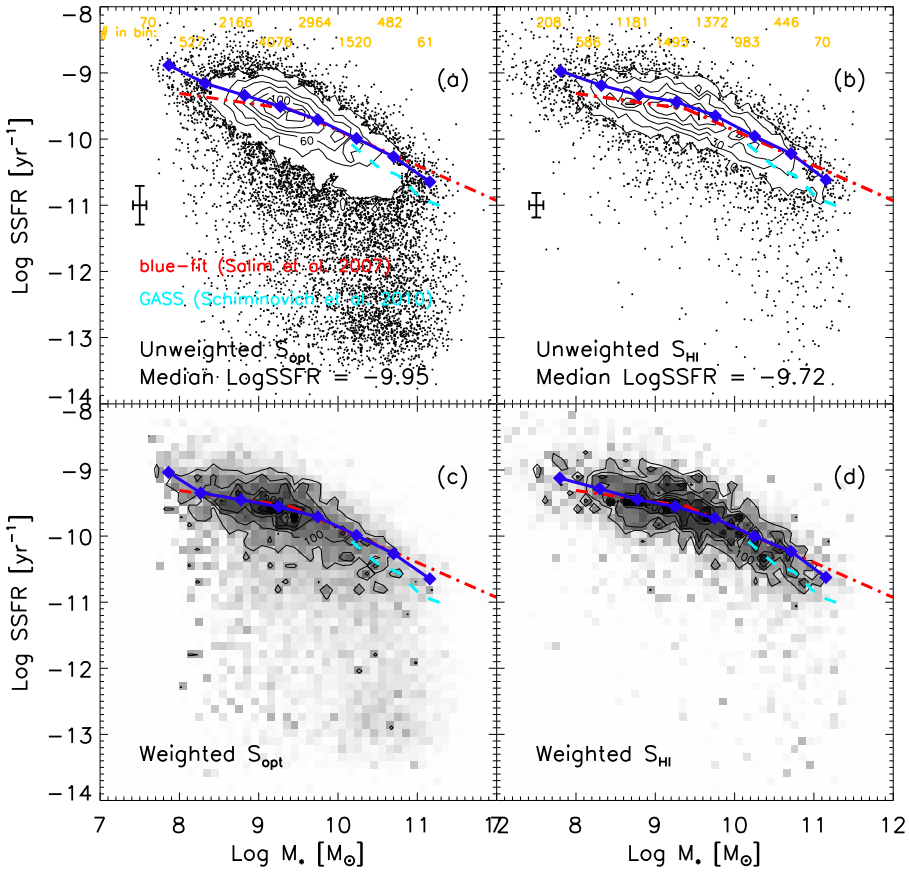

Figure 3.13: Similar diagrams of SSFR versus M_*. The numbers of galaxies in each stellar mass bin are listed, as well as the median SSFRs for both samples. The contours outlying the high number density region roughly trace the star forming sequence. The red dashed line shows the fit to such a sequence of the blue galaxies with $(\mathrm{NUV} - r) < 4$ [Salim et al., 2007], derived from a typical local SDSS-*GALEX* cross-matched catalog, with the majority confined to the stellar mass range $10^8 - 10^{10}\ M_\odot$. The blue diamonds and lines are obtained by applying the same color criteria to the $S_{\rm opt}$ or $S_{\rm HI}$ galaxies. The cyan dashed line comes from Schiminovich et al. [2010] based on the high M_* GASS sample; it well represents the contours of $S_{\rm opt}$, but lies systematically below the average of $S_{\rm HI}$. When only blue galaxies are considered in both samples, the discrepancy between the main trend of $S_{\rm opt}$ and $S_{\rm HI}$ is small. Furthermore, both agree well with the red dashed line. Galaxies selected by HI criteria have on average higher SSFRs than optically-selected ones. The breakdown of the star forming sequence above $M_* \sim 2 \times 10^{10} M_\odot$ is only evident among the $S_{\rm opt}$ sample, whereas the $S_{\rm HI}$ galaxies are strongly biased against massive and low SSFR galaxies.

the majority falling in the stellar mass range of $10^8 - 10^{10}\ M_\odot$:

$$\log \mathrm{SSFR} = \begin{cases} -0.17(\log M_* - 10) - 9.65, & \log M_* \leq 9.4 \\ -0.53(\log M_* - 10) - 9.87, & \log M_* > 9.4. \end{cases}$$

For comparison, the blue diamonds in Figure 3.13 are derived for our datasets but also considering only the blue galaxies ($\mathrm{NUV} - r < 4$). Note these fits are different from the one given as equation 3.8, shown in Figure 3.4(d).

Similar to what was seen in Figure 3.12, the S_{HI} population has on average higher SSFRs than the S_{opt} galaxies. The median SSFR is $10^{-9.95}\ \mathrm{yr}^{-1}$ for S_{opt} versus $10^{-9.72}\ \mathrm{yr}^{-1}$ for S_{HI}. The breakdown of the star forming sequence above stellar mass $\sim 2 \times 10^{10}\ M_\odot$ is only evident among the S_{opt} population, whereas comparably low SSFR galaxies are almost entirely absent from the S_{HI} sample. The GASS result agrees with the contours of S_{opt} above $10^{10}\ M_\odot$ (panel a and c), but lies below the average of S_{HI} (panel b and d).

In panel (c), the contours, associated with the high number density regions, that fall far below the main star forming sequence ($\log \mathrm{SSFR} < -11$) mostly show up only at the highest and lowest M_* ends, suggesting that the scatter in the SSFR distribution is larger at both M_* ends than in intermediate mass range. However, the effective M_r cutoff applied to S_{opt} inhibits us from a more convincing conclusion on the possible breakdown of the star forming sequence at the low mass end.

At the high M_* end, the averaged SSFRs are systematically higher in the S_{HI} population than in the S_{opt} one. However, when only blue galaxies are considered in either sample, the discrepancy between the two is reduced so that the trends indicated by the blue diamonds are comparable in both. The blue diamonds are in good agreement with the definition of the star forming sequence

in Salim et al. [2007], particularly for the high mass galaxies ($M_* \gtrsim 10^{9.4}\ M_\odot$) in the weighted plots, whereas the $S_{\rm HI}$ distribution is slightly offset to higher SSFRs in an un-weighted plot (panel b). In addition, note that we obtain a steeper slope than the blue fit in Salim et al. [2007] for low mass galaxies, even in the $S_{\rm opt}$ sample. Again because of the cutoff applied to $S_{\rm opt}$, the averaged SSFR value in the lowest mass bin is artificially high.

Finally, we inspect the cross-match rate of $S_{\rm opt}$ to $\alpha.40$ over the SSFR - M_* diagram in the right panel of Figure 3.11. The detection rate is the highest among galaxies with high SSFRs at both high and low M_* ends (above $\sim 60\%$) and is close to the overall average ($\sim\ 40\%$) throughout the high number density region along the star forming sequence. However, it drops to below ∼20% from the lower edge of the star-forming sequence, and the slope of the low match rate division, which corresponds to a cross-match rate of $\sim 25\%$ (yellow band in this plot), coincides well with that of the star-forming sequence. The SF properties of a galaxy have a significant impact on its likelihood of detection by an HI survey.

We again note that the blue diamonds in Figure 3.13(b) are slightly above the red dot-dashed line suggesting that not all star-forming galaxies are detected by ALFALFA. From the fact that the HI detection rate of the galaxies in the SF sequence is far from 100% (see right panel of Figure 3.11), one may naively conclude that not all star-forming galaxies contain HI. However, this conclusion is not necessarily correct. For example, given the beam size of the ALFA frontend (∼3.5′), confusion can contribute to a lower effective detection rate, e.g. when a close pair of star-forming HI bearing galaxies is unresolved. In fact, the red dot-dashed line is in excellent agreement with the blue diamonds in Figure 3.13(d), indicating that the mean trend of the star forming sequence can be well

reproduced by the $\alpha.40$ galaxies *after* volume correction. An HI-selected sample can effectively trace the average of the star forming sequence despite the non-detection of some star-forming galaxies by ALFALFA (which is by design a short-integration time survey). In order to predict the SSFR of an HI-selected sample, one should still use equation (3.8) rather than the average scaling relations derived in this section. The latter relations, as well as the star forming sequence derived in Salim et al. [2007] rely on additional information, e.g., UV magnitudes or emission lines, to define the star-forming galaxies. However, the $(\mathrm{NUV} - r) < 4$ (or similarly $\log \mathrm{SSFR} < -11$ yr^{-1}) is crude, since the SSFR generally decreases with increasing M_*. Furthermore, there are actually some very low SSFR galaxies detected in HI [e.g. Hallenbeck et al., 2012]. Direct adoption of the SF sequence defined in Salim et al. [2007] will overpredict the SSFR of an HI-selected sample.

3.5 The host halos of HI-selected galaxies

The results of the previous sections suggest that HI blind surveys detect in abundance the star-forming population but are highly biased against red sequence galaxies. Conversely, nearly all star-forming galaxies contain HI. Because ALFALFA is both wide area and sensitive, it samples the HI mass function over 4 orders of magnitude $7 < \log M_{\mathrm{HI}} < 11$ with a mean of 9.56 dex [Martin et al., 2010] and, while not as deep as the SDSS, both surveys probe the same range of M_r. The brightest and reddest galaxies are missing from $\alpha.40$, but an HI-selected sample provides an important perspective on the star forming sequence. While galaxies in rich clusters are well known to be HI deficient because of the secular evolutionary processes (ram pressure stripping, thermal viscosity, harassment),

HI-bearing galaxies dominate the extragalactic population in the low density field. As discussed in §3.3.2, the ALFALFA galaxies have, on average, lower SFEs, and equivalently therefore, longer t_R than the optically selected population. Both this work and the study of the lowest HI mass dwarf population by [Huang et al., 2012b] suggest that overall, the HI-selected population is less evolved and has higher SFR and SSFR but lower SFE and extinction than one selected by optical brightness or stellar mass.

Perhaps the most surprising result of the ALFALFA survey has been the detection of a large number of galaxies with very high HI masses, log $M_{\rm HI} > 10.3$, including a significant number with abnormally high HI gas fractions (for their stellar mass), dubbed the HIgh HI Mass (HIghMass) galaxies. The existence of this population, albeit rare, begs the question: how can such massive disks retain their huge gas reservoirs *without* forming stars? One explanation is that, while recent inflow of HI gas has taken place, SF in that gas has not yet been triggered. Alternatively, the overall low SFEs characteristic of the ALFALFA population may be explained by the semi-analytic models of galaxy formation in Boissier and Prantzos [2000], which predict that more extended disks with larger scale length and lower stellar surface density are associated with dark matter halos of high spin parameter λ. Selected examples of very massive but gas-rich galaxies have been studied in recent years [e.g., Portas et al., 2010], with most belonging to the extreme category of low surface brightness (LSB) galaxies known as the "crouching giants" [Disney and Phillipps, 1987] or "Malin 1 cousins" [Bothun et al., 1987, Impey and Bothun, 1997]. Their characteristic huge size, low optical surface brightness, star formation rate and low metal abundances may be explained by the large angular momentum and thus the low surface density of their ISM; star formation in such disks is suppressed ac-

cording to canonical star formation laws. However, we note that many of the HIghMass galaxies are not crouching giants. Instead of being quiescent objects like Malin 1, most of the HIghMass galaxies have blue disks and exhibit healthy on-going SF.

The discussion throughout this chapter is based on the scenario of hierarchical galaxy formation through mergers. Alternatively, cold mode accretion [Kereš et al., 2005] can build up gaseous galaxies rapidly at high redshift ($z > 1$). In the local universe volume probed by ALFALFA, it is likely that a large fraction of the gas accretion happens in a slower "hidden" mode, e.g., from the ionized hot corona or driven by the galactic-fountain process [Marinacci et al., 2010]. In a future work, we will investigate the angular momentum distribution in the HIghMass galaxies to investigate whether the majority of the HI in local gas-rich galaxies reaches the assembling halo through filaments of cold flow at high redshift or results from gradual cooling out of the hot corona.

According to the Boissier and Prantzos [2000] model, for a given halo mass, galaxies whose halos are characterized by different values of λ have similar stellar masses and current SFRs. However, galaxies in high λ halos exhibit higher gas fractions, lower metallicities and bluer colors than those in low λ halos. In this picture, the halo mass controls current absolute values while the spin parameter determines mainly the shape of the SFH. Blue colors indicate high SSFRs, i.e., suppressed SF in the past relative to the current SFR. Massive compact disks have the shortest time scales of gas infall, rapid early SF, and thus are dominated by old stars today. In contrast, the low mass galaxies reside in high λ halos can even have a rising SFH instead of an exponentially decaying one; their timescales of gas infall, as well as SF, are long. This picture agrees with the

downsizing scenario of galaxy formation (§3.3.2).

Meanwhile, the low stellar surface density found in gas-rich systems results in a weaker gravitational field, and, by extension, a lower mid plane gas pressure and a higher fraction of diffuse HI gas [Ostriker et al., 2010]. The model constructed by Fu et al. [2010], tracking both the atomic and molecular gas in disk galaxies, predicts a low HI to H_2 conversion efficiency in the high λ galaxies. The HI, stellar and SF properties of the $\alpha.40$-SDSS-*GALEX* galaxies, relative to the other local samples, therefore suggest that the HI-selected galaxies are biased towards ones in high λ halos, and thus are blue, inefficient in SF and less evolved. Nevertheless, they have comparable or even slightly higher current SFRs relative to the ones in the low λ halos with similar halo mass (see §3.4.2). In this section, we test this hypothesis.

3.5.1 Spin parameters derived from the Tully-Fisher relation

In their analysis, Boissier and Prantzos [2000] adopted the scaling properties derived by Mo et al. [1998], in the framework of the CDM scenario for galaxy formation. In this scenario, primordial density fluctuations give rise to dark matter halos of maximum rotational velocity $V_{\rm halo}$, with the mass of the halo $M_{\rm halo} \propto V_{\rm halo}^3$. Inspired by theoretical studies to break the degeneracy, a second parameter, the spin parameter λ , is introduced to describe the halo [e.g. Mo et al., 1998], defined as $\lambda = J|E|^{1/2}G^{-1}M_{\rm halo}^{-5/2}$, where J is the angular momentum and E is the total energy of the halo. Observationally, λ is seen to determine properties such as color, disk thickness and bulge-to-disk ratio [Hernandez and Cervantes-Sodi, 2006]. Within the halo, baryonic gas condenses later and forms

the stellar disk with mass M_* and characterized by an exponential surface density profile with disk scale length $r_{\rm d}$. Those authors also assumed that the density profile of the dark matter halo is isothermal and responsible for establishing the flat disk rotation curve $V_{\rm rot}$. Under the further assumptions that the potential energy of the galaxy is dominated by that of the halo and that it is a virialized gravitational structure, etc., Boissier and Prantzos [2000] related the quantities describing the halo to those describing the disk, and express the spin parameter as

$$\lambda = \frac{\sqrt{2} V_{\rm rot}^2 r_{\rm d}}{G M_{\rm halo}}. \tag{3.9}$$

See also Hernandez and Cervantes-Sodi [2006] for similar derivation of equation (3.9). The only unobservable quantity $M_{\rm halo}$ can be replaced by $M_{\rm baryon}/F$ where F is the baryonic fraction, or, alternatively, $M_*/F_{\rm d}$ where $F_{\rm d}$ is the stellar disk mass fraction.

Based on this framework Hernandez et al. [2007] analyzed the empirical λ distribution of samples taken from the SDSS. Because their sample lacked direct measures of $V_{\rm rot}$, those authors invoked the Tully-Fisher relation to infer $V_{\rm rot}$ from the disk luminosity. Furthermore, a disk mass Tully-Fisher relation and a constant disk mass fraction $F_{\rm d} = 0.04$ are assumed to eliminate the $M_{\rm halo}$ term. As a first approach for direct comparison with Hernandez et al. [2007], we repeat the method used in that work to derive the distributions, separately, of the λ spin parameter for the the HI-selected $S_{\rm HI}$ and the optically-selected $S_{\rm opt}$ galaxies. We adopt the λ estimator proposed by Hernandez et al. [2007],

$$\lambda = 21.8 \frac{r_{\rm d}[{\rm kpc}]}{(V_{\rm rot}[{\rm km\ s^{-1}}])^{3/2}}. \tag{3.10}$$

Hernandez et al. [2007] adopted the R-band Tully-Fisher relation derived by Barton et al. [2001] to assign $V_{\rm rot}$ to the observed galaxies; since this relation is

valid only over the absolute magnitude range $-20 > M_R > -22.5$, they restrict their analysis to that range. To minimize errors due to internal extinction, they trim the sample to leave only spiral galaxies [Park and Choi, 2005] having $b/a > 0.6$.

The R-band luminosity is inferred from the SDSS bands based on Lupton (2005),

$$(M_R)_0 = r_0 - 0.2936 \times (r-i)_0 - 0.1439.$$

We applied the same absolute magnitude cut $-20 > (M_R)_0 > -22.5$ to both the $S_{\rm HI}$ and the $S_{\rm opt}$ samples. Within our distance range, the SDSS is volume limited to $M_r \sim -19$ mag (Figure 3.6a). We also require that the r-band light profile should be better fitted by an exponential profile than a deVaucouleurs profile to be sure we were including mainly disk galaxies. Since Hernandez et al. [2007] ignored internal extinction but we have corrected for it using the SED fitting estimate of A_R, the b/a requirement in our case is less strict, $b/a > 0.35$. Such a cut is adopted so that the b/a distribution is close to being flat above 0.35. Like Hernandez et al. [2007], we convert the SDSS r-band axial ratio to inclination i,

$$\cos^2 i = \frac{(b/a)^2 - q_0^2}{1 - q_0^2},$$

adopting an intrinsic axial ratio of the disk of $q_0 = 0.18$ as proposed by Courteau [1997]. We note, however, that since that study was restricted to a relatively small number of Sb-Sc galaxies, a more conventional value of $q_0 = 0.2$ may be more appropriate (see §3.5.2).

First, we confirm that the TF relation Hernandez et al. [2007] used is systematically consistent with the $S_{\rm HI}$ galaxies, albeit with significant scatter. The HI line width of the $S_{\rm HI}$ galaxies, W_{50}, is converted to $V_{\rm rot}$ through $V_{\rm rot} =$

$(W_{50}/2/\sin i)$, where the small broadening effect (~ 5 km s^{-1}) of turbulence and non-circular motions on the observed HI linewidths is ignored. The average trend evident between $(M_R)_0$ and $V_{\rm rot}$ agrees with the relation, i.e., applying such a TF relation should have little effect on the mean value of the λ distribution. The difference of the mean λ value derived here as compared with that derived next in §3.5.2 will be mainly due to the different assumptions of the baryon fraction F.

Next, we obtain the λ distributions of the $S_{\rm HI}$ and the $S_{\rm opt}$ samples, according to equation (3.10), and following Hernandez et al. [2007], we confirm that they both are well fit by a lognormal function:

$$P(\lambda_0, \sigma_\lambda; \lambda)\mathrm{d}\lambda = \frac{1}{\sigma_\lambda\sqrt{2\pi}} \exp\left[-\frac{\ln^2(\lambda/\lambda_0)}{2\sigma_\lambda^2}\right] \frac{\mathrm{d}\lambda}{\lambda}.$$

The best fit parameters are $\lambda_0 = 0.0525$, $\sigma_\lambda = 0.422$ for the $S_{\rm HI}$ distribution of the HI selected galaxies $S_{\rm HI}$ and $\lambda_0 = 0.0489$, $\sigma_\lambda = 0.446$ for the SDSS-selected $S_{\rm opt}$ distribution. Because we correct M_R for extinction, our λ_0 value is slightly below the value found by Hernandez et al. [2007], $\lambda_0 = 0.0585$. While suggestive, this difference of λ_0 between the two samples $S_{\rm HI}$ and $S_{\rm opt}$, *under the assumption of a constant disk-to-total mass fraction* $F_{\rm d}$, is small. The various cuts and selection effects applied to both samples, e.g. detected in UV, better fit by an exponential profile, small dynamic range of M_r, may have already minimized the possible difference in λ_0 within the full sample. Given that the remaining galaxies in the $S_{\rm HI}$ sample are brighter on average than those in the $S_{\rm opt}$ sample, i.e., $V_{\rm rot}$ is higher on average, the slightly higher λ_0 found by this analysis is due to the fact that $S_{\rm HI}$ galaxies have on average larger $r_{\rm d}$ values (see equation 3.10). HI selection instills a bias towards more extended galaxies.

3.5.2 λ distribution of the parent population

The SDSS galaxies analyzed by Hernandez et al. [2007] lack direct measurements of $V_{\rm rot}$, whereas the $\alpha.40$–SDSS–*GALEX* sample has homogeneous W_{50} measurements for all its galaxies. We hence improve the derivation of the λ distribution for all the $\alpha.40$–SDSS–*GALEX* galaxies in this section. Assuming that an HI-selected sample has little contamination from galaxies which are not disk dominated, we drop the requirement of a higher probability of an exponential fit and adopt an intrinsic $q_0 = 0.2$. Because HI line widths are available, we no longer rely on the Tully-Fisher relation to infer $V_{\rm rot}$, and for that reason, the $(M_r)_0$ limit is also dropped. Most importantly, we estimate λ directly from equation (3.9) assuming a non-constant F to derive $M_{\rm halo}$.

Following Hernandez et al. [2007], the preceding assumes that all halos are associated with the same disk mass fraction $F_{\rm d} = 0.04$. However, based on abundance matching between the observed stellar mass function and dark matter halo mass function derived from CDM simulations, it is quite well established that $F_{\rm d}$ is not a constant [Behroozi et al., 2010, and references therein]. Instead, the distribution of $F_{\rm d}$ as a function of $M_{\rm halo}$ peaks around $M_{\rm halo} \sim 10^{12}\ M_\odot$ [e.g. Guo et al., 2010], i.e., low mass galaxies, corresponding to $M_* \lesssim 10^{10.5}\ M_\odot$, retain fewer baryons as their halo mass declines. The trend turns over above $M_* \sim 10^{10.5}\ M_\odot$. Based on the $\alpha.40$ catalog, Papastergis et al. [2011] have studied how galaxies with different $V_{\rm rot}$ populate dark matter halos, by applying similar abundance matching to the velocity width function, under the assumption that rotational velocity well traces the dark matter mass. We adopt the $V_{\rm halo}$–$V_{\rm rot}$ relation from Table 1 of Papastergis et al. [2011], assuming $V_{\rm halo,max} = 360\ {\rm km\ s^{-1}}$. The resulting $V_{\rm halo}$ is converted into the virial mass of the halo following the

simulation result of Klypin et al. [2011]: $V_{\rm halo} = 2.8 \times 10^{-2} (M_{\rm halo} h)^{0.316}$. For the disk scale length $r_{\rm d}$, we use that measured by the SDSS pipeline in the r-band,

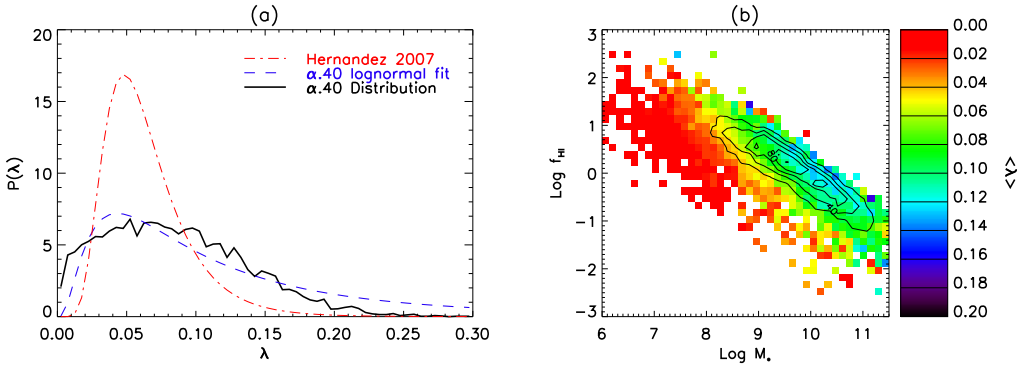

Figure 3.14: Spin parameter λ distribution obtained by assigning the $M_{\rm halo}$ through a $V_{\rm rot}$–$V_{\rm halo}$ relationship. *Panel (a)* - The black solid line is the normalized PDF of the λ distribution of 7459 galaxies from the $\alpha.40$–SDSS-*GALEX* sample. The blue dashed line is the best lognormal fit to the distribution. The red dash-dotted line is the lognormal fit to a sample of spiral galaxies from the SDSS, assuming constant baryonic mass fraction $F = 0.04$ [$\lambda_0 = 0.0585$ Hernandez et al., 2007]. The λ distribution of the $\alpha.40$ galaxies has a higher mean λ (0.0852) and a wider dispersion, mainly arising from the adopted distribution of baryonic fraction. *Panel (b)* - $f_{\rm HI}$ vs. M_* diagram color coded by the mean λ values of the galaxies in each grid. Below $M_* \sim 10^{10.5}\,M_\odot$, $< \lambda >$ increases with increasing $f_{\rm HI}$ at a given M_*, but remains almost constant along constant $M_{\rm HI}$ lines. Such a trend reflects the adopted variation of F: HI-selected gas-rich galaxies favor high λ halos.
(A color version of this figure is available in the online journal.)

Among the 9417 $\alpha.40$–SDSS-*GALEX* galaxies, 1829 are dropped because of the adopted axial ratio cut ($b/a > 0.35$ as in §3.5.1), and a further 130 are dropped because they lie outside of the valid range of the $V_{\rm rot}$–$V_{\rm halo}$ relation ($16\ {\rm km\ s^{-1}} < V_{\rm rot} < 431\ {\rm km\ s^{-1}}$). In the end, λ values are estimated for 7458 $\alpha.40$ galaxies; their distribution is shown in the Figure 3.14(a). The black solid line traces the normalized PDF for the $\alpha.40$ galaxies. The red dash-dotted line in Figure 3.14(a) shows the best log-normal fit with $\lambda_0 = 0.0585$ and $\sigma_\lambda = 0.446$ from Hernandez et al. [2007] and the blue dashed line is the best fit to the $\alpha.40$ galaxies with $\lambda_0 = 0.0929$ and $\sigma_\lambda = 0.875$. Hernandez et al. [2007] noted that values they

found for both λ_0 and σ_λ are in good agreement with results from cosmological simulations. However, the λ distribution of the $\alpha.40$-SDSS-*GALEX* galaxies has a mean well above this value, $\lambda = 0.0852$. Furthermore, the distribution for the $\alpha.40$–SDSS–*GALEX* sample has a much wider dispersion than the previous result, arising mainly from the fact that we adopt different F values according to the $V_{\rm rot}$, rather than treating it as a constant. As a result, the distribution of spin parameters of the HI-selected population is no longer well fit by a lognormal function. The KS statistic implies that the probability that the λ distribution for the HI-selected population is drawn from the same underlying distribution with a PDF of the best-fit lognormal function with $\lambda_0 \sim 0.0929$ is negligible.

The technique of assigning $M_{\rm halo}$ is valid only in a statistical sense, rather than as a concrete measure for individual galaxies. For this reason, we look only for a general trend in the dependence of the luminous component on the λ of the halos. Figure 3.14(b) shows a $f_{\rm HI}$–M_* diagram similar to Figure 3.2(c), but color coded by the mean λ value of galaxies in each grid. The black contours outline the distribution of the 7458 $\alpha.40$ galaxies in the high number density region. A trend is evident that, in a given M_* bin, the gas rich galaxies with higher $f_{\rm HI}$ on average reside in halos with higher λ. Meanwhile, along lines of constant $M_{\rm HI}$ (straight lines with slope of '-1' in the $f_{\rm HI}$–M_* diagram), $\langle\lambda\rangle$ barely changes with increasing M_*. Taking into account the mean scaling relation defined by the $\alpha.40$ galaxies (blue diamonds in Figure 3.2c) relative to the similar relations obtained for other samples, this result reinforces the hypothesis that the HI-selected galaxies favor high λ halos. The $f_{\rm HI}$–M_* relations confined by the 'HI-normal' or the 'outside Virgo' galaxies in Figure 3.2(c) are close to the well accepted $\lambda \sim 0.05$ region, the yellow band in Figure 3.14(b).

We note that such a clear trend is only weakly due to the overall larger $r_{\rm d}$, i.e., lower surface brightness, which the more gas-rich galaxies have in a given M_* bin, but is instead largely due to the rapidly increasing $F = (M_{\rm HI}+M_*)/M_{\rm halo}$ with $M_{\rm HI}$ in a given M_* bin. However, it is known that the increase in F with $M_{\rm halo}$ is reversed near $M_* \sim 10^{10.5}\ M_\odot$. In fact, the variation of $\langle\lambda\rangle$ along the $f_{\rm HI}$ axis disappears around $M_* \sim 10^{10.5}\ M_\odot$ in Figure 3.14(b). In addition, we note that within the luminosity range of $-20 > (M_R)_0 > -22.5$, the stellar disk fraction, $F_{\rm d}$, inferred by this method spreads over a range with a median of 0.04; the $M_{\rm halo}$–F relation crosses the turnover around $(M_R)_0 \sim -21.5$. Despite the systematic variation of $F_{\rm d}$ we adopt, the median is consistent with the assumption followed in §3.5.1

Because the $V_{\rm rot}$–$V_{\rm halo}$ relation we have used is less constrained at the highest masses, it barely reproduces the trend of decreasing F with $M_{\rm halo}$ above $M_* \sim 10^{10.5}\ M_\odot$. Alternatively, we can estimate the $M_{\rm halo}$ following the M_*–$M_{\rm halo}$ relation [Guo et al., 2010],

$$\frac{M_*}{M_{\rm halo}} = 0.129 \times \left[\left(\frac{M_{\rm halo}}{10^{11.4}\ M_\odot} \right)^{-0.926} + \left(\frac{M_{\rm halo}}{10^{11.4}\ M_\odot} \right)^{0.261} \right]^{-2.440}.$$

The fit is valid in the $M_{\rm halo}$ range of $10^{10.8}$ to $10^{14.9}\ M_\odot$, and thus describes better the most massive $\alpha.40$ galaxies. However, it cannot constrain the low mass HI-bearing halos. As expected, such a M_*–$M_{\rm halo}$ relation, with a turnover $M_{\rm halo} \sim 10^{12}\ M_\odot$, produces a similar trend of the $\langle\lambda\rangle$ variation as seen in Figure 3.14(b) for galaxies with $M_* \lesssim 10^{10.5}\ M_\odot$. However, for the most massive galaxies with $M_* \gtrsim 10^{10.5}\ M_\odot$, such a trend disappears, and galaxies with similar M_* have similar λ, regardless of their $f_{\rm HI}$. Meanwhile, $\langle\lambda\rangle$ turns over to decrease with increasing M_* with approximately constant $M_{\rm HI}$.

As a result, the pattern of colors in Figure 3.14(b) predicts that the most gas

rich ones with M_* near $10^{10}\ M_\odot$ should be associated with halos with the highest λ parameters. We are testing this prediction by studying the stellar, gas and dark matter components of a sample of very high HI mass ($M_{\rm HI} > 10^{10}\ M_\odot$), high gas fraction (for their stellar mass) galaxies, the HIghMass sample. Visual inspection of the HIghMass galaxies shows that the ones with intermediate M_* shows the strongest color gradient (bluer in outer regions), as predicted for high λ galaxies [Hernandez and Cervantes-Sodi, 2006]. Future work will constrain the spin parameters using velocity fields derived from HI synthesis maps for 20 of the HIghMass galaxies. Furthermore, the HI distributions and sites of star formation will be examined to yield more detail on the SFL and possible mechanisms which inhibit the formation of stars in these massive HI disks.

The HI, stellar and SF properties of the ALFALFA population as exemplified by the $\alpha.40$-SDSS-*GALEX* galaxies suggest that the HI-selected population is biased towards extended disks which reside in high λ dark matter halos. As such, their disks are currently forming stars but in an inefficient manner. Despite the low SFE, such galaxies can have comparable or even slightly higher current SFRs relative to the ones in the low λ halos of similar halo mass (see §3.4.2). This combination of on-going star formation and inefficiency in the conversion of gas into stars causes their disks to be extended, blue and of low metallicity, suggestive of their being less evolved. Remembering too that the $\alpha.40$ galaxies are among the least clustered population [Martin et al., 2012], we are reminded that these systems likely follow a quite different, quiescent evolutionary history relative to galaxies residing in higher density volumes. Although the details of the involved processes still elude us, the study of the ALFALFA population strongly suggests that where a galaxy is born and resides determines to a large extent how and when it converts its gas into stars.

3.6 Conclusion

Given the importance of proposed future extragalactic HI surveys at high redshift by the SKA, it is critical to develop a full understanding of the characteristics of gas rich galaxies at the present epoch. ALFALFA is an on-going blind HI survey, for the first time providing a full census of HI-bearing objects over a cosmologically significant volume of the local universe. Building on the $\alpha.40$ catalog [Haynes et al., 2011], we use the corresponding photometry available from the SDSS DR7 and *GALEX* GR6 catalogs to explore the population of galaxies detected by ALFALFA. The combined $\alpha.40$-SDSS-*GALEX* sample includes 9417 galaxies. SED-fitting to the seven UV and optical bands yields the stellar properties of the HI-selected galaxies, including their stellar masses, SFRs and internal extinctions. The lack of a correction for internal extinction can lead to systematic underestimates of the optical luminosities and SFRs. In order to reduce the overestimate of internal extinction and thus the SFR with decreasing M_* while still accounting for the effect of dust in these mostly disk-dominated systems, we apply a prior distribution of τ_V in the fitting process. Although extinction is even more of an issue at the short wavelengths, the addition of photometry in the UV bands is critical to the diagnostic power of the SFH because the UV measures break the degeneracy evident in optical-only colors, particularly among the red sequence galaxies.

ALFALFA offers a complete statistical sampling of the full range of $M_{\rm HI}$ and M_*, from the most massive giant spirals with $M_{\rm HI} > 10^{10}\ M_\odot$ to the lowest HI mass dwarfs with log $M_{\rm HI} < 10^{7.5}\ M_\odot$, thereby providing a firmer basis for the derivation of the fundamental scaling relations linking the global properties. First, we confirm the existence of the relations which have been found in typical

local optical-UV catalogs [e.g. Salim et al., 2007]. For example, (1) SFRs increase but SSFRs decrease with increasing M_*, with different slopes in the high and low M_* ranges, with the transition occurring at $M_* \sim 10^{9.5}\ M_\odot$; (2) the SSFR is tightly correlated with the $(\mathrm{NUV} - r)$ color, especially after the latter is corrected for internal extinction. Second, we investigate similar relations involving the HI mass. For example, (3) SFRs also increase but SSFRs decrease with increasing $M_{\rm HI}$, though with larger scatter. The HI gas contributes a significant fraction of the baryons in HI-selected galaxies, and their SFRs show a good correlation with $M_{\rm HI}$, suggesting that a global, atomic, volumetric SFL applies in HI-selected systems. (4) The HI fraction, $f_{\rm HI} \equiv M_{\rm HI}/M_*$, nicely correlates with M_*, but a change in the slopes of the relation is evident near $M_* \sim 10^9\ M_\odot$. (5) Galaxies with bluer colors in general have higher $f_{\rm HI}$. (6) The star formation efficiency, $\mathrm{SFE} \equiv \mathrm{SFR}/M_{\rm HI}$, mildly increases with stellar mass with a slightly steeper relation for $M_* \lesssim 10^{9.5}\ M_\odot$. In §3.3.1, we give the best linear fits to the principal scaling relations among the ALFALFA population, including the $M_{\rm HI}$–M_* and SSFR–M_* correlations, as well as the fundamental planes of $f_{\rm HI}$–$(\mathrm{NUV} - r)$–μ_*, etc. In particular, we argue that Equation (3.2-3.7) provides the most robust predictor based on optical properties of the detection rate by future HI line surveys with the SKA and its pathfinders.

Besides the scaling relations themselves, the combined $\alpha.40$-SDSS-*GALEX* dataset, as a large and homogeneous sample with HI measures, enables the quantitative appraisal of the scatter in relations and a deeper understanding of the role HI plays in the galaxy evolution. In particular, the decreasing $f_{\rm HI}$ with increasing M_* is related to the star-forming sequence identified in the SSFR–M_* diagram, or the evolutionary tracks of galaxies on the CMD, i.e. as galaxies assemble their stellar masses, they evolve gradually to relatively red and gas

poor regimes, and also show lower SSFRs. Furthermore, *only* evident among the low mass galaxies ($M_* \lesssim 10^{9.5}\ M_\odot$), the galaxies with higher $f_{\rm HI}$ on average also have higher SSFR *in a given M_* bin*. Similarly, within a given M_r bin, higher $f_{\rm HI}$ on average indicates bluer ($\rm NUV - r$) color. However, the corresponding trend that the HI-rich galaxies are more likely to be blue starburst galaxies with high SSFRs is weak among the high mass galaxies, i.e., the regulation of SF by HI is weaker in more massive systems. Similarly, the dispersion of the color distribution in a given M_r bin and the dispersion of the SSFR distribution in a given M_* bin are both at a minimum near $M_* \sim 10^{9.5}\ M_\odot$, and both increase at masses lower than that. It appears that SF is no longer regulated principally by the stellar mass in low mass systems. In their shallow potential wells, gas can be easily removed so that the SF quenches causing the galaxy to migrate onto the red sequence.

We also focus on the nature of the population detected by the ALFALFA survey, in the context of populations better understood through observations at other wavelengths, e.g. optical or UV. The $\alpha.40$ galaxies on average have higher HI fractions in a given stellar mass bin, compared to the optically-selected samples, with an overall average of $f_{\rm HI} \sim 1.5$. 95.6% of the $\alpha.40$-SDSS-*GALEX* galaxies have $(\rm NUV - r) < 4$ and belong to the blue cloud on a UV-to-optical CMD. The red ALFALFA detections include early type galaxies with quenched SF but unusually high HI masses, suggesting a recent acquisition of HI. The very blue HI-rich galaxies may be attributed to a SFH that steadily rises to the present day with little integrated past SF. The SFEs of the HI-selected galaxies are lower on average, or equivalently, their gas depletion timescales are longer (average $t_R = 8.9$ Gyr), compared to the high stellar mass galaxies included in the GASS survey [Schiminovich et al., 2010]. Given the fact that the overall SFRs of $\alpha.40$

galaxies are even higher than those in GASS at a given M_*, the low SFEs found for HI-selected galaxies are caused by their high HI masses rather than by lower SFRs. This result is consistent with the idea that HI-selected sample is biased towards the most gas-rich galaxies and that the SFE is low in HI-dominated systems. A bottleneck may exist in the HI to H_2 conversion, or the process of SF from H_2 may obey an unusual SFL with low efficiency in the very HI-dominated galaxies. For a given $(\mathrm{FUV} - \mathrm{NUV})$ color, HI-selected galaxies have on average lower extinctions, suggesting that they have different SFHs or dust geometries.

To quantify better the bias of the HI-selected population relative to the optically-selected galaxies, we constructed two volume-corrected control samples, starting from the $\alpha.40$ and the SDSS DR7 catalogs, which we designate S_{HI} and S_{opt} respectively. The HI-selected S_{HI} sample is found to be biased against red-sequence galaxies as well as massive but low SFR, low SSFR galaxies. However, if only the blue cloud galaxies with $(\mathrm{NUV} - r) < 4$ are considered, both samples define similar SF sequences, i.e., an HI survey well samples the star forming population. For the SDSS-selected volume-limited S_{opt} sample, the rate of detection by ALFALFA decreases towards redder colors. Virtually all very blue S_{opt} galaxies at both the high and low stellar mass ends are detected by ALFALFA; however, among the blue population, the HI detection rate drops to $\sim 40\%$ throughout the high number density region along the SF sequence. At the same time, only a very few of the galaxies which lie below the SF sequence in an SSFR vs. M_* diagram are detected by ALFALFA. Furthermore, ALFALFA misses a substantial fraction of the optical galaxies lying on the redder side of the blue cloud. The volume-corrected optically-selected S_{opt} sample well reproduces various scaling relations derived from the high stellar mass GASS sample [Catinella et al., 2010, Schiminovich et al., 2010]. However, at the highest stellar

masses, the HI-selected $S_{\rm HI}$ galaxies show systematically larger discrepancies in their SF properties from the GASS results as the fraction of the total population which is detected by ALFALFA in a given stellar mass bin declines. In comparison with optically-selected samples, HI-selected galaxies that have high gas fractions are relatively less evolved and have, on average, bluer colors, higher SFRs and SSFRs, but lower SFEs, extinctions and metallicities.

Previous authors, notably Boissier and Prantzos [2000], have proposed that the overall low SFEs found in gas-rich systems may be explained if, their disks are characterized by large disk scale lengths and lower stellar surface densities because their host dark matter haloes have high spin parameters λ. We explore this hypothesis comparing the spin parameter distributions of the volume-limited $S_{\rm HI}$ and $S_{\rm opt}$ samples following the approach outlined in Hernandez et al. [2007] which estimates the $V_{\rm rot}$ using the Tully-Fisher relation. As presented by Hernandez et al. [2007], this estimate of λ assumes that all galaxies are characterized by the same disk mass fraction $F_{\rm d} = 0.04$. Under that (unlikely) assumption, we find a spin parameter distribution close to that found by Hernandez et al. [2007] for their SDSS disk subsample and well-fit by a log normal distribution in agreement with numerical simulations. There is a slight hint that the HI-selected population $S_{\rm HI}$ has a slightly higher λ_0 than the $S_{\rm opt}$ sample which could reflect the bias that the HI-selected sample is characterized by more extended disks. However, abundance matching between the observed stellar mass functions and the CDM halo mass functions derived from simulations strongly suggests that that F is not a constant but rather peaks around a halo mass of $M_{\rm halo} \sim 10^{12}\ M_{\odot}$ [e.g. Guo et al., 2010]. At the low mass end, baryon depletion again grows in the shallow potential wells [Hoeft et al., 2006]. Because the $\alpha.40$ catalog contains HI line widths, we calculate spin parame-

ters from them adopting the $V_{\rm halo}$–$V_{\rm rot}$ relation from Table 1 of Papastergis et al. [2011]. While this method of assigning $M_{\rm halo}$ is only valid in a statistical sense, the result is clear: the distribution of λ is no longer log normal and has a mean value well in excess of the expectation, strongly reinforcing the hypothesis that the ALFALFA population favors high λ dark matter hosts.

In the future, our multiwavelength program to study the HIghMass sample of high gas fraction, high HI mass galaxies will explore the star formation process and the interrelationships of the stellar, gas, dust and dark matter components within this set of exceptionally massive HI disks. The Survey of HI in Extremely Low mass Dwarfs (SHIELD) is exploring similar relationships among the lowest HI mass galaxies detected by ALFALFA [Cannon et al., 2011] and has already uncovered evidence that the SFL in those galaxies is unusual.

CHAPTER 4

HIGH HI MASS, HI-RICH GALAXIES AT Z$\sim$0 – SAMPLE, OPTICAL AND Hα IMAGING, AND STAR FORMATION PROPERTIES

4.1 Introduction

While the scenario that galaxies evolve through mergers and gas condensation at the center of dark matter (DM) halos is now widely accepted, the details of gas acquisition and galaxy assembly remain largely unknown. The amount of cold gas in a galaxy reflects the complex interplay between processes that either replenish it, such as cooling and accretion, mergers with gas-rich galaxies; or deplete it, such as environmental effects, star formation (SF), and feedback from massive stars and AGNs. In the "downsizing" scenario of galaxy evolution, massive galaxies are most efficient in consuming their gas reservoirs. Very massive galaxies with a substantial supply of cold gas are thus expected to be rare locally, an expectation that was seemingly corroborated by the HI mass function derived from the HIPASS survey [Zwaan et al., 2005]. Note that the THINGS [Walter et al., 2008] sample includes only two objects (NGC 3198 and M 101) with HI mass $M_{\rm HI} > 10^{10}\ M_{\odot}$ and then barely so ($10^{10.01}$ and $10^{10.15}\ M_{\odot}$ respectively). However, the Arecibo Legacy Fast ALFA (ALFALFA) survey [Giovanelli et al., 2005b, Haynes et al., 2011], an extragalactic blind HI-line survey, identified a set of such galaxies, which resemble the HI massive disks detected at $z \sim 0.2$ [Catinella et al., 2008]. They represent the present day counterparts of the populations which are likely to dominate future studies of HI in galaxies at higher z with the next generation of radio telescopes, e.g., Square Kilometer Array.

Selected examples of very massive but gas-rich galaxies have been studied in

recent years, with most belonging to the extreme category of low surface brightness (LSB) galaxies known as the "crouching giants" [Disney and Phillipps, 1987] or "Malin 1 cousins". For instance, NGC 765 is shown to have one of the highest HI-to-optical ratios and one of the largest known HI disks, with $M_{\rm HI} \sim 4.7 \times 10^{10} M_{\odot}$ [Portas et al., 2010]. Moreover, UGC 8802 detected by the GASS survey [Catinella et al., 2010] is found to have $M_{\rm HI} \sim 2.1 \times 10^{10} M_{\odot}$, yet low and remarkably evenly distributed star formation rate (SFR) surface density [Moran et al., 2010]. The extremely high ratio of current SFR to existing stellar mass (M_*) surface density in the outer disk implies that all its stars must have formed within the past ∼1 Gyr. The ALFALFA survey, providing the first full census of HI-bearing objects over a cosmologically significant volume in the local universe, is most effective in detecting such gas-rich systems [Huang et al., 2012a]. It enables, for the first time, a *systematic study* of the local galaxies with $M_{\rm HI} > 10^{10} M_{\odot}$. In fact, the most surprising result of ALFALFA to date is the richness of the high $M_{\rm HI}$ galaxy population [Martin et al., 2010] which HIPASS seriously undercounted by up to a factor of ten at the highest masses, due to the insufficient volume it covered. Our study will establish a baseline $z \sim 0$ sample for comparison with the planned deep field HI surveys.

The presence of massive HI disks in the local universe remains a puzzle, which implies unusual physical conditions of gas depletion and/or supply. On one hand, the higher-than-averaged HI gas fraction ($f_{\rm HI} \equiv M_{\rm HI}/M_*$) may be due to underluminous stellar disks, i.e., the galaxies perhaps were in an arrested stage of evolution in the past. Theoretical models predict that galaxies in high spin parameter (λ, characterizing the mass-normalized angular momentum) DM halos have unusually extended gaseous disks with large disk scale lengths and low surface density [e.g. Mo et al., 1998, Boissier and Prantzos, 2000,

Kravtsov, 2013]. As a result, the gas infall and consumption times are long and the galaxies have never reached a phase of significant SF in the past [Li et al., 2012]. Observationally, classical LSB galaxies are found to have low HI surface brightness, though their total HI masses are quite high. SF is an extremely inefficient process in such diffuse disks, e.g., Malin 1 [Bothun et al., 1987, Impey and Bothun, 1997], in agreement with the canonical star formation laws (SFLs). The slowly rising rotation curves imply that the Malin type galaxies are dominated kinematically by DM and the halos are less concentrated with larger λs [Pickering et al., 1997]. Giant LSB galaxies are observed to have a large amount of angular momentum in their disks, in agreement with the formation of LSB galaxies as predicted by recent hydrodynamic simulation [Kim and Lee, 2013]. This scenario is also consistent with the small DM perturbation easily found in low density regions with late formation [Mo et al., 1994].

On the other hand, the extraordinarily high $f_{\rm HI}$ may be attributed to late cold gas accretion. Rather than hot accretion (post-shock cooling from a quasi-spherical halo), cold accretion (clouds, streams, filaments) is theoretically considered an important aspect in the process of galaxy formation at high z, and is perhaps still the dominant mode in low-mass galaxies and in low-density regions today [Kereš et al., 2005, Croton et al., 2006]. In fact, the models that assume a slowly evolving equilibrium between gas inflow, outflow, and SF, can well reproduce the observed evolution of the SF sequence and Tully-Fisher relation [e.g., Bouché et al., 2010, Fraternali and Tomassetti, 2012], etc. In the local universe, it is now possible to detect the emission from the diffuse infalling structures with sensitive HI observations, e.g., extra-planar HI, HI tails and filaments [Sancisi et al., 2008]. While in a canonical picture, gas cooling from the virial temperature spends a considerable amount of time in the galactic halo so

that it has the same specific angular momentum as the underlying DM, high-resolution cosmological hydrodynamic simulations found that cold mode accreted gas enters a galaxy halo along filaments with $\sim 70\%$ more specific angular momentum than dark matter averaged over cosmic time, and the gas is well characterized by $\lambda \sim 0.1$, at accretion [Stewart et al., 2013]. The resulting disks of cool gas are dense enough to form HI, which may help explain the observations of extended UV disks [Lemonias et al., 2011], extended, warped, or lopsided HI disks [Sancisi et al., 2008]. Such newly accreted gas may be retarded in producing SF if it is stable against contraction and stays in the low surface density outer disk where HI dominates over H_2. However, the presence of a bar may induce radial gas flow [Martin and Roy, 1994] so that SF is triggered.

To unravel the origin of the High HI mass, HI-rich (i.e., with high $f_{\rm HI}$) galaxies at $z \sim 0$, we began a campaign in 2009, entitled 'HIghMass', to gather multi-wavelength data for a volume-limited sample of 34 galaxies selected from ALFALFA. The complete dataset will enable the understanding of their gaseous, stellar, and DM components. This chapter presents a summary of the project definition and optical properties of the full sample, including the SF properties as probed by the Hα narrowband imaging. We note that not all of our galaxies are of LSB in the optical, although some of them are, e.g., AGC 190796 is classified as Malin-like according to NED. We present the sample, observing status, and basic physical properties of our targets relative to other Hα surveys in Section 4.2. Our Hα and R-band observation and data processing are described in Section 4.3, together with the catalogs. Reprocessed SDSS photometry is discussed in Section 4.4. Star formation rates (SFRs) are calculated in multiple ways and are compared against each other in Section 4.5. Section 4.6 introduces optical characteristics of the HIghMass galaxies. We summarize the main results in

Section 4.7.

4.2 Sample

4.2.1 Sample Selection and Program Overview

Exploiting the capability of the Arecibo *L*-band feed array (ALFA) and the sensitivity of the Arecibo 305 m antenna, the ALFALFA survey [Giovanelli et al., 2005b] finished mapping ∼7000 deg^2 of high galactic latitude sky between 0° and +36° in Oct 2012. The HIghMass galaxies are selected from the 2011 ALFALFA catalog, α.40 [Haynes et al., 2011], covering 40% of the final targeted survey area, yielding $M_{\rm HI}$, systemic velocity (cz), and HI line widths (W_{50}) for ∼16,000 high-quality detections. With a centroiding accuracy of better than 20″ and a resolution of $\sim 3.5'$, the α.40 catalog also includes an assignment of the most probable optical counterpart (OC) to each extragalactic HI source. The current published SDSS crossmatches to the α.40 catalog are referenced to the SDSS Data Release 7 [Abazajian et al., 2009], where the footprints of the surveys overlap [Haynes et al., 2011].

Indeed, ALFALFA detects thousands of galaxies with $M_{\rm HI} > 10^{10}\ M_\odot$, and among them, we focus on the set of most gas rich galaxies with high HI fractions. To derive $f_{\rm HI}$, we estimate the M_* by spectral energy distribution (SED) fitting to seven *GALEX*-SDSS bands [Huang et al., 2012b,a]. Fig. 4.1 shows the $f_{\rm HI}$ *vs.* M_* diagram as a result of the fit. Black contours and greyscales represent the SDSS-*GALEX*-α.40 common sample, weighted by the $V/V_{\rm max}$ values as determined by the ALFALFA sensitivity limit [Huang et al., 2012a]. The sharp

lower edge of the general distribution is due to the fact that only the galaxies with weights below 60, or equivalently with $M_{\rm HI} > 10^{8.2}\ M_{\odot}$, are included. The solid blue curve illustrates the weighted running average defined by the SDSS-*GALEX*-α.40 galaxies, in agreement with the result derived from the GASS survey at $M_* > 10^{10} \odot$ [Catinella et al., 2010, cyan dash-dotted line in Fig. 4.1]. The decreasing trend of $f_{\rm HI}$ with M_* confirms the expectation that the massive galaxies are mostly gas poor. Such a gas depletion sequence can be understood with, and has a similar slope as the SF sequence in a SSFR *vs.* M_* diagram [Huang et al., 2012a, specific SFR defined as SSFR $\equiv$ SFR/M_*]. The hint of a $f_{\rm HI}$ bimodal distribution as driven by the higher portion of gas-poor galaxies at the high stellar mass end will be more prominent if the HI detections with higher weights are included. This is also consistent with the fact that the relative number of passive red galaxies increases among massive galaxies with $M_* \gtrsim 10^{10} M_{\odot}$.

The HIghMass galaxies are extreme cases identified from the ALFALFA population, which is already biased towards gas-rich galaxies in terms of the unweighted distribution [Huang et al., 2012a]. The black lines in Fig. 4.1 corresponds to the selection criteria of HIghMass galaxies: (*i*) has a $M_{\rm HI} > 10^{10}\ M_{\odot}$, lying above the dashed line; and (*ii*) has a $f_{\rm HI}$ more than than 1σ above the running average in a given M_* bin, lying above the dotted line. The criteria are partly motivated by the semi-analytic model prediction in Boissier and Prantzos [2000] that the galaxies reside in high-λ DM halos have preferentially high gas fraction at fixed circular velocity. To be conservative, we visually inspected these galaxies to eliminate the cases in which the HI fluxes suffer from confusion in the ALFA beam, or the SDSS magnitudes suffer from shredding or blending, because both cases yield unreliable mass estimates. This study of the optical images is part of a coordinated effort to make use of multi-wavelength data

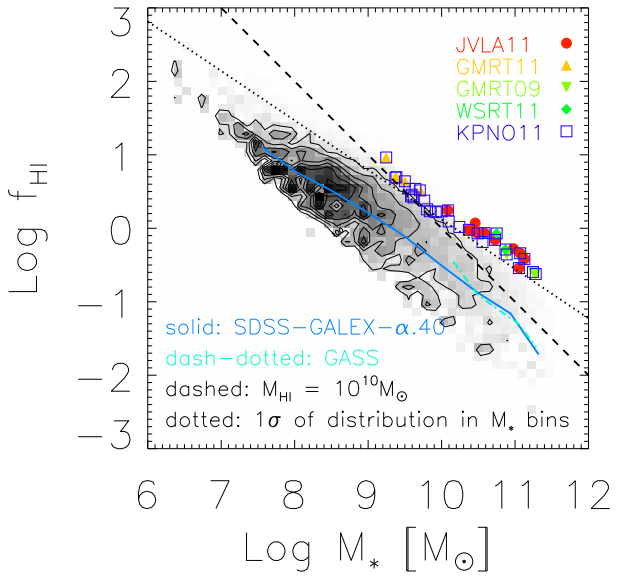

Figure 4.1: Gas depletion sequence and HIghMass sample selection. Black contours and greyscales represent the SDSS-*GALEX*-α.40 common sample, weighted by the $V/V_{\rm max}$ values. The solid blue curve illustrates our weighted running average, in agreement with the GASS result [Catinella et al., 2010] as cyan dash-dotted line. Colored symbols are overlaid on the diagram for 34 HIghMass galaxies. They are selected to have $M_{\rm HI} > 10^{10}\ M_{\odot}$ (above the dashed line) and have HI fraction more than 1σ above the running average (above the dotted line). Targets of the HI synthesis mapping and Hα imaging programs are denoted by filled and open symbols respectively (see text).

(UV, optical, NIR, FIR/submm, millimeter, radio) of the HIghMass galaxies to explore the interrelationships of their star, SF, gas, dust and DM components. Further selections are imposed to account for the technical feasibility of each observing program. For instance, targets close to bright stars are avoided in the *GALEX* proposal (GI6; Haynes PI); targets close to strong continuum sources or with low HI fluxes are avoided in the HI synthesis mapping programs; targets in the ALFALFA fall sky (for which SDSS photometry was not available at the time) or lying too distant to be covered by any KPNO Hα narrowband filters

are dropped from the KPNO spring run (2011; Huang PI); etc.

The final HIghMass sample consists of 34 galaxies as colored symbols in Fig. 4.1, either in the HI synthesis programs (20 filled symbols), or with the Hα images (31 open squares). The $f_{\rm HI}$ ranges between 0.24 and 9.2, with 20/34 having $f_{\rm HI} > 1$. Because ALFALFA does not provide the angular resolution needed to resolve the HI disks, we have obtained HI synthesis maps of the 20 objects which can be feasibly mapped with existing HI synthesis instrument (see Table 4.1), including first three at GMRT for massive galaxies (2009; Chengalur PI; downward triangles in Fig. 4.1), additional five at GMRT later for low mass galaxies (2011; Adams PI; upward triangles), two at WSRT (2011; Haynes PI; diamonds), and last ten at JVLA (2011; Haynes PI; circles). These observations will yield clues on the origin and nature of the HIghMass galaxies via the constraint of DM halos by gas dynamics (Hallenbeck et al. 2013 in preparation). Plus, recent accretion of IGM or minor mergers of faint companions may leave signatures in HI morphology or disturbed velocity fields.

Due to the failure of the *GALEX* detector, our approved FUV observations were not conducted. However, existing *GALEX* archival data still unravel intriguing behavior in some of the HIghMass galaxies. *GALEX* images reveal that SF in more gas-rich galaxies often extends much farther in radius than had previously been appreciated [Thilker et al., 2007]. An extended UV disk is evident in UGC 9234, hosting irregular and patchy SF, but only two faint loose spiral arms are seen in optical images, indicative of recent gas infall and disk regrowth. It is known that the extent of the UV disk (normalized to the optical size) is strongly correlated to the integrated $f_{\rm HI}$, as expected if that the amount of HI regulates the growth of SF disk in the outskirt of galaxies [Cortese et al.,

2012]. In combination with the resolved HI column density map, resolved SF measures derived from both UV photometry and Hα imaging will address the questions concerning the gas-SF interplay.

The 18 overlapping symbols denote the *Herschel* targets (OT2; Haynes PI) with both HI maps and Hα images (see Table 4.1). PACS and SPIRE scan maps cover a critical wavelength range of the dust emission SED at 70, 110, 160, 250, 350, and 500 μm, allowing us to determine the dust masses, temperatures and grain size distributions. All 90 Astronomical Observation Requests (AORs) had been observed before the *Herschel* ran out of helium. FIR/submm emissions are visible in most maps reduced by the standard pipeline, except for UGC 6066 and UGC 9234. It is plausible to combine the dust mass with $M_{\rm HI}$ to yield dust-to-gas ratio (D/G) maps when applicable. Whether the gas reservoir is recently accreted from the IGM or is inhibited from forming stars, the gas is expected to have an unusual enrichment history and thus a different present-day D/G from normal spirals. Though the two scenarios are both likely to result in a lower than normal D/G, recently accreted gas should have undergone even less enrichment or mixture, so that a future D/G study will help to distinguish between the two scenarios. Warm-*Spitzer* IRAC imaging at 3.6 and 4.5 μm (2013; Huang PI) have been approved for 32 HIghMass galaxies (AORs for 9 galaxies partly executed at present, see Table 4.1). They will provide insight into the underlying older stellar population: how many stars were formed at early times and where within their disks did that early SF take place?

In addition, we have CO ($J = 1 - 0$) observations with the IRAM 30-m and CARMA telescopes to trace the molecular content. The integrated CO line observing run with IRAM 30-m (Haynes PI) was a complement to the COLD GASS

program [Saintonge et al., 2011a]. CO lines are detected in 15 out of 16 HIgh-Mass targets (only AGC 213964 undetected), three being marginal detections (UGC 6066, UGC 7220, UGC 9234). The high detection rate is consistent with the overall blue NUV$-r$ colors of our targets [Saintonge et al., 2011a]. Preliminary results show that these galaxies have unusually high HI-to-H_2 ratios, globally, suggesting the existence of a bottleneck in the formation of H_2. Five galaxies have been mapped in CO with CARMA (Hallenbeck PI) and the data are being reduced. The resolved molecular gas distribution will enable a detailed study of HI-to-H_2 conversion, SFL and SF thresholds. Finally, we have acquired optical spectra for 31 HIghMass galaxies with INT in March 2013 (Brinchmann PI), yielding detections of emission lines in all but UGC 6066. Both observations and simulations indicate that metal gradients become shallower as a result of a merger [Kewley et al., 2010]. If a steep metal gradient is found, it will indicate a comparatively quiet evolutionary history of the disks. Meanwhile, the spectra will be crucial to determine across the disks the metal dependent CO-to-H_2 conversion factor.

Fig. 4.2 illustrates the multi-wavelength data we obtained for the highest stellar mass galaxy in our sample, UGC 8475 (or NGC 5174). The left panel shows the HI column density contours superposed on an optical image from our 2009 GMRT pilot program. The HI column density peaks in an outer LSB disk which also hosts the locus of current SF, whereas HI extends significant beyond the star-forming disk out to $\sim 3r_{25}$, indicating gas recreation and/or high angular momentum of the gaseous disk. The middle and right panels show, respectively, on the same scale the *GALEX* MIS image and the continuum subtracted Hα image after cleaning (see Section 4.3). Note that the central SF visible in Hα is largely missing from the FUV, possibly due to high attenuation in the

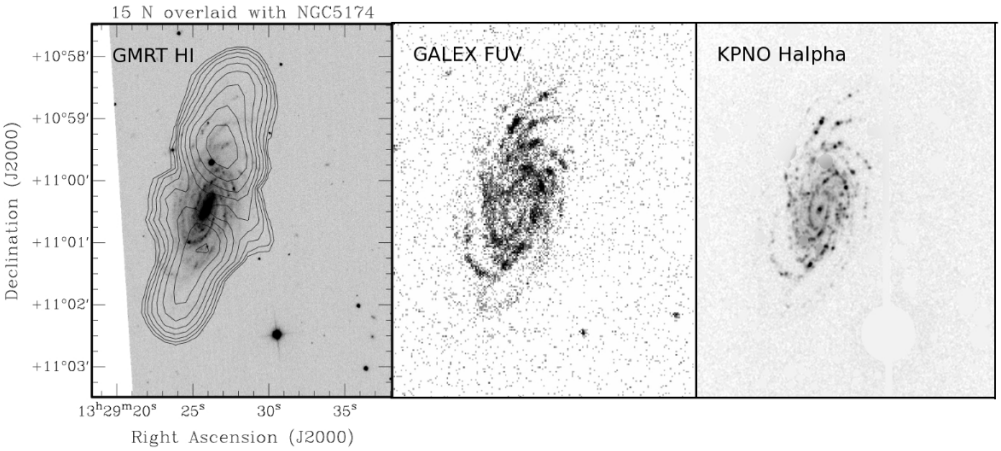

Figure 4.2: Example of the multi-wavelength data for UGC 8475 (= NGC 5174), the most stellar massive galaxy in our sample. The left panel shows the HI column density contours superposed on an optical images from our 2009 GMRT program. The middle and right panels show, respectively, on the same scale the *GALEX* MIS image and the continuum subtracted Hα image after cleaning.

FUV band. The SF complexes are detected along the spiral arms and associated with the outer LSB disk.

4.2.2 Basic Physical Properties and Comparison to Other Hα Surveys

Table 4.1 presents the existing multi-wavelength data and basic properties from the ALFALFA measurements for the full sample of 34 HIghMass galaxies. Columns are as follows:

- Col(1): ALFALFA catalog identifier (also known as the AGC number).
- Col(2): Other name resolution by NED; same as AGC numbers in the UGC cases.
- Col(3) and (4): J2000 position of the OC assigned to the HI source, in de-

grees.

- Col(5): Galaxy morphology classification according to NED.
- Col(6): The HI line width W_{50}, in km s^{-1}, taken from the $\alpha.40$ catalog [Haynes et al., 2011].
- Col(7): The adopted distance in Mpc, taken from the $\alpha.40$ catalog [Haynes et al., 2011].
- Col(8): The logarithm of the $M_{\rm HI}$ and its error, in $M_{\odot}$, taken from the $\alpha.40$ catalog [Haynes et al., 2011].
- Col(9): Type of archival *GALEX* images, AIS = all sky imaging survey; MIS = medium imaging survey; DIS = deep imaging survey; GII = guest invited investigation; null if outside of footprint.
- Col(10): Source of Hα images, K = our KPNO 2011 spring run; K* = KPNO 2012 fall run by Angie Van Sistine; G = GOLDmine data [Gavazzi et al., 2003]; null if too far away.
- Col(11): Code for our HI synthesis mapping programs as discussed in Section 4.2.1.
- Col(12): Code for our *Herschel* program, D = detected; M = marginal; U = undetected; null if not included.
- Col(13): Code for our *Spitzer* program, O = observed but not reduced; N = currently not observed yet; null if not included because archival data exist.
- Col(14): Code for our IRAM 30-m program, D = detected; M = marginal; U = undetected; null if not included.
- Col(15): Code for our CARMA program, D = detected; O = observed but not reduced; null if not included.

- Col(16): Code for our INT program, D = detected; U = undetected; null if not observed.

Table 4.1: Basic properties and observing programs of the HIghMass sample

AGC	Other	R.A. [°]	Dec. [°]	morph	W_{50} [km s^{-1}]	D [Mpc]	log $M_{\rm HI}$ [M$_\odot$]	*GALEX*	Hα	HI	*Herschel*	*Spitzer*	IRAM	CARMA	INT
188749	SDSS J080649.98+120341.7	121.7079	12.062	ExtendedSrc	136	160	10.14(0.03)	AIS	K	GMRT11	M	N	D	...	D
4599	UGC 04599	131.9238	13.419	(R)SA0	148	32	10.04(0.15)	AIS	K		...	N	...	...	D
190796	LSBC F634-V02	137.7754	13.122	S/Malin-like	123	131	10.14(0.02)	AIS	K	...	...	N	D	...	D
721391	CGCG 121-063	140.3658	25.062	...	293	111	10.07(0.02)	AIS	K	...	...	N	D	...	D
190277	CGCG 062-031	141.3088	12.156	Sdm(flat)	286	128	10.22(0.02)	MIS	K	...	...	N	...	...	D
5543	UGC 05543	154.0850	4.822	Sc	547	201	10.73(0.03)	MIS	K	JVLA11	D	N	D	...	D
5648	UGC 05648	156.5362	4.372	S	322	103	10.14(0.02)	MIS	K	...	...	N	...	...	D
5711	NGC 3270	157.8750	24.869	SAB(r)b:	522	93	10.51(0.01)	AIS	K	JVLA11	D	...	...	...	D
203522	SDSS J103304.79+073453.2	158.2700	7.581	...	190	160	10.21(0.04)	AIS	K	GMRT11	M	N	...	...	D
6043	UGC 06043	164.0642	15.223	Scd:	276	121	10.06(0.03)	AIS	K	...	...	N	...	...	D
6066	UGC 06066	164.7471	6.522	SAab:edge-on	667	173	10.71(0.02)	...	K	JVLA11	U	N	M	...	U
6168	UGC 06168	166.7679	7.804	(R')SB(r)bc:	363	120	10.35(0.02)	AIS	K	JVLA11	D	N	D	O	D
6536	NGC 3728	173.3158	24.447	Sb	430	103	10.58(0.01)	AIS	K	WSRT11	D	N	...	...	D
6692	NGC 3833	175.8704	10.161	Sc	390	91	10.37(0.01)	AIS	K	...	...	N	D	...	...
213964	SDSS J114637.62+061017.0	176.6567	6.171	...	88	146	10.08(0.03)	AIS	K	GMRT11	D	N	U	...	D
6895	NGC 3968	178.8696	11.968	SAB(rs)bc	490	96	10.65(0.01)	AIS	K	GMRT09	D	N	...	...	D
6967	NGC 4017	179.6908	27.452	SABbc	253	51	10.23(0.09)	GII	K	...	...	N	...	...	D
7220	IC 3046	183.2829	12.918	S?/Sc(s)I	443	120	10.52(0.01)	GII	K	JVLA11	D	N	M	O	D
7686	IC 3467	188.1025	11.787	Scd:	274	112	10.22(0.02)	DIS	G	GMRT11	D	O	D	O	D
7899	IC 3704	190.9400	10.770	Sbc/Sc	433	128	10.42(0.02)	GII	K	JVLA11	D	N	D	D	D
8089	UGC 08089	194.6254	9.544	Sdm:	117	106	10.06(0.01)	...	K	GMRT11	D	N	D	...	...
8408	NGC 5115	200.7512	13.951	SBcd:	290	108	10.26(0.02)	AIS	K	...	...	O	...	...	D
8475	NGC 5162	202.3575	11.008	Scd:	591	101	10.66(0.01)	GII	K	GMRT09	D	N	...	...	...

Table4.1 – Continued

AGC	Other	R.A. [°]	Dec. [°]	morph	W_{50} [km s^{-1}]	D [Mpc]	log $M_{\rm HI}$ [M$_\odot$]	*GALEX*	Hα	HI	*Herschel*	*Spitzer*	IRAM	CARMA	INT
8573	NGC 5230	203.8829	13.676	SA(s)c	152	101	10.53(0.01)	AIS	K	GMRT09	D	...	D	D	D
8797	UGC 08797	208.2600	24.560	S?	559	247	10.70(0.04)	AIS	...	JVLA11	...	O	...	...	D
9023	UGC 09023	211.7129	9.321	Scd:	231	106	10.05(0.02)	AIS	K	...	...	N	...	...	D
248881	KUG 1405+151	211.8550	14.919	Spiral	192	112	10.10(0.02)	AIS	K	...	...	O	...	...	D
9037	UGC 09037	212.1213	7.058	Scd:	294	88	10.33(0.01)	MIS	K	JVLA11	D	N	D	...	D
726428	2MASX J14220675+2659490	215.5283	26.997	...	208	129	10.02(0.03)	AIS	K	...	...	O	...	...	D
9234	UGC 09234	216.1942	26.139	S?	589	158	10.68(0.02)	GII	K	WSRT11	U	O	M	...	D
9334	NGC 5650	217.7542	5.978	SABbc	413	110	10.57(0.01)	MIS	K	JVLA11	D	O	D		D
714145	2MASX J14342549+0835510	218.6063	8.597	...	283	121	10.18(0.03)	AIS	K	...	...	O	...	...	D
9410	UGC 09410	219.3079	8.646	Sbc	317	123	10.19(0.03)	AIS	K	...	...	O	...	...	D
12506	UGC 12506	349.8771	16.074	Scd:	457	98	10.53(0.01)	AIS	K*	JVLA11	...	N	...	...	D

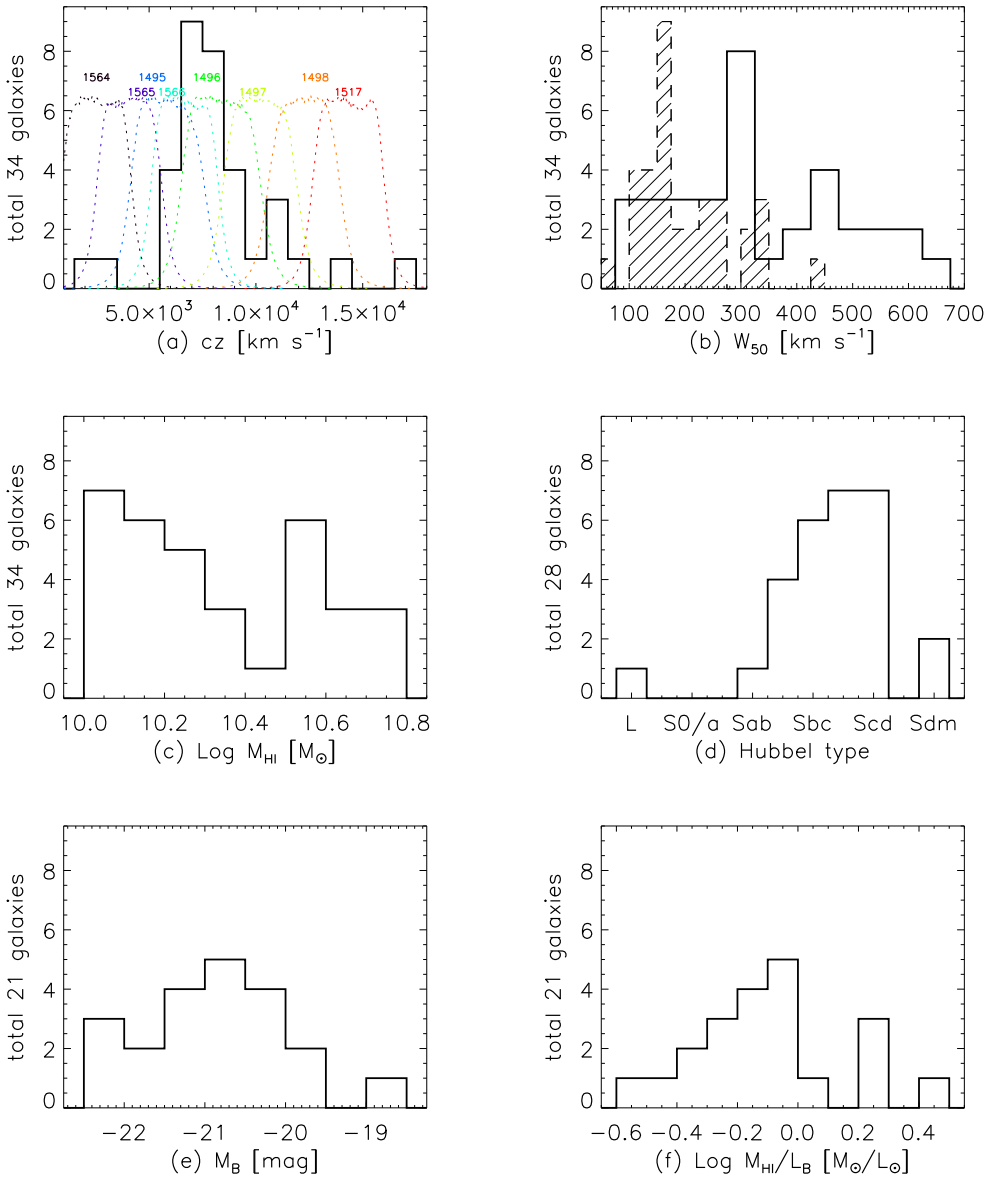

Figure 4.3: Black solid lines in all panels show distributions of the HIghMass galaxies: (a) HI systematic velocity; (b) observed HI line width; (c) logarithm of HI mass; (d) morphological type; (e) B-band absolute magnitudes; (f) logarithm of the HI mass to B-band luminosity ratio. Colored dashed lines in panel (a) illustrate the transmission curves of the Hα filters used in our KPNO run, together with the corresponding filter names. The filled dashed histogram in panel (b) indicates the distribution of inclination-corrected HI rotational velocities.

Panel (a)-(d) in Fig. 4.3 show, respectively, histograms of the heliocentric recessional velocity cz, observed HI line width W_{50}, logarithm of the $M_{\rm HI}$, and NED morphology classification on the Third Reference Catalog (RC3) system [de Vaucouleurs et al., 1991, available for 28 galaxies]. Rotational velocities are estimated from W_{50} and inclinations are inferred by their axial ratios (derived in Section 4.4), adopting an intrinsic axial ratio of 0.2. The results, overlaid in Panel (b) by the filled histogram, are large, consistent with their status as HI massive disk galaxies (see Panel c). The only early type galaxy in the sample, UGC 4599, is a face on S0 galaxy with an outer ring, where vigorous star forming regions are found. The total asymptotic magnitudes in the B band are available from RC3 for 21 galaxies, ranging from 15.73 mag to 12.60 mag, with a median of 14.35 mag. Last two panels in Fig. 4.3 show the RC3 B-band absolute magnitude and logarithm of the $M_{\rm HI}/L_B$, assuming $B = 5.47$ for the sun. These B-band magnitudes are systematically brighter than our reprocessed SDSS magnitudes (measured inside elliptical Petrosian apertures, see Section 4.4), but the differences are within the uncertainty. The final set of 34 HIghMass galaxies span a range of colors, morphologies, luminosities, M_*, and SFRs (see Section 4.5).

Fig. 4.4 illustrates the distribution of parent α.40-SDSS sample on an optical color-magnitude diagram, together with the HIghMass galaxies. Definition of the color symbols is the same as that in Fig. 4.1. Contours and points represent the α.40-SDSS sample. The number density of galaxies in each grid cell is labeled on selected contours, e.g., the lowest contour level beyond which scatter points are plotted is 10 galaxies per grid cell. The grid size is shown by the interval of minor ticks on both axes. The approximate dividing line which separates the "red sequence" from the "blue cloud" as presented by Baldry et al. [2004] is shown as the dash-dotted curve. In this plot, SDSS magnitudes of the parent

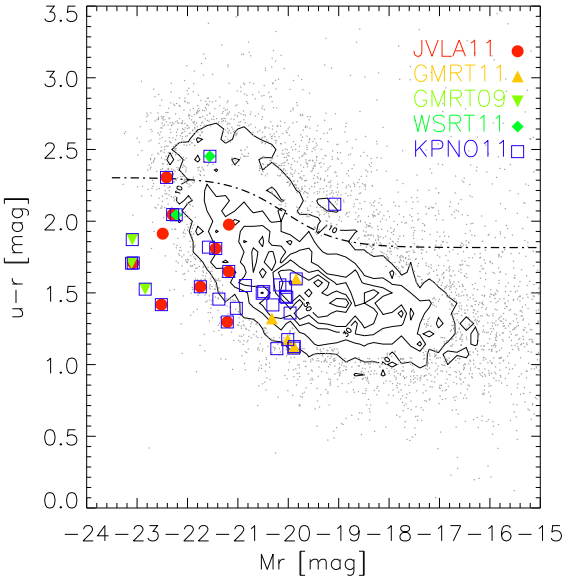

Figure 4.4: Optical color-magnitude diagram. Definition of the colored symbols is the same as that in Fig. 4.1. Contours and points represent the α.40-SDSS(DR8) sample in high and low number density regions, respectively. The approximate dividing line which separates the "red sequence" from the "blue cloud" as presented by Baldry et al. [2004] is shown as the dash-dotted curve.

sample are DR8 pipeline values, but those of the HIghMass galaxies are our reprocessed measurements (see Section 4.4 for details of our SDSS re-photometry and how does it compare with the DR8 pipeline results). The vast majority of the galaxies in the α.40-SDSS population are found in the blue cloud region. Similarly, most of the HIghMass galaxies, especially the GMRT09 and JVLA11 targets, are exceptionally blue given their high luminosities. Only three HIghMass galaxies lie in the red sequence above the division, UGC 6066, UGC 9234, and UGC 4599. UGC 6066 is an edge on red spiral and UGC 4599 is an S0 galaxy; they have the earliest T-types in our sample. Although the stellar light is dominated by red central regions in both UGC 9234 and UGC 4599, the first one has two loose arms and the second one has an outer ring, all being LSB and blue features along which multiple star-forming regions are identified in our net Hα

images (see Section 4.3). The huge HI reservoirs in these red galaxies are apparently involved in the current regrowth of such outer features. However, their overall red optical colors are still consistent with the non-detections by the *Herschel*, IRAM, or INT observations (see Table 4.1). For instance, UGC 6066 and UGC 9234 are the only two non-detections by *Herschel*; there are no available *Herschel* data for UGC 4599.

To quantify the environment of the HIghMass galaxies we used a galaxy's nth nearest neighbors as a metric. The first 10 nearest neighbors of the high signal-to-noise galaxies in α.40 were found using the SDSS DR7 spectroscopic catalog galaxies [Abazajian et al., 2009]. The catalogs were cut in R.A. and Dec., as well as redshift, such that the ALFALFA sample was volume-limited in the range $90 - 170$ Mpc (within which 28 of the HIghMass galaxies fall), and the SDSS sample was volume-limited out to 215 Mpc. The search for neighbors then proceeded within an expanding spherical bubble (in plane of the sky and redshift distances), out to a limit of 45 Mpc. Finally a minimum separation of 10 arcsec was applied. Such close neighbors are unlikely to be indicative of the surrounding environment, and would not be distinguishable from the parent galaxy in ALFALFA anyway.

Measures of local galaxy density were estimated by averaging the logarithm of the 2nd and 3rd nearest neighbor densities [similar to Baldry et al., 2006], and are plotted for the ALFALFA and HIghMass galaxies in Fig. 4.5. The two distributions appear to have very similar shapes, and peak at almost the same density. A K-S test comparing them gives a P-value of 0.18, indicating that there may be slight differences between them, but they are still consistent with both being randomly drawn from the same underlying distribution. K-S tests of the

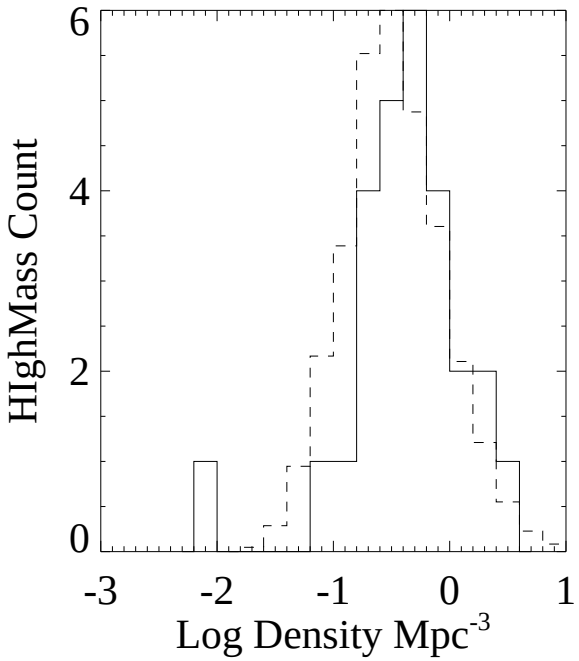

Figure 4.5: Local galaxy density estimated by averaging the logarithm of the 2nd and 3rd nearest neighbor densities, plotted for the HIghMass (solid line) and ALFALFA (dashed line, normalized to the HIghMass distribution), respectively. The HIghMass distribution is to the higher density side compared to ALFALFA, but the K-S test shows it is not significant given the small number of points.

distributions of all 10 nearest neighbors point to the same conclusion. ALFALFA is naturally biased to blue galaxies, which tend to be less clustered, so perhaps it is unsurprising that the environment of the HIghMass galaxies is consistent with that of the average ALFALFA galaxy. However, it is worth noting that due to the magnitude cut any neighbor galaxies with an absolute r-band magnitude fainter than -19.1 will be excluded. If there is a difference in the number of these galaxies surrounding the ALFALFA and HIghMass galaxies then this analysis would not be sensitive to it.

Several programs of Hα imaging for large and robustly defined samples of cluster/group galaxies have been accomplished in the last decade, including the

survey of 52 dwarf-dominated galaxies in the local volume [Karachentsev and Kaisin, 2010], the survey of eight nearby Abell clusters [Sakai et al., 2012], and GOLDmine survey of the Virgo cluster and Coma superclusters [Gavazzi et al., 2003]. Note that UGC 7686 happens to be a background galaxy in the Virgo direction so that is imaged by the GOLDmine survey. However, the ALFALFA galaxies are biased against cluster environments [Martin et al., 2012]. Therefore, we will next focus on a comparison between our survey and the other Hα surveys of predominantly field galaxies.

The HIghMass survey can be most easily distinguished by the different optical luminosity ranges they probe, from a series of surveys by Hunter and collaborators [Hunter and Elmegreen, 2004], or the 11 Mpc Hα UV Galaxy Survey [11HUGS; Kennicutt et al., 2008]. The 140 local irregular galaxies imaged by Hunter and Elmegreen [2004] contains 94 Im systems, 26 blue compact dwarfs (BCDs), and 20 Sm's, with absolute magnitude $-9 > M_V > -19$, most lying closer than 30 Mpc (see a comparison between our Fig. 4.3e and their Fig. 2). Similarly, the 11HUGS selects galaxies with $B \leqslant 15$ and $D \leqslant 11$ Mpc [Kennicutt et al., 2008]. This sample is dominated by galaxies with T-type $\geqslant 9$ and $M_B > -19$. In contrast, the majority of our galaxies have $M_B < -19$ and they all have T-type $\leqslant 8$ (Sdm), lying beyond 30 Mpc (see a comparison between our Fig. 4.3e and their Fig. 6). Note that Hunter and Elmegreen [2004] have used 74 spiral galaxies spanning the range of morphologies from Sab to Sd as compiled by Kennicutt [1983] for comparison reasons. However, the $\log M_{\rm HI}/L_B$ distribution of that Sab-Sd sample peaks around -1, which is significantly HI poorer than our galaxies with similar T-types. Instead, the less massive BCDs in Hunter and Elmegreen [2004] have comparable $\log M_{\rm HI}/L_B$ values to our galaxies (see Fig. 4 in their paper). This can be understood as a result of the general

increasing trend of $f_{\rm HI}$ with decreasing M_* in Fig. 4.1.

Most Hα surveys covering the complete morphological spectrum have also been limited to local 30 Mpc, including the SIRTF Nearby Galaxies Survey[SINGS; Kennicutt et al., 2003], the Hα Galaxy Survey sampling 334 galaxies [HαGS; James et al., 2004], and the JCMT Nearby Galaxies Legacy Survey of 156 nearby galaxies [NGLS; Sánchez-Gallego et al., 2012]. Similar to ours, the sample of the last survey has been HI flux selected in order to avoid an SFR-driven selection while ensuring that the galaxies have a rich ISM. However, such a small volume of the universe contains few truly massive disks. Indeed, the T-type distributions of spirals from these surveys are similar, peaking around 3 (Sc), whereas our sample has a larger fraction of galaxies with later types. This is consistent with the pre-known correlation between high $f_{\rm HI}$ and late-type morphology.

In addition, there are several Hα surveys of particular galaxy types rather than attempting to census a characteristic sample. For example, Analysis of Interstellar Medium of Isolated Galaxies [AMIGA; Verdes-Montenegro et al., 2005] compiles 206 galaxies from the Catalog of Isolated Galaxies [CIG; Karachentseva, 1973]. Only UGC 5711 in our sample is included in the CIG. Schombert et al. [2011] present a recent Hα imaging survey for a large sample of LSB galaxies. Although the optical color of their galaxies are blue, being comparable to the dwarf galaxies and gas-rich irregulars, their SSFRs are a factor of ten less than other galaxies of the same baryonic mass [Schombert et al., 2011]. It was also found by Helmboldt et al. [2005], based on a sample of 69 galaxies with $cz < 2500$ km s^{-1} selected from HIPASS, that the conditions under which SF occurs in LSB galaxies are different than in more typical spiral galaxies. In con-

trast, the HIghMass galaxies exhibit healthy ongoing SF, neither do they belong exclusively to the isolated population. Note that only UGC 6536, UGC 190796, and UGC 6967 have been studied as LSB galaxies in previous works [Bothun et al., 1985, Schombert et al., 1992, Sprayberry et al., 1995], and none of the HIghMass galaxies have been imaged by any of these field galaxy surveys mentioned so far.

Most of the galaxies observed to date with resolved Hα imaging are closer than 50 Mpc, although only 11HUGS and HαGS apply the distance selection criterion. An exception is the Survey for Ionization in Neutral-Gas Galaxies [SINGG; Meurer et al., 2006], consisting of 468 galaxies selected from the HIPASS. All of their targets are detected in Hα, indicating that non star-forming galaxies with $M_{\rm HI} \gtrsim 10^7\ M_\odot$ are very rare. SINGG includes galaxies as far as 80 Mpc, although the majority still have $cz < 3000$. In comparison, only one of the HIghMass galaxies, UGC 4599 has $cz < 3000$, whereas our median cz = 7660 km s^{-1} (D $\sim$100 Mpc). While SINGG Release 1 [Meurer et al., 2006] includes 13 HIPASS sources with $10 < \log M_{\rm HI} < 10.3$ and 3 with $10.3 < \log M_{\rm HI} < 10.6$, multiple emission line galaxies are found to be associated with a single HI source for 9/16 of them. In contrast, we have dropped targets with massive companions to minimize such kind of confusion. In all, the HIghMass galaxies, being extremely HI massive and HI rich, are still underrepresented by even the SINGG sample, which probes a smaller volume than we do.

Finally, we mention that there are two other ALFALFA-related ongoing Hα programs. The first, called Hα3 [Gavazzi et al., 2012], is being undertaken at the San Pedro Martir (SPM) Observatory and aims to investigate the relationships

between HI and newly formed stars in different environments and morphological types. Hα3 is also based on a sample derived from the ALFALFA catalog but covering the full range of $M_{\rm HI}$. It images all galaxies that contain $M_{\rm HI} > 10^7\ M_\odot$; in $11^{\rm h} <$ R.A. $< 16^{\rm h}$, $4^\circ <$ Dec. $< 16^\circ$, and 350 $< cz <$ 2000 km s^{-1}. The second is at KPNO, "Making Hay with ALFALFA" (Salzer PI). Targets for that project are randomly selected from ALFALFA grids, in order to determine the SFR cosmic density of the local universe. HIghMass galaxies are chosen from a more updated ALFALFA catalog, and there is no overlap with Hα3 targets in that redshift range.

4.3 Hα and R-band Observations and Data Reduction

4.3.1 Observations

All of the Hα and R imaging reported hereafter was obtained in Spring 2011 over 5 nights (2 other nights were lost to bad whether), using the T2KB detector on the 2.1m telescope at KPNO. The CCD has a pixel scale of 0.43″ pixel^{-1} and a chip size of 2048 $\times$ 2048, whereby all our targets can be easily imaged by a single pointing. The detector was used in the 3.1 e^- ADU^{-1} gain mode. The standard R filter is used to provide broadband imaging along with continuum subtraction for the narrowband images. Due to the wide spread of cz, a series of eight Hα filters are used, in ascending central wavelength, kp1564, kp1565, kp1495, kp1566, kp1496, kp1497, kp1498, and kp1517. Their bandpasses are superimposed on the velocity histograms in Fig. 4.3(a) by dotted lines in colors, with peak transmission $\sim 75\%$. The Hα filter for each source is selected to be

the one whose central wavelength best matches the cz of HI line; the FWHM of filters (~ 75 Å) are confirmed to be sufficient to cover the velocity width of HI line. However, [NII]$\lambda\lambda$6548 and [NII]$\lambda\lambda$6584 are in the filter bandpass with Hα in most cases. For the sake of clarity, while we will correct for this contamination when we calculate SFR from Hα luminosity in Section 4.5, we will generically refer to Hα as the total flux Hα+[NII] before then. The most distant galaxy UGC 8797 is excluded because of the lack of an appropriate availability of Hα filter. Two other HIghMass galaxies are dropped from this run: UGC 12506 (in fall sky) and UGC 7686 (GOLDmine data).

We utilized an observing mode similar to, but deeper than that used by the 'Making Hay with ALFALFA': a typical set of three Hα exposures (15 min each) and two or three R band exposures (3 min each). The R-band exposures provide sufficient S/N that the noise contribution of the R-band to the continuum-subtracted images will be insignificant, as well as important ancillary data. Calibration frames included afternoon bias and dome flat field. Observations of galaxies were bracketed by standard star exposures of both spectrophotometric standards HD19445, HD84937, and BD +26 2606 [Oke and Gunn, 1983], and Landolt [1992] standards (in both R and I bands yielding the color term), several times per night to calibrate the flux zero points. Galaxies requiring the same Hα filter were grouped into same nights to minimize the standard star exposures. There were three clear nights under photometric condition, only on which the standard stars were imaged, whereas the galaxy frames taken on the other non-photometric nights are calibrated by bootstrapping to the photometric frames, making best use of the observing time on non-photometric nights. The smoothed images (see below) have an average seeing of $\sim 1.''5$. However, none of the images were taken on photometric nights for UGC 4599. Plus, a

very bright star near UGC 190277 causes serious bleeding on the CCD, so it is further excluded. As a result, the final Hα measurements to be presented are for 29 HIghMass galaxies. Given the high Hα detection rate in HI-selected galaxies [Meurer et al., 2006] and even in LSB galaxies [Schombert et al., 2011], it is not surprising that Hα is detected in all of our targets.

4.3.2 Image Processing and Continuum Subtraction

The preliminary Hα and R-band image reduction follows standard procedures in IRAF: fixing header keywords, pedestal removing, trimming, bias subtracting, flat fielding, interpolating across the columns of bad pixels, and cosmic ray cleaning [using the task 'lacos_im'; van Dokkum, 2001]. All the frames have noticeable curvature at the edges; however, all the sample galaxies occupy only the inner 10% of the chip or less.

The processed narrowband images contain contributions from both Hα and underlying stellar continuum, and the accuracy of the continuum scaling and subtraction can be the dominant error source for galaxies with low emission-line equivalent widths [Kennicutt et al., 2008]. We adapt the IRAF package kindly provided by Salzer to our program, which conducts continuum subtraction, etc. A set of exposures for the same galaxy, including three Hα frames and two/three R frames, are first shifted to register to an R-band image taken on a photometric night (called R-reference frame), using $\gtrsim 12$ foreground stars across the images. The frame with lower airmass is preferred as the reference in case of multiple R frames. Given the rough central coordinates and pixel scales, astrometry is obtained by shifting and rotating, so as to cross correlate the po-

sitions of two stars, one at the center and another in the corner, to the J2000 coordinates of these stars in the USNO all-sky catalog. This solution of WCS is applied to all images which have been spatially aligned first. Then we average the FWHM of over seven stars near our galaxies and find out a frame with the worst seeing. All the other frames are convolved with a gaussian kernel to match this worst PSF. The same set of stars are used to determine the scaling factors subsequently.

All Hα images are normalized to the one taken on a photometric night and combined as the final 'ON' frame; similarly combined R image yields the final 'OFF' frame. Net Hα images are obtained by subtracting a scaled 'OFF' frame from the 'ON' frame. IRAF tasks 'geomap' and 'geotran' are run before the subtraction to improve image alignment if necessary. This scaling factor is determined by the ratio of transmissivity of two filters, the sky transparency if under non-photometric conditions, and the difference in exposure time, but we estimate it by the average of ratios between foreground star counts in the two frames, forcing the residual fluxes of stars to reach a minimum in the net Hα images. Our method implicitly assumes that field stars have no significant Hα emission on average, which is most likely to be valid, and it allows for sky transparency changes. For some large programs, e.g., Kennicutt et al. [2008], a uniform scaling factor can be derived by averaging the values from all galaxies observed in the same Hα filter. In our case, 5/8 Hα filters were used for only one or two galaxies thereby we skip this process.

4.3.3 Hα and R-band Surface Photometry

The reduction steps outlined above produced three combined images per galaxy that will be of further use: a net Hα, an unscaled R-band, and a scaled R-band. Considering the future studies, e.g., a comparison between the gas and SF surface density, both the integrated fluxes and one-dimensional profiles are of interest. Therefore, we performed careful surface photometry with the GALPHOT package [Huang et al., 2012b], a collection of IRAF scripts maintained by our group and modified to accommodate the KPNO images. Here we describe the procedures of measurements.

Isophotal Fitting

Several sky boxes are first selected surrounding the target galaxy but being far enough to avoid its extended emission. A constant sky background as the mean of pixel values in these boxes, excluding any sources got rejected by the 'imsurfit', is subtracted. Outside of the galaxy region, we use a automatic procedure to mask the contamination from foreground stars, background galaxies, and any of their residuals in the net Hα images. Then we mask by hand any unrelated sources within 2 radii of our targets. Starting from an initial guess, elliptical surface brightness contours were fitted to these cleaned images, using the STSDAS package ISOPHOTE, outwards to the radius at which the fitting fails to converge and inwards to the seeing limit. Final fits were visually inspected for robustness. This process is applied to all three combined images in order to refill the masked regions by interpolation. However, for consistency, only the set of ellipses as a result of fit to the unscaled R-band image are retained and used for aperture photometry on Hα and scaled R-band images, yielding

the azimuthally-averaged surface brightness profiles comparable in all bands. Disk portion of the surface brightness profile, with the most linear appearance, is selected; within this semi-major-axis range of the disk, averages of ellipse centroids, position angles (θ) and ellipticities ($\epsilon \equiv 1 - b/a$) are measured to characterize the global properties of a galaxy (tabulated in Table 4.2). This region is then fit to an exponential profile, yielding the disk scale length $r_{\rm d}$ and surface brightness interpolating to center, μ_0.

Global Magnitudes

Although we record several sets of global magnitudes, including ones at fixed isophotal levels, partial magnitudes integrated to a certain number of disk scale length (e.g., $\rm mag_8$ to $8r_{\rm d}$), and asymptotic magnitudes extrapolated to infinity from the exponential outer disk fit, we report hereafter the Petrosian magnitudes for the majority of our galaxies. SDSS adopts a definition of the Petrosian ratio as:

$$R_P(r) \equiv \frac{\int_{0.8r}^{1.25r} dr' 2\pi r' I(r') / [\pi(1.25^2 - 0.8^2) r^2]}{\int_0^r dr' 2\pi r' I(r') / (\pi r^2)}. \quad (4.1)$$

We follow a similar approach, but calculate the ratio in elliptical annuali rather than in circular rings. The Petrosian radius (r_P) is defined as the semi-major axis at which $R_P(r) = 0.2$, i.e., the radius where local surface brightness drops to 0.2 of the enclosed surface brightness. Our Petrosian magnitude denotes the flux in an elliptical aperture with $r = 2r_P$, and centroid, θ, and ϵ as given by the global measurements. We also calculate $r_{\rm petro,50}$ and $r_{\rm petro,90}$ as the semi-major axes of ellipses that contain 50% and 90% of the Petrosian flux, respectively.

The errors given on magnitudes in this chapter include the contributions from the photometric zero point error for a given night and the uncertainty in

determining the sky level (set to 0.15σ of the sky values in the sky boxes), in addition to the formal errors. In most cases, the Petrosian magnitudes agree with mag_8 (similar to the model magnitudes of disk galaxies in SDSS), within the magnitude errors (see below for the exception). However, in four galaxies, AGC 190796, AGC 203522, UGC 8089, and AGC 726428, the LSB Hα emission drops so slowly outwards that the outermost ellipse of confidential surface brightness measurement is reached before the Petrosian radius can be determined. We report mag_8 instead of Petrosian magnitudes for them in Table 4.2.

Absolute Flux Calibration

The instrumental magnitudes, $m_{\rm inst} \equiv -2.5 \log \mathrm{CR}$ (CR being the observed count rate in unites of counts s^{-1}), are calibrated to Johnson-Cousins and AB magnitude systems, respectively for R-band and Hα images, using the standard stars observed during the same nights as the objects. First, $m_{\rm inst}$ of standards are measured by 'phot'; the appropriate aperture size was determined for each star based on the radius at which the curve of growth for the sky leveled. For R-band calibration, we solve for the color coefficient (cc), extinction coefficient (κ), and zero point magnitude (ZP) in this equation with all Landolt standards from the same night:

$$m = m_{\rm inst} + cc(R - I) - \kappa\ \mathrm{AM} + \mathrm{ZP}, \tag{4.2}$$

where m is the calibrated magnitudes available in Landolt [1992], $R - I$ is the color of stars we measured, and AM is airmass. Note the colors of galaxies are later derived from SDSS magnitudes (see below). We get $\kappa = 0.091 \pm 0.002$, given multiple exposures for the same star on the first photometric night. The ZP are determined to be 23.968$\pm$0.006, 24.034$\pm$0.003, and 23.982$\pm$0.008 for the

three photometric nights, respectively, with high photometric quality.

For calibrations of Hα filters, because of the narrow bandpasses, color term is dropped and we adopt the standard KPNO κ values from IRAF STSDAS table, 'kpnoextinct'. The width of Hα filters we used translates to a ZP offset, and we only need to solve for ZP in this equation:

$$m_\nu - 2.5 \log \mathrm{FWHM} = m_{\mathrm{inst}} - \kappa \ \mathrm{AM} + \mathrm{ZP}, \tag{4.3}$$

where m_ν is the monochromatic magnitudes of spectrophotometric standards available in Oke and Gunn [1983] and FWHM is the width of Hα filters in unit of Å. AB magnitude can be converted to flux density, f_ν in units of erg s^{-1} cm^{-2} Å, via $m_\nu = -2.5 \log f_\nu - 48.60$ [Oke and Gunn, 1983], so that

$$m_\nu = -2.5 \log(\lambda^2 f_\lambda) - 2.408, \tag{4.4}$$

where wavelength λ is in unit of Å. Therefore, given the calibrated Hα magnitude $m_{\mathrm{cal}} = m_{\mathrm{inst}} - \kappa \ \mathrm{AM} + \mathrm{ZP}$, the line flux in units of erg s^{-1} cm^{-2} can be derived as

$$f_{\mathrm{H}\alpha+[\mathrm{NII}]} = 10^{-0.4(m_{\mathrm{cal}}+2.408+5 \log \lambda)}. \tag{4.5}$$

It must be taken into account that the R-band image used is contaminated by Hα flux, so that the continuum is over-subtracted. We correct for this effect following Kennicutt et al. [2008]. Because cz of our targets match very well with the central wavelengths of the Hα filters, the normalized Hα filter transmission is close to unit. The final correction factor is thus '$1/(1 - \frac{T_R}{T_{\mathrm{H}\alpha}} \frac{t_R}{t_{\mathrm{H}\alpha}} \frac{1}{F})$', where T_{filter} is filter transmission at wavelength λ, t_{filter} is exposure time (3 min in R and 15 min in Hα), and the R frame is divided by factor F so as to scale to Hα frame for the purpose of continuum subtraction. This corresponds to an increment of the final Hα flux by $\sim 4\%$ for most of our galaxies.

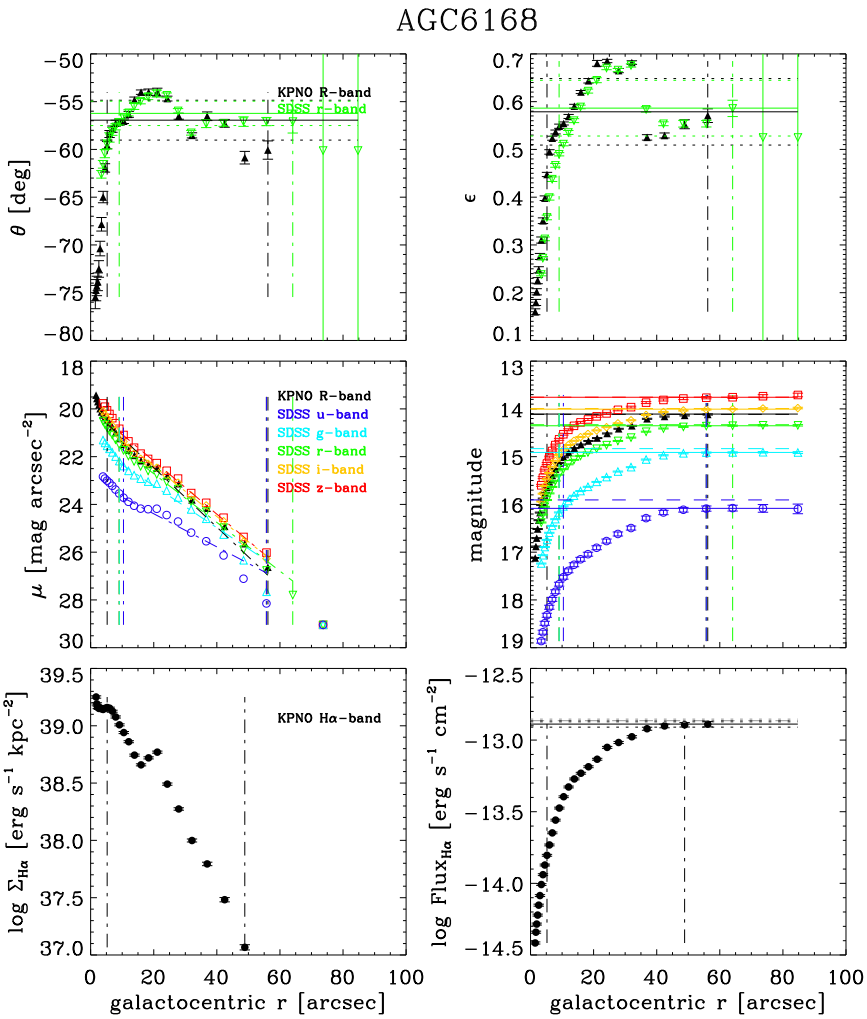

Figure 4.6: Example of the optical isophotal fitting for UGC 6168, a typical HIgh-Mass galaxy. The variation with semi-major axis of our KPNO measurements are shown by black filled symbols, and that of our SDSS measurements are shown by colored open symbols. All panels in order from left to right and from top to bottom are position angle (θ), ellipticity ($\epsilon \equiv 1 - b/a$), surface brightness (μ), enclosed magnitude (AB system), Hα surface brightness ($\Sigma_{\rm H\alpha+[NII]}$), and enclose H$\alpha$+[NII] flux. The marked inner disk region is denoted by vertical dash-dotted lines. Horizontal lines represent the magnitudes within $8r_{\rm d}$ ($\rm mag_8$, dashed) and Petrosian magnitudes (solid) in the magnitude or flux plot, and final values determined from the mean of data points in the inner disk region in the θ and ϵ plots. In between the horizontal dotted lines is the uncertainty range. Dashed lines in the μ plots show the linear fit to the light profiles.

Examples of the variation with semi-major axis of our KPNO measurements are shown by filled symbols in Fig. 4.6 – 4.8 for three galaxies, UGC 6168,

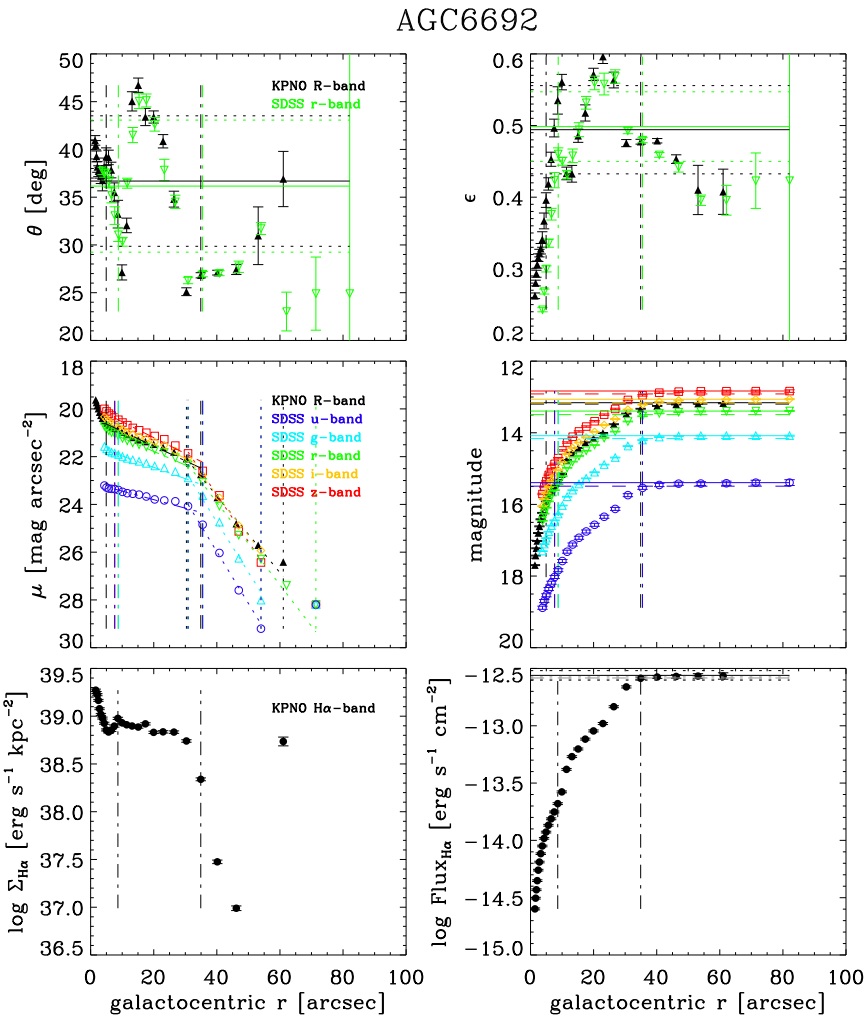

Figure 4.7: Example of the isophotal fitting for UGC 6692. The symbol definition is the same as that in Fig. 4.6. This galaxy exhibits a broken exponential disk feature (downward break) and the outer disk is in between the vertical dotted lines. Similar results are observed in a total of six HIghMass galaxies, implying a threshold in SF (see text).

UGC 6692, and UGC 9234, respectively (see more discussions of these profiles below). Black upwards triangles with error bars denote the R-band results in all of these plots; black filled circles with error bars are data points from Hα. The top two panels show position angles and ellipticities of a series of elliptical apertures as a result of the isophotal fitting. Black solid horizontal lines mark the global values as averages in the disk region (in between the two ver-

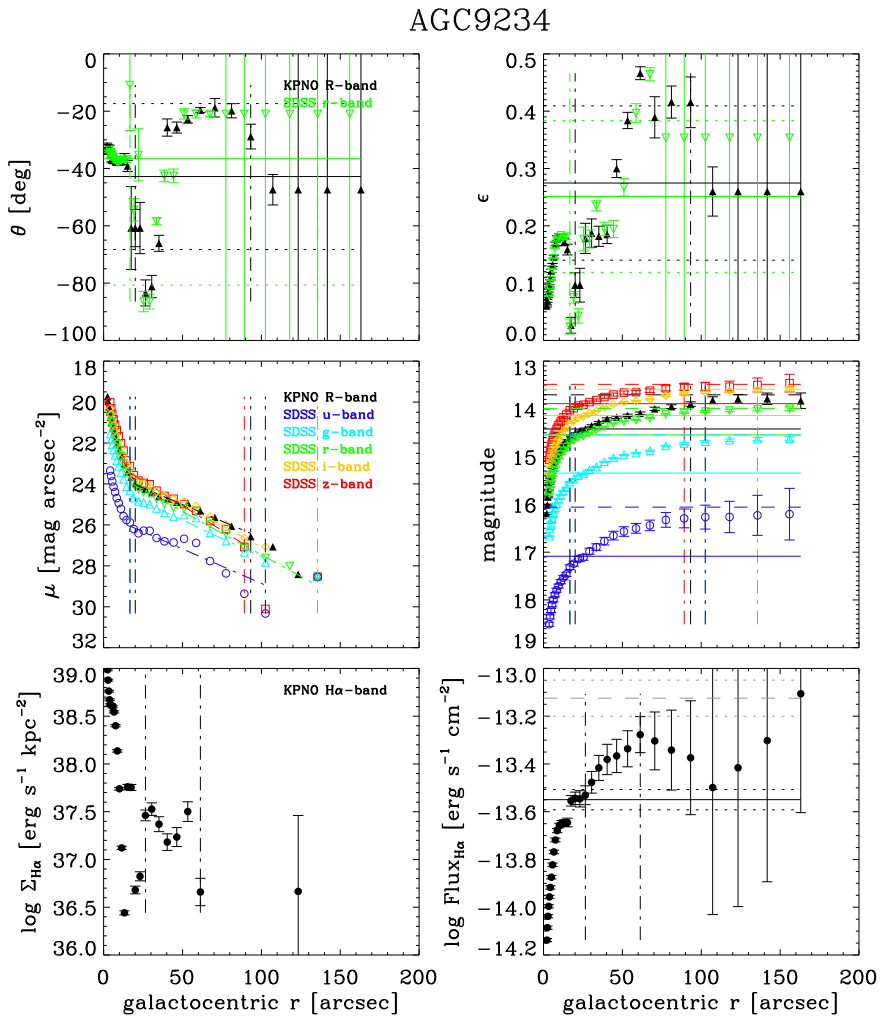

Figure 4.8: Example of the isophotal fitting for UGC 9234. The symbol definition is the same as that in Fig. 4.6. This galaxy has a compact central bulge but a LSB shallow outer disk (bright in UV). As a result, significant discrepancies between the mag_8 and Petrosian magnitudes exist.

tical dash-dotted lines); dotted horizontal lines illustrate the uncertainty range. The middle panels are surface brightness profiles and accumulated magnitudes, converted to AB magnitude system to be consistent with the SDSS results (see Section 4.4). Solid horizontal lines mark the Petrosian magnitudes; dashed horizontal lines mark the mag_8. The Petrosian magnitudes recover essentially all of the flux of our disk galaxies. The bottom panels are the same quantities from Hα in physical units, corrected for continuum over-subtraction. Definitions of

solid and dashed horizontal lines are the same as in the middle panels; dotted horizontal lines illustrate the uncertainty range. It is demonstrated that the Petrosian magnitudes generally agree with mag_8 within the uncertainty (in Fig. 4.6 and 4.7). The only exception is UGC 9234 with a compact central bulge but a shallow outer disk (see the middle left panel of Fig. 4.8). The strong break in surface brightness profile of this galaxy causes a large deviation between the two magnitudes, in a sense that the Petrosian magnitude severely undercounts the extended flux (see the middle and bottom right panels).

Hα Equivalent Widths

Finally, we calculated the Hα equivalent widths (EWs) from net Hα and scaled R-band images. By definition, it compares the line flux against underlying continuum level, so that EW can be derived without a calibration of absolute flux. It characterizes the strength of current SF relative to the past. Following Kennicutt et al. [2008], the EW in unit of Å, corrected for continuum over-subtraction is:

$$\mathrm{EW}_{\mathrm{H}\alpha+[\mathrm{NII}]} = \mathrm{FWHM}\frac{t_{\mathrm{H}\alpha}}{t_R}\frac{1}{10^{0.4(m_{\mathrm{H}\alpha}-m_{R'})} - T_R/T_{\mathrm{H}\alpha}}, \tag{4.6}$$

where FWHM, T_{filter}, and t_{filter} are defined as before, m_{filter}s are instrumental magnitudes in net Hα and scaled R-band images, respectively. We present the EW profiles of all 29 HIghMass galaxies with our KPNO measurements in Fig. 4.9, in order of ascending galaxy M_*. The EW is plotted as a function of semi-major axis in the second column; disk region with an exponential surface brightness profile is marked in between the vertical dash-dotted lines. Cleaned R-band and Hα images are shown in the third and forth columns, color scales inverted. Apertures within which the Petrosian magnitudes are measured are overlaid on these images, being absent if Petrosian radius is undefined.

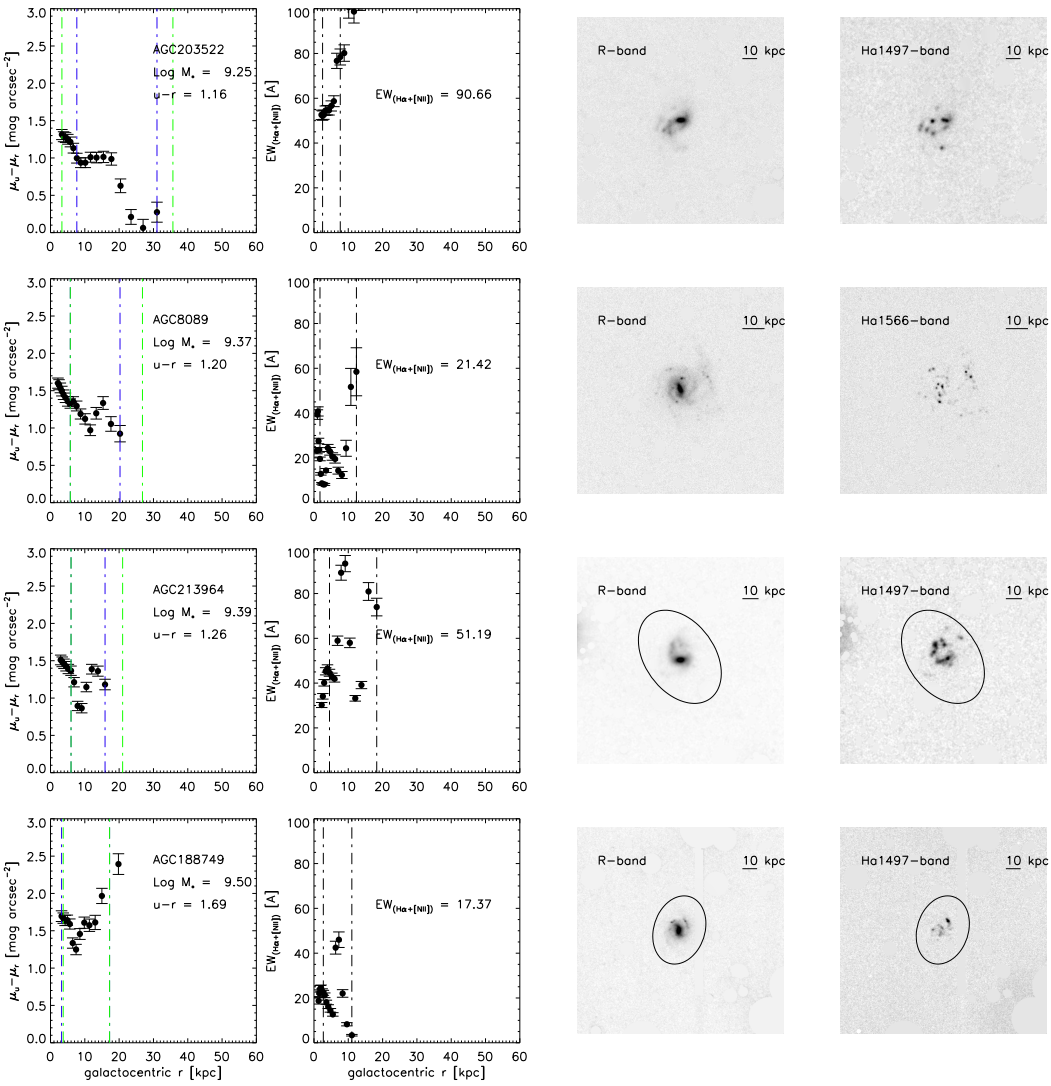

Figure 4.9: Profile measurements along with the inverted R-band and net Hα images (cleaned) for all 29 KPNO targets with photometry, in order of increasing M_*. Plotted in the first and second columns are the $u-r$ color and $\mathrm{EW}_{\mathrm{H}\alpha+[\mathrm{NII}]}$ profiles, respectively. The vertical line definition is the same as that in Fig. 4.6. The global color and EW values are given in corresponding panels. Petrosian magnitudes represent the flux within the elliptical apertures overlaid on the images, The mag_8 are adopted alternatively if the Petrosian radius are undetermined, in which cases the elliptical apertures are absent in the images.

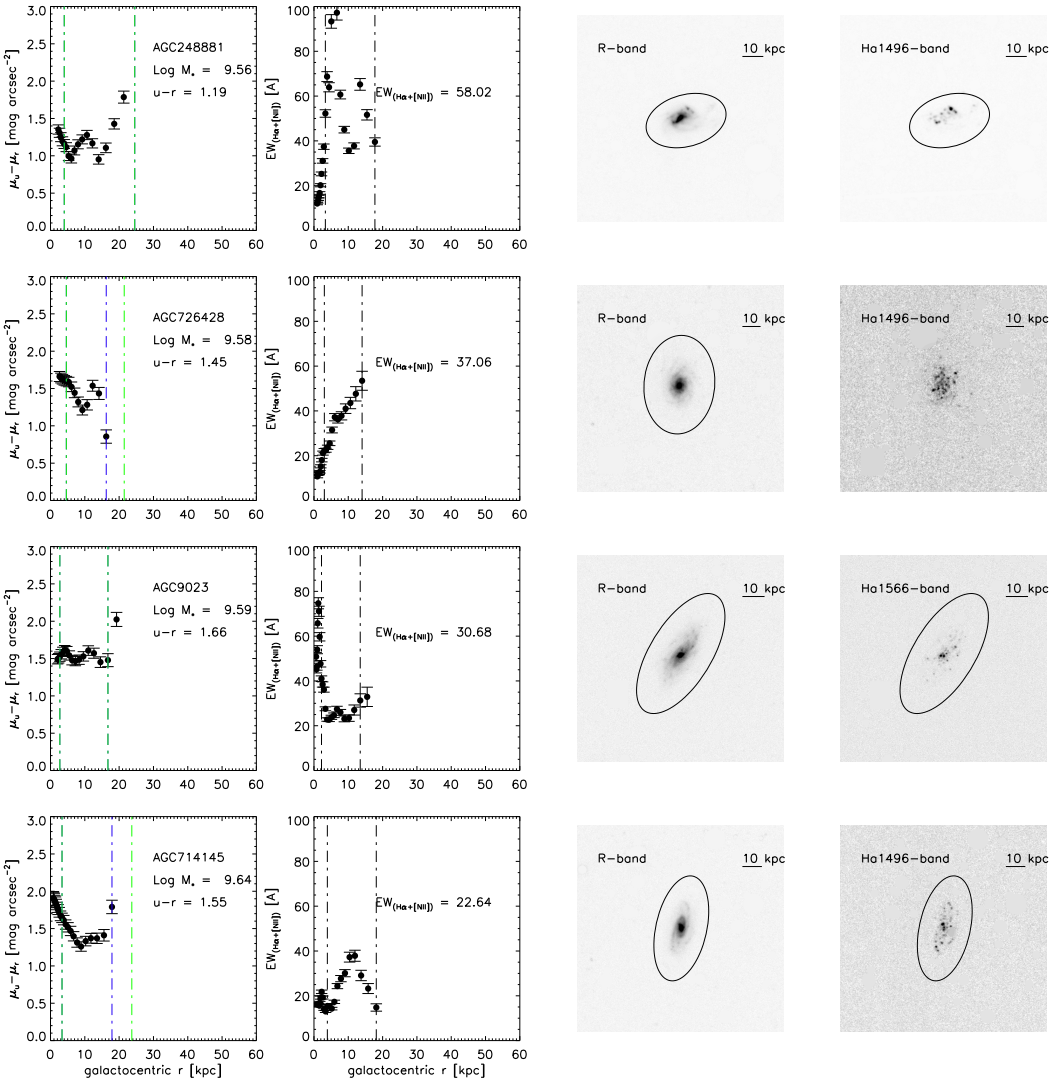

Figure 4.9: *Continued.*

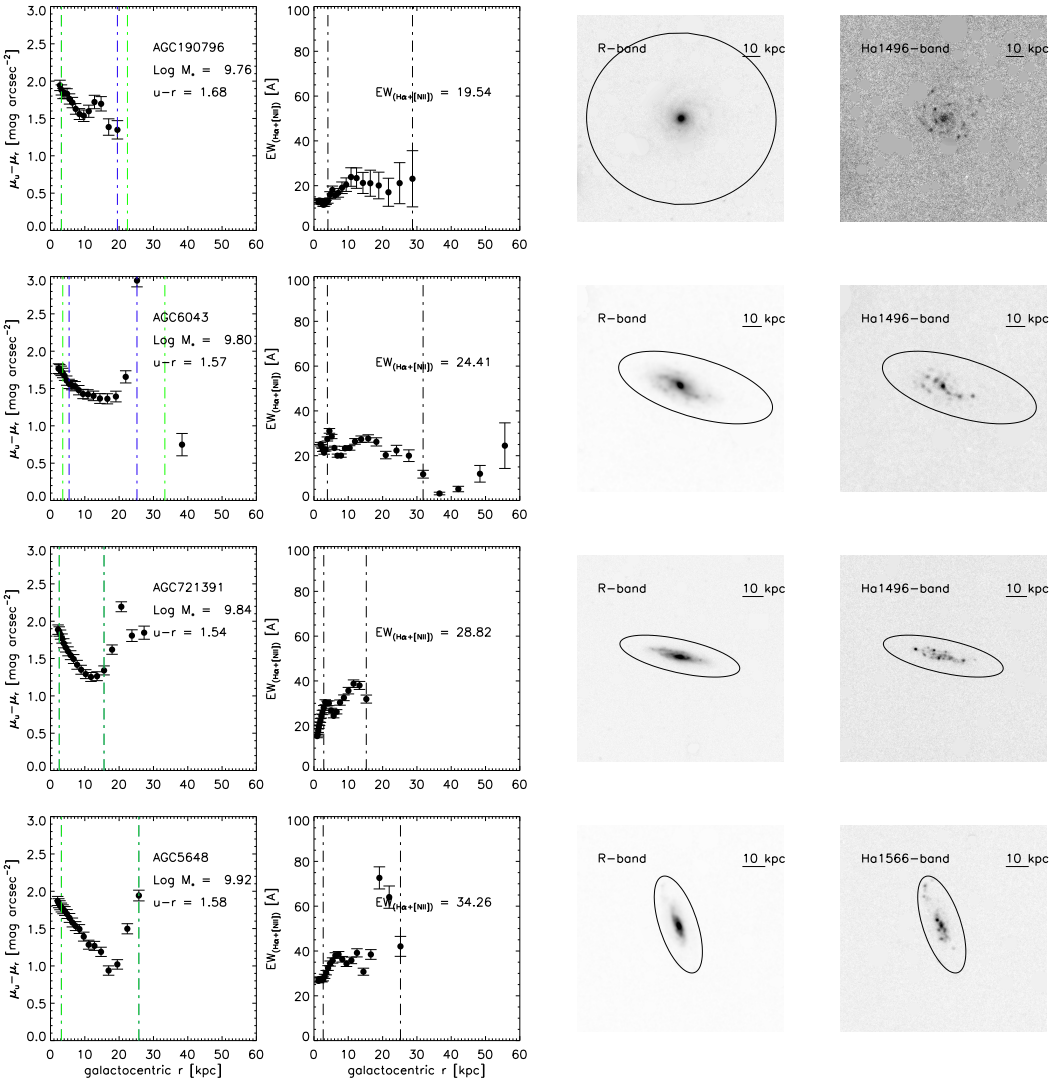

Figure 4.9: *Continued.*

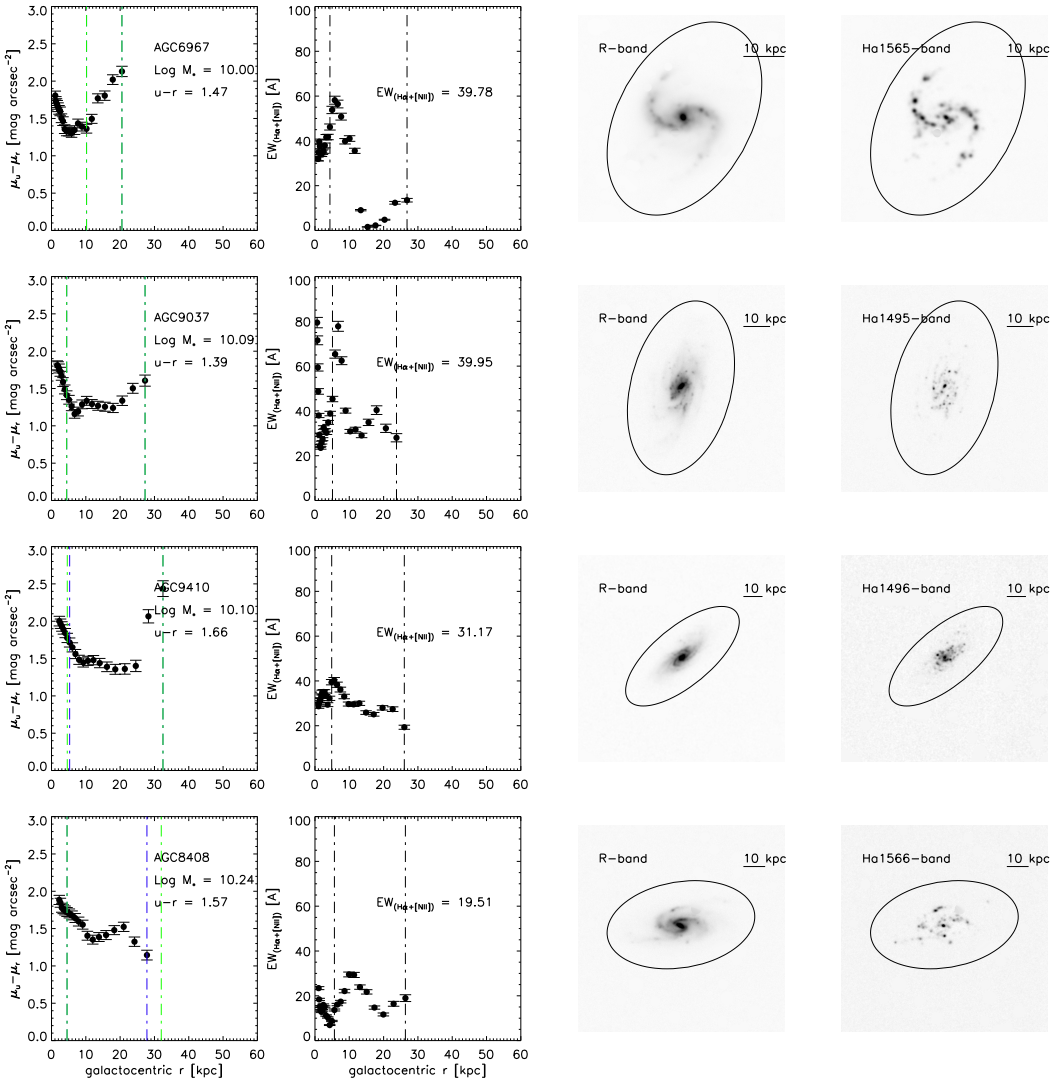

Figure 4.9: *Continued.*

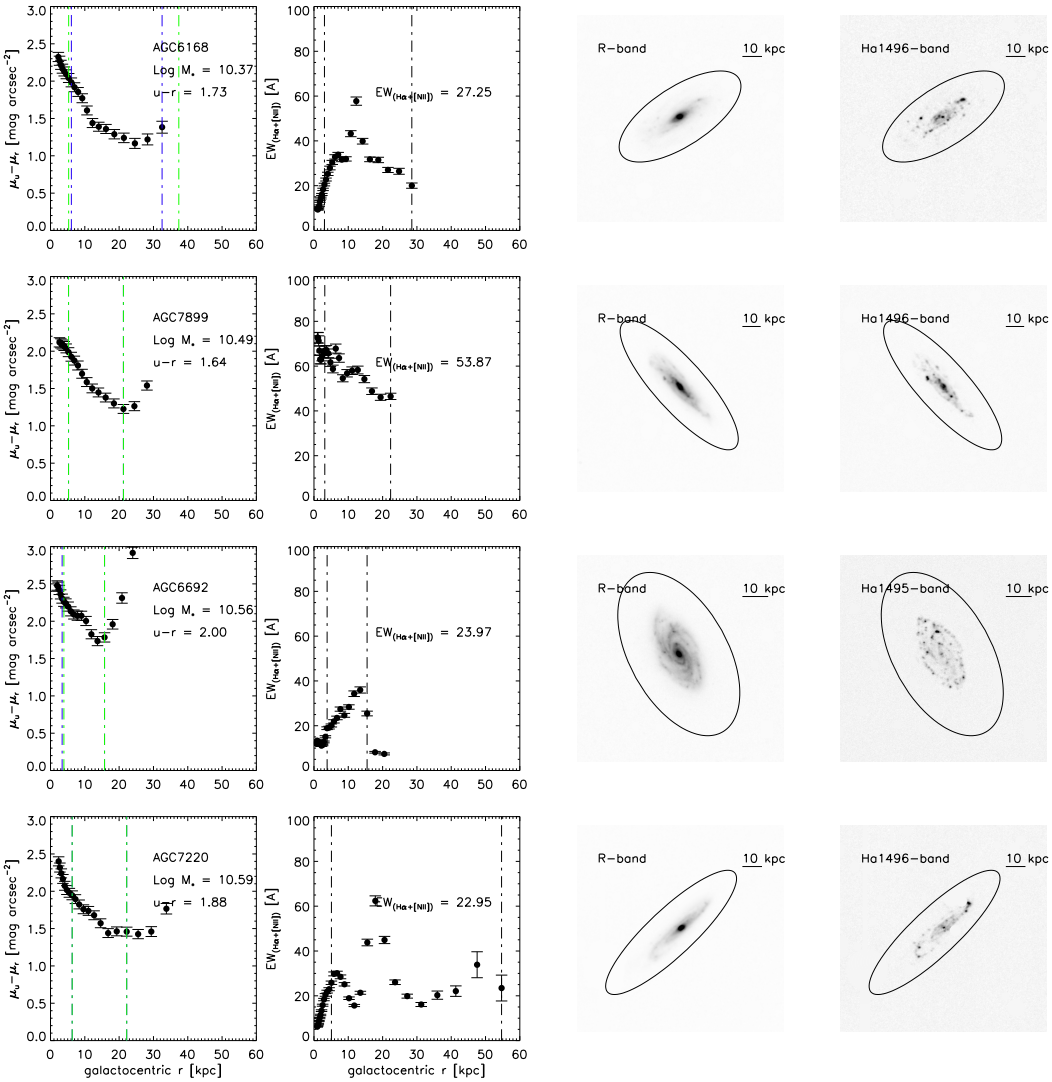

Figure 4.9: *Continued.*

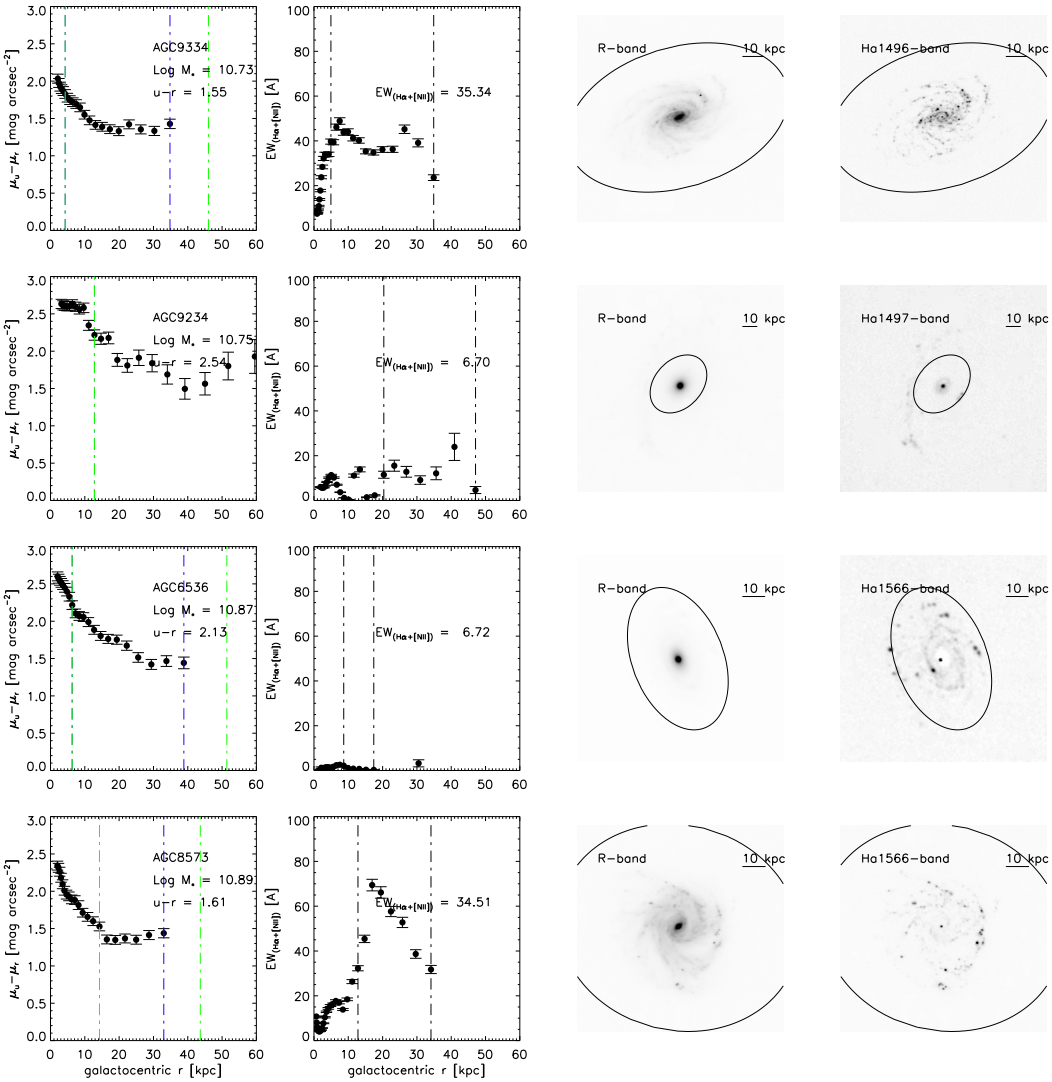

Figure 4.9: *Continued.*

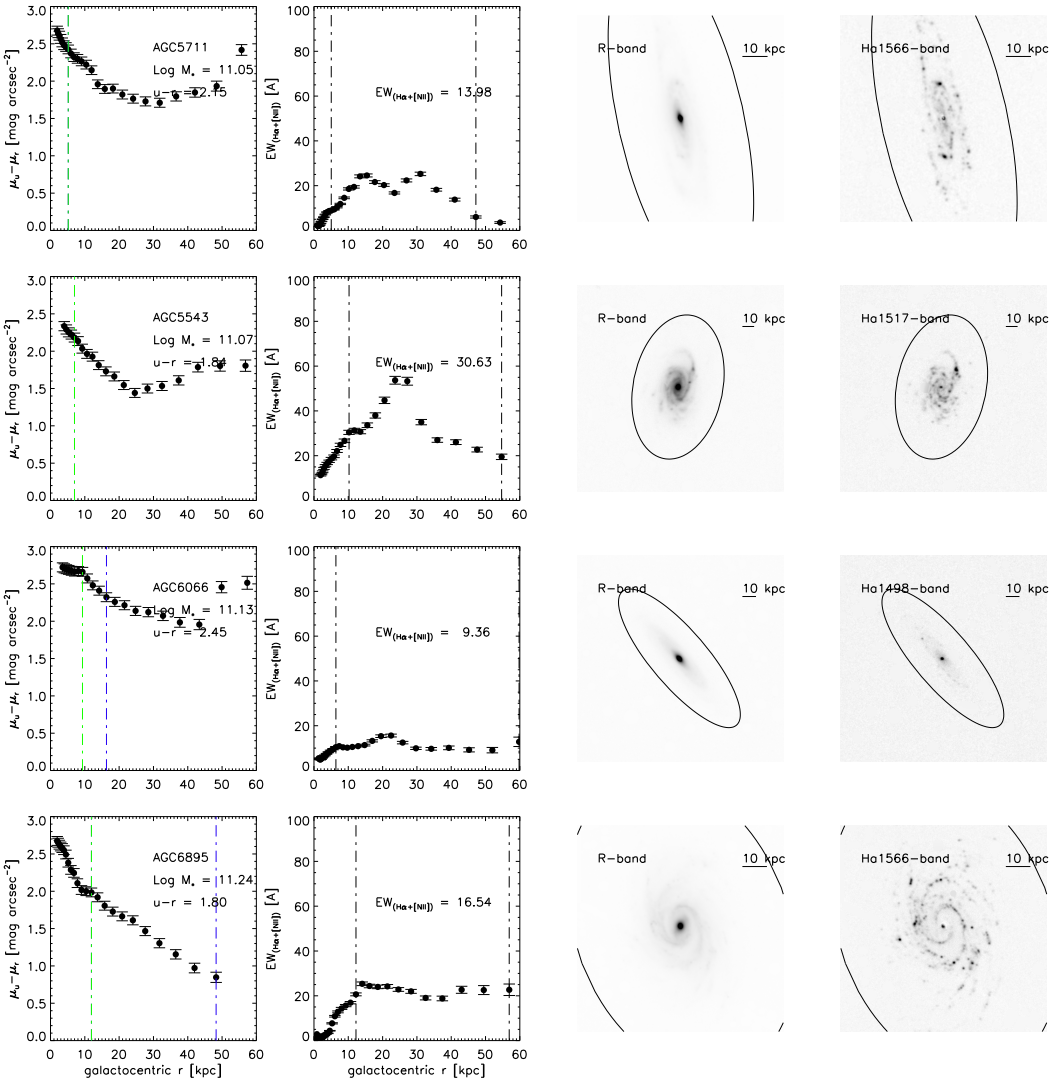

Figure 4.9: *Continued.*

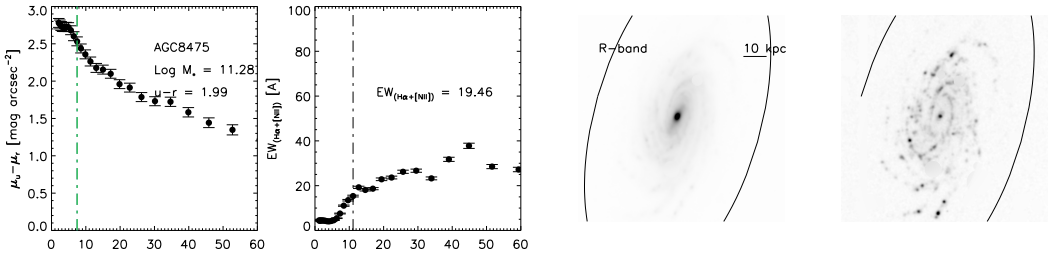

Figure 4.9: *Continued.*

4.3.4 Hα Photometry External Check

UGC 7686 in the GOLDmine dataset is not re-observed. All the Hα images presented here are new narrowband observations, and there are few literature measurements to compare for the purpose of external photometry quality check. We only find that UGC 8573 (NGC 5230) has been observed spectroscopically by Jansen et al. [2000a]. Jansen et al. [2000a] obtained integrated and nuclear spectra for 196 nearby galaxies (Nearby Field Galaxy Survey), in order to measure the current SFRs and metallicities of these galaxies. The spectrophotometric atlas of spectra as well as tables of EWs are presented. For UGC 8573, 77% of the total B-filter light is sampled in the integrated spectra, resulting in the spectroscopic induce measurements of $EW_{[NII]\lambda\lambda6548}$ = 2.1, $EW_{H\alpha}$ = 20.0, and $EW_{[NII]\lambda\lambda6584}$ = 7.0 Å for the integrated spectra. The corresponds numbers for the nuclear spectra are 1.2, 8.0, and 3.4 Å, respectively. Our global $EW_{H\alpha+[NII]}$ is determined to be 34.51±2.84 Å, given the flux inside the Petrosian aperture. Taking into account of the different apertures and the variation of EW in the galaxy, this agreement is satisfactory. Although only the emission-line fluxes relative to Hβ are presented in Jansen et al. [2000a], Kewley et al. [2002] calibrate these integrated fluxes to absolute fluxes by comparison with the B-band photometry. Accounting for the extinction inferred from the IR data, they derived an Hα SFR for NGC 5230 to be log SFR = 0.93 $M_{\odot}$ yr^{-1}, in rough agreement with our SED fitting result, being log SFR = 0.89±0.23 $M_{\odot}$ yr^{-1} (see Section 4.5).

We perform an independent check of the calibration of our Hα measurements by comparing the fluxes in the 3 arcsec nuclear apertures in our Hα images with the flux in the Hα+[NII] lines in the SDSS DR8 spectroscopic data [Brinchmann et al., 2004] obtained in 3 arcsec fibers (UGC 12506 is outside of

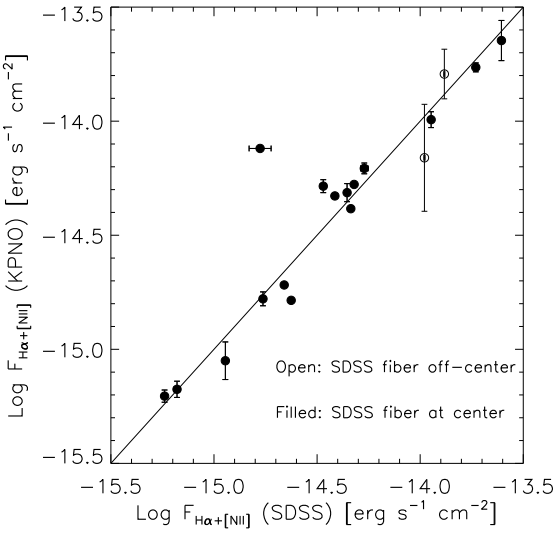

Figure 4.10: Hα photometry external check by comparing the fluxes in the nuclear apertures in our net Hα images with the fluxes in the Hα+[NII] lines according to the SDSS DR8 spectroscopic measurements. The open symbols represent the galaxies with the SDSS fiber position off-center, in opposite to the filled symbols at center. The solid diagonal line marks one-to-one relation.

the SDSS spectroscopic footprint). To reduce the impact of aperture effect, we focus on 18 galaxies with decent smoothed PSFs. Additional flux uncertainties are introduced into this comparison as a result of our astrometry uncertainty, as well as the offset from center in case of the SDSS fiber positions (e.g., UGC 8573, UGC 9334). We characterize this by the difference in fluxes we obtained from our net Hα image when placing the 3 arcsec aperture (1) at the coordinate of SDSS-reported fiber position and (2) at the R-band global centroid we derived earlier. In addition, we improve our astrometry by matching with the catalog in *scamp* [Bertin, 2006] and applying the new solution of astrometry with *swarp* [Bertin et al., 2002]. Note that the SDSS line fluxes are corrected for Galactic extinction. We assume $A(\mathrm{H}\alpha) = 2.6E(B-V)$ following Kennicutt et al. [2008], and $E(B-V)$ is given by the DIRBE measurements of diffuse IR emission [Schlegel et al., 1998]. Based on the HI systematic velocity, we find that [NII]$\lambda\lambda$6584 is

outside of the Hα filter for AGC 203522, UGC 8408, UGC 9023, UGC 9234, and AGC 188749, so that only the SDSS line fluxes of Hα and [NII]$\lambda\lambda$6548 are added up. The final comparison is shown in Fig. 4.10. Considering that the fluxes from our survey and the SDSS dataset have been measured using entirely different techniques (imaging *vs.* spectroscopic), the consistency of the respective fluxes is excellent. The only outlier, UGC 6066, has large uncertainties in SDSS measurements as a result of the low S/N spectra, making our flux more reliable.

4.3.5 Hα and R-band Photometry Catalog

Here we present the Hα and R-band measurements from our KPNO images of 29 HIghMass galaxies in Table 4.2. The [NII] and extinction corrections are applied only when calculating SFRs in the present chapter; hence any Hα EW values and line fluxes presented here are in fact for Hα+[NII], uncorrected for internal or Galactic extinction, but corrected for continuum over-subtraction. However, we have checked that all these corrections do not affect the qualitative results to be presented. Columns are as follows:

- Col(1): ALFALFA catalog identifier (also known as the AGC number).
- Col(2): KPNO Hα filter used in our observing run.
- Col(3): θ, PA with error measured on the R-band image, in unit of degree; north 0, increasing counterclockwise.
- Col(4): ϵ, ellipticity with error measured on the R-band image.
- Col(5): μ_0, disk surface brightness interpolating to center measured on the R-band image, in units of mag arcsec^{-2}, not corrected for inclination (see Section 4.6).

- Col(6): $r_{\rm d}$, disk scale length measured on the R-band image, in unit of arcsec.
- Col(7): $r_{\rm d,out}$, disk scale length of the outer disk (see Section 4.6); null if single disk.
- Col(8): $r_{\rm petro,50}$, semi-major axis of the ellipse that contains 50% of the R-band Petrosian flux, in unit of arcsec.
- Col(9): $r_{\rm petro,90}$, semi-major axis of the ellipse that contains 90% of the R-band Petrosian flux, in unit of arcsec.
- Col(10): d_{25}, major axis of the ellipse that associates with an isophot of 25 mag arcsec^{-2}, in unit of arcsec.
- Col(11): R-band magnitude with error in Johnson-Cousins system; with (without) superscription if mag$_8$ (Petrosian magnitude).
- Col(12): Logarithm of the line flux of Hα+[NII] with error, in units of erg s^{-1} cm^{-2}; with (without) superscription if mag$_8$ (Petrosian magnitude).
- Col(13): EW of the Hα+[NII] lines with error, in unit of Å.
- Col(14): Logarithm of the SFR derived from Hα luminosity (see Section 4.5), in units of $M_\odot$ yr^{-1}; all corrections applied.

Table 4.2: KPNO measurements of the HIghMass sample

AGC	Hα filter	θ [deg]	ϵ	μ_0 [mag arcsec^{-2}]	$r_{\rm d}$ [arcsec]	$r_{\rm d,out}$ [arcsec]	$r_{\rm petro,50}$ [arcsec]	$r_{\rm petro,90}$ [arcsec]	d_{25} [arcsec]	R [mag]	$\log F_{\rm H\alpha+[NII]}$ [erg s^{-1} cm^{-2}]	EW$_{\rm H\alpha+[NII]}$ [Å]	$\log {\rm SFR(H}\alpha)$ [$M_\odot$ yr^{-1}]
188749	1497	-17.86(28.92)	0.27(0.14)	20.87	4.24	...	8.52	18.55	32.22	16.00(0.03)	-13.86(0.13)	17.37(5.56)	-0.39(0.18)
190796	1496	85.62(43.28)	0.09(0.05)	21.92	8.77	...	17.92	57.88	49.78	14.96(0.19)	-13.47(0.12)*	19.54(5.68)	-0.22(0.19)
721391	1496	78.82(1.34)	0.69(0.05)	20.22	9.89	5.66	12.38	27.80	86.98	14.81(0.03)	-13.16(0.04)	28.82(2.95)	0.32(0.28)
5543	1517	-11.19(6.06)	0.39(0.06)	19.83	10.13	...	15.19	37.68	96.49	13.30(0.02)	-12.53(0.02)	30.63(1.41)	1.25(0.24)
5648	1566	18.36(1.73)	0.63(0.05)	19.46	6.72	...	10.64	26.96	68.54	14.40(0.01)	-12.98(0.02)	34.26(1.83)	0.34(0.24)
5711	1566	12.69(1.82)	0.65(0.06)	20.16	23.37	...	29.89	89.65	208.48	12.22(0.01)	-12.45(0.03)	13.98(0.88)	1.03(0.36)
203522	1497	-84.24(5.90)	0.43(0.06)	21.13	4.35	5.13	...	...	30.98	15.98(0.02)*	-13.14(0.01)*	90.66(2.85)	0.47(0.17)
6043	1496	62.59(6.44)	0.56(0.04)	21.07	10.71	34.70	17.92	37.03	77.61	14.75(0.01)	-13.21(0.06)	24.41(3.90)	0.22(0.25)
6066	1498	40.47(2.15)	0.68(0.08)	20.45	14.54	...	10.89	49.22	121.71	13.62(0.02)	-13.17(0.06)	9.36(1.29)	0.88(0.34)
6168	1496	-56.94(2.09)	0.58(0.07)	19.92	8.72	...	13.11	36.45	81.67	14.05(0.01)	-12.89(0.02)	27.25(1.50)	0.57(0.26)
6536	1566	21.22(5.61)	0.38(0.05)	20.88	18.22	...	11.73	48.33	138.11	12.68(0.01)	-12.95(0.01)	6.72(0.25)	0.13(0.20)
6692	1495	36.68(6.83)	0.49(0.06)	20.27	17.63	6.75	24.26	38.62	153.57	13.10(0.01)	-12.56(0.04)	23.97(2.45)	0.49(0.20)
213964	1497	35.84(46.63)	0.32(0.10)	21.18	5.69	...	10.93	29.34	39.99	15.68(0.02)	-13.26(0.03)	51.19(3.91)	0.08(0.15)
6895	1566	20.85(13.22)	0.31(0.04)	19.78	19.75	...	28.97	74.64	190.00	11.62(0.02)	-12.11(0.04)	16.54(1.42)	0.96(0.24)
6967	1565	-29.26(51.46)	0.36(0.17)	19.41	12.40	...	28.62	47.49	127.79	12.60(0.02)	-12.03(0.01)	39.78(1.32)	0.31(0.11)
7220	1496	-49.21(1.78)	0.70(0.09)	20.26	14.58	11.67	14.69	43.21	127.32	13.84(0.01)	-12.88(0.03)	22.95(1.61)	0.90(0.35)
7899	1496	41.23(2.30)	0.70(0.06)	19.53	11.71	4.96	17.32	37.51	118.02	13.63(0.01)	-12.45(0.01)	53.87(1.14)	1.20(0.30)
8089	1566	-19.33(44.79)	0.29(0.19)	21.17	7.03	...	...	...	49.65	15.23(0.03)*	-13.50(0.04)*	21.42(2.22)	-0.47(0.14)
8408	1566	99.44(3.31)	0.42(0.11)	20.08	10.56	...	16.89	39.10	95.78	13.52(0.02)	-12.83(0.04)	19.51(2.04)	0.41(0.19)
8475	1566	-15.90(3.65)	0.52(0.05)	19.88	23.58	...	37.95	86.77	222.35	11.73(0.01)	-12.10(0.01)	19.46(0.62)	1.33(0.30)
8573	1566	75.96(46.60)	0.15(0.06)	19.84	15.46	...	25.87	51.98	147.03	12.01(0.02)	-11.97(0.03)	34.51(2.84)	0.96(0.15)
9023	1566	138.14(5.93)	0.51(0.09)	20.96	10.11	5.95	14.44	32.22	75.22	14.88(0.06)	-13.19(0.12)	30.68(8.99)	0.04(0.21)
248881	1496	-64.47(14.67)	0.43(0.12)	19.82	4.95	12.47	10.51	25.27	47.29	14.85(0.02)	-12.90(0.01)	58.02(2.44)	0.38(0.22)

Table4.2 – Continued

AGC	Hα filter	θ [deg]	ϵ	μ_0 [mag arcsec^{-2}]	$r_{\rm d}$ [arcsec]	$r_{\rm d,out}$ [arcsec]	$r_{\rm petro,50}$ [arcsec]	$r_{\rm petro,90}$ [arcsec]	d_{25} [arcsec]	R [mag]	$\log F_{\rm H\alpha+[NII]}$ [erg s^{-1} cm^{-2}]	EW$_{\rm H\alpha+[NII]}$ [Å]	$\log {\rm SFR(H}\alpha)$ [$M_\odot$ yr^{-1}]
9037	1495	-14.28(6.10)	0.43(0.07)	20.20	12.22	...	17.19	45.88	108.03	13.29(0.02)	-12.43(0.04)	39.95(3.62)	0.56(0.20)
726428	1496	-4.86(7.18)	0.28(0.05)	20.93	5.78	...	9.23	25.79	43.34	15.42(0.05)	-13.34(0.02)*	37.06(1.65)	-0.13(0.12)
9234	1497	-42.81(25.46)	0.27(0.13)	23.32	33.31	...	6.21	19.19	103.18	14.36(0.02)	-13.55(0.04)	6.70(0.67)	-0.02(0.19)
9334	1496	-73.01(5.29)	0.38(0.09)	19.71	13.12	...	22.83	52.09	127.70	12.53(0.02)	-12.16(0.03)	35.34(2.54)	1.02(0.21)
714145	1496	-12.56(5.34)	0.52(0.05)	20.56	6.67	...	9.86	25.22	54.50	15.23(0.04)	-13.43(0.07)	22.64(3.80)	-0.07(0.22)
9410	1496	-50.44(2.65)	0.58(0.04)	20.21	8.68	...	12.60	33.26	76.61	14.45(0.01)	-12.99(0.02)	31.17(1.58)	0.40(0.22)

4.4 Reprocessed SDSS Photometry

4.4.1 Surface and Integral Photometry

Because many gas rich galaxies appear to be patchy due to star forming regions throughout the disk, the standard SDSS pipeline will easily suffer from shredding [Huang et al., 2012b]. Furthermore, the automatic sky background subtraction is optimized for more distant galaxies with small angular sizes, but will lead to over subtraction for large or LSB galaxies. As a result, we independently recomputed photometric quantities for all 34 HIghMass galaxies, making use of an IRAF pipeline adapted from 'GALPHOT'.

Header-supplemented corrected frames are retrieved from SDSS DR7 in five bands, *u, g, r, i, z*. Multiple adjacent frames are combined if our target is on image edge. Following the treatment to Hα and R-band images in Section 4.3, all the other bands are first shifted to align with the r-band image and smoothed to a common PSF. The target region is marked by hand and images are trimmed to have the target lie at center. A constant local sky background is subtracted and the two step cleaning procedure is conducted. Elliptical isophotal fitting is applied to all images in order to interpolate over the contaminating sources for all bands, but we use the same set of apertures given by the r-band fitting on all images for consistency. We obtain one-dimensional profiles, as a function of semi-major axis, of the centroid, θ, ϵ, and surface brightness of all elliptical isophots.

Among various global magnitudes we calculated, the Petrosian magnitudes are preferred. Alternatively, we adopt mag_8 in all bands if Petrosian radius is

undetermined in any band to ensure the reliability of colors that are obtained from comparable apertures. To convert counts to AB magnitudes, we follow the convention of SDSS asinh magnitudes:

$$m_{\rm SDSS} = -(2.5/\ln(10)) \times [{\rm asinh}(({\rm CR} \times 10^{0.4(aa+kk{\rm AM})})/2b) + \ln(b)],$$

where the photometric zeropoint (aa), extinction coefficient (kk), and softening parameter (b) are found in image headers. However, we confirm that all of our galaxies are detected in SDSS bands with high S/N so that the difference between asinh magnitudes and conventional magnitudes is less than 1%.

The SDSS measurements of three galaxies are presented by colored open symbols along with the KPNO results by black filled symbols in the top four panels of Fig. 4.6 – 4.8; u-band data are denoted by blue circles, g by cyan upward triangles, r by green downward triangles, i by yellow diamonds, and z by red squares. Definitions of the lines are the same as those of the KPNO data. Although only three representative cases are shown, it is generally true that the elliptical isophot fitting to r-band image performed independently from the R-band fitting generates similar sets of apertures possessing similar variations of the θ and ϵ with semi-major axis: the fitting result is robust and insensitive to the initial assumptions of aperture orientation. The global θ and ϵ measurements from r- and R-band images also agree with each other within the uncertainties. Because R and Hα surface photometries are performed in the same set of apertures, we can derive EW$_{\rm H\alpha}$ profiles. Meanwhile, surface brightness is measured in the same set of apertures for all SDSS bands, and thus we can obtain the azimuthally-averaged broadband color profiles, which are demonstrated in the first column of Fig. 4.9 for the $u-r$ color. In between the vertical dash-dotted lines are the disk regions in u (blue lines) and r (green lines) bands, respectively.

4.4.2 Broadband Photometry Quality Check

Internal Comparison

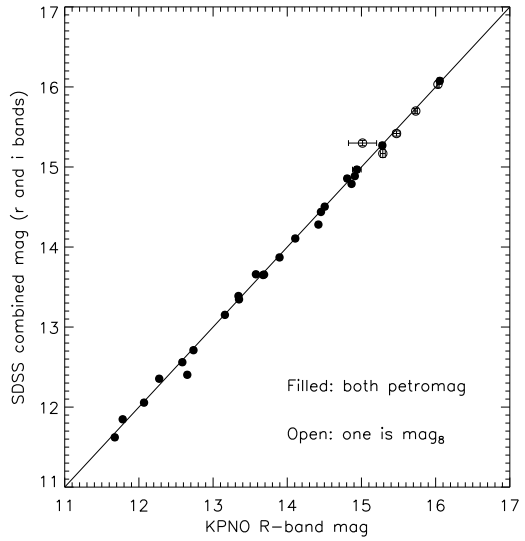

Figure 4.11: Broadband photometry internal check by comparing the global R-band magnitudes measured on the KPNO images with the r- and i-band combined magnitudes measured on the SDSS images. The filled symbols denote galaxies for which the Petrosian magnitudes are adopted in all bands, being open symbols otherwise. The solid diagonal line marks one-to-one relation.

In Fig. 4.11, we check the internal consistency of broadband photometry by comparing the KPNO R-band magnitudes with the same quantities inferred by the combined SDSS magnitudes, using the transformation, $R = r - 0.2936(r-i) - 0.1439;\ \sigma = 0.0072$. The KPNO magnitudes on the Johnson-Cousins standard photometric system are placed onto the AB system by correcting for the color zero-point differences between these systems: $R_{\rm Johnson} = R_{\rm AB} - 0.055$. The most extreme outlier in this plot is AGC 190796. Its KPNO R-band magnitude is measured inside the Petrosian aperture, whereas its SDSS combined magnitude comes from $\rm mag_8$ because the Petrosian radius is available only on the r-band image. This Malin-like galaxy has a relatively steeper inner disk but the surface

brightness drops off slowly throughout the outer disk. The disk scale length is thus underestimated from the inner fit. In all, we demonstrate that our SDSS-derived R-band magnitudes agree with the KPNO measurements without any systematic offset. This gives further confidence that our KPNO flux calibration is reliable. Plus, the two separate ellipse fittings give consistent θ, ϵ, and surface brightness profiles.

External Comparison

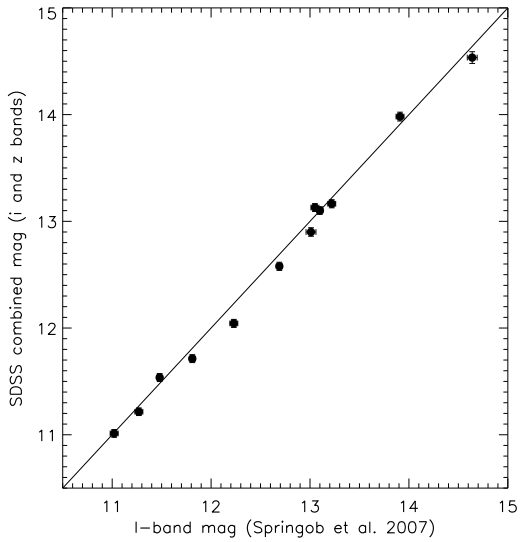

Figure 4.12: Broadband photometry external check by comparing the global I-band magnitudes given in the Springob et al. [2007] with the i- and z-band combined magnitudes obtained from the SDSS images. The solid diagonal line marks one-to-one relation.

We perform external checks with the I-band catalog from SFI++ Tully-Fisher Survey [Springob et al., 2007], as well as the SDSS DR8 pipeline measurements. I-band magnitudes are derived from our SDSS magnitudes via $I = i - 0.3780(i - z) - 0.3974;\ \sigma = 0.0063$. We note that the SFI++ program was led by our early group members and a similar photometry procedure was

followed. It is not surprising to see he excellent agreement between our results (Petrosian magnitudes preferred) and the SFI++ results (mag_8) for 12 galaxies in common in Fig. 4.12. We mention that UGC 8573 has been observed by Jansen et al. [2000b] and their B-band magnitude also agree with ours.

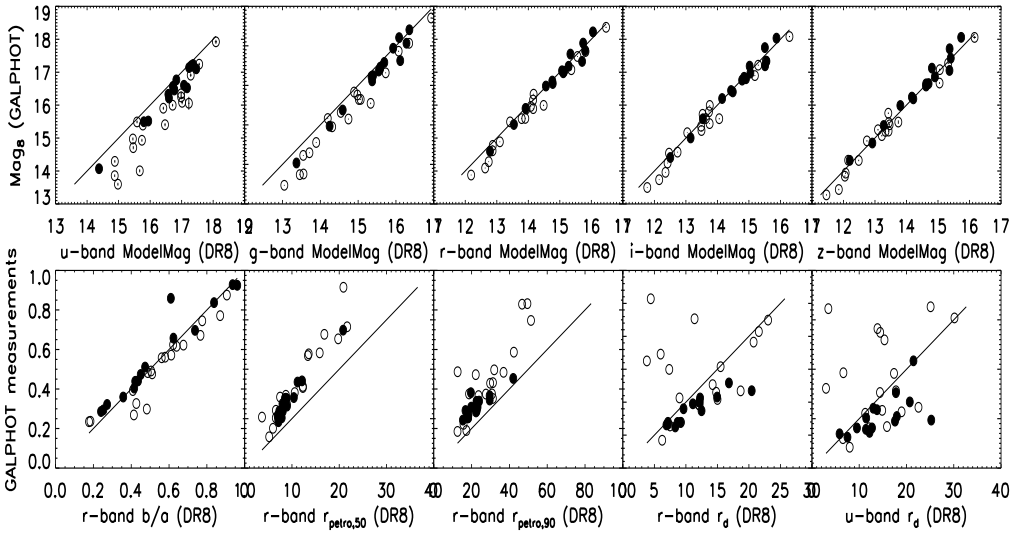

Figure 4.13: GALPHOT measurements in comparison with the SDSS DR8 pipeline results. The solid diagonal line marks one-to-one relation in all panels. GALPHOT-derived mag_8 are plotted against the SDSS model magnitudes for all five bands in the first row. The shredded pipeline measurements confirmed by visual inspections are represented by open symbols, being filled if no evident shredding. Additional comparisons are presented in the second row for the r-band axial ratio, $r_{\mathrm{petro},50}$, $r_{\mathrm{petro},90}$, and disk scalelength, as well as the u-band disk scalelength.

In addition we retrieved the SDSS images from DR7 database but we compare our results with the DR8 pipeline measurements, given the fact that DR8 is superior to DR7 mainly due to the changes in image processing rather than

re-observing. Although the sky background subtraction is improved in DR8 [Blanton et al., 2011], the problem of shredding still retains. We identify the HIghMass galaxies with problematic DR8 photometry in at least one band and they are represented by open circles in Fig. 4.13. The rest of galaxies as filled circles in the same figure can be cross correlated to a single photometric object that dominates in flux. The top panels illustrate comparisons between our mag_8 and the DR8 model magnitudes in five bands, respectively. Obviously, fluxes are under represented by the pipeline magnitudes, especially in bluer bands and among the galaxies suffering from shredding. It suggests an inconsistency of flux redistribution among multiple children in different bands, in a sense that the bluer star-forming regions are more likely to be identified as separate photometric objects. Therefore, the pipeline magnitudes result in redder colors than our measurements, and subsequently lower SSFRs. The lower panels show comparisons of more quantities, e.g., axial ratio, $r_{\mathrm{petro},50}$, $r_{\mathrm{petro},90}$, and disk scale length r_{d}. Both axial ratio measurements have been corrected for the seeing effect and no systematic deviation exists. However, our Petrosian magnitudes are derived in elliptical apertures, so that our $r_{\mathrm{petro},50}$ and $r_{\mathrm{petro},90}$ are systematically larger than the same pipeline values derived in circular apertures. Large scatters are seen in the last two panels; the most extreme outliers with much smaller pipeline r_{d}s suffer from shredding at the same time (being open circles). These indicate that the pipeline axial ratio can be a good proxy to infer the circular velocity from HI line width by an inclination correction, whereas the derived quantities depending on r_{d} are more vulnerable to large scatter, e.g., the empirical λ values obtained in Huang et al. [2012a].

4.4.3 SDSS photometry Catalog

Here we present the SDSS measurements by our modified GALPHOT package of all 34 HIghMass galaxies, along with the SED fitting derived quantities to these five bands in Table 4.3. Magnitudes are in the AB systems, uncorrected for internal or Galactic extinction. Columns are as follows:

- Col(1): ALFALFA catalog identifier (also known as the AGC number).
- Col(2)-Col(6): Magnitudes with error in five bands, respectively; with (without) superscription if mag_8 (Petrosian magnitude).
- Col(7): A_r, r-band internal extinction with error, derived by SED fitting [prior A_r distribution applied; Huang et al., 2012a], in unit of mag.
- Col(8): Logarithm of stellar mass with error, derived by SED fitting, in unit of $M_\odot$.
- Col(9): Logarithm of SFR with error, derived by SED fitting, in units of $M_\odot$ yr^{-1}; all corrections applied.

Table 4.3: SDSS measurements of the HIghMass sample

AGC	u [mag]	g [mag]	r [mag]	i [mag]	z [mag]	A_r [mag]	$\log M_*$ [$M_\odot$]	$\log \mathrm{SFR(SED)}$ [$M_\odot$ yr^{-1}]
188749	18.00(0.14)	16.68(0.02)	16.31(0.02)	16.01(0.02)	16.05(0.09)	0.18(0.14)	9.50(0.08)	-1.28(0.98)
4599	15.71(0.05)	14.18(0.01)	13.54(0.01)	13.14(0.01)	12.95(0.02)	0.16(0.13)	9.62(0.17)	-2.05(0.93)
190796	17.23(0.07)*	15.94(0.01)*	15.55(0.01)*	15.18(0.01)*	15.12(0.03)*	0.20(0.16)	9.76(0.11)	-0.61(0.88)
721391	16.57(0.05)	15.45(0.01)	15.02(0.01)	14.71(0.01)	14.54(0.03)	0.62(0.30)	9.84(0.08)	0.41(0.25)
190277	17.25(0.06)	16.11(0.01)	15.62(0.01)	15.27(0.01)	15.28(0.04)	0.50(0.22)	9.70(0.07)	0.07(0.23)
5543	15.44(0.05)	14.16(0.01)	13.60(0.01)	13.23(0.01)	13.07(0.02)	0.47(0.26)	11.07(0.09)	1.08(0.31)
5648	16.23(0.05)	15.12(0.01)	14.66(0.01)	14.40(0.01)	14.19(0.02)	0.54(0.27)	9.92(0.08)	0.38(0.23)
5711	14.76(0.07)	13.31(0.01)	12.61(0.01)	12.23(0.01)	11.92(0.03)	0.90(0.39)	11.05(0.10)	0.83(0.58)
203522	17.39(0.15)	16.43(0.02)	16.23(0.02)	16.04(0.03)	16.12(0.13)	0.33(0.19)	9.25(0.08)	0.12(0.51)
6043	16.63(0.11)	15.45(0.01)	15.05(0.02)	14.87(0.02)	14.61(0.06)	0.50(0.27)	9.80(0.10)	0.18(0.61)
6066	16.38(0.07)	14.70(0.01)	13.93(0.01)	13.47(0.01)	13.22(0.02)	0.91(0.37)	11.13(0.10)	-0.01(1.03)
6168	16.08(0.06)	14.91(0.01)	14.35(0.01)	14.00(0.01)	13.76(0.03)	0.55(0.29)	10.37(0.08)	0.57(0.24)
6536	15.08(0.05)	13.63(0.01)	12.96(0.01)	12.61(0.01)	12.35(0.02)	0.34(0.22)	10.87(0.10)	-0.06(0.90)
6692	15.39(0.07)	14.08(0.01)	13.39(0.01)	13.06(0.01)	12.83(0.03)	0.35(0.21)	10.56(0.09)	0.20(0.46)
213964	17.14(0.05)*	16.21(0.01)*	15.88(0.01)*	15.75(0.01)*	15.71(0.03)*	0.21(0.16)	9.39(0.06)	0.06(0.18)
6895	13.67(0.06)	12.49(0.01)	11.88(0.01)	11.49(0.01)	11.27(0.02)	0.41(0.26)	11.24(0.09)	1.15(0.24)
6967	14.07(0.05)	13.04(0.01)	12.60(0.01)	12.41(0.01)	12.33(0.03)	0.16(0.12)	10.00(0.12)	0.19(0.23)
7220	16.00(0.06)	14.73(0.01)	14.12(0.01)	13.76(0.01)	13.40(0.03)	0.92(0.38)	10.59(0.08)	0.88(0.27)
7686	16.47(0.07)	15.40(0.01)	15.01(0.01)	14.75(0.01)	14.65(0.04)	0.56(0.27)	9.71(0.07)	0.39(0.23)
7899	15.53(0.05)	14.37(0.01)	13.90(0.01)	13.57(0.01)	13.39(0.02)	0.75(0.33)	10.49(0.08)	0.99(0.25)
8089	16.53(0.06)*	15.63(0.01)*	15.33(0.02)*	15.19(0.01)*	15.05(0.04)*	0.18(0.15)	9.37(0.07)	0.04(0.17)
8408	15.46(0.05)	14.34(0.01)	13.88(0.01)	13.61(0.01)	13.49(0.03)	0.32(0.20)	10.24(0.08)	0.50(0.22)
8475	14.09(0.06)	12.79(0.01)	12.10(0.01)	11.74(0.01)	11.41(0.02)	0.74(0.33)	11.28(0.09)	1.31(0.27)

Table4.3 – Continued

AGC	u [mag]	g [mag]	r [mag]	i [mag]	z [mag]	A_r [mag]	$\log M_*$ [$M_\odot$]	$\log \mathrm{SFR(SED)}$ [$M_\odot$ yr^{-1}]
8573	13.90(0.05)	12.77(0.01)	12.29(0.01)	11.98(0.01)	11.86(0.03)	0.20(0.16)	10.89(0.09)	0.89(0.23)
8797	16.62(0.06)	15.26(0.01)	14.59(0.01)	14.21(0.01)	14.00(0.03)	0.62(0.31)	10.98(0.09)	0.79(0.42)
9023	16.83(0.14)	15.57(0.02)	15.17(0.02)	14.96(0.02)	14.88(0.08)	0.31(0.19)	9.59(0.08)	-0.81(1.01)
248881	16.27(0.05)	15.32(0.01)	15.08(0.01)	14.90(0.01)	14.68(0.03)	0.41(0.24)	9.56(0.11)	0.43(0.23)
9037	14.99(0.06)	13.97(0.01)	13.60(0.01)	13.37(0.01)	13.19(0.04)	0.36(0.22)	10.09(0.08)	0.63(0.21)
726428	17.10(0.05)*	16.07(0.01)*	15.66(0.01)*	15.33(0.01)*	15.43(0.03)*	0.18(0.13)	9.58(0.08)	-0.21(0.19)
9234	17.09(0.06)	15.34(0.01)	14.54(0.01)	14.14(0.01)	13.89(0.02)	0.28(0.20)	10.75(0.09)	-1.21(0.95)
9334	14.33(0.05)	13.24(0.01)	12.78(0.01)	12.53(0.01)	12.29(0.03)	0.40(0.23)	10.73(0.08)	1.11(0.21)
714145	17.04(0.11)	15.90(0.02)	15.49(0.02)	15.23(0.02)	15.11(0.06)	0.40(0.23)	9.64(0.08)	0.01(0.30)
9410	16.39(0.09)	15.25(0.01)	14.73(0.01)	14.44(0.01)	14.28(0.04)	0.44(0.24)	10.10(0.08)	0.35(0.24)
12506	16.13(0.09)	14.65(0.01)	13.96(0.01)	13.71(0.01)	13.22(0.03)	0.82(0.38)	10.46(0.11)	0.40(0.64)

4.5 Calculation of SFRs

4.5.1 SFRs from SED fitting, SFR(SED)

While Hα is recognized as an instantaneous indicator being sensitive to SF activities over the timescale of $\sim$10 Myr, images obtained in the SDSS u-band will respond to variations in SFR over $\sim$500 Myr. Meanwhile, through a coincidence of dust and stellar population evolution physics, the dust-age-metallicity degeneracy actually helps in the estimate of M_*/L [Taylor et al., 2011], so that M_* can be well constrained by optical broadband photometry only. In this section, we make use of the photometry derived in Section 4.4 to perform SED fitting to five SDSS bands, in order to obtain the M_* and SFR estimates.

Further details of the method and fitting quality for the α.40–SDSS (DR7) sample are found in Huang et al. [2012b]. A Chabrier [2003] IMF is adopted. We correct the observed magnitudes for Galactic reddening and implicitly apply K-corrections by convolving the redshifted model SEDs with SDSS bandpasses in the rest frame. In addition, the Gausian prior distribution of the effective optical depth in V band, τ_V, is applied, accounting for the fact that the extinction depends not only on the inclination but also on the luminosity of galaxy [Giovanelli et al., 1997]. As a result, the fitting-derived internal extinction is improved [Huang et al., 2012a], in terms of both systematic and random uncertainties. Although dust has little effect on the M_* estimates, the uncertainty of extinction correction can be the dominate term in the SFR estimates, in case of the optical or UV SFR indicators, e.g., Hα. Approximately half of the starlight emitted in the optical and UV is absorbed by interstellar dust and reradiated at infrared wavelengths [Kennicutt and Evans, 2012], so that it is important to

assume a prior τ_V distribution to better constrain the extinction. Our SED fitting derived M_*, SFR, and A_r are listed in Table 4.3.

4.5.2 SFRs from $L_{\mathrm{H}\alpha}$, SFR(Hα)

Hα lines trace stars with masses greater than $\sim$ 15 $M_\odot$ and hence recent SF. The principal drawbacks of Hα-based SFRs are the need for large and uncertain extinction corrections; the need to assume an IMF to extrapolate from the quantity of high mass stars; contamination in most of the filters used by the [NII]$\lambda\lambda$6548 and 6584 Å lines; and possible contributions to the line emission by central AGN. In general, the largest systematic errors are dust attenuation and sensitivity to the population of the upper IMF in regions with low absolute SFRs [Kennicutt and Evans, 2012]. Given their integrated SFRs, the incomplete IMF sampling has no impact on the HIghMass galaxies, but the uncertainties in the internal extinction corrections to Hα fluxes probably dominate over photometric errors as the main error in derived SFRs [James et al., 2004]. [NII] is less significant in high-EW galaxies.

We derive the SFRs from Hα luminosity adopting a recent Hα calibration in Kennicutt and Evans [2012],

$$\log \mathrm{SFR}\ [M_\odot\ \mathrm{yr}^{-1}] = \log L_{\mathrm{H}\alpha}\ [\mathrm{erg\ s}^{-1}] - 41.27 + 0.06. \tag{4.7}$$

Here, the last term converts a Kroupa IMF used in their work to a Chabrier [2003] IMF used by us [Bell et al., 2003]. We note that the correction of stellar absorption underlying Hα is already taken care of by the continuum subtraction [Kennicutt et al., 2008]. In addition to the (1) continuum over-subtraction and (2) Galactic extinction corrections mentioned earlier, the following corrections

are applied on the observed $L_{\mathrm{H}\alpha}$:

(3) Redshift correction by a factor of $(1+z)^2$.

(4) [NII] contamination. Although SDSS spectra are available for 33/34 of the HIghMass galaxies, they are limited by the small aperture (3 arcsec) that covers only the nuclear regions of the majority. Plus, according to the BPT diagram [Brinchmann et al., 2004], there are five AGNs, two low S/N LINERs, and two composite galaxies with both AGN and SF contributions among our sample. The nuclear [NII]/Hα ratios are most likely to deviate from the overall values. Alternatively, we adopt the scaling relation between [NII]/Hα and M_B Kennicutt et al. [2008],

$$\log([\mathrm{NII}]\lambda\lambda 6548, 6584/\mathrm{H}\alpha) = \begin{cases} -0.173 M_B - 3.903, \text{ if } M_B > -21, \\ \log 0.54, \text{ if } M_B \leq -21, \end{cases}$$

where M_B comes from the combined SDSS magnitudes. Despite of a large scatter, we have confirmed this relation to be systematically consistent with the SDSS flux measurements, excluding the AGNs. We further assume a line ratio [NII]$\lambda\lambda$6584/[NII]$\lambda\lambda 6548 = 3$ to exclude the [NII]$\lambda\lambda$6584 contribution in five galaxies because it is outside of the Hα filter (see Section 4.3).

(5) Dust extinction correction. We make use of the continuum extinction given by the SED fitting and assume a constant ratio between the nebular line and stellar continuum extinctions at the same wavelength, $A_r = 0.44 A_{\mathrm{H}\alpha}$ [Calzetti et al., 2000]. Due to the same concern of small aperture, we choose not to rely on the Balmer decrement derived from SDSS spectra in order to infer $A_{\mathrm{H}\alpha}$ in this work. Moreover, use of the Balmer decrement may lead to an underestimate of the extinction because lines of sight with low extinction are more heavily weighted within the beam [Kennicutt and Evans, 2012]. Note we can

explore further this issue with the long-slit spectroscopic or MIPS data in hand in the future.

The final SFR(Hα) values after all these corrections are presented in Table 4.2. Our SFR(Hα)s range from 0.34 to 21 $M_{\odot}$ yr^{-1}, with the median value being 2.5 $M_{\odot}$ yr^{-1}, which is significantly higher than the median SFR of the other Hα surveys, e.g., 11HUGS, HαGS, or SINGG. It should not be attributed to the different corrections we applied, because a comparison of the $L_{\rm H\alpha}$ distributions (only continuum over-subtraction and Galactic extinction corrected) show as well that our survey is highly biased towards the high $L_{\rm H\alpha}$ galaxies. This is in opposite to the previous understanding that the HI-selected galaxies have somewhat lower $L_{\rm H\alpha}$ and SFRs [Sánchez-Gallego et al., 2012], but agree with the finding in Huang et al. [2012a] that the HI-rich galaxies have on average higher SFRs at fixed M_*.

4.5.3 SFR(SED) vs. SFR(Hα)

Fig. 4.14 illustrates a comparison between the SFR(SED)s and SFR(Hα)s of the HIghMass galaxies. The two quantities are in rough agreement for the majority within the uncertainties. Therefore, the standard calibration of the Hα SFR indicator, assuming a Chabrier [2003] IMF, is applicable to our galaxies. There is no evidence that the extraordinary $f_{\rm HI}$s are due to the abnormal SF behavior of massive stars, so that the galaxies are devoid high mass stars. We also rule out a significant decaying or rising SF history in the last $\sim$10 Myr relative to the last $\sim$100 Myr.

However, the SED fitting results in much lower SFRs for a few sources by

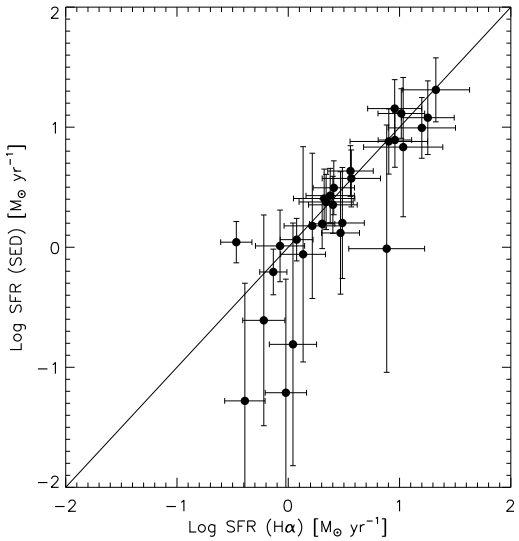

Figure 4.14: A comparison between the SFR(SED)s and SFR(Hα)s with all corrections applied. The two estimates are in agreement within the uncertainty.

almost a factor of ten. The huge error bars on the SFR(SED) characterize broad possibility density functions of the SFR estimates in these cases, indicating alternatively the SFR(Hα) to be a more realistic result. We further assess this statement by referring to the *GALEX* archive for NUV measurements, which are available for more galaxies than the FUV ones. With a poorer resolution ($\sim$ 4 arcsec FWHM) and a larger impact from the dust extinction, the NUV images are less preferred than our high quality Hα data for the purpose of tracing SFRs. We only make use of them here to judge which one is correct in the cases of disagreement, SFR(SED) or SFR(Hα). Excluding the shredded pipeline NUV magnitudes, we apply corrections for Galactic extinction, redshift, internal extinction (self-consistent values given by the SED fitting), and K-corrections. The final NUV luminosity inferred SFRs, adopting a Kennicutt and Evans [2012] calibration, reach a better agreement with the higher SFR(Hα)s rather than the SFR(SED)s.

In conclusion, we have double checked that our SFR(SED)s and SFR(Hα)s

are both reliable taking into account of the careful error analysis, whereas the additional Hα data are still highly desirable considering the less constrained SED fitting results in some cases.

4.6 Optical Characteristics of the HIghMass galaxies

In this section, we put our galaxies in a bigger scheme by studying their detailed optical properties relative to the other galaxies. We first take a brief look at the global EW properties but mainly focus on inspecting various surface profiles later. Intriguing features are identified, being indicative of unusual behavior in their gas accumulation and SF.

4.6.1 Hα Properties

Global EW$_{\mathrm{H}\alpha+[\mathrm{NII}]}$

In order to understand the EW$_{\mathrm{H}\alpha+[\mathrm{NII}]}$ distribution of our galaxies, we have to account for the potential variation of EW with luminosity, considering the different luminosity ranges probed by other Hα surveys. A number of works have shown controversial results on this issue: a weak declining trend of EW with brighter M_R was seen in Jansen et al. [2000a] and Lee et al. [2007], in contrast to the others who found no significant trend between the two quantities [James et al., 2004, Sánchez-Gallego et al., 2012]. Sánchez-Gallego et al. [2012] show that the EWs have little dependence on luminosity but a rise by a factor of 5 from early- to late- type galaxies. We investigate these correlations among the HIgh-

Mass galaxies in Fig. 4.15. The Spearman's rank correlation coefficients are 0.32 and 0.15, respectively, for the log EW *vs.* M_r and log EW *vs.* T-type relations, suggesting basically flat distributions in general. Given our limited dynamic range of luminosity, we have not rule out the possibility of increasing EWs on average among the dwarf galaxies. However, we do see that the scatter in EW at a given luminosity is large in lower luminosity systems (EW is plotted on log scale). In particular, the galaxy with the lowest M_* in our sample, AGC 203522, which can be classified as a starburst galaxy, has the highest EW (90.66 Å). Note the galaxies that are not assigned a morphological type in the NED and thus are missing in the EW *vs.* T-type plot belong almost exclusively to the late type low mass galaxies, e.g., AGC 203522. A weak rising trend from early- to late-type galaxies may be visible if we include these galaxies.

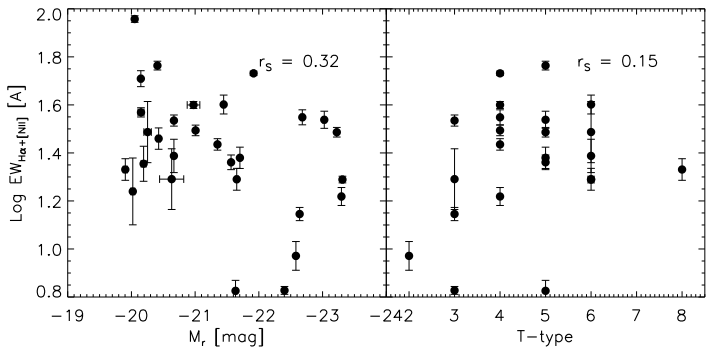

Figure 4.15: Left panel: Hα EW vs. r-band absolute magnitude. The two quantities are weakly correlated. Given that the EWs are plotted on logarithm scales, the scatter in EW at a given luminosity is larger in lower luminosity systems. Right panel: Hα EW vs. T-type. The distribution is basically flat.

By definition, the EW infers the ratio of current SF to the past average, i.e., the birth parameter $b \equiv \mathrm{SFR}/\langle \mathrm{SFR} \rangle$. For instance, the EW distribution of SINGG centered and peaked at $\sim$ 24 Å, indicating a $b \sim 0.2$ [Meurer et al., 2006]. In the luminosity range of $-22 < M_B < -19$, Lee et al. [2007] obtained $\langle \log \mathrm{EW} \rangle = 1.17$; $\sigma = 0.40$. The EWs of NGLS galaxies, also HI selected, range

from 1 to 880 Å with a median value of 27 Å. For the later-type spirals (Sc-Sm), Kennicutt [1983] and James et al. [2004] get higher average EWs: 29 Å and 35 Å, respectively. In comparison, the HIghMass galaxies have $\langle \log \mathrm{EW} \rangle = 1.41$ ($\sigma = 0.26$) and the average is 30 Å. In fact, our average is even slightly higher than most of the others, although not significantly given the σ. This rules out the hypothesis that the high f_{HI} values in our galaxies result from gas being inhibited from converting into stars *at present.* Either past SF has been suppressed due to the high λ value of DM halo, or the galaxy has undergone recent gas accretion, gas in these galaxies is apparently involved in current SF activities.

SFR Surface Density

Data point at a galactocentric radius r in the lower left panels of Fig. 4.6 – 4.8 represents the mean Hα surface brightness inside a tilted ring with an inner radius of $0.8r$ and outer of $1.25r$, following the convention to calculate the Petrosian ratio. These $\Sigma_{\mathrm{H}\alpha}$ radial profiles are expected to be less smooth than the starlight since they represent a shorter lived evolutionary stage. Here we convert them to Σ_{SFR} for our future studies of SFLs or SF thresholds. In addition to the global corrections applied to the total $L_{\mathrm{H}\alpha}$ in Section 4.5, including Galactic extinction, redshift, and [NII] contamination corrections, we follow Leroy et al. [2008] to deproject the $\Sigma_{\mathrm{H}\alpha}$ by a factor of $\cos i$, where i is the inclination of disk. We do not apply a spatially-resolved internal extinction correction in order to be comparable to the others who use Hα (*vs.* IR) emission to characterize unobscured (*vs.* obscured) SF, separately. Deriving the radial profile of internal extinction is beyond the scope of this chapter but it can be constrained in our future works by either our MIPS maps or Balmer decrements from long-slit spectroscopy.

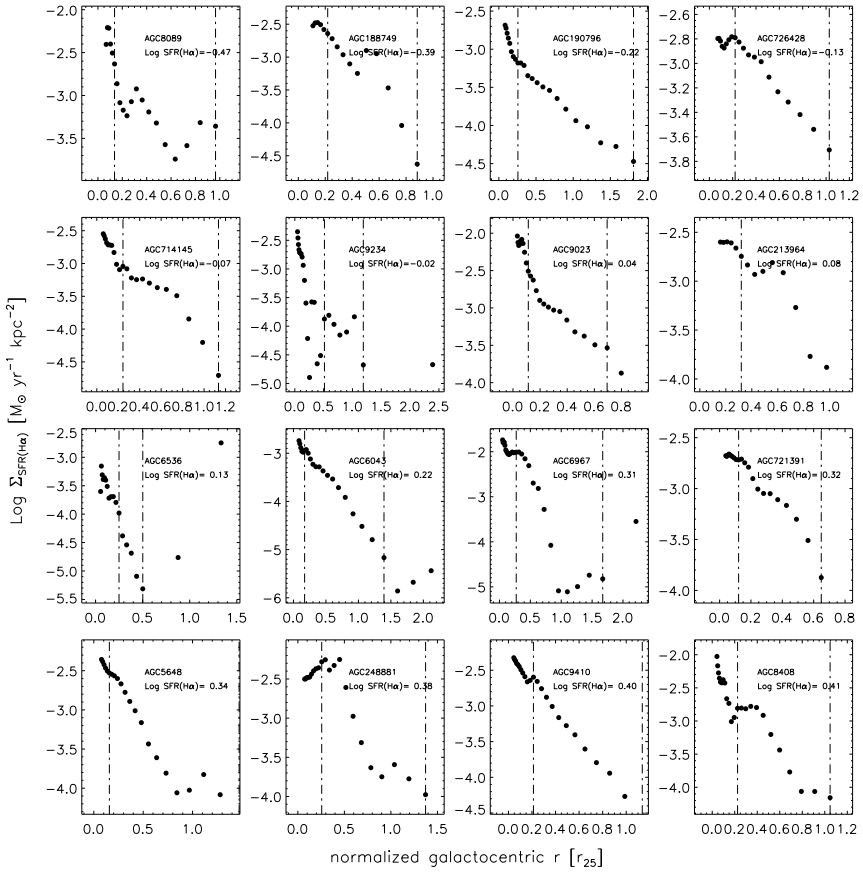

Figure 4.16: The $\Sigma_{\rm SFR}$ radial profiles of 29 HIghMass galaxies, in order of increasing integrated SFR(Hα). The galactocentric radius is normalized by r_{25} on the x-axis. The marked inner disk region is denoted by vertical dash-dotted lines.

We present the $\Sigma_{\rm SFR}$ radial profiles of 29 HIghMass galaxies in Fig. 4.16, in order of ascending integrated SFR(Hα), with galactocentric radius normalized by r_{25}. In between the dash-dotted lines are the disk regions. The typical value of $\Sigma_{\rm SFR,25}$, defined as the integrated SFR normalized by the area πr_{25}^2, is 10^{-3} $M_\odot$ yr^{-1} among Im galaxies [Hunter and Elmegreen, 2004], whereas typical spirals reach this $\Sigma_{\rm SFR}$ between $0.35r_{25}$ and $0.81r_{25}$, the average being $0.5r_{25}$ [Kennicutt, 1989]. Thus, the Im galaxies more closely resemble the outer parts of spirals in $\Sigma_{\rm SFR}$. Our galaxies have overall *lower* $\Sigma_{\rm SFR,25}$ relative to the Sab-

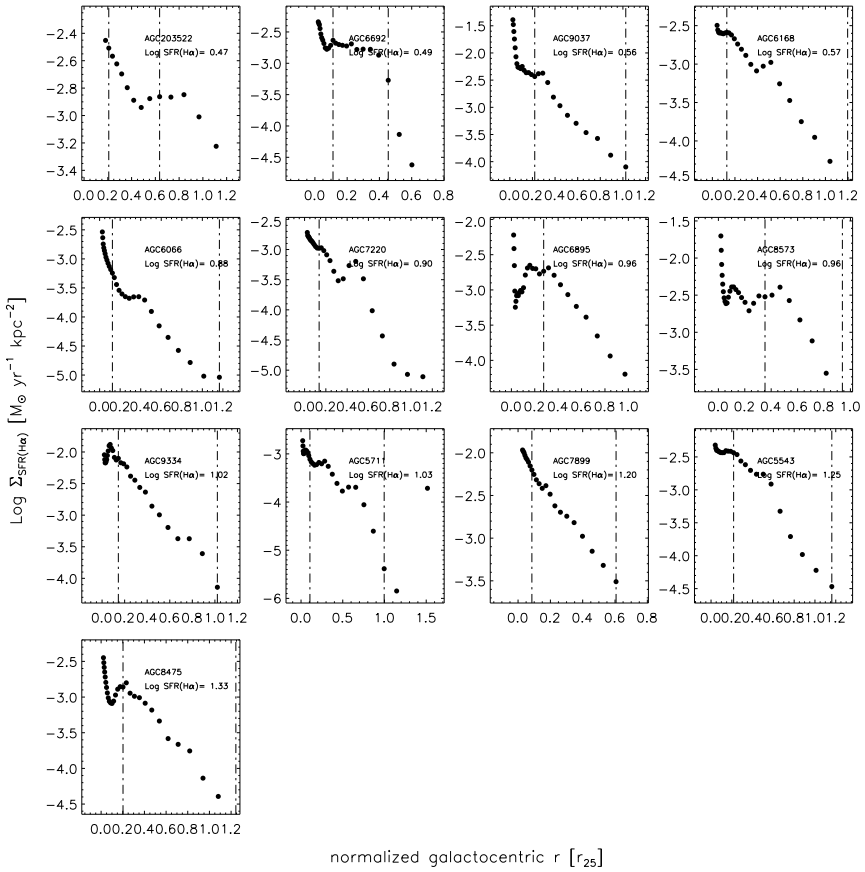

Figure 4.16: *Continued.*

Sd galaxies in Kennicutt [1989], but marginally higher $\Sigma_{\rm SFR,25}$ relative to the Im galaxies Hunter and Elmegreen [2004]. This is consistent with the earlier finding that the galaxies with higher ratios of gas relative to their luminosity or total baryonic mass have lower $\Sigma_{\rm SFR}$ [Hunter and Elmegreen, 2004]. In fact, the $\Sigma_{\rm SFR}$ drops below 10^{-3} $M_\odot$ yr^{-1} within $0.35r_{25}$ in 9/29 of the HIghMass galaxies. Compared to a subset of the SINGS galaxies that are HI dominated over H_2 [Bigiel et al., 2008, Leroy et al., 2008], mostly being late-type spirals or dwarf irregulars, our galaxies have on average slightly higher $\Sigma_{\rm SFR}$. However, many of the massive spirals in the SINGS with H_2 dominated centers have higher $\Sigma_{\rm SFR}$ than ours. It was found that most of the SF activities take place within $3r_{\rm d}$

[Hunter and Elmegreen, 2004], but Hα emission is traceable beyond that in most of our galaxies, to as far as $6r_{\rm d}$ in UGC 6043, UGC 6967 (LSB galaxy), UGC 5648, and AGC 248881.

Although our galaxies have high integrated $f_{\rm HI}$s, $L_{\rm H\alpha}$s (absolute value), and EWs (vigorous current SF relative to the past), the SF activities spread throughout the disks whereas concentrated intense star formation is uncommon.

$\mathbf{EW_{H\alpha+[NII]}}$ Profiles

We use the same set of tilted rings to measure the $\Sigma_{\rm H\alpha}$ and Σ_R profiles, yielding the $\rm EW_{H\alpha+[NII]}$ profiles as presented in the second column of Fig. 4.9. Comparable EW profiles are shown in James et al. [2004], among which the centrally-concentrated SF, characterized by a central peak in EW curve and a decline with radius, is quite common. Similarly, the EWs of BCDs are most often found to drop steeply with radius, implying that the SF has migrated to the center within the last gigayear [Hunter and Elmegreen, 2004]. In contrast, only two HIghMass galaxies exhibit prominent central EW peaks: UGC 9023 and UGC 9037, both being members of cluster Z1400+0949 [Giovanelli and Haynes, 1985]. According to the BPT diagram derived from their SDSS spectra, AGN activity makes little contribution to the line emission in their nuclear regions. The cluster environment may play a role in the inwards gas driven and subsequently the enhanced nuclear SF. Our JVLA maps of UGC 9037 demonstrate evident inwards streaming motion in the HI velocity fields (Hallenbeck et al. 2013 in preparation), which may explain the highly efficient current SF relative to the past in its central region.

On the other hand, most HIghMass galaxies have higher EWs in the outer disk regions, implying younger outer disks relative to the older central bulges dominated by continuum emission. Such strong variances of the EWs suggest the caveat of a widely used method to correct for the aperture effect when using nuclear emission line strengths to infer global SFRs, i.e., scaling the SDSS nuclear SFRs by the ratio of the nuclear and overall broadband luminosities [e.g., Hopkins et al., 2003]. In particular, the EW profiles rise almost monotonically in AGC 203522 (starburst), AGC 726428, AGC 721391, and UGC 6692; the stellar population becomes increasingly dominated by young stars with radius. Similar behavior of EW is found in UGC 8802 [Moran et al., 2010], which is consistent with a scenario of inside-out disk growth as such the SF activity is migrating outwards.

We also pay special attention to the profiles of galaxies with central bars. James et al. [2004] claim that the Hα+[NII] distributions of bared spiral galaxies always have a significant central peak, a SF "desert" in the region swept out by the bar, and substantial SF in HII regions scattered around the disk. This results in an EW profile with a strong central peak, a broad dip, and a gentle outer rise to the plateau level at 15-30 Å. There are four HIghMass galaxies classified as SAB types (UGC 5711, UGC 6895, UGC 6967, UGC 9334) and two others as SB types (UGC 6168, UGC 8408). Despite the existence of inner dips possibly swept out by the bar, we only see a weak central peak in the EW profile of UGC 8408. Plus, James et al. [2004] suggest a relationship between moderately higher SFRs and the presence of bars; the five galaxies with the highest SFRs in their sample are all barred. Such a statement is not evident among our galaxies; UGC 6967 and UGC 8408 both have relatively low SFRs. Bars have not left clear imprints in the SF activities by inducing bar-driven feeding of gas into the central regions

of our galaxies. It seems that the gas reservoir is stable against collapse into the nuclear region in the majority of HIghMass galaxies. While the highly inefficient inward gas transfer may be attributed to high λ of the halos, the galaxies are still undergoing active disk growth in the extended outer regions.

4.6.2 Broadband Properties

LSB Galaxies in the HIghMass sample

The correlation between gas richness, less concentrated stellar disks, and high λ halos are predicted by both semi-analytical models and hydrodynamic simulations of galaxy formation [e.g., Mo et al., 1998, Boissier and Prantzos, 2000, Kim and Lee, 2013, Kravtsov, 2013]. The overall lower $\Sigma_{\rm SFR}$ of the HIghMass galaxies is already indicative. In this section, we will quantify the broadband surface brightness of the HIghMass galaxies, in order to observationally confirm the hypothesis that such gaseous disks are due to fast spinning halos in which LSB galaxies preferentially reside. In alternative, the high $f_{\rm HI}$s of the high surface brightness galaxies in our sample are most likely to be a result of recent gas accretion.

A literature search shows that UGC 6536, UGC 190796 (Malin-like), and UGC 6967 have been studied as LSB galaxies before [Bothun et al., 1985, Schombert et al., 1992, Sprayberry et al., 1995]. We obtain two widely-used measurements of disk surface brightness that will enable us to systematically identify the LSB galaxies in our sample. The first one is effective surface brightness, μ_e, defined as the face-on surface brightness at half light radii, $r_{\rm petro,50}$. We correct the R-band μ_e for Galactic extinction and convert it to the AB magnitude

system, to be consistent with the SINGG calculation. Compared to Fig. 15 in Meurer et al. [2006], our cumulative histogram of $\mu_e(R)$ demonstrates that the HIghMass galaxies on average have lower surface brightness. Similarly, we calculate the $\mu_e(r)$ values of HIghMass galaxies, plotted on the x-axis in Fig. 4.17, in order to compare with the results derived from 28,000 low-z SDSS galaxies in Blanton et al. [2005]. Blanton et al. [2005] note that the deficit of the lowest surface brightness galaxies with $\mu_e(r') > 23.5$ mag arcsec^{-2} is largely a result of their spectroscopic selection bias. There are 11/34 HIghMass galaxies which meet such criteria of LSB galaxies, lying leftwards of the vertical dashed line in Fig. 4.17: AGC 188749, AGC 190796, AGC 190277, AGC 203522, UGC 6043, AGC 213964, UGC 7220 (marginally), UGC 7686, UGC 8089, UGC 9023, and UGC 12506. They are the strong candidates of galaxies residing high λ halos. In fact, we have confirmed this within one of them, UGC 12506, in our pilot study of the JVLA rotation curve (Hallenbeck et al. 2013 in preparation), whereas another source, UGC 9037, believed to be undergoing gas accretion, is not in this list. We note that UGC 6536 and UGC 6967 as previously identified LSB galaxies are both excluded from the list, again suggesting the overall LSB of HIghMass galaxies.

However, the μ_e values can be easily effected by the bulge component, whose formation is weakly correlated with the angular momentum distribution of the host halos. In addition, μ_0, defined as the disk surface brightness interpolating to center, describes only disk properties. After a similar inclination correction is applied to μ_e, the two quantities μ_e and μ_0 measured in the same band assuming a perfect exponential light profile should be related by $\mu_0 = \mu_e - 1.822$. We use the combined SDSS magnitudes to characterize $\mu_0(V)$, $V = g - 0.5784(g - r) - 0.0038; \sigma = 0.0054$, plotted on the

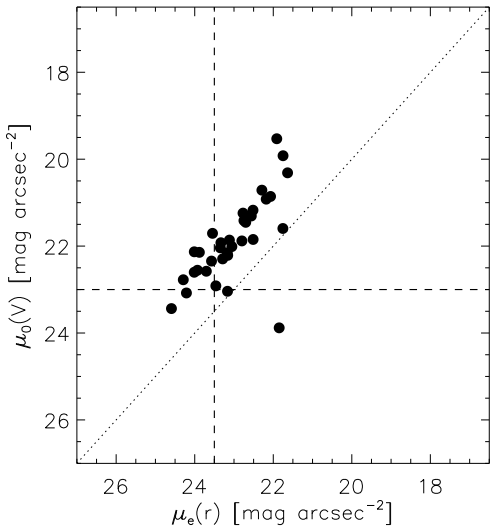

Figure 4.17: r-band Effective surface brightness on the x-axis and V-band surface brightness interpolated to center on the y-axis, both after inclination correction. The dotted diagonal line illustrates the one-to-one relation. The dashed lines mark criteria of LSB galaxies adopted by previous works.

y-axis in Fig. 4.17. Compared to the central surface brightness $\mu_c(V)$ of the LSB galaxies in Schombert et al. [2011], the $\mu_0(V)$ values of our galaxies are brighter in general. The majority of HIghMass galaxies have $\mu_0(V)$ fainter than the Freeman value (21 mag arcsec^{-2}). Adopting a brightness standard cut of $\mu_0(V)$ >23 mag arcsec^{-2}, four HIghMass galaxies fall in the category of extreme LSB galaxies: UGC 190277, UGC 6066, UGC 9234, and UGC 12506, lying below the horizontal dashed line in Fig. 4.17. UGC 6066 and UGC 9234 are not in the previous $\mu_e(r)$-defined list. Due to the presence of both prominent bulges and extended outer disks in these galaxies, their μ_e is significantly brighter than the $\mu_0 + 1.822$.

As a most HI rich massive population, the HIghMass galaxies have on average lower surface brightness relative to the general surveys covering the entire morphological spectra, but not all of them meet the criteria of extreme LSB

galaxies. All of the non-detections and marginal detections from any of our observing runs (*Herschel*, IRAM, or INT) are included either in the previous $\mu_e(r)$-defined list, or in the current $\mu_0(V)$-defined list of LSB galaxies; the FIR, CO, and spectra line emission all can be easily detected in relatively high surface brightness galaxies.

Broken Exponential Disks

The structural properties of the outer regions of galactic disks must be intimately linked to the mechanisms involved in the growing and shaping of galaxies. It was found in Pohlen and Trujillo [2006] that only $\sim 10\%$ of their galaxies have a normal/standard purely exponential disk down to the noise limit. They claimed that the surface brightness distribution of the rest of the galaxies is better described as a broken exponential. About 60% of their galaxies have a break in the exponential profile between $\sim$ 1.5 – 4.5$r_{\rm d}$ followed by a downbending, steeper outer regions. Another $\sim 30\%$ shows also a clear break between $\sim$ 4 – 6$r_{\rm d}$ but followed by an upbending, shallower outer region. Quite intriguingly, the shape of the profiles correlates with Hubble type. Downbending breaks are more frequent in later Hubble types while the fraction of upbending breaks rises towards earlier types. Such a trend is further confirmed by studies of the UV surface brightness profiles with dwarf samples [Hunter et al., 2010, Huang et al., 2012b]. Among the relatively HI poor BCDs, most of the broken exponential disks show upbending, whereas most of the double disks in HI-rich dwarf irregulars have steeper outer disks. This phenomenon may be explained as a result of size shrinking of the actively star-forming disks in BCDs due to gas removal in the outer disks [Huang et al., 2012b].

In contrast to the relatively gas-poor ALFALFA dwarfs in our previous study, the HIghMass galaxies are selected to be the most HI-rich sources with late Hubble types. If a significant change in slope exists in the light profile, we mark the inner and outer disk regions and fit two exponential functions to each portion individually. The inner fit is used to determine the general disk properties, e.g., $r_{\rm d}$, θ, and ϵ as presented in Table 4.2 and 4.3, as well as the Petrosian aperture, whereas the outer fit is used to extrapolate the surface brightness profile beyond the outermost measured isophote in the calculation of $\rm mag_8$. An example of UGC 6692 is shown in the middle left panel of Fig. 4.7. The inner disk region is in between the vertical dash-dotted lines and the outer one is in between the vertical dotted lines. Separate fitting results to the two portions are overlaid on the light profiles by dotted lines. As expected, the broken exponential disks in the current sample mostly belong to the category of downbending. We will next focus on the 29 galaxies in Table 4.2 with Hα profile measurements, but we briefly mention that the SDSS images reveal double disks in two additional HIghMass galaxies not included in our KPNO run, UGC 8797 and UGC 7686, both being downbending.

Broken exponential disks in the optical broadband images are found in seven out of 29 KPNO targets. The majority of them have steeper outer disks: AGC 203522, AGC 721391, UGC 6692, UGC 7220, UGC 7899, and UGC 9023. The only upbending optical disk is present in UGC 6043. In agreement with the results in Pohlen and Trujillo [2006], the downward breaks happen at 2 – 3$r_{\rm d}$ (2.5$r_{\rm d}$ on average) in the six downbending disks, in contrast to UGC 6043 at $\sim 5r_{\rm d}$. We find an interesting coincidence of three overlapping sources in this list of downbending disks and the list of four disks with apparent rising Hα EW profiles with radii identified earlier: AGC 203522 (starburst), AGC 721391,

UGC 6692. In the cases of upbending BCDs, being relatively gas-poorer, the shallower outer profile represents the underlying old stellar population, while the steeper inner profile is dominated by the centrally concentrated and intense recent star formation, i.e., the SF activities are migrating inwards [Hunter et al., 2010]. Our results, on the other hand, suggest a correlation between the gas-richness, downbending profile, and active outer disk growth.

Although we have confirmed that the downbending breaks are more frequent in late type disks with high $f_{\rm HI}$ in which SF is migrating outwards, the origin of this downbending remains a puzzle, and even seems to be contrary to the actively forming outer disk evident at first look. Two downbending features were differentiated in Martín-Navarro et al. [2012]: an innermost 'transition' radius at distances of $\sim 0.77 \pm 0.06 r_{25}$ and a second characteristic radius, or 'truncation' radius, close to the outermost optical extent $\sim 1.09 \pm 0.05 r_{25}$ of galaxy. They propose that such a transition might be phenomena related to a threshold in the SF, while truncations are more likely a real drop in the stellar mass density of the disk associated with the maximum angular momentum of the stars [Martín-Navarro et al., 2012]. Similarly, Roškar et al. [2008] claimed that the transition corresponds to a rapid drop in the SFR associated with a drop in the cooled gas surface density, but the outer exponential is populated by stars that were scattered outwards on nearly circular orbits from the inner disk by spiral arms. An inspection of the six downbending HIghMass galaxies shows that the changes in slope all happen within r_{25}, with an average of $\sim 0.7 r_{25}$, implying a threshold in SF rather than stellar disk truncation. In fact, most of our galaxies have Hα emission traceable to $\sim r_{25}$ and beyond (Fig. 4.16), except for UGC 721391, UGC 6692, UGC 7899, and UGC 9023. This matches very well with the list of downbending disks. Therefore, we conclude that the inner tran-

sition is related to a threshold in SF as proposed by Martín-Navarro et al. [2012]. It will be interesting to see if these Hα truncations are also visible in the FUV, because stochasticity may lead Hα to show signs of knees and turnoffs while the FUV remains smooth [Boissier et al., 2007].

Overall, while the shallower outer stellar disks quiescent in current SF are seldom seen in gas-rich galaxies, there are a handful of downbending double exponential disks in the HIghMass sample. Although their disks are growing inside-out at the current epoch, SF thresholds exist. Considering that the SF threshold is always explained as a result of a gas surface density dropoff or global dynamic stability [Leroy et al., 2008], we will further examine the JVLA maps of UGC 7220 to see if its gas has a very compact distribution, in contrast to the extended HI disks we observed in UGC 8475 or UGC 12506, relative to the optical disks. As a final note, Leroy et al. [2008] found the transition between a mostly-HI and mostly-H_2 ISM occurs at a characteristic radius of $0.43 \pm 0.18 r_{25}$. Our transition radii are typically further out so that the SF threshold is unlikely to be caused by such a phase transition.

Disk Color Gradients

If galaxies indeed grow from inside out, stars should be younger on average in the outer parts, leading to radial color gradients. The $u - r$ surface brightness profiles of 29 KPNO targets are presented in the first column of Fig. 4.9. Indeed, most of the them exhibit strong color gradients. The bluing of galaxies at larger radii is not a new result. For instance, it is found inside the SINGS galaxies [Muñoz-Mateos et al., 2011], as well as in another HI-rich massive galaxy, UGC 8802 [Moran et al., 2010]. Our galaxies are brighter than $M_B \sim -17$ so

that they are expected to be redder in their inner parts, according to Tully et al. [1996]. Whereas the color profiles remain fairly constant for most of the early-type galaxies, the strength of the color gradient should increase moving from S0/a to Sa. Such a trend was believed to reverse for late-type spirals by other authors, reflecting the decreasing prominence of bulges and the more extended SF [Jansen et al., 2000b]. However, many of our late-type spirals still have relatively redder centers, and the colors become continuously bluer throughout the disks (e.g., UGC 8475 in the last row), not purely due to the color differences between the bulge and disk components. Relative to the $B-V$ color maps of LSB galaxies presented in [Schombert et al., 2011], our galaxies demonstrate clearer systematic bluing trends in their disks.

Measuring age gradients in disks from color profiles is not straightforward, since the radial decrease in the internal extinction and metallicity also conspire to yield bluer colors at larger radius [Muñoz-Mateos et al., 2011]. In supplement, we present the Hα EW profiles in the second column of Fig. 4.9. Because the Hα lines lie within the wavelength range of the R filter, the differential reddening should have less impact on the Hα EW gradients than on the optical color gradients. A comparison between the EW and color profiles of HIghMass galaxies shows evidence of an anti-correlation between the EWs and the colors. Globally, bluer galaxies have overall higher EWs (e.g., AGC 203522 in the first row) and vice versa (e.g., UGC 8475 in the last row). Within a galaxy, the reddening trend of color as a function of radius is always associated with the declining EW (e.g., AGC 188749 in the forth row) and vice versa (e.g., AGC 726428). Despite the effect of differential reddening, the overall lower central Hα EWs support the inference of older central regions in most of the HIghMass galaxies relative to the disks, in agreement with the scenario of inside-out disk formation.

In addition, reverse reddening trends in the outermost regions are observed in a number of galaxies, leading to the 'U'-shape color profiles in, e.g., AGC 714145, UGC 6168, UGC 5711, UGC 5543, etc. Their EW profiles appear to have 'Λ' shapes correspondingly. N-body simulations show that such features may result from a combination of a drop in the SFR (seeded by warps in the gaseous disk, radial distribution of angular momentum, misalignment between the rotation of the infalling gas and the disk, etc.) and radial stellar migration, which would populate the outskirts of disk with old stars formed inward [Muñoz-Mateos et al., 2011].

4.7 Summary

The main goal of this chapter is to describe the HIghMass program and in particular to present a dataset of high-quality Hα imaging for 29 HIghMass galaxies. Taking advantage of the great sensitivity and large sky volume of the ALFALFA, we identify the galaxies with extraordinarily high $M_{\rm HI}$ and $f_{\rm HI}$ for their M_* from the α.40 catalog. The higher-than-average gas fractions may due to suppressed SF in the past as a result of the high λ host halos, or may be attributed to late cold gas accretion. These objects represent the present day counterparts of the populations which are likely to dominate the planned deep field surveys of HI in galaxies at higher redshift with the SKA and its pathfinders [e.g. Meyer, 2009].

We assembled multi-wavelength data (radio, mm/submm, FIR/NIR, optical, UV) in order to distinguish between the two scenarios. The sample contains several LSB galaxies, e.g., AGC 190796, AGC 190277, and UGC 12506, which are the first candidates of the galaxies in high λ halos. Many of these LSB galaxies

are non-detections and marginal detections by our *Herschel*, IRAM, or INT observations, e.g., UGC 6066 and AGC 213964. By the contrary, an extended UV disk emission (outer disk re-growth) is evident in UGC 9234 whereby UGC 9037 has centrally-peaked SFH, suggesting gas acquisition at the outskirt and nuclear gas infall, respectively. The final set of 34 HIghMass galaxies span a range of luminosities, M_*, and SFRs. Except for UGC 6066, UGC 9234, and UGC 4599, all the others are blue cloud galaxies on a color-magnitude diagram. UGC 4599 and UGC 6066 have the earliest Hubble types among the sample while the majority are late-type spirals. The environment difference between the HIghMass and α.40 galaxies is insignificant. The basic properties and status of observing programs are listed in Table 4.1.

This is the first systematic Hα study of galaxies in this $M_{\rm HI}$ regime. Relative to the existing large Hα surveys of field galaxies, the HIghMass galaxies lie at further distances and are thus more massive in general. We report the details of our observation and the procedures of image reduction, continuum subtraction, as well as Hα and R-band surface photometry, using the modified IRAF package, GALPHOT. KPNO measurements are presented in Table 4.2, including the disk sizes, ellipticities, position angles, R-band Petrosian magnitudes, Hα fluxes, EWs, etc. Considering the shortcomings of standard photometry pipeline, e.g., shredding and sky background over subtraction, we obtain supplementary measurements from the SDSS images, which are presented in Table 4.3. Multiple internal and external checks ensure the consistency of the KPNO and SDSS results and the quality of absolute flux calibration.

Current SFRs of the HIghMass galaxies are obtained in two ways. The first is by fitting the model SEDs to reprocessed SDSS magnitudes, assuming prior dis-

tributions of the internal extinctions. This approach yields SFR(SED) together with the M_* and posterior extinction estimates, which are all presented in Table 4.3. The second is converting the $L_{\mathrm{H}\alpha}$ to SFR(Hα), adopting a standard conversion factor. Various corrections have been applied, including [NII] contamination and internal extinction corrections, and the final numbers are given in Table 4.2. Albeit the poorer constraint of SFR(SED) for the red galaxies in particular, the two results agree within the uncertainty ranges for most of the sources. There is no evidence that the high f_{HI} values are due to an excess or deficit in the formation of massive stars. We also rule out a significant decaying or rising SF history in the last ~ 10 Myr relative to the last ~ 100 Myr.

We examine the optical characteristics and the SF properties as inferred from the Hα data. In comparison with the SFRs derived in other Hα surveys, the HIghMass galaxies have overall higher integrated SFRs. This rules out the hypothesis that the high HI fractions in our galaxies result from gas being inhibited from converting into stars *at present*. The HIghMass galaxies exhibit healthy ongoing SF despite potentially inactive SF in the past, which is confirmed by the overall high Hα EWs. However, the SFR surface density profiles demonstrate that the SF activity is spread throughout the extended disks so that they have overall lower SFR surface densities. Similarly, the HIghMass galaxies have on average lower surface brightness in the R-band images.

Only two of them have prominent central EW peaks: UGC 9023 and UGC 9037 (central HI infall), whereas all the others have higher EWs in the outer disk regions, implying inside-out disk growth. In particular, the EW profiles rise almost monotonically in AGC 203522, AGC 726428, AGC 721391, and UGC 6692, i.e., the SF activity is migrating outwards. While the shallower

outer stellar disks are seldom seen in gas-rich galaxies, there are a handful of downbending double exponential disks in the HIghMass sample. Although their disks are growing inside-out at the current epoch, SF thresholds exist in the downbending disks, probably as a result of concentrated gas distribution. The majority of HIghMass galaxies have strong color gradients, being redder in center, in agreement with the scenario of inside-out disk formation. The color gradients reverse at the very outermost regions in some disks, which may result from a combination of a drop in the SFR and radial stellar migration.

CHAPTER 5

FUTURE WORK

Massive HI disks imply intriguing physical condition of SF and gas infall. Analysis of the Hα images and HI synthesis maps of a subset of the HIghMass galaxies demonstrates potentially different origins of such galaxies. Further understanding on a more physical basis naturally requires scrutinizing the galaxies at sub-galactic scales. In the future, we will make use of the multi-wavelength dataset of HIghMass galaxies in order to explore detailed processes that regulate cold gas evolution.

By collecting observational evidence of multiple pieces in the gas circulation cycle, we can examine the balance between gas replenishment and depletion. At present, we have reduced the Hα and UV images, probing unobscured SF. The FIR fluxes obtained by the *Herschel* PACS observations will be a reliable tracer of the obscured SF. The two can be combined to get a robust SFR estimate. Observation of the *Spitzer* program is underway, which will be studied together with the optical data so as to estimate the SF history. The molecular gas is the missing piece in the entire chain that leads from gas to stars. While the pilot CO($J = 1 - 0$) mapping with CARMA was accomplished for only five of these galaxies, it is necessary to expand the CO data (as an H_2 tracer). We will request SMA observing time at other CO transitions to complete our view of the spatially-resolved CO distribution in the HIghMass galaxies. Here follows a discussion of the detailed science questions to be addressed with these data.

5.1 Gas Consumption through SF

The well-established empirical SFLs describing the SFEs serve as an essential prescription in galaxy evolution models. Recently, it has become clear that the SF, at least on local scales, is better correlated with H_2 than with HI [Schruba et al., 2011]. However, in the low surface density HI-dominated outer disk, the UV and HI emission show a tight spatial correlation [Bigiel et al., 2010b]. Theoretical studies suggest that perhaps the reason for a good correlation between H_2 and SF is not that H_2 is a prerequisite for SF, but instead that the formation of H_2 and the SF both correlate with some other factor [Krumholz et al., 2012]. Although it is likely that SF on local scales concentrates in molecular-dominated regions, the formation of H_2 from HI remains a critical and possibly controlling step [Kennicutt and Evans, 2012].

Using the THINGS HI maps [Walter et al., 2008] and the HERACLES CO maps [Leroy et al., 2009], SFEs were measured and compared with expectations from proposed SFLs and thresholds in Leroy et al. [2008]. However, those samples include only two objects with $M_{\rm HI} > 10^{10}\ M_{\odot}$, and then barely so ($10^{10.01}$ and $10^{10.15}\ M_{\odot}$). The HIghMass galaxies form a unique sample of extremely gas rich massive galaxies in the local universe. Their high $f_{\rm HI}$ may be explained by the suppressed past-integrated SF. Our preliminary IRAM 30-m results (with the EMIR receiver) show that they have unusually high HI-to-H_2 ratios, globally, suggesting that a bottleneck exists in the formation of H_2. With future synthesis observations, we will study in detail the HI-to-H_2 conversion, the SFLs, and the SF threshold. The midplane hydrostatic gas pressure can be estimated from surface densities and velocity dispersions of both gas and star, probing the physical conditions in disks. Subsequently, we will test the theoretical predic-

tion that pressure alone determines the HI-to-H_2 ratio averaged over a radius in disk galaxies.

5.2 Recent Cold Gas Accretion

Rather than hot accretion (slow post-shock cooling from a quasi-spherical halo), cold accretion (clouds, streams, filaments) is theoretically considered an important aspect in the process of galaxy formation at high redshifts, and is perhaps still the dominant mode in low-mass galaxies and in low-density regions today [Kereš et al., 2005]. In the local universe, it is now possible to detect the emission from the diffuse infalling structures with sensitive HI observations. For example, nearby spirals exhibit both extra-planar HI and disturbances (e.g., warped, lopsided, kinematic asymmetric) which may be attributed to gas infall [Sancisi et al., 2008].

We will search for such effects of ongoing minor mergers and recent gas arrival surrounding the HIghMass galaxies, e.g., nearby gas-rich dwarfs, HI tails and filaments, XUV disks, and even bursts of SF. If extra-planar HI is detected in the edge-on systems, its external origin will be tested. Our precursor GMRT map reveals an extended outer layer of HI in UGC 8475, which may be due to recent accretion. One of the HIghMass galaxies, UGC 9234 has a patchy XUV disk, but only two faint spiral arms are seen in the optical. Moreover, some optical disks appear to be lopsided; thus it will be intriguing to know if their HI disks are also lopsided both morphologically and kinematically. In Sancisi et al. [2008], an attempt was made to infer from the WSRT observations at what mass rate fresh HI is accreted by galaxies, and the estimates are 0.1 – 0.2 $M_\odot\ \mathrm{yr}^{-1}$. We

will carry out this experiment to quantify the accretion visible in HI.

Besides the signatures of HI accretion, we will search for the indirect evidence of gas infall, in light of current galaxy evolution models. The model introduced in Fu et al. [2010] suggests that a galaxy residing in a high λ halo behaves similarly as a galaxy that has experienced recent accretion. For example, they both have high $f_{\rm HI}$ and high HI-to-H_2 ratios, which are the characteristics of many HIghMass galaxies. However, if the galaxy also has a high gas surface density, this gas excess is an unambiguous clue of recent accretion. This can be easily tested with the gas maps obtained in our proposed project. Furthermore, adopting a simplified model of gas and stellar density evolution, Fraternali and Tomassetti [2012] presents a method to determine the gas infall rate as a function of time and radius. Taking the SF history (estimated from the SED fitting) as an input, together with the SFL calibrated from the HIghMass galaxies, we will follow the technique in Fraternali and Tomassetti [2012] to quantify the accretion rate by gas density. Those authors have applied this method to the Milky Way and the THINGS disks. We will compare our result with theirs and explore the relationships between gas accretion and galaxy morphology/environment, in order to study the accretion quenching mechanism suggested by cosmological simulations.

5.3 AGN Feedback and Gas Content

Recent HI absorption observations of the radio-loud AGNs detect substantial HI outflow presumably expelled from the host by the radio jets [Morganti et al., 2007]. AGN feedback as a quencher of SF is appealing, either through heating

gas in a galaxy or preventing cold gas from being accreted. An M_* threshold of 10^9 $M_\odot$ was found in Geha et al. [2012], above which some processes become effective to quench SF in the field galaxies. Interestingly, this coincides with the critical M_* first identified in my recent paper [Huang et al., 2012a], above which the slope of the $f_{\rm HI}$ vs. M_* correlation changes. Many current simulations invoke AGN feedback as an ingredient in massive galaxies to solve the overcooling problem [Croton et al., 2006]. Observationally, however, the situation is still unclear. The statistical studies show that AGN hosts tend to be at least as gas rich as quiescent objects, both in terms of HI [Ho et al., 2008, Fabello et al., 2011] and H_2 [Saintonge et al., 2012], which indicates that the energy output of AGN does not influence the large-scale cool gas properties in local galaxies.

Because AGNs may only heat gas close to the center of galaxies, spatially-resolved kinematics of the gas will be needed before pinpointing the actual physical mechanisms responsible for central SF suppression. Within the HIgh-Mass sample, there are five AGNs, two low S/N LINERs, and two composite galaxies with both AGN and SF contributions according to the BPT diagram [Brinchmann et al., 2004]. Among them, four have unobscured broadline emission (type 1). As a start, we will investigate if the HIghMass galaxies lie on the global scaling relationships between AGN and gas, e.g., the trends with Eddington ratio identified in Ho et al. [2008]. Then, through the resolved maps, the imprint of an AGN left on the gas motion and the SF distribution across galaxies will be identified. Finally, an interesting extension is to compare the type 2 sources with their type 1 counterparts and investigate whether they are more gas rich [Ho et al., 2008], as suggested by the prevailing theory that type 2 sources are the evolutionary precursors [Kim et al., 2006].

The Ultimate goal of the research proposed here is to obtain a robust view and refine our understanding of the cold gas evolution at sub-galactic scales; together with the DM component, the gas supply governs the galaxy evolution.

BIBLIOGRAPHY

K. N. Abazajian, J. K. Adelman-McCarthy, M. A. Agüeros, S. S. Allam, C. Allende Prieto, D. An, K. S. J. Anderson, S. F. Anderson, J. Annis, N. A. Bahcall, and et al. The Seventh Data Release of the Sloan Digital Sky Survey. *ApJS*, 182:543, June 2009. doi: 10.1088/0067-0049/182/2/543.

F. B. Abdalla and S. Rawlings. Probing dark energy with baryonic oscillations and future radio surveys of neutral hydrogen. *MNRAS*, 360:27–40, June 2005. doi: 10.1111/j.1365-2966.2005.08650.x.

M. Asplund, N. Grevesse, A. J. Sauval, C. Allende Prieto, and D. Kiselman. Line formation in solar granulation. IV. [O I], O I and OH lines and the photospheric O abundance. *A&A*, 417:751–768, April 2004. doi: 10.1051/0004-6361:20034328.

I. K. Baldry, K. Glazebrook, J. Brinkmann, Ž. Ivezić, R. H. Lupton, R. C. Nichol, and A. S. Szalay. Quantifying the Bimodal Color-Magnitude Distribution of Galaxies. *ApJ*, 600:681–694, January 2004. doi: 10.1086/380092.

I. K. Baldry, M. L. Balogh, R. G. Bower, K. Glazebrook, R. C. Nichol, S. P. Bamford, and T. Budavari. Galaxy bimodality versus stellar mass and environment. *MNRAS*, 373:469–483, December 2006. doi: 10.1111/j.1365-2966.2006.11081.x.

D. G. Barnes, L. Staveley-Smith, W. J. G. de Blok, T. Oosterloo, I. M. Stewart, A. E. Wright, G. D. Banks, R. Bhathal, P. J. Boyce, M. R. Calabretta, M. J. Disney, M. J. Drinkwater, R. D. Ekers, K. C. Freeman, B. K. Gibson, A. J. Green, R. F. Haynes, P. te Lintel Hekkert, P. A. Henning, H. Jerjen, S. Juraszek, M. J. Kesteven, V. A. Kilborn, P. M. Knezek, B. Koribalski, R. C. Kraan-Korteweg, D. F. Malin, M. Marquarding, R. F. Minchin, J. R. Mould, R. M. Price, M. E. Putman, S. D. Ryder, E. M. Sadler, A. Schröder, F. Stootman, R. L. Webster, W. E. Wilson, and T. Ye. The HI Parkes All Sky Survey: southern observations, calibration and robust imaging. *MNRAS*, 322:486–498, April 2001. doi: 10.1046/j.1365-8711.2001.04102.x.

E. J. Barton, M. J. Geller, B. C. Bromley, L. van Zee, and S. J. Kenyon. The Tully-Fisher Relation as a Measure of Luminosity Evolution: A Low-Redshift Baseline for Evolving Galaxies. *AJ*, 121:625–648, February 2001. doi: 10.1086/318759.

A. Begum, J. N. Chengalur, I. D. Karachentsev, M. E. Sharina, and S. S. Kaisin. FIGGS: Faint Irregular Galaxies GMRT Survey - overview, observations and first results. *MNRAS*, 386:1667–1682, May 2008. doi: 10.1111/j.1365-2966.2008.13150.x.

P. S. Behroozi, C. Conroy, and R. H. Wechsler. A Comprehensive Analysis of Uncertainties Affecting the Stellar Mass-Halo Mass Relation for $0 < z < 4$. *ApJ*, 717:379–403, July 2010. doi: 10.1088/0004-637X/717/1/379.

E. F. Bell, D. H. McIntosh, N. Katz, and M. D. Weinberg. The Optical and Near-Infrared Properties of Galaxies. I. Luminosity and Stellar Mass Functions. *ApJS*, 149:289–312, December 2003. doi: 10.1086/378847.

E. Bertin. Automatic Astrometric and Photometric Calibration with SCAMP. In C. Gabriel, C. Arviset, D. Ponz, and S. Enrique, editors, *Astronomical Data Analysis Software and Systems XV*, volume 351 of *Astronomical Society of the Pacific Conference Series*, page 112, July 2006.

E. Bertin and S. Arnouts. SExtractor: Software for source extraction. *A&AS*, 117: 393–404, June 1996.

E. Bertin, Y. Mellier, M. Radovich, G. Missonnier, P. Didelon, and B. Morin. The TERAPIX Pipeline. In D. A. Bohlender, D. Durand, and T. H. Handley, editors, *Astronomical Data Analysis Software and Systems XI*, volume 281 of *Astronomical Society of the Pacific Conference Series*, page 228, 2002.

F. Bigiel, A. Leroy, F. Walter, E. Brinks, W. J. G. de Blok, B. Madore, and M. D. Thornley. The Star Formation Law in Nearby Galaxies on Sub-Kpc Scales. *AJ*, 136:2846–2871, December 2008. doi: 10.1088/0004-6256/136/6/2846.

F. Bigiel, A. Leroy, M. Seibert, F. Walter, L. Blitz, D. Thilker, and B. Madore. Tightly Correlated H I and FUV Emission in the Outskirts of M83. *ApJL*, 720: L31–L35, September 2010a. doi: 10.1088/2041-8205/720/1/L31.

F. Bigiel, A. Leroy, F. Walter, L. Blitz, E. Brinks, W. J. G. de Blok, and B. Madore. Extremely Inefficient Star Formation in the Outer Disks of Nearby Galaxies. *AJ*, 140:1194–1213, November 2010b. doi: 10.1088/0004-6256/140/5/1194.

F. Bigiel, A. K. Leroy, F. Walter, E. Brinks, W. J. G. de Blok, C. Kramer, H. W. Rix, A. Schruba, K.-F. Schuster, A. Usero, and H. W. Wiesemeyer. A Constant Molecular Gas Depletion Time in Nearby Disk Galaxies. *ApJL*, 730:L13, April 2011. doi: 10.1088/2041-8205/730/2/L13.

B. Binggeli, A. Sandage, and G. A. Tammann. Studies of the Virgo Cluster. II - A catalog of 2096 galaxies in the Virgo Cluster area. *AJ*, 90:1681–1759, September 1985. doi: 10.1086/113874.

M. R. Blanton and J. Moustakas. Physical Properties and Environments of Nearby Galaxies. *ARA&A*, 47:159–210, September 2009. doi: 10.1146/annurev-astro-082708-101734.

M. R. Blanton and S. Roweis. K-Corrections and Filter Transformations in the Ultraviolet, Optical, and Near-Infrared. *AJ*, 133:734–754, February 2007. doi: 10.1086/510127.

M. R. Blanton, R. H. Lupton, D. J. Schlegel, M. A. Strauss, J. Brinkmann, M. Fukugita, and J. Loveday. The Properties and Luminosity Function of Extremely Low Luminosity Galaxies. *ApJ*, 631:208–230, September 2005. doi: 10.1086/431416.

M. R. Blanton, E. Kazin, D. Muna, B. A. Weaver, and A. Price-Whelan. Improved Background Subtraction for the Sloan Digital Sky Survey Images. *AJ*, 142:31, July 2011. doi: 10.1088/0004-6256/142/1/31.

S. Boissier and N. Prantzos. Chemo-spectrophotometric evolution of spiral galaxies - II. Main properties of present-day disc galaxies. *MNRAS*, 312:398–416, February 2000. doi: 10.1046/j.1365-8711.2000.03133.x.

S. Boissier, A. Boselli, V. Buat, J. Donas, and B. Milliard. The radial extinction profiles of late-type galaxies. *A&A*, 424:465–476, September 2004. doi: 10.1051/0004-6361:20047024.

S. Boissier, A. Gil de Paz, A. Boselli, B. F. Madore, V. Buat, L. Cortese, D. Burgarella, J. C. Muñoz-Mateos, T. A. Barlow, K. Forster, P. G. Friedman, D. C. Martin, P. Morrissey, S. G. Neff, D. Schiminovich, M. Seibert, T. Small, T. K. Wyder, L. Bianchi, J. Donas, T. M. Heckman, Y.-W. Lee, B. Milliard, R. M. Rich, A. S. Szalay, B. Y. Welsh, and S. K. Yi. Radial Variation of Attenuation and Star Formation in the Largest Late-Type Disks Observed with GALEX. *ApJS*, 173: 524–537, December 2007. doi: 10.1086/516642.

S. Boissier, A. Gil de Paz, A. Boselli, V. Buat, B. Madore, L. Chemin, C. Balkowski, P. Amram, C. Carignan, and W. van Driel. GALEX Observations of Low Surface Brightness Galaxies: UV Color and Star Formation Efficiency. *ApJ*, 681:244–257, July 2008. doi: 10.1086/588580.

A. Boselli, G. Gavazzi, J. Donas, and M. Scodeggio. 1.65 Micron (H Band) Surface Photometry of Galaxies. VI. The History of Star Formation in Normal Late-Type Galaxies. *AJ*, 121:753–767, February 2001. doi: 10.1086/318734.

A. Boselli, S. Boissier, L. Cortese, and G. Gavazzi. The Origin of Dwarf Ellipticals in the Virgo Cluster. *ApJ*, 674:742–767, February 2008. doi: 10.1086/525513.

G. D. Bothun, T. C. Beers, J. R. Mould, and J. P. Huchra. A redshift survey of low-surface-brightness galaxies. I - The basic data. *AJ*, 90:2487–2494, December 1985. doi: 10.1086/113951.

G. D. Bothun, C. D. Impey, D. F. Malin, and J. R. Mould. Discovery of a huge low-surface-brightness galaxy - A protodisk galaxy at low redshift? *AJ*, 94: 23–29, July 1987. doi: 10.1086/114443.

M. S. Bothwell, R. C. Kennicutt, and J. C. Lee. On the interstellar medium and star formation demographics of galaxies in the local universe. *MNRAS*, 400: 154–167, November 2009. doi: 10.1111/j.1365-2966.2009.15471.x.

N. Bouché, A. Dekel, R. Genzel, S. Genel, G. Cresci, N. M. Förster Schreiber, K. L. Shapiro, R. I. Davies, and L. Tacconi. The Impact of Cold Gas Accretion Above a Mass Floor on Galaxy Scaling Relations. *ApJ*, 718:1001–1018, August 2010. doi: 10.1088/0004-637X/718/2/1001.

J. Brinchmann, S. Charlot, S. D. M. White, C. Tremonti, G. Kauffmann, T. Heckman, and J. Brinkmann. The physical properties of star-forming galaxies in the low-redshift Universe. *MNRAS*, 351:1151–1179, July 2004. doi: 10.1111/j.1365-2966.2004.07881.x.

G. Bruzual and S. Charlot. Stellar population synthesis at the resolution of 2003. *MNRAS*, 344:1000–1028, October 2003. doi: 10.1046/j.1365-8711.2003.06897.x.

V. Buat, E. Giovannoli, T. T. Takeuchi, S. Heinis, F.-T. Yuan, D. Burgarella, S. Noll, and J. Iglesias-Páramo. Spectral energy distributions of an AKARI-SDSS-GALEX sample of galaxies. *A&A*, 529:A22, May 2011. doi: 10.1051/0004-6361/201015944.

D. Calzetti. Reddening and Star Formation in Starburst Galaxies. *AJ*, 113:162–184, January 1997. doi: 10.1086/118242.

D. Calzetti, A. L. Kinney, and T. Storchi-Bergmann. Dust extinction of the stellar continua in starburst galaxies: The ultraviolet and optical extinction law. *ApJ*, 429:582–601, July 1994. doi: 10.1086/174346.

D. Calzetti, L. Armus, R. C. Bohlin, A. L. Kinney, J. Koornneef, and T. Storchi-Bergmann. The Dust Content and Opacity of Actively Star-forming Galaxies. *ApJ*, 533:682–695, April 2000. doi: 10.1086/308692.

J. M. Cannon, E. D. Skillman, D. R. Garnett, and R. J. Dufour. Dust in I Zw 18 from Hubble Space Telescope Narrowband Imaging. *ApJ*, 565:931–940, February 2002. doi: 10.1086/324691.

J. M. Cannon, R. Giovanelli, M. P. Haynes, S. Janowiecki, A. Parker, J. J. Salzer, E. A. K. Adams, E. Engstrom, S. Huang, K. B. W. McQuinn, J. Ott, A. Saintonge, E. D. Skillman, J. Allan, G. Erny, P. Fliss, and A. Smith. The Survey of H I in Extremely Low-mass Dwarfs (SHIELD). *ApJL*, 739:L22, September 2011. doi: 10.1088/2041-8205/739/1/L22.

J. A. Cardelli, G. C. Clayton, and J. S. Mathis. The relationship between infrared, optical, and ultraviolet extinction. *ApJ*, 345:245–256, October 1989. doi: 10.1086/167900.

B. Catinella, M. P. Haynes, R. Giovanelli, J. P. Gardner, and A. J. Connolly. A Pilot Survey of H I in Field Galaxies at Redshift z ˜ 0.2. *ApJL*, 685:L13–L17, September 2008. doi: 10.1086/592328.

B. Catinella, D. Schiminovich, G. Kauffmann, S. Fabello, J. Wang, C. Hummels, J. Lemonias, S. M. Moran, R. Wu, R. Giovanelli, M. P. Haynes, T. M. Heckman, A. R. Basu-Zych, M. R. Blanton, J. Brinchmann, T. Budavári, T. Gonçalves, B. D. Johnson, R. C. Kennicutt, B. F. Madore, C. D. Martin, M. R. Rich, L. J. Tacconi, D. A. Thilker, V. Wild, and T. K. Wyder. The GALEX Arecibo SDSS Survey - I. Gas fraction scaling relations of massive galaxies and first data release. *MNRAS*, 403:683–708, April 2010. doi: 10.1111/j.1365-2966.2009.16180.x.

G. Chabrier. Galactic Stellar and Substellar Initial Mass Function. *PASP*, 115: 763–795, July 2003. doi: 10.1086/376392.

S. Charlot and S. M. Fall. A Simple Model for the Absorption of Starlight by Dust in Galaxies. *ApJ*, 539:718–731, August 2000. doi: 10.1086/309250.

L. Cortese and T. M. Hughes. Evolutionary paths to and from the red sequence: star formation and HI properties of transition galaxies at z ˜ 0. *MNRAS*, 400: 1225–1240, December 2009. doi: 10.1111/j.1365-2966.2009.15548.x.

L. Cortese, A. Boselli, V. Buat, G. Gavazzi, S. Boissier, A. Gil de Paz, M. Seibert, B. F. Madore, and D. C. Martin. UV Dust Attenuation in Normal Star-Forming Galaxies. I. Estimating the L_{TIR}/L_{FUV} Ratio. *ApJ*, 637:242–254, January 2006. doi: 10.1086/498296.

L. Cortese, B. Catinella, S. Boissier, A. Boselli, and S. Heinis. The effect of the environment on the H I scaling relations. *MNRAS*, 415:1797–1806, August 2011. doi: 10.1111/j.1365-2966.2011.18822.x.

L. Cortese, S. Boissier, A. Boselli, G. J. Bendo, V. Buat, J. I. Davies, S. Eales, S. Heinis, K. G. Isaak, and S. C. Madden. The GALEX view of the Herschel Reference Survey. Ultraviolet structural properties of nearby galaxies. *A&A*, 544:A101, August 2012. doi: 10.1051/0004-6361/201219312.

S. Courteau. Optical Rotation Curves and Linewidths for Tully-Fisher Applications. *AJ*, 114:2402, December 1997. doi: 10.1086/118656.

L. L. Cowie, A. Songaila, E. M. Hu, and J. G. Cohen. New Insight on Galaxy Formation and Evolution From Keck Spectroscopy of the Hawaii Deep Fields. *AJ*, 112:839, September 1996. doi: 10.1086/118058.

D. J. Croton, V. Springel, S. D. M. White, G. De Lucia, C. S. Frenk, L. Gao, A. Jenkins, G. Kauffmann, J. F. Navarro, and N. Yoshida. The many lives of active galactic nuclei: cooling flows, black holes and the luminosities and colours of galaxies. *MNRAS*, 365:11–28, January 2006. doi: 10.1111/j.1365-2966.2005.09675.x.

R. Davé, K. Finlator, and B. D. Oppenheimer. An analytic model for the evolution of the stellar, gas and metal content of galaxies. *MNRAS*, 421:98–107, March 2012. doi: 10.1111/j.1365-2966.2011.20148.x.

R. D. Davies and B. M. Lewis. Neutral hydrogen in Virgo cluster galaxies. *MNRAS*, 165:231–244, 1973.

G. de Vaucouleurs, A. de Vaucouleurs, H. G. Corwin, Jr., R. J. Buta, G. Paturel, and P. Fouqué. *Third Reference Catalogue of Bright Galaxies. Volume I: Explanations and references. Volume II: Data for galaxies between 0^h and 12^h. Volume III: Data for galaxies between 12^h and 24^h.* 1991.

M. Disney and S. Phillipps. Icebergs and crouching giants. *Nature*, 329:203, September 1987. doi: 10.1038/329203a0.

M. J. Disney, J. D. Romano, D. A. Garcia-Appadoo, A. A. West, J. J. Dalcanton, and L. Cortese. Galaxies appear simpler than expected. *Nature*, 455:1082–1084, October 2008. doi: 10.1038/nature07366.

J. L. Donovan, P. Serra, J. H. van Gorkom, S. C. Trager, T. Oosterloo, J. E. Hibbard, R. Morganti, D. Schiminovich, and J. M. van der Hulst. ESO 381 - 47: An Early-Type Galaxy with Extended H I and a Star-Forming Ring. *AJ*, 137: 5037–5056, June 2009. doi: 10.1088/0004-6256/137/6/5037.

B. T. Draine, D. A. Dale, G. Bendo, K. D. Gordon, J. D. T. Smith, L. Armus, C. W. Engelbracht, G. Helou, R. C. Kennicutt, Jr., A. Li, H. Roussel, F. Walter, D. Calzetti, J. Moustakas, E. J. Murphy, G. H. Rieke, C. Bot, D. J. Hollenbach, K. Sheth, and H. I. Teplitz. Dust Masses, PAH Abundances, and Starlight Intensities in the SINGS Galaxy Sample. *ApJ*, 663:866–894, July 2007. doi: 10.1086/518306.

S. Fabello, B. Catinella, R. Giovanelli, G. Kauffmann, M. P. Haynes, T. M. Heckman, and D. Schiminovich. ALFALFA H I data stacking - I. Does the bulge quench ongoing star formation in early-type galaxies? *MNRAS*, 411:993–1012, February 2011. doi: 10.1111/j.1365-2966.2010.17742.x.

F. Fraternali and M. Tomassetti. Estimating gas accretion in disc galaxies using the Kennicutt-Schmidt law. *MNRAS*, 426:2166–2177, November 2012. doi: 10.1111/j.1365-2966.2012.21650.x.

J. Fu, Q. Guo, G. Kauffmann, and M. R. Krumholz. The atomic-to-molecular transition and its relation to the scaling properties of galaxy discs in the local Universe. *MNRAS*, 409:515–530, December 2010. doi: 10.1111/j.1365-2966.2010.17342.x.

A. Gallazzi, S. Charlot, J. Brinchmann, S. D. M. White, and C. A. Tremonti. The ages and metallicities of galaxies in the local universe. *MNRAS*, 362:41–58, September 2005. doi: 10.1111/j.1365-2966.2005.09321.x.

F. Galliano, S. C. Madden, A. P. Jones, C. D. Wilson, J.-P. Bernard, and F. Le Peintre. ISM properties in low-metallicity environments. II. The dust spectral energy distribution of NGC 1569. *A&A*, 407:159–176, August 2003. doi: 10.1051/0004-6361:20030814.

D. A. Garcia-Appadoo, A. A. West, J. J. Dalcanton, L. Cortese, and M. J. Disney. Correlations among the properties of galaxies found in a blind HI survey, which also have SDSS optical data. *MNRAS*, 394:340–356, March 2009. doi: 10.1111/j.1365-2966.2008.14292.x.

D. R. Garnett. The Luminosity-Metallicity Relation, Effective Yields, and Metal Loss in Spiral and Irregular Galaxies. *ApJ*, 581:1019–1031, December 2002. doi: 10.1086/344301.

G. Gavazzi, D. Pierini, and A. Boselli. The phenomenology of disk galaxies. *A&A*, 312:397–408, August 1996.

G. Gavazzi, A. Boselli, A. Donati, P. Franzetti, and M. Scodeggio. Introducing GOLDMine: A new galaxy database on the WEB. *A&A*, 400:451–455, March 2003. doi: 10.1051/0004-6361:20030026.

G. Gavazzi, M. Fumagalli, V. Galardo, F. Grossetti, A. Boselli, R. Giovanelli, M. P. Haynes, and S. Fabello. Hα3: an Hα imaging survey of HI selected galaxies from ALFALFA. I. Catalogue in the Local Supercluster. *A&A*, 545: A16, September 2012. doi: 10.1051/0004-6361/201218788.

G. Gavazzi, M. Fumagalli, M. Fossati, V. Galardo, F. Grossetti, A. Boselli, R. Giovanelli, and M. P. Haynes. Hα3: an Hα imaging survey of HI selected galaxies from ALFALFA. II. Star formation properties of galaxies in the Virgo cluster and surroundings. *A&A*, 553:A89, May 2013. doi: 10.1051/0004-6361/201218789.

M. Geha, M. R. Blanton, R. Yan, and J. L. Tinker. A Stellar Mass Threshold for Quenching of Field Galaxies. *ApJ*, 757:85, September 2012. doi: 10.1088/0004-637X/757/1/85.

A. Gil de Paz, S. Boissier, B. F. Madore, M. Seibert, Y. H. Joe, A. Boselli, T. K. Wyder, D. Thilker, L. Bianchi, S.-C. Rey, R. M. Rich, T. A. Barlow, T. Conrow,

K. Forster, P. G. Friedman, D. C. Martin, P. Morrissey, S. G. Neff, D. Schiminovich, T. Small, J. Donas, T. M. Heckman, Y.-W. Lee, B. Milliard, A. S. Szalay, and S. Yi. The GALEX Ultraviolet Atlas of Nearby Galaxies. *ApJS*, 173:185–255, December 2007. doi: 10.1086/516636.

R. Giovanelli and M. P. Haynes. Gas deficiency in cluster galaxies - A comparison of nine clusters. *ApJ*, 292:404–425, May 1985. doi: 10.1086/163170.

R. Giovanelli, M. P. Haynes, J. J. Salzer, G. Wegner, L. N. da Costa, and W. Freudling. Extinction in SC galaxies. *AJ*, 107:2036–2054, June 1994. doi: 10.1086/117014.

R. Giovanelli, M. P. Haynes, J. J. Salzer, G. Wegner, L. N. da Costa, and W. Freudling. Dependence on Luminosity of Photometric Properties of Disk Galaxies: Surface Brightness, Size, and Internal Extinction. *AJ*, 110:1059, September 1995. doi: 10.1086/117586.

R. Giovanelli, M. P. Haynes, T. Herter, N. P. Vogt, G. Wegner, J. J. Salzer, L. N. da Costa, and W. Freudling. The I band Tully-Fisher relation for cluster galaxies: data presentation. *AJ*, 113:22–52, January 1997. doi: 10.1086/118233.

R. Giovanelli, M. P. Haynes, B. R. Kent, P. Perillat, B. Catinella, G. L. Hoffman, E. Momjian, J. L. Rosenberg, A. Saintonge, K. Spekkens, S. Stierwalt, N. Brosch, K. L. Masters, C. M. Springob, I. D. Karachentsev, V. E. Karachentseva, R. A. Koopmann, E. Muller, W. van Driel, and L. van Zee. The Arecibo Legacy Fast ALFA Survey. II. Results of Precursor Observations. *AJ*, 130:2613–2624, December 2005a. doi: 10.1086/497432.

R. Giovanelli, M. P. Haynes, B. R. Kent, P. Perillat, A. Saintonge, N. Brosch, B. Catinella, G. L. Hoffman, S. Stierwalt, K. Spekkens, M. S. Lerner, K. L. Masters, E. Momjian, J. L. Rosenberg, C. M. Springob, A. Boselli, V. Charmandaris, J. K. Darling, J. Davies, D. Garcia Lambas, G. Gavazzi, C. Giovanardi, E. Hardy, L. K. Hunt, A. Iovino, I. D. Karachentsev, V. E. Karachentseva, R. A. Koopmann, C. Marinoni, R. Minchin, E. Muller, M. Putman, C. Pantoja, J. J. Salzer, M. Scodeggio, E. Skillman, J. M. Solanes, C. Valotto, W. van Driel, and L. van Zee. The Arecibo Legacy Fast ALFA Survey. I. Science Goals, Survey Design, and Strategy. *AJ*, 130:2598–2612, December 2005b. doi: 10.1086/497431.

R. Giovanelli, M. P. Haynes, B. R. Kent, A. Saintonge, S. Stierwalt, A. Altaf, T. Balonek, N. Brosch, S. Brown, B. Catinella, A. Furniss, J. Goldstein, G. L. Hoffman, R. A. Koopmann, D. A. Kornreich, B. Mahmood, A. M. Martin, K. L. Masters, A. Mitschang, E. Momjian, P. H. Nair, J. L. Rosenberg, and B. Walsh. The Arecibo Legacy Fast ALFA Survey. III. H I Source Catalog of the Northern Virgo Cluster Region. *AJ*, 133:2569–2583, June 2007. doi: 10.1086/516635.

M. L. P. Gunawardhana, A. M. Hopkins, R. G. Sharp, S. Brough, E. Taylor, J. Bland-Hawthorn, C. Maraston, R. J. Tuffs, C. C. Popescu, D. Wijesinghe, D. H. Jones, S. Croom, E. Sadler, S. Wilkins, S. P. Driver, J. Liske, P. Norberg, I. K. Baldry, S. P. Bamford, J. Loveday, J. A. Peacock, A. S. G. Robotham, D. B. Zucker, Q. A. Parker, C. J. Conselice, E. Cameron, C. S. Frenk, D. T. Hill, L. S. Kelvin, K. Kuijken, B. F. Madore, B. Nichol, H. R. Parkinson, K. A. Pimbblet, M. Prescott, W. J. Sutherland, D. Thomas, and E. van Kampen. Galaxy and Mass Assembly (GAMA): the star formation rate dependence of the stellar initial mass function. *MNRAS*, 415:1647–1662, August 2011. doi: 10.1111/j.1365-2966.2011.18800.x.

Q. Guo, S. White, C. Li, and M. Boylan-Kolchin. How do galaxies populate dark matter haloes? *MNRAS*, 404:1111–1120, May 2010. doi: 10.1111/j.1365-2966.2010.16341.x.

G. Hallenbeck, E. Papastergis, S. Huang, M. P. Haynes, R. Giovanelli, A. Boselli, S. Boissier, S. Heinis, L. Cortese, and S. Fabello. Gas-bearing Early-type Dwarf Galaxies in Virgo: Evidence for Recent Accretion. *AJ*, 144:87, September 2012. doi: 10.1088/0004-6256/144/3/87.

M. P. Haynes, R. Giovanelli, J. J. Salzer, G. Wegner, W. Freudling, L. N. da Costa, T. Herter, and N. P. Vogt. The I-Band Tully-Fisher Relation for SC Galaxies: Optical Imaging Data. *AJ*, 117:1668–1687, April 1999. doi: 10.1086/300817.

M. P. Haynes, R. Giovanelli, A. M. Martin, K. M. Hess, A. Saintonge, E. A. K. Adams, G. Hallenbeck, G. L. Hoffman, S. Huang, B. R. Kent, R. A. Koopmann, E. Papastergis, S. Stierwalt, T. J. Balonek, D. W. Craig, S. J. U. Higdon, D. A. Kornreich, J. R. Miller, A. A. O'Donoghue, R. P. Olowin, J. L. Rosenberg, K. Spekkens, P. Troischt, and E. M. Wilcots. The Arecibo Legacy Fast ALFA Survey: The α.40 H I Source Catalog, Its Characteristics and Their Impact on the Derivation of the H I Mass Function. *AJ*, 142:170, November 2011. doi: 10.1088/0004-6256/142/5/170.

J. F. Helmboldt, R. A. M. Walterbos, G. D. Bothun, and K. O'Neil. Star Formation in H I-selected Galaxies. II. H II Region Properties. *ApJ*, 630:824–836, September 2005. doi: 10.1086/432500.

X. Hernandez and B. Cervantes-Sodi. A dimensional study of disc galaxies. *MNRAS*, 368:351–360, May 2006. doi: 10.1111/j.1365-2966.2006.10115.x.

X. Hernandez, C. Park, B. Cervantes-Sodi, and Y.-Y. Choi. Empirical distributions of galactic λ spin parameters from the Sloan Digital Sky Survey. *MNRAS*, 375:163–170, February 2007. doi: 10.1111/j.1365-2966.2006.11274.x.

L. C. Ho, J. Darling, and J. E. Greene. Properties of Active Galaxies Deduced from H I Observations. *ApJ*, 681:128–140, July 2008. doi: 10.1086/588207.

M. Hoeft, G. Yepes, S. Gottlöber, and V. Springel. Dwarf galaxies in voids: suppressing star formation with photoheating. *MNRAS*, 371:401–414, September 2006. doi: 10.1111/j.1365-2966.2006.10678.x.

D. W. Hogg, M. R. Blanton, D. J. Eisenstein, J. E. Gunn, D. J. Schlegel, I. Zehavi, N. A. Bahcall, J. Brinkmann, I. Csabai, D. P. Schneider, D. H. Weinberg, and D. G. York. The Overdensities of Galaxy Environments as a Function of Luminosity and Color. *ApJL*, 585:L5–L9, March 2003. doi: 10.1086/374238.

A. M. Hopkins, C. J. Miller, R. C. Nichol, A. J. Connolly, M. Bernardi, P. L. Gómez, T. Goto, C. A. Tremonti, J. Brinkmann, Ž. Ivezić, and D. Q. Lamb. Star Formation Rate Indicators in the Sloan Digital Sky Survey. *ApJ*, 599:971–991, December 2003. doi: 10.1086/379608.

S. Huang, M. P. Haynes, R. Giovanelli, and J. Brinchmann. The Arecibo Legacy Fast ALFA Survey: The Galaxy Population Detected by ALFALFA. *ApJ*, 756: 113, September 2012a. doi: 10.1088/0004-637X/756/2/113.

S. Huang, M. P. Haynes, R. Giovanelli, J. Brinchmann, S. Stierwalt, and S. G. Neff. Gas, Stars, and Star Formation in ALFALFA Dwarf Galaxies. *AJ*, 143: 133, June 2012b. doi: 10.1088/0004-6256/143/6/133.

D. A. Hunter and B. G. Elmegreen. Star Formation Properties of a Large Sample of Irregular Galaxies. *AJ*, 128:2170–2205, November 2004. doi: 10.1086/424615.

D. A. Hunter, B. G. Elmegreen, and B. C. Ludka. Galex Ultraviolet Imaging of Dwarf Galaxies and Star Formation Rates. *AJ*, 139:447–475, February 2010. doi: 10.1088/0004-6256/139/2/447.

C. Impey and G. Bothun. Low Surface Brightness Galaxies. *ARA&A*, 35:267–307, 1997. doi: 10.1146/annurev.astro.35.1.267.

P. A. James, N. S. Shane, J. E. Beckman, A. Cardwell, C. A. Collins, J. Etherton, R. S. de Jong, K. Fathi, J. H. Knapen, R. F. Peletier, S. M. Percival, D. L. Pollacco, M. S. Seigar, S. Stedman, and I. A. Steele. The Hα galaxy survey. I. The galaxy sample, Hα narrow-band observations and star formation parameters for 334 galaxies. *A&A*, 414:23–43, January 2004. doi: 10.1051/0004-6361:20031568.

R. A. Jansen, D. Fabricant, M. Franx, and N. Caldwell. Spectrophotometry of Nearby Field Galaxies: The Data. *ApJS*, 126:331–397, February 2000a. doi: 10.1086/313308.

R. A. Jansen, M. Franx, D. Fabricant, and N. Caldwell. Surface Photometry of Nearby Field Galaxies: The Data. *ApJS*, 126:271–329, February 2000b. doi: 10.1086/313303.

B. D. Johnson, D. Schiminovich, M. Seibert, M. A. Treyer, S. Charlot, T. M. Heckman, D. C. Martin, S. Salim, G. Kauffmann, L. Bianchi, J. Donas, P. G. Friedman, Y.-W. Lee, B. F. Madore, B. Milliard, P. Morrissey, S. G. Neff, R. M. Rich, A. S. Szalay, K. Forster, T. A. Barlow, T. Conrow, T. Small, and T. K. Wyder. Dissecting Galaxy Colors with GALEX, SDSS, and Spitzer. *ApJL*, 644:L109–L112, June 2006. doi: 10.1086/505741.

B. D. Johnson, D. Schiminovich, M. Seibert, M. Treyer, D. C. Martin, T. A. Barlow, K. Forster, P. G. Friedman, P. Morrissey, S. G. Neff, T. Small, T. K. Wyder, L. Bianchi, J. Donas, T. M. Heckman, Y.-W. Lee, B. F. Madore, B. Milliard, R. M. Rich, A. S. Szalay, B. Y. Welsh, and S. K. Yi. Ultraviolet through Infrared Spectral Energy Distributions from 1000 SDSS Galaxies: Dust Attenuation. *ApJS*, 173:392–403, December 2007. doi: 10.1086/522960.

S. J. Kannappan. Linking Gas Fractions to Bimodalities in Galaxy Properties. *ApJL*, 611:L89–L92, August 2004. doi: 10.1086/423785.

S. J. Kannappan, J. M. Guie, and A. J. Baker. E/S0 Galaxies on the Blue Color-Stellar Mass Sequence at z = 0: Fading Mergers or Future Spirals? *AJ*, 138: 579–597, August 2009. doi: 10.1088/0004-6256/138/2/579.

I. D. Karachentsev and S. S. Kaisin. More Galaxies in the Local Volume Imaged in Hα. *AJ*, 140:1241–1253, November 2010. doi: 10.1088/0004-6256/140/5/1241.

V. E. Karachentseva. The Catalogue of Isolated Galaxies,. *Astrofizicheskie Issledovaniia Izvestiya Spetsial'noj Astrofizicheskoj Observatorii*, 8:3–49, 1973.

G. Kauffmann, T. M. Heckman, S. D. M. White, S. Charlot, C. Tremonti, J. Brinchmann, G. Bruzual, E. W. Peng, M. Seibert, M. Bernardi, M. Blanton, J. Brinkmann, F. Castander, I. Csábai, M. Fukugita, Z. Ivezic, J. A. Munn, R. C. Nichol, N. Padmanabhan, A. R. Thakar, D. H. Weinberg, and D. York. Stellar masses and star formation histories for 10^5 galaxies from the Sloan Digital Sky Survey. *MNRAS*, 341:33–53, May 2003a. doi: 10.1046/j.1365-8711.2003.06291.x.

G. Kauffmann, T. M. Heckman, S. D. M. White, S. Charlot, C. Tremonti, E. W. Peng, M. Seibert, J. Brinkmann, R. C. Nichol, M. SubbaRao, and D. York. The dependence of star formation history and internal structure on stellar mass for 10^5 low-redshift galaxies. *MNRAS*, 341:54–69, May 2003b. doi: 10.1046/j.1365-8711.2003.06292.x.

R. C. Kennicutt and N. J. Evans. Star Formation in the Milky Way and Nearby Galaxies. *ARA&A*, 50:531–608, September 2012. doi: 10.1146/annurev-astro-081811-125610.

R. C. Kennicutt, Jr. Star Formation in Galaxies Along the Hubble Sequence. *ARA&A*, 36:189–232, 1998a. doi: 10.1146/annurev.astro.36.1.189.

R. C. Kennicutt, Jr. The Global Schmidt Law in Star-forming Galaxies. *ApJ*, 498: 541, May 1998b. doi: 10.1086/305588.

R. C. Kennicutt, Jr. The rate of star formation in normal disk galaxies. *ApJ*, 272: 54–67, September 1983. doi: 10.1086/161261.

R. C. Kennicutt, Jr. The star formation law in galactic disks. *ApJ*, 344:685–703, September 1989. doi: 10.1086/167834.

R. C. Kennicutt, Jr., L. Armus, G. Bendo, D. Calzetti, D. A. Dale, B. T. Draine, C. W. Engelbracht, K. D. Gordon, A. D. Grauer, G. Helou, D. J. Hollenbach, T. H. Jarrett, L. J. Kewley, C. Leitherer, A. Li, S. Malhotra, M. W. Regan, G. H. Rieke, M. J. Rieke, H. Roussel, J.-D. T. Smith, M. D. Thornley, and F. Walter. SINGS: The SIRTF Nearby Galaxies Survey. *PASP*, 115:928–952, August 2003. doi: 10.1086/376941.

R. C. Kennicutt, Jr., J. C. Lee, S. J. Funes, José G., S. Sakai, and S. Akiyama. An Hα Imaging Survey of Galaxies in the Local 11 Mpc Volume. *ApJS*, 178:247–279, October 2008. doi: 10.1086/590058.

D. Kereš, N. Katz, D. H. Weinberg, and R. Davé. How do galaxies get their gas? *MNRAS*, 363:2–28, October 2005. doi: 10.1111/j.1365-2966.2005.09451.x.

L. J. Kewley, M. J. Geller, R. A. Jansen, and M. A. Dopita. The Hα and Infrared Star Formation Rates for the Nearby Field Galaxy Survey. *AJ*, 124:3135–3143, December 2002. doi: 10.1086/344487.

L. J. Kewley, D. Rupke, H. J. Zahid, M. J. Geller, and E. J. Barton. Metallicity Gradients and Gas Flows in Galaxy Pairs. *ApJL*, 721:L48–L52, September 2010. doi: 10.1088/2041-8205/721/1/L48.

J.-h. Kim and J. Lee. How does the surface density and size of disc galaxies measured in hydrodynamic simulations correlate with the halo spin parameter? *MNRAS*, 432:1701–1708, June 2013. doi: 10.1093/mnras/stt632.

M. Kim, L. C. Ho, and M. Im. Constraints on the Star Formation Rate in Active Galaxies. *ApJ*, 642:702–710, May 2006. doi: 10.1086/501422.

S. Kim, S.-C. Rey, T. Lisker, and S. T. Sohn. Color-Magnitude Relations of Early-type Dwarf Galaxies in the Virgo Cluster: An Ultraviolet Perspective. *ApJL*, 721:L72–L77, September 2010. doi: 10.1088/2041-8205/721/1/L72.

A. A. Klypin, S. Trujillo-Gomez, and J. Primack. Dark Matter Halos in the Standard Cosmological Model: Results from the Bolshoi Simulation. *ApJ*, 740:102, October 2011. doi: 10.1088/0004-637X/740/2/102.

X. Kong, S. Charlot, J. Brinchmann, and S. M. Fall. Star formation history and dust content of galaxies drawn from ultraviolet surveys. *MNRAS*, 349:769–778, April 2004. doi: 10.1111/j.1365-2966.2004.07556.x.

A. V. Kravtsov. The Size-Virial Radius Relation of Galaxies. *ApJL*, 764:L31, February 2013. doi: 10.1088/2041-8205/764/2/L31.

M. R. Krumholz, C. F. McKee, and J. Tumlinson. The Atomic-to-Molecular Transition in Galaxies. I. An Analytic Approximation for Photodissociation Fronts in Finite Clouds. *ApJ*, 689:865–882, December 2008. doi: 10.1086/592490.

M. R. Krumholz, C. F. McKee, and J. Tumlinson. The Star Formation Law in Atomic and Molecular Gas. *ApJ*, 699:850–856, July 2009. doi: 10.1088/0004-637X/699/1/850.

M. R. Krumholz, A. Dekel, and C. F. McKee. A Universal, Local Star Formation Law in Galactic Clouds, nearby Galaxies, High-redshift Disks, and Starbursts. *ApJ*, 745:69, January 2012. doi: 10.1088/0004-637X/745/1/69.

A. U. Landolt. UBVRI photometric standard stars in the magnitude range 11.5-16.0 around the celestial equator. *AJ*, 104:340–371, July 1992. doi: 10.1086/116242.

R. H. Lang, P. J. Boyce, V. A. Kilborn, R. F. Minchin, M. J. Disney, C. A. Jordan, M. Grossi, D. A. Garcia, K. C. Freeman, S. Phillipps, and A. E. Wright. First results from the HI Jodrell All Sky Survey: inclination-dependent selection effects in a 21-cm blind survey. *MNRAS*, 342:738–758, July 2003. doi: 10.1046/j.1365-8711.2003.06535.x.

J. C. Lee, R. C. Kennicutt, S. J. Funes, José G., S. Sakai, and S. Akiyama. The Star Formation Demographics of Galaxies in the Local Volume. *ApJL*, 671: L113–L116, December 2007. doi: 10.1086/526341.

J. C. Lee, A. Gil de Paz, C. Tremonti, R. C. Kennicutt, Jr., S. Salim, M. Bothwell, D. Calzetti, J. Dalcanton, D. Dale, C. Engelbracht, S. J. J. G. Funes, B. Johnson, S. Sakai, E. Skillman, L. van Zee, F. Walter, and D. Weisz. Comparison of Hα and UV Star Formation Rates in the Local Volume: Systematic Discrepancies for Dwarf Galaxies. *ApJ*, 706:599, November 2009a. doi: 10.1088/0004-637X/706/1/599.

J. C. Lee, R. C. Kennicutt, Jr., S. J. J. G. Funes, S. Sakai, and S. Akiyama. Dwarf Galaxy Starburst Statistics in the Local Volume. *ApJ*, 692:1305, February 2009b. doi: 10.1088/0004-637X/692/2/1305.

J. C. Lee, A. Gil de Paz, R. C. Kennicutt, Jr., M. Bothwell, J. Dalcanton, J. José G. Funes S., B. D. Johnson, S. Sakai, E. Skillman, C. Tremonti, and L. van Zee. A GALEX Ultraviolet Imaging Survey of Galaxies in the Local Volume. *ApJS*, 192:6, January 2011. doi: 10.1088/0067-0049/192/1/6.

J. J. Lemonias, D. Schiminovich, D. Thilker, T. K. Wyder, D. C. Martin, M. Seibert, M. A. Treyer, L. Bianchi, T. M. Heckman, B. F. Madore, and R. M. Rich. The Space Density of Extended Ultraviolet (XUV) Disks in the Local Universe and Implications for Gas Accretion onto Galaxies. *ApJ*, 733:74, June 2011. doi: 10.1088/0004-637X/733/2/74.

A. Leroy, A. D. Bolatto, J. D. Simon, and L. Blitz. The Molecular Interstellar Medium of Dwarf Galaxies on Kiloparsec Scales: A New Survey for CO in Northern, IRAS-detected Dwarf Galaxies. *ApJ*, 625:763–784, June 2005. doi: 10.1086/429578.

A. Leroy, A. Bolatto, S. Stanimirovic, N. Mizuno, F. Israel, and C. Bot. The Spitzer Survey of the Small Magellanic Cloud: Far-Infrared Emission and Cold Gas in the Small Magellanic Cloud. *ApJ*, 658:1027–1046, April 2007. doi: 10.1086/511150.

A. K. Leroy, F. Walter, E. Brinks, F. Bigiel, W. J. G. de Blok, B. Madore, and M. D. Thornley. The Star Formation Efficiency in Nearby Galaxies: Measuring Where Gas Forms Stars Effectively. *AJ*, 136:2782–2845, December 2008. doi: 10.1088/0004-6256/136/6/2782.

A. K. Leroy, F. Walter, F. Bigiel, A. Usero, A. Weiss, E. Brinks, W. J. G. de Blok, R. C. Kennicutt, K.-F. Schuster, C. Kramer, H. W. Wiesemeyer, and H. Roussel. Heracles: The HERA CO Line Extragalactic Survey. *AJ*, 137:4670–4696, June 2009. doi: 10.1088/0004-6256/137/6/4670.

C. Li, G. Kauffmann, J. Fu, J. Wang, B. Catinella, S. Fabello, D. Schiminovich, and W. Zhang. The clustering of galaxies as a function of their photometrically estimated atomic gas content. *MNRAS*, 424:1471–1482, August 2012. doi: 10.1111/j.1365-2966.2012.21337.x.

U. Lisenfeld, I. Hermelo, M. Relaño, R. J. Tuffs, C. C. Popescu, J. Fischera, and B. Groves. Dust in dwarf galaxies: The case of NGC 4214. In R. J. Tuffs and C. C. Popescu, editors, *IAU Symposium*, volume 284 of *IAU Symposium*, pages 152–155, August 2012. doi: 10.1017/S1743921312008952.

F. Mannucci, G. Cresci, R. Maiolino, A. Marconi, and A. Gnerucci. A fundamental relation between mass, star formation rate and metallicity in local and high-redshift galaxies. *MNRAS*, 408:2115–2127, November 2010. doi: 10.1111/j.1365-2966.2010.17291.x.

F. Marinacci, J. Binney, F. Fraternali, C. Nipoti, L. Ciotti, and P. Londrillo. The mode of gas accretion on to star-forming galaxies. *MNRAS*, 404:1464–1474, May 2010. doi: 10.1111/j.1365-2966.2010.16352.x.

A. M. Martin, E. Papastergis, R. Giovanelli, M. P. Haynes, C. M. Springob, and S. Stierwalt. The Arecibo Legacy Fast ALFA Survey. X. The H I Mass Function

and Ω_H I from the 40% ALFALFA Survey. *ApJ*, 723:1359–1374, November 2010. doi: 10.1088/0004-637X/723/2/1359.

A. M. Martin, R. Giovanelli, M. P. Haynes, and L. Guzzo. The Clustering Characteristics of H I-selected Galaxies from the 40% ALFALFA Survey. *ApJ*, 750: 38, May 2012. doi: 10.1088/0004-637X/750/1/38.

P. Martin and J.-R. Roy. The influence of bars on the chemical composition of spiral galaxies. *ApJ*, 424:599–614, April 1994. doi: 10.1086/173917.

I. Martín-Navarro, J. Bakos, I. Trujillo, J. H. Knapen, E. Athanassoula, A. Bosma, S. Comerón, B. G. Elmegreen, S. Erroz-Ferrer, D. A. Gadotti, A. Gil de Paz, J. L. Hinz, L. C. Ho, B. W. Holwerda, T. Kim, J. Laine, E. Laurikainen, K. Menéndez-Delmestre, T. Mizusawa, J.-C. Muñoz-Mateos, M. W. Regan, H. Salo, M. Seibert, and K. Sheth. A unified picture of breaks and truncations in spiral galaxies from SDSS and S^4G imaging. *MNRAS*, 427:1102–1134, December 2012. doi: 10.1111/j.1365-2966.2012.21929.x.

K. L. Masters. *Galaxy flows in and around the Local Supercluster*. PhD thesis, Cornell University, New York, USA, 2005.

K. L. Masters, M. Mosleh, A. K. Romer, R. C. Nichol, S. P. Bamford, K. Schawinski, C. J. Lintott, D. Andreescu, H. C. Campbell, B. Crowcroft, I. Doyle, E. M. Edmondson, P. Murray, M. J. Raddick, A. Slosar, A. S. Szalay, and J. Vandenberg. Galaxy Zoo: passive red spirals. *MNRAS*, 405:783–799, June 2010. doi: 10.1111/j.1365-2966.2010.16503.x.

G. R. Meurer, T. M. Heckman, and D. Calzetti. Dust Absorption and the Ultraviolet Luminosity Density at Z˜3 as Calibrated by Local Starburst Galaxies. *ApJ*, 521:64–80, August 1999. doi: 10.1086/307523.

G. R. Meurer, D. J. Hanish, H. C. Ferguson, P. M. Knezek, V. A. Kilborn, M. E. Putman, R. C. Smith, B. Koribalski, M. Meyer, M. S. Oey, E. V. Ryan-Weber, M. A. Zwaan, T. M. Heckman, R. C. Kennicutt, Jr., J. C. Lee, R. L. Webster, J. Bland-Hawthorn, M. A. Dopita, K. C. Freeman, M. T. Doyle, M. J. Drinkwater, L. Staveley-Smith, and J. Werk. The Survey for Ionization in Neutral Gas Galaxies. I. Description and Initial Results. *ApJS*, 165:307–337, July 2006. doi: 10.1086/504685.

M. Meyer. Exploring the HI Universe with ASKAP. In *Panoramic Radio Astronomy: Wide-field 1-2 GHz Research on Galaxy Evolution*, 2009.

M. J. Meyer, M. A. Zwaan, R. L. Webster, L. Staveley-Smith, E. Ryan-Weber, M. J. Drinkwater, D. G. Barnes, M. Howlett, V. A. Kilborn, J. Stevens, M. Waugh, M. J. Pierce, R. Bhathal, W. J. G. de Blok, M. J. Disney, R. D. Ekers, K. C. Freeman, D. A. Garcia, B. K. Gibson, J. Harnett, P. A. Henning, H. Jerjen, M. J. Kesteven, P. M. Knezek, B. S. Koribalski, S. Mader, M. Marquarding, R. F.

Minchin, J. O'Brien, T. Oosterloo, R. M. Price, M. E. Putman, S. D. Ryder, E. M. Sadler, I. M. Stewart, F. Stootman, and A. E. Wright. The HIPASS catalogue - I. Data presentation. *MNRAS*, 350:1195–1209, June 2004. doi: 10.1111/j.1365-2966.2004.07710.x.

H. J. Mo, S. S. McGaugh, and G. D. Bothun. Spatial distribution of low-surface-brightness galaxies. *MNRAS*, 267:129, March 1994.

H. J. Mo, S. Mao, and S. D. M. White. The formation of galactic discs. *MNRAS*, 295:319–336, April 1998. doi: 10.1046/j.1365-8711.1998.01227.x.

S. M. Moran, G. Kauffmann, T. M. Heckman, J. Gracia-Carpio, A. Saintonge, B. Catinella, J. Wang, Y.-M. Chen, L. Tacconi, D. Schiminovich, P. Cox, R. Giovanelli, M. Haynes, and C. Kramer. UGC8802: A Massive Disk Galaxy in Formation. *ApJ*, 720:1126–1135, September 2010. doi: 10.1088/0004-637X/720/2/1126.

R. Morganti, P. T. de Zeeuw, T. A. Oosterloo, R. M. McDermid, D. Krajnović, M. Cappellari, F. Kenn, A. Weijmans, and M. Sarzi. Neutral hydrogen in nearby elliptical and lenticular galaxies: the continuing formation of early-type galaxies. *MNRAS*, 371:157–169, September 2006. doi: 10.1111/j.1365-2966.2006.10681.x.

R. Morganti, J. Holt, L. Saripalli, T. A. Oosterloo, and C. N. Tadhunter. IC 5063: AGN driven outflow of warm and cold gas. *A&A*, 476:735–743, December 2007. doi: 10.1051/0004-6361:20077888.

P. Morrissey, T. Conrow, T. A. Barlow, T. Small, M. Seibert, T. K. Wyder, T. Budavári, S. Arnouts, P. G. Friedman, K. Forster, D. C. Martin, S. G. Neff, D. Schiminovich, L. Bianchi, J. Donas, T. M. Heckman, Y.-W. Lee, B. F. Madore, B. Milliard, R. M. Rich, A. S. Szalay, B. Y. Welsh, and S. K. Yi. The Calibration and Data Products of GALEX. *ApJS*, 173:682–697, December 2007. doi: 10.1086/520512.

J. C. Muñoz-Mateos, S. Boissier, A. Gil de Paz, J. Zamorano, R. C. Kennicutt, Jr., J. Moustakas, N. Prantzos, and J. Gallego. Radial Distribution of Stars, Gas, and Dust in SINGS Galaxies. III. Modeling the Evolution of the Stellar Component in Galaxy Disks. *ApJ*, 731:10, April 2011. doi: 10.1088/0004-637X/731/1/10.

P. Noterdaeme, P. Petitjean, C. Ledoux, and R. Srianand. Evolution of the cosmological mass density of neutral gas from Sloan Digital Sky Survey II - Data Release 7. *A&A*, 505:1087–1098, October 2009. doi: 10.1051/0004-6361/200912768.

D. Obreschkow, H.-R. Klöckner, I. Heywood, F. Levrier, and S. Rawlings. A Virtual Sky with Extragalactic H I and CO Lines for the Square Kilometre Array

and the Atacama Large Millimeter/Submillimeter Array. *ApJ*, 703:1890–1903, October 2009. doi: 10.1088/0004-637X/703/2/1890.

J. B. Oke and J. E. Gunn. Secondary standard stars for absolute spectrophotometry. *ApJ*, 266:713–717, March 1983. doi: 10.1086/160817.

T. Oosterloo, R. Morganti, A. Crocker, E. Jütte, M. Cappellari, T. de Zeeuw, D. Krajnović, R. McDermid, H. Kuntschner, M. Sarzi, and A.-M. Weijmans. Early-type galaxies in different environments: an HI view. *MNRAS*, 409:500–514, December 2010. doi: 10.1111/j.1365-2966.2010.17351.x.

E. C. Ostriker, C. F. McKee, and A. K. Leroy. Regulation of Star Formation Rates in Multiphase Galactic Disks: A Thermal/Dynamical Equilibrium Model. *ApJ*, 721:975–994, October 2010. doi: 10.1088/0004-637X/721/2/975.

E. Papastergis, A. M. Martin, R. Giovanelli, and M. P. Haynes. The Velocity Width Function of Galaxies from the 40% ALFALFA Survey: Shedding Light on the Cold Dark Matter Overabundance Problem. *ApJ*, 739:38, September 2011. doi: 10.1088/0004-637X/739/1/38.

C. Park and Y.-Y. Choi. Morphology Segregation of Galaxies in Color-Color Gradient Space. *ApJL*, 635:L29–L32, December 2005. doi: 10.1086/499243.

T. E. Pickering, C. D. Impey, J. H. van Gorkom, and G. D. Bothun. Neutral Hydrogen Distributions and Kinematics of Giant Low Surface=20 Brightness Disk Galaxies. *AJ*, 114:1858, November 1997. doi: 10.1086/118611.

M. Pohlen and I. Trujillo. The structure of galactic disks. Studying late-type spiral galaxies using SDSS. *A&A*, 454:759–772, August 2006. doi: 10.1051/0004-6361:20064883.

C. C. Popescu, R. J. Tuffs, M. A. Dopita, J. Fischera, N. D. Kylafis, and B. F. Madore. Modelling the spectral energy distribution of galaxies. V. The dust and PAH emission SEDs of disk galaxies. *A&A*, 527:A109, March 2011. doi: 10.1051/0004-6361/201015217.

A. M. Portas, E. Brinks, M. E. Filho, A. Usero, E. M. Dyke, and P.-E. Belles. NGC765 - a disturbed HI giant. *MNRAS*, 407:1674–1688, September 2010. doi: 10.1111/j.1365-2966.2010.16994.x.

M. S. Roberts. The Content of Galaxies: Stars and Gas. *ARA&A*, 1:149, 1963. doi: 10.1146/annurev.aa.01.090163.001053.

J. L. Rosenberg and S. E. Schneider. The Arecibo Dual-Beam Survey: The H I Mass Function of Galaxies. *ApJ*, 567:247–257, March 2002. doi: 10.1086/338377.

R. Roškar, V. P. Debattista, G. S. Stinson, T. R. Quinn, T. Kaufmann, and J. Wadsley. Beyond Inside-Out Growth: Formation and Evolution of Disk Outskirts. *ApJL*, 675:L65–L68, March 2008. doi: 10.1086/586734.

S. Roychowdhury, J. N. Chengalur, A. Begum, and I. D. Karachentsev. Star formation in extremely faint dwarf galaxies. *MNRAS*, 397:1435–1453, August 2009. doi: 10.1111/j.1365-2966.2009.14931.x.

A. Saintonge, G. Kauffmann, C. Kramer, L. J. Tacconi, C. Buchbender, B. Catinella, S. Fabello, J. Graciá-Carpio, J. Wang, L. Cortese, J. Fu, R. Genzel, R. Giovanelli, Q. Guo, M. P. Haynes, T. M. Heckman, M. R. Krumholz, J. Lemonias, C. Li, S. Moran, N. Rodriguez-Fernandez, D. Schiminovich, K. Schuster, and A. Sievers. COLD GASS, an IRAM legacy survey of molecular gas in massive galaxies - I. Relations between H_2, H I, stellar content and structural properties. *MNRAS*, 415:32–60, July 2011a. doi: 10.1111/j.1365-2966.2011.18677.x.

A. Saintonge, G. Kauffmann, J. Wang, C. Kramer, L. J. Tacconi, C. Buchbender, B. Catinella, J. Graciá-Carpio, L. Cortese, S. Fabello, J. Fu, R. Genzel, R. Giovanelli, Q. Guo, M. P. Haynes, T. M. Heckman, M. R. Krumholz, J. Lemonias, C. Li, S. Moran, N. Rodriguez-Fernandez, D. Schiminovich, K. Schuster, and A. Sievers. COLD GASS, an IRAM legacy survey of molecular gas in massive galaxies - II. The non-universality of the molecular gas depletion time-scale. *MNRAS*, 415:61–76, July 2011b. doi: 10.1111/j.1365-2966.2011.18823.x.

A. Saintonge, L. J. Tacconi, S. Fabello, J. Wang, B. Catinella, R. Genzel, J. Graciá-Carpio, C. Kramer, S. Moran, T. M. Heckman, D. Schiminovich, K. Schuster, and S. Wuyts. The Impact of Interactions, Bars, Bulges, and Active Galactic Nuclei on Star Formation Efficiency in Local Massive Galaxies. *ApJ*, 758:73, October 2012. doi: 10.1088/0004-637X/758/2/73.

S. Sakai, R. C. Kennicutt, Jr., and C. Moss. A Deep, Wide-field Hα Survey of Nearby Clusters of Galaxies: Data. *ApJS*, 199:36, April 2012. doi: 10.1088/0067-0049/199/2/36.

S. Salim, S. Charlot, R. M. Rich, G. Kauffmann, T. M. Heckman, T. A. Barlow, L. Bianchi, Y.-I. Byun, J. Donas, K. Forster, P. G. Friedman, P. N. Jelinsky, Y.-W. Lee, B. F. Madore, R. F. Malina, D. C. Martin, B. Milliard, P. Morrissey, S. G. Neff, D. Schiminovich, M. Seibert, O. H. W. Siegmund, T. Small, A. S. Szalay, B. Y. Welsh, and T. K. Wyder. New Constraints on the Star Formation Histories and Dust Attenuation of Galaxies in the Local Universe from GALEX. *ApJL*, 619:L39–L42, January 2005. doi: 10.1086/424800.

S. Salim, R. M. Rich, S. Charlot, J. Brinchmann, B. D. Johnson, D. Schiminovich, M. Seibert, R. Mallery, T. M. Heckman, K. Forster, P. G. Friedman, D. C. Martin, P. Morrissey, S. G. Neff, T. Small, T. K. Wyder, L. Bianchi, J. Donas, Y.-W.

Lee, B. F. Madore, B. Milliard, A. S. Szalay, B. Y. Welsh, and S. K. Yi. UV Star Formation Rates in the Local Universe. *ApJS*, 173:267–292, December 2007. doi: 10.1086/519218.

J. R. Sánchez-Gallego, J. H. Knapen, C. D. Wilson, P. Barmby, M. Azimlu, and S. Courteau. The JCMT Nearby Galaxies Legacy Survey - VII. Hα imaging and massive star formation properties. *MNRAS*, 422:3208–3248, June 2012. doi: 10.1111/j.1365-2966.2012.20845.x.

R. Sancisi, F. Fraternali, T. Oosterloo, and T. van der Hulst. Cold gas accretion in galaxies. *A&ARv*, 15:189–223, June 2008. doi: 10.1007/s00159-008-0010-0.

A. Sandage. Star formation rates, galaxy morphology, and the Hubble sequence. *A&A*, 161:89–101, June 1986.

D. Schiminovich, T. K. Wyder, D. C. Martin, B. D. Johnson, S. Salim, M. Seibert, M. A. Treyer, T. Budavári, C. Hoopes, M. Zamojski, T. A. Barlow, K. G. Forster, P. G. Friedman, P. Morrissey, S. G. Neff, T. A. Small, L. Bianchi, J. Donas, T. M. Heckman, Y.-W. Lee, B. F. Madore, B. Milliard, R. M. Rich, A. S. Szalay, B. Y. Welsh, and S. Yi. The UV-Optical Color Magnitude Diagram. II. Physical Properties and Morphological Evolution On and Off of a Star-forming Sequence. *ApJS*, 173:315–341, December 2007. doi: 10.1086/524659.

D. Schiminovich, B. Catinella, G. Kauffmann, S. Fabello, J. Wang, C. Hummels, J. Lemonias, S. M. Moran, R. Wu, R. Giovanelli, M. P. Haynes, T. M. Heckman, A. R. Basu-Zych, M. R. Blanton, J. Brinchmann, T. Budavári, T. Gonçalves, B. D. Johnson, R. C. Kennicutt, B. F. Madore, C. D. Martin, M. R. Rich, L. J. Tacconi, D. A. Thilker, V. Wild, and T. K. Wyder. The GALEX Arecibo SDSS Survey - II. The star formation efficiency of massive galaxies. *MNRAS*, 408: 919–934, October 2010. doi: 10.1111/j.1365-2966.2010.17210.x.

D. J. Schlegel, D. P. Finkbeiner, and M. Davis. Maps of Dust Infrared Emission for Use in Estimation of Reddening and Cosmic Microwave Background Radiation Foregrounds. *ApJ*, 500:525, June 1998. doi: 10.1086/305772.

J. Schombert, T. Maciel, and S. McGaugh. Stellar Populations and the Star Formation Histories of LSB Galaxies – Part I: Optical and Hα Imaging. *Advances in Astronomy*, 2011, 2011. doi: 10.1155/2011/143698.

J. M. Schombert, G. D. Bothun, S. E. Schneider, and S. S. McGaugh. A catalog of low surface brightness galaxies - List II. *AJ*, 103:1107–1133, April 1992. doi: 10.1086/116129.

A. Schruba, A. K. Leroy, F. Walter, F. Bigiel, E. Brinks, W. J. G. de Blok, G. Dumas, C. Kramer, E. Rosolowsky, K. Sandstrom, K. Schuster, A. Usero,

A. Weiss, and H. Wiesemeyer. A Molecular Star Formation Law in the Atomic-gas-dominated Regime in Nearby Galaxies. *AJ*, 142:37, August 2011. doi: 10.1088/0004-6256/142/2/37.

P. Serra, T. Oosterloo, R. Morganti, K. Alatalo, L. Blitz, M. Bois, F. Bournaud, M. Bureau, M. Cappellari, A. F. Crocker, R. L. Davies, T. A. Davis, P. T. de Zeeuw, P.-A. Duc, E. Emsellem, S. Khochfar, D. Krajnović, H. Kuntschner, P.-Y. Lablanche, R. M. McDermid, T. Naab, M. Sarzi, N. Scott, S. C. Trager, A.-M. Weijmans, and L. M. Young. The ATLAS^{3D} project - XIII. Mass and morphology of H I in early-type galaxies as a function of environment. *MNRAS*, 422: 1835–1862, May 2012. doi: 10.1111/j.1365-2966.2012.20219.x.

Z. Shao, Q. Xiao, S. Shen, H. J. Mo, X. Xia, and Z. Deng. Inclination-dependent Luminosity Function of Spiral Galaxies in the Sloan Digital Sky Survey: Implications for Dust Extinction. *ApJ*, 659:1159–1171, April 2007. doi: 10.1086/511131.

J. M. Solanes, T. Sanchis, E. Salvador-Solé, R. Giovanelli, and M. P. Haynes. The Three-dimensional Structure of the Virgo Cluster Region from Tully-Fisher and H I Data. *AJ*, 124:2440–2452, November 2002. doi: 10.1086/344074.

D. Sprayberry, C. D. Impey, G. D. Bothun, and M. J. Irwin. Properties of the class of giant low surface brightness spiral galaxies. *AJ*, 109:558–571, February 1995. doi: 10.1086/117300.

C. M. Springob, M. P. Haynes, and R. Giovanelli. Morphology, Environment, and the H I Mass Function. *ApJ*, 621:215–226, March 2005. doi: 10.1086/427432.

C. M. Springob, K. L. Masters, M. P. Haynes, R. Giovanelli, and C. Marinoni. SFI++. II. A New I-Band Tully-Fisher Catalog, Derivation of Peculiar Velocities, and Data Set Properties. *ApJS*, 172:599–614, October 2007. doi: 10.1086/519527.

K. R. Stewart, A. M. Brooks, J. S. Bullock, A. H. Maller, J. Diemand, J. Wadsley, and L. A. Moustakas. Angular Momentum Acquisition in Galaxy Halos. *ApJ*, 769:74, May 2013. doi: 10.1088/0004-637X/769/1/74.

S. Stierwalt, M. P. Haynes, R. Giovanelli, B. R. Kent, A. M. Martin, A. Saintonge, I. D. Karachentsev, and V. E. Karachentseva. The Arecibo Legacy Fast Alfa Survey. IX. The Leo Region H I Catalog, Group Membership, and the H I Mass Function for the Leo I Group. *AJ*, 138:338–361, August 2009. doi: 10.1088/0004-6256/138/2/338.

M. A. Strauss, D. H. Weinberg, R. H. Lupton, V. K. Narayanan, J. Annis, M. Bernardi, M. Blanton, S. Burles, A. J. Connolly, J. Dalcanton, M. Doi, D. Eisenstein, J. A. Frieman, M. Fukugita, J. E. Gunn, Ž. Ivezić, S. Kent, R. S. J.

Kim, G. R. Knapp, R. G. Kron, J. A. Munn, H. J. Newberg, R. C. Nichol, S. Okamura, T. R. Quinn, M. W. Richmond, D. J. Schlegel, K. Shimasaku, M. SubbaRao, A. S. Szalay, D. Vanden Berk, M. S. Vogeley, B. Yanny, N. Yasuda, D. G. York, and I. Zehavi. Spectroscopic Target Selection in the Sloan Digital Sky Survey: The Main Galaxy Sample. *AJ*, 124:1810–1824, September 2002. doi: 10.1086/342343.

E. N. Taylor, A. M. Hopkins, I. K. Baldry, M. J. I. Brown, S. P. Driver, L. S. Kelvin, D. T. Hill, A. S. G. Robotham, J. Bland-Hawthorn, D. H. Jones, R. G. Sharp, D. Thomas, J. Liske, J. Loveday, P. Norberg, J. A. Peacock, S. P. Bamford, S. Brough, M. Colless, E. Cameron, C. J. Conselice, S. M. Croom, C. S. Frenk, M. Gunawardhana, K. Kuijken, R. C. Nichol, H. R. Parkinson, S. Phillipps, K. A. Pimbblet, C. C. Popescu, M. Prescott, W. J. Sutherland, R. J. Tuffs, E. van Kampen, and D. Wijesinghe. Galaxy And Mass Assembly (GAMA): stellar mass estimates. *MNRAS*, 418:1587–1620, December 2011. doi: 10.1111/j.1365-2966.2011.19536.x.

D. A. Thilker, L. Bianchi, G. Meurer, A. Gil de Paz, S. Boissier, B. F. Madore, A. Boselli, A. M. N. Ferguson, J. C. Muñoz-Mateos, G. J. Madsen, S. Hameed, R. A. Overzier, K. Forster, P. G. Friedman, D. C. Martin, P. Morrissey, S. G. Neff, D. Schiminovich, M. Seibert, T. Small, T. K. Wyder, J. Donas, T. M. Heckman, Y.-W. Lee, B. Milliard, R. M. Rich, A. S. Szalay, B. Y. Welsh, and S. K. Yi. A Search for Extended Ultraviolet Disk (XUV-Disk) Galaxies in the Local Universe. *ApJS*, 173:538–571, December 2007. doi: 10.1086/523853.

T. X. Thuan, M. Sauvage, and S. Madden. Dust in an Extremely Metal-Poor Galaxy: Mid-infrared Observations ofSBS 0335-052. *ApJ*, 516:783–787, May 1999. doi: 10.1086/307152.

M. C. Toribio, J. M. Solanes, R. Giovanelli, M. P. Haynes, and A. M. Martin. H I Content and Optical Properties of Field Galaxies from the ALFALFA Survey. II. Multivariate Analysis of a Galaxy Sample in Low-density Environments. *ApJ*, 732:93, May 2011. doi: 10.1088/0004-637X/732/2/93.

C. A. Tremonti, T. M. Heckman, G. Kauffmann, J. Brinchmann, S. Charlot, S. D. M. White, M. Seibert, E. W. Peng, D. J. Schlegel, A. Uomoto, M. Fukugita, and J. Brinkmann. The Origin of the Mass-Metallicity Relation: Insights from 53,000 Star-forming Galaxies in the Sloan Digital Sky Survey. *ApJ*, 613:898–913, October 2004. doi: 10.1086/423264.

M. Treyer, D. Schiminovich, B. Johnson, M. Seibert, T. Wyder, T. A. Barlow, T. Conrow, K. Forster, P. G. Friedman, D. C. Martin, P. Morrissey, S. G. Neff, T. Small, L. Bianchi, J. Donas, T. M. Heckman, Y.-W. Lee, B. F. Madore, B. Milliard, R. M. Rich, A. S. Szalay, B. Y. Welsh, and S. K. Yi. Extinction-corrected Star Formation Rates Empirically Derived from Ultraviolet-Optical Colors. *ApJS*, 173:256–266, December 2007. doi: 10.1086/521794.

R. B. Tully, M. A. W. Verheijen, M. J. Pierce, J.-S. Huang, and R. J. Wainscoat. The Ursa Major Cluster of Galaxies.I.Cluster Definition and Photometric Data. *AJ*, 112:2471, December 1996. doi: 10.1086/118196.

P. G. van Dokkum. Cosmic-Ray Rejection by Laplacian Edge Detection. *PASP*, 113:1420–1427, November 2001. doi: 10.1086/323894.

W. van Driel, H. van Woerden, U. J. Schwarz, and J. S. Gallagher, III. Distribution and motions of atomic hydrogen in lenticular galaxies. V - NGC 4203: A gas-rich S0 with an inner and an outer H I ring. *A&A*, 191:201–214, February 1988.

L. Verdes-Montenegro, J. Sulentic, U. Lisenfeld, S. Leon, D. Espada, E. Garcia, J. Sabater, and S. Verley. The AMIGA project. I. Optical characterization of the CIG catalog. *A&A*, 436:443–455, June 2005. doi: 10.1051/0004-6361:20042280.

F. Walter, J. M. Cannon, H. Roussel, G. J. Bendo, D. Calzetti, D. A. Dale, B. T. Draine, G. Helou, R. C. Kennicutt, Jr., J. Moustakas, G. H. Rieke, L. Armus, C. W. Engelbracht, K. Gordon, D. J. Hollenbach, J. Lee, A. Li, M. J. Meyer, E. J. Murphy, M. W. Regan, J.-D. T. Smith, E. Brinks, W. J. G. de Blok, F. Bigiel, and M. D. Thornley. Dust and Atomic Gas in Dwarf Irregular Galaxies of the M81 Group: The SINGS and THINGS View. *ApJ*, 661:102–114, May 2007. doi: 10.1086/514807.

F. Walter, E. Brinks, W. J. G. de Blok, F. Bigiel, R. C. Kennicutt, Jr., M. D. Thornley, and A. Leroy. THINGS: The H I Nearby Galaxy Survey. *AJ*, 136:2563, December 2008. doi: 10.1088/0004-6256/136/6/2563.

J. Wang, G. Kauffmann, R. Overzier, B. Catinella, D. Schiminovich, T. M. Heckman, S. M. Moran, M. P. Haynes, R. Giovanelli, and X. Kong. The GALEX Arecibo SDSS survey - III. Evidence for the inside-out formation of Galactic discs. *MNRAS*, 412:1081–1097, April 2011. doi: 10.1111/j.1365-2966.2010.17962.x.

M. Wardle and G. R. Knapp. The statistical distribution of the neutral-hydrogen content of S0 galaxies. *AJ*, 91:23–48, January 1986. doi: 10.1086/113976.

A. A. West, D. A. Garcia-Appadoo, J. J. Dalcanton, M. J. Disney, C. M. Rockosi, and Ž. Ivezić. H I-Selected Galaxies in the Sloan Digital Sky Survey. II. The Colors of Gas-Rich Galaxies. *AJ*, 138:796–807, September 2009. doi: 10.1088/0004-6256/138/3/796.

A. A. West, D. A. Garcia-Appadoo, J. J. Dalcanton, M. J. Disney, C. M. Rockosi, Ž. Ivezić, M. C. Bentz, and J. Brinkmann. H I-Selected Galaxies in the Sloan Digital Sky Survey. I. Optical Data. *AJ*, 139:315–328, February 2010. doi: 10.1088/0004-6256/139/2/315.

V. Wild, S. Charlot, J. Brinchmann, T. Heckman, O. Vince, C. Pacifici, and J. Chevallard. Empirical determination of the shape of dust attenuation curves in star-forming galaxies. *MNRAS*, 417:1760–1786, November 2011. doi: 10.1111/j.1365-2966.2011.19367.x.

O. I. Wong, E. V. Ryan-Weber, D. A. Garcia-Appadoo, R. L. Webster, L. Staveley-Smith, M. A. Zwaan, M. J. Meyer, D. G. Barnes, V. A. Kilborn, R. Bhathal, W. J. G. de Blok, M. J. Disney, M. T. Doyle, M. J. Drinkwater, R. D. Ekers, K. C. Freeman, B. K. Gibson, S. Gurovich, J. Harnett, P. A. Henning, H. Jerjen, M. J. Kesteven, P. M. Knezek, B. S. Koribalski, S. Mader, M. Marquarding, R. F. Minchin, J. O'Brien, M. E. Putman, S. D. Ryder, E. M. Sadler, J. Stevens, I. M. Stewart, F. Stootman, and M. Waugh. The Northern HIPASS catalogue - data presentation, completeness and reliability measures. *MNRAS*, 371:1855–1864, October 2006. doi: 10.1111/j.1365-2966.2006.10846.x.

T. K. Wyder, D. C. Martin, D. Schiminovich, M. Seibert, T. Budavári, M. A. Treyer, T. A. Barlow, K. Forster, P. G. Friedman, P. Morrissey, S. G. Neff, T. Small, L. Bianchi, J. Donas, T. M. Heckman, Y.-W. Lee, B. F. Madore, B. Milliard, R. M. Rich, A. S. Szalay, B. Y. Welsh, and S. K. Yi. The UV-Optical Galaxy Color-Magnitude Diagram. I. Basic Properties. *ApJS*, 173:293–314, December 2007. doi: 10.1086/521402.

T. Xiao, T. Wang, H. Wang, H. Zhou, H. Lu, and X. Dong. Dust reddening in star-forming galaxies. *MNRAS*, 421:486–501, March 2012. doi: 10.1111/j.1365-2966.2011.20327.x.

W. Zhang, C. Li, G. Kauffmann, H. Zou, B. Catinella, S. Shen, Q. Guo, and R. Chang. Estimating the HI gas fractions of galaxies in the local Universe. *MNRAS*, 397:1243–1253, August 2009. doi: 10.1111/j.1365-2966.2009.15050.x.

M. A. Zwaan, F. H. Briggs, D. Sprayberry, and E. Sorar. The H i Mass Function of Galaxies from a Deep Survey in the 21 Centimeter Line. *ApJ*, 490:173, November 1997. doi: 10.1086/304872.

M. A. Zwaan, M. J. Meyer, L. Staveley-Smith, and R. L. Webster. The HIPASS catalogue: Ω_{HI} and environmental effects on the HI mass function of galaxies. *MNRAS*, 359:L30–L34, May 2005. doi: 10.1111/j.1745-3933.2005.00029.x.